Dynamic Performance of Small Fishing Vessels in Waves with Varied Loading Conditions

Muhammad Iqbal

A thesis presented in fulfilment of the requirements for the degree of
Doctor of Philosophy

Department of Naval Architecture, Ocean and Marine Engineering
University of Strathclyde
2024

Declarations

This thesis is the result of the Author's original research. It has been composed by the Author and has not been previously submitted for examination which has led to the award of a degree.

Signed: Date:

Acknowledgements

First and foremost, I am profoundly grateful to Allah the Almighty, the Most Gracious, and the Most Merciful, for granting me the strength and patience to undertake and complete this PhD journey. Without His mercies, none of this would have been possible. May blessings and peace always be upon Prophet Muhammad PBUH.

I would like to express my heartfelt appreciation to the many individuals and organisations who have supported me during this challenging yet rewarding journey. Without their support, this thesis would not have been possible.

First and foremost, I owe an immense debt of gratitude to my three supervisors, whose expertise, mentorship, and patience have guided me through the complexities of my research. Professor Atilla Incecik, my main supervisor, please accept my deepest gratitude for your knowledge, support, and advice you gave to me. Your profound knowledge and insight have been invaluable to my academic development. Your passion for research has consistently inspired me to strive for excellence. Dr Tahsin Tezdogan, who accepted me as a PhD student and opened the gate to this PhD journey. Your guidance was invaluable. I am deeply grateful for your continuous encouragement. Your dedication to my progress has been a source of immense motivation.

Another my gratitude goes to Dr Momchil Terziev, who has been a constant and steadfast guide throughout this journey. Your tireless efforts, thoughtful insights, and unwavering support have gone beyond the role of a supervisor. You not only helped me refine my research but also taught me how to approach challenges with patience and perseverance. I am truly thankful to you for your kindness, and for always pushing me to achieve more than I thought. I will always remember you for pursuing me in STEM for Britain competition. This thesis would not have reached its current form without your dedication and belief in my potential.

I would also like to extend my sincere thanks to my PhD funder, BPSDM – Diponegoro University. Their generous financial support made this research possible, and their investment in my education has allowed me to focus wholeheartedly on my academic work. I am honoured to have had the opportunity to represent my institution on an international stage, and I hope my work reflects the values and commitment to excellence that Diponegoro University upholds.

Finally, I would like to express my deepest love and appreciation to my parents, Endang Hariswanda and Umi Kalsum, for their endless encouragement and sacrifices. You have always been there to guide, support, and advise me—thank you from the bottom of my heart. I could not have finished my PhD without you. I will always remember how you held me up when I was on the verge of giving up at the beginning. You always listened to my problems with genuine care. Your unwavering support will always be remembered. To my little brother and sister, Ahmad Bayhaqi and Endah

Mahmudah, for always being my biggest supporters—I owe you more than words can express. This accomplishment is as much yours as it is mine. Your encouragement has meant the world to me. My PhD life felt like I was with you, and you both made me feel less alone. To my wife, Maya Sukma Widyakumara, and my children, Farhan Z.A, Hasna Z.A, and Naureen Z.A, I sincerely hope that, through this achievement, I grow into someone you can look upon with pride, knowing that every step I take is with you in my heart and with the desire to make you proud.

To my friends, I extend heartfelt gratitude. You have been a vital source of comfort and motivation, offering not only intellectual support but also the much-needed laughter and companionship during the most challenging times. Thank you for being there to listen, encourage, and remind me that there is always light at the end of the tunnel.

This thesis is dedicated to all of you. Without your support, this milestone would not have been possible. Thank you from the bottom of my heart.

Table of Contents

List of Figures

List of Tables

Abstract

The widespread occurrence of accidents involving fishing vessels is an important issue that needs to be addressed by the maritime community. Most of these accidents involve small fishing vessels. On the other hand, small fishing vessels can support sustainability in fishing by preventing overfishing, unlike the large-scale fishing industry. In Indonesia, the government aims to enhance food security through the maritime sector by providing fishermen with many small fishing vessels. Therefore, research on enhancing safety for fishing vessels is essential. This thesis explores this topic by investigating the dynamic performance of small fishing vessels in waves under varied loading conditions.

Fishing vessels operate in different areas. With the same hull form and loading conditions, the dynamic responses of the fishing vessel vary. Therefore, an operability assessment is required to determine the seaworthiness of the vessel in a given area. There are eleven fishing management areas in Indonesia. This thesis focuses on the Java Sea as the operational area for the investigated fishing vessels. A new methodology is developed to assess a single operability index for a single fishing vessel, applicable across multiple loading conditions. A case study assessing a single operability index for three different sizes of fishing vessels provides recommendations of the appropriate vessel size for operations in the Java Sea.

A detailed investigation into stability in waves is conducted, centring on parametric roll, a type of stability failure highlighted by the International Maritime Organization (IMO) using Computational Fluid Dynamics (CFD). It is discovered that small fishing boats can experience parametric roll, in contrast to previous understanding of the phenomenon. The GM ratio, that is, ratio between the amplitude GM in waves and the GM in calm water, is not only an indicator of the magnitude of the parametric roll amplitude but also of the heave and pitch amplitudes for the same hull form and displacement. This discovery is subsequently used to develop a novel optimisation methodology. Radius of Gyration in the Y-Axis (R_y) is identified as an effective indicator to determine heave and pitch amplitudes in head waves. A minimal R_y results in a lower moment of inertia, which increases the pitch damping ratio and subsequently reduces the pitch amplitude. Both GM ratio and R_y are straightforward to calculate and require no functional evaluations that are costly or time-consuming. These parameters can be used to indirectly assess seakeeping performance and are suitable as objective functions in seakeeping optimisation, helping to accelerate the optimisation process by an order of magnitude compared to existing practice.

Hydrodynamic optimisation can be an effective way to enhance ship performance, either by improving seakeeping and stability in waves or by minimising total resistance to reduce carbon footprint, promote decarbonisation, and lower fuel consumption. A new methodology based on the aforementioned indicators is developed in hull form optimisation, enabling the simultaneous minimisation of total resistance and dynamic

responses at sea, thereby avoiding the need for multi-objective optimisation. The hull form is optimised to achieve minimal total resistance, and during this process, the longitudinal centre of gravity (LCG) and vertical centre of gravity (KG) of each hull form variation are adjusted to achieve minimal R_y. As a result, the optimal hull form achieves both minimal total resistance and minimal dynamic responses.

1. Introduction

1.1. Research Motivation

Indonesia, an archipelagic country, comprises 17,504 islands with a coastline length of 108,000 km. Its exclusive economic zone covers approximately 6,400,000 km^2, which is 3.37 times larger than its land area. This vast maritime area significantly contributes to the local population's welfare and sustenance, with fishing vessels playing a crucial role in supplying fish. Proper utilisation of these resources is vital, making the research on fishing vessel and ensuring the safety of fishing activities in Indonesia through comprehensive research is essential.

To support local fishers, the Ministry of Maritime Affairs and Fisheries of the Republic of Indonesia has allocated fishing boats. From 2010 to 2014, the Ministry distributed 1,000 fishing boats with a 30 Gross Tonnage (GT) capacity to local fishers. In 2016, an additional 3,500 fibreglass fishing boats, ranging from 5 GT to 30 GT, were allocated. This policy aims to enhance Indonesia's food security through the maritime sector (Bappenas, 2010). According to Statistics Indonesia (2019), the total number of fishing vessels from 2000 to 2016 was 543,845, both with and without engines.

However, fishing at sea is inherently risky, with a high mortality rate due to accidents. The UN’s Food and Agriculture Organization (2000) reported that the mortality rate for fishers is significantly higher than the national average in several countries: up to 30 times higher in the US, 21 times higher in Italy, and 143 per 100,000 in Australia compared to the national average of 8.1 per 100,000.

Research on fishing vessel accidents highlights various causes and types. Wang et al. (2005) and Ugurlu et al. (2020) presented data on different types of fishing vessel accidents, as shown in Table 1.1. Some researchers studied a particular accident. Davis et al. (2019) and Obeng et al. (2022a) investigated the primary causes of capsizing, identifying human factors such as training and experience as critical factors. Domeh et al. (2021) examined man overboard (MOB) incidents, providing valuable safety information for small fishing vessel operations.

Small ships, particularly those shorter than 24 metres, experience a higher rate of accidents than larger commercial vessels (Caamaño et al., 2018; Ugurlu et al., 2020; Wang et al., 2005). Stability-related accidents are more frequent in these small vessels due to their poor seakeeping performance (González et al., 2012).

Accidents can be attributed either to human factors or environmental conditions. Human factors include fatigue, multitasking occupation, alcohol and drug use, and improper loading practices, which lead to collisions and sinkings (Ugurlu et al., 2020). Obeng et al. (2022a) found that inadequate training and experience, alcohol use, and improper handling of equipment significantly increase the risk of capsizing.

The second group, environmental conditions such as weather, operational area, season, and vessel characteristics also play a crucial role in accidents (Jin and Thunberg, 2005). These factors affect the physical comfort and occupational health of the crew, with harsh conditions exacerbating the risks. Research on the impact of environmental conditions on fishing boats is essential to prevent accidents. Environmental factor also influences the human factor that contributes to the ship accident, as stated in the study of Obeng et al. (2022b). This thesis focuses on preventing fishing vessel accidents by enhancing fishing boat safety through improvements in seakeeping and stability aspects.

Table 1.1. Accident types for fishing vessels

Sources	Accident Type	Total	Percentage
(Ugurlu et al., 2020)	Collision	56	27.05
	Sinking	55	26.57
	Occupational Accident	39	18.84
	Grounding	26	12.56
	Man Overboard	26	12.56
	Fire-Explosion	2	0.97
	Others	3	1.45
(Wang et al., 2005)	Machinery damage	233	62.97
	Foundering and flooding	57	15.41
	Grounding	31	8.38
	Collisions and contacts	22	5.95
	Fires and explosions	15	4.05
	Capsizing and listing	7	1.89
	Heavy weather damage	2	0.81
	Others	2	0.54

In Indonesia, fish management areas are divided into eleven regions according to the Minister of Maritime Affairs and Fisheries Regulation No. 18/2014, as shown in Figure 1.1 and discussed by Muawanah et al. (2018). Based on this, regardless of their size, small fishing vessels must be designed to handle such environmental condition while ensuring safety during fishing. Thus, conducting a seakeeping assessment for fishing vessels by involving the operational area is required.

The evaluation of seakeeping in regular waves, depicted by RAO curves, may not comprehensively assess seakeeping performance across various operational areas. Typically, this analysis merely compares RAO curves to ascertain superior performance among multiple options, as demonstrated by Sayli et al. (2007), Bagheri et al. (2014), and Khosravi Babadi and Ghassemi (2024).

Conversely, seakeeping analysis in irregular waves (spectral analysis) can offer a more detailed appraisal of seakeeping performance compared to regular wave analysis, albeit with certain limitations, such as the exclusion of Wave Scatter Diagrams (WSD) for the operational area. These diagrams illustrate the frequency of *Hs*-*Tp* combinations annually or seasonally. Irregular analysis focuses solely on specific combinations of peak period (*Tp*) and Significant Wave Height (*Hs*) to construct the sea spectrum and determine ship responses. These responses are then evaluated according to seakeeping criteria to determine whether they meet the required standards, similar to the approach in Tello et al. (2009) and (Wulandari et al., 2024).

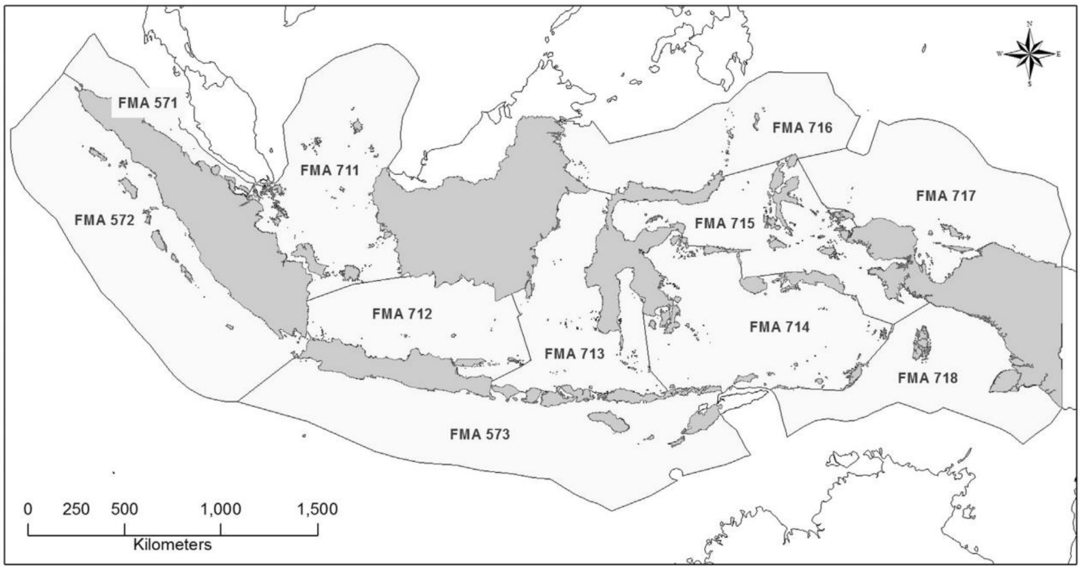

Figure 1.1. Fisheries management area (FMA) in Indonesia (Muawanah et al., 2018)

To provide a comprehensive evaluation of seakeeping performance, the operability analysis can be used by considering the predetermined seakeeping criteria and the ship's operational area. This analysis involves quantifying motion performance in waves in relation to mission requirements and aids in making decisions about preferred vessel designs. It can also serve as a comprehensive assessment of the benefits of ship motion control systems (Perez, 2015). The same hull form and loading conditions will result in different operability indices due to varying WSD, even within the same operational area, as demonstrated by Tezdogan et al. (2014).

For fishing vessels, loading conditions constantly change during operations. The speed and displacement of these vessels also vary over time (Tran et al., 2023; Zhao et al., 2021). Therefore, the operability index must be assessed by considering wave scatter diagrams for multiple loading conditions. Consequently, a dedicated study on the operability of fishing vessels is required, as their ability to perform under varying operational and loading conditions directly impacts the safety during fishing operations.

Another safety indicator for a ship is meeting the stability criteria. Initially, the intact stability criteria referred to the Intact Stability Code by the International Maritime Organization (2008a), which evaluates the *GZ* curve. The new code, known as the Second Generation of Intact Stability, was introduced and finalised by the IMO in 2020 (IMO, 2020). It focuses on dynamic stability assessments that consider the effect of waves on a ship's stability. The new code requires evaluation of five dynamic stability failures. The implementation of these criteria, along with example calculations, was discussed by Marlantes et al. (2021).

One of the five stability failures is known as parametric roll. This dangerous form of instability occurs under specific wave conditions, particularly when the wave encounter frequency is close to twice the vessel's natural roll frequency. The occurrence of this phenomenon depends on the variation in the roll-restoring moment, influenced by the variation of hull geometry, such as longitudinal flare distribution (Neves et al., 1999) and above-waterline geometry (France et al., 2003). This can lead to excessive rolling amplitudes, especially in head or stern waves, and in the worst-case scenario, the ship may capsize (Hosseini, 2009).

Fishing vessels, which change their speed during operation, can influence the encounter wave frequency. Additionally, changes in displacement and the centre of gravity position alter the natural roll frequency. Their small size results in a low natural roll period, which may be close to the wave period, leading to roll resonance or parametric roll. Understanding and mitigating parametric roll for a fishing vessel is crucial to preventing accidents and ensuring the safety of the vessel and crew.

Hydrodynamic optimisation can be an effective way to enhance ship performance, either by improving seakeeping and stability in waves or by minimising total resistance to reduce carbon footprint, promote decarbonisation, and lower fuel consumption. As the loading conditions of fishing vessels change during operation, arranging and managing the centre of gravity (*CoG*) is essential for maintaining stability, improving seakeeping, ensuring overall safety, and reducing fuel consumption. This optimisation is quite similar with trim optimisation, which is one of the easiest and cheapest method in ship performance and reducing the fuel consumption, as this method does not change the hull shape modification (Reichel et al., 2014).

Similar work related to managing *CoG* involves trim and ballast optimisation to minimise total resistance, as evidenced by the work of Reichel et al. (2014) and Hüffmeier et al. (2020). However, changes trim condition affects seakeeping and added resistance, as demonstrated by Shivachev et al. (2020) for the KCS model. Based on their investigation, motion responses increase slightly in long wave region at bigger trim angles. The added resistance trend is similar to calm water in short wave but not always in the long waves. Trim by stern also affects ship stability, where the trim by stern can increase stability levels from 0.5% to 5.4% (Wen and Fadillah, 2022) for Tanker, Container, and Bulk Carrier Ship. Therefore, an optimised *CoG* for fishing vessels is a part of key focus of this thesis, helping to reduce the risk of capsizing and enhance operational efficiency.

In addition to *CoG* optimisation, the design of the vessel’s hull form plays a significant role in its performance and must be considered in the early-stage design. An optimal hull form can improve resistance in both calm and wave conditions, as well as enhance seakeeping behaviour, thereby improving safety. Hull form optimisation can be conducted globally (Bagheri et al., 2014) or partially, such as optimising the bow shape (Zhang et al., 2018) or stern shape (Rotteveel et al., 2017).

Optimising the hull form of fishing vessels to minimise total resistance can involve various scenarios, with each scenario's duration differing based on the time spent at sea. These scenarios include variations in displacement and speed (Tran et al., 2023; Zhao et al., 2021). However, one scenario, such as full load condition, can be used to optimise the hull form to minimise the resistance, improving the seakeeping and vessel stability, as demonstrated in Gammon's work (Gammon, 2011).

Many fishing boats in Indonesia are small, and during operations, they experience varying loading conditions. Starting from an empty fish tank at the port, the boat's displacement changes as the tank fills during fishing. Fish temporarily stored on the deck before being placed in the tank causes shifts in Centre of Gravity vertically (*KG*) and longitudinally (*LCG*).

These changes in loading conditions lead to changes in hydrodynamic properties, such as variations in the natural period and damping coefficient, which result in different dynamic responses of the vessels. When the vessel experiences excessive dynamic responses, it can increase the total resistance in waves and harm the vessel through insufficient dynamics stability (potentially causing parametric roll), and, in the worst case, capsize.

This thesis aims to provide a comprehensive study of the dynamic performance of small fishing vessels in waves under varied loading conditions. By addressing the operability, parametric roll, *CoG* and hull form optimisation, the study seeks to enhance the design and operational safety of small fishing vessels.

The thesis presented here investigates the dynamic performance of small fishing vessels in waves with varied loading conditions across three key areas, as shown in Figure 1.2:

1. **Operability Assessment.** An operability assessment was conducted to determine how the boat can operate safely and comfortably within its operational area, ensuring it does not exceed predetermined seakeeping criteria. This investigation aims to inform fishers about the optimal standby duration onshore until weather conditions are favourable for operation. It also identifies which seakeeping criteria require enhancement. Given the unique nature of fishing boat operations, the assessment must account for changes in loading conditions and speed, combined with the duration of each condition, to establish a unified operability index. A comprehensive operability metric is developed that incorporates these factors, thereby allowing stakeholders to assess seakeeping performance among various options as a single index and determine the best boat size for a given operational region.
2. **Ship Stability in Waves.** During fishing operations, boats frequently experience varying loading conditions, causing shifts in the Centre of Gravity, longitudinally (*LCG*) and vertically (*KG*). These changes lead to variations in the roll natural period (Tn) and damping ratio, which can cause parametric roll, one of the five stability failures in waves assessed by the IMO. This study provides guidance to fishing boat operators on optimal methods for handling the fish they catch during operations, enhancing stability and safety.
3. **Seakeeping and Resistance Optimisation.** Optimising the position of the Centre of Gravity (*CoG*) and the hull form of fishing vessels is crucial to avoid parametric roll and reduce heave, pitch, and roll motions as well as the total resistance. The complexity of seakeeping optimisation, with numerous

objective functions, parameters, and techniques, often necessitates the use of multi-objective functions. This study addresses this complexity by introducing new objective functions (R_y and *GM* ratio) in the seakeeping optimisation process to indirectly determine seakeeping performance. By simplifying the optimisation process with a single objective function, it becomes less complex and can be solved quickly using straightforward techniques such as the response surface method. Additionally, improving dynamic performance must be accompanied by reducing total resistance to support lower fuel consumption and thereby decarbonisation, benefiting fishermen economically. Therefore, this research also investigates hull form optimisation to minimise total resistance along with dynamic responses.

The optimisation process in Figure 1.2 illustrates two approaches: the left-hand side and the right-hand side. The optimisation on the left-hand side does not alter the hull form, but instead varies the position of the centre of gravity (CoG) to minimise R_y. Minimising R_y helps to reduce dynamic responses without significantly increasing total resistance. On the right-hand side, the hull form is modified by minimising the *GM* ratio and total resistance in calm water. Each hull form variation achieves a minimal R_y to improve seakeeping. The optimised hull form for *GM* ratio reduces dynamic responses but increases total resistance. Meanwhile, the optimised hull form for the total resistance decreases resistance and also reduces dynamic responses, even though to a smaller extent compared to the hull with minimal *GM* ratio.

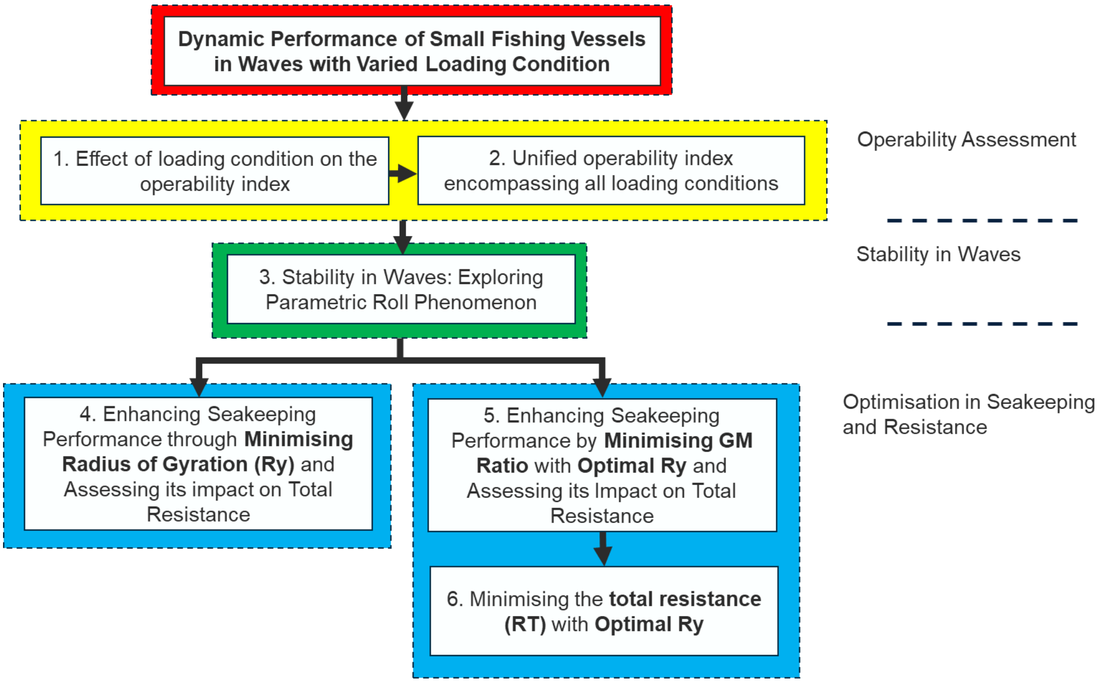

Figure 1.2. Thesis structure

1.2. Research Aim and Objectives

The aim of this thesis is to investigate the behaviour of small fishing vessels during their operations, focusing on changes in payload and its position, to enhance the safety of fishing vessel and fishermen while reducing total resistance. The recommendations based on this research can be implemented by stakeholders to ultimately reduce accidents, save the fuel consumption and reduce emissions.

The specific objectives of this thesis are described as follows:

1. **Literature Review.** To conduct a comprehensive literature review related to operability assessment, ship stability in waves, and strategies for enhancing seakeeping performance by identifying gaps that this research aims to fill as its novel contribution.
2. **Operability Index Assessment.** To assess the operability index of small fishing vessels and identify criteria that require improvement.
3. **Optimal Vessel Size Determination.** To investigate the best size for fishing vessels among various options using a single operability index.
4. **Impact of Payload Changes.** To examine how changes in payload and its position influence the occurrence of parametric roll.
5. **Optimisation of Fish Placement and Hull Form Design.** To enhance the seakeeping performance by conducting optimisation for fish placement, represented by the Centre of Gravity (CoG), and hull form design to avoid parametric roll and potential capsizing, and to reduce the total resistance using novel single objective functions, the radius of gyration in the y-axis (R_y) and GM ratio, the ratio between GM in waves and calm water.
6. **Recommendation for Stakeholder**. To provide the recommendation for the suitable fishing vessel size, placement and hull form for the stakeholders, including the optimisation method used in this thesis.

1.3. The Novelties of this Thesis

In this thesis, as described in Section 1.1, three distinct areas are explored: operability assessment, ship stability in waves, and seakeeping and resistance optimisation. The specific aim and objectives of this thesis have been clearly stated in Section 1.2. Through the successful achievement of each objective, new findings and methods have been discovered and developed, collectively referred to as the "novelties." This section summarises the novelties, highlighting the contributions and significance of this thesis to the existing body of knowledge.

The main novelties of this thesis are as follows:

1. **A new methodology** has been developed to assess a single operability index for a single fishing vessel, applicable across multiple loading conditions. A case study assessing a single operability index for three different sizes

provides recommendations of the appropriate vessel size for operation in the Java Sea.

2. **New findings** have emerged for observations of the behaviour of small fishing boat under parametric rolling condition with varying loading conditions:
    - **The *GM* ratio**, ratio between amplitude *GM* in waves and *GM* in calm water, is not only an indicator of the magnitude of parametric roll amplitude but also of heave and pitch amplitude for the same hull form and displacement.
    - **Radius Gyration in Y-Axis (R_y)** has been identified as an effective indicator for determining heave and pitch amplitude in head waves. A minimal R_y results in a lower moment of inertia, which increases the pitch damping ratio and subsequently reduces the pitch amplitude.

    Both *GM* ratio and R_y are straightforward to calculate. These parameters can be used to indirectly assess seakeeping performance and are suitable as objective functions in seakeeping optimisation, helping to accelerate the optimisation process.
3. **A new methodology** has been developed in hull form optimisation, enabling the simultaneous minimisation of total resistance and dynamic responses for small fishing vessels, thus avoiding the need for multi-objective optimisation. The hull form is optimised to achieve minimal total resistance, and during this process, the longitudinal centre of gravity (*LCG*) and vertical centre of gravity (*KG*) of each hull form variation are adjusted to achieve minimal R_y. As a result, the optimal hull form achieves minimal total resistance along with minimal dynamic responses.

1.4. Thesis Structure

The thesis is structured as follows:

- **Chapter 2** reviews the existing literature relevant to the study. It covers the operability assessment for ships, particularly fishing vessels, and the stability in waves represented by parametric roll. The literature on seakeeping optimisation is also reviewed. This research aims to address the gaps identified during the literature review.
- **Chapter 3** describes the subject ships used in this thesis, the simulation conditions, and the methodology adopted in various chapters, including details on seakeeping analysis, Computational Fluid Dynamics (CFD) modelling, and the optimisation process using Response Surface Methodology (RSM).
- **Chapter 4** presents the operability index of small fishing boats in Indonesia to determine the effect of load changes on their operability, considering the

ships' intact stability. The response of the ship's roll motion is highlighted to prevent stability failure. The stability curve is used to relate ship stability analysis to seakeeping analysis. Percentage operability and the Operability Robustness Index are used to assess the root mean square (RMS) roll response and the ship's expected maximum roll motion.

- **Chapter 5** discusses the assessment of the operability index as a single assessment covering the conditions of small fishing boat operations. It demonstrates how vessel size influences percentage operability improvement. By assessing the seakeeping performance among various vessel sizes, this research provides stakeholders with information on the optimal size for operations in the Java Sea.
- **Chapter 6** examines how small fishing boats respond to parametric roll. Given that the loading condition of small fishing boats constantly changes during operation, their natural period also changes. The boats may experience parametric roll, one of the five stability failures assessed by the IMO. This chapter identifies crucial parameters to be minimised to avoid parametric roll and enhance seakeeping performance.
- **Chapter 7** discusses seakeeping optimisation by minimising the radius of gyration in the y-axis (R_y), as identified in Chapter 6. This approach reduces the complexity of seakeeping optimisation. Additionally, the optimal placement of fish during operation, represented by the Centre of Gravity (*CoG*), is determined to increase the safety of the ship and fishermen. The impact on total resistance in calm water is also discussed.
- **Chapter 8** uses the *GM* ratio, another single objective function identified in Chapter 6, to enhance seakeeping performance through hull form deformation. The utilisation of R_y, as discussed in Chapter 7, is employed to determine the optimal *CoG* position for the best hull form in terms of the *GM* ratio.
- **Chapter 9** continues hull form optimisation using the same design variables to deform the hull but uses total resistance (RT) in calm water as the objective function. The minimisation of R_y is also adopted as an objective function to identify the best *CoG* locations, resulting in the optimal hull form with minimum total resistance and dynamic responses.

2. Literature Review

2.1. Introduction

Recent literature is reviewed, focusing on three key areas outlined in the Chapter 1: operability, parametric roll, and seakeeping optimisation. Firstly, the literature discusses operability assessment, which is essential for measuring the seakeeping performance of a ship which involving the operational area. Based on operability assessment, the lowest dynamic ship responses can be identified, one of which is roll motion, related to stability in waves. Therefore, exploring the second generation of intact stability, specifically the parametric roll phenomenon, is the next step in the literature review. Since heave and pitch motions contribute to this phenomenon, understanding some variables to minimise the amplitude of parametric roll can also reduce heave and pitch motions. Finally, once these variables are identified, they can be used as new objective functions in seakeeping optimisation. Hence, the final literature reviewed in this chapter is seakeeping optimisation.

2.2. Operability

An operability index is a metric to determine how a boat can operate safely and comfortably in its operational area over specific periods (monthly, seasonally, or annually). This index ensures that the boat meets the pre-determined seakeeping criteria. Depending on the method used, the index can range from 0 to 100 for the Percentage Operability (PO) method, or from 0 to 1 for the Operability Robustness Index (ORI).

Seakeeping criteria refer to the standards used to evaluate the seakeeping performance for a particular ship type. Different types of ships have different standards. For a fishing vessel, the seakeeping criteria in this thesis is based on Tello at al. (2011), which consist of RMS (Root Mean Square) and probability values. The RMS covers roll and pitch motions, as well as lateral and vertical acceleration, while the probability values cover slamming and deck wetness.

The methodology to calculate an operability index as an assessment of seakeeping performance was initially presented by Fonseca and Soares (2002). In their study, two different types of vessels, a container ship and a fishing vessel, were selected as case studies to evaluate the sensitivity analysis. Due to differences in their type, mission, and operational area, these vessels exhibited different operability indexes. Additionally, Tello et al. (2009) investigated the operability of four fully-loaded fishing vessels. Their research revealed that roll motion and lateral acceleration had the lowest percentage operability among various responses. The boat with a "U" type hull demonstrated a higher operability index compared to the "V" type boat. It was inferred that the overall operability of fishing vessels was dependent on the vessel's dimensions. The longest vessel operated better compared to others, with an operability index of 0.94 for zero speed and 0.87 for $F_r = 0.3$. Conversely, the smallest vessels had operability indexes of 0.44 and 0.64 for $F_r = 0.0$ and $F_r = 0.3$, respectively.

Furthermore, Tello et al. (2011) evaluated the seakeeping performance of fully loaded fishing vessels operating in sea states 5 and 6. They found that pitch and roll were the most crucial degrees of freedom, as their responses frequently surpassed the limiting criteria. Their research also identified that GM (metacentric height) is the essential parameter governing roll responses. A higher GM resulted in a lower roll period, potentially matching the wave modal period of the sea and leading to resonance, which can significantly increase roll responses and pose a danger to the vessel.

Tezdogan et al. (2014) investigated the percentage operability of a high-speed catamaran passenger ship using annual and seasonal wave scatter diagrams (WSD) on the west coast of Scotland. They applied three theories to define the Response Amplitude Operator (RAO) curve: the 2-D conventional strip theory, the 2½-D high-speed strip theory formulation excluding hull interaction and including hull interaction. These theories were then compared to experimental data, with the latter showing better agreement with experimental data compared to 2½-D high-speed strip theory. However, 2-D conventional strip theory demonstrated the best overall agreement with experimental data among the three theories.

Recently, researchers have developed new operability indexes focusing on single seakeeping criteria, such as RMS roll. Gutsch et al. (2017) introduced the Integrated Operability Factor (IOF), defined as the ratio of the area under the curve of percentage operability for a single criterion from zero to its maximum limitation ($OP_{tot\,max}$) to the area of the maximum possible operability ($100\% \times OP_{tot\,max}$). In this context, the $OP_{tot\,max}$ for the RMS Roll motion criterion was determined according to A Standardisation Agreement (STANAG) (Eriksen et al., 2000) for replenishment operations at sea, which is 2.2°. Gutsch et al. (2017) examined the impact of various main dimensions of Offshore Construction Vessels (OCV), such as length, breadth, draught, transversal GM, and radius of gyration of roll (R_{44}) on the IOF value of RMS Roll.

Sandvik et al. (2018) extended the use of Integrated Operability Factor (IOF) to assess the RMS of heave, pitch, roll, and vertical crane displacement for Offshore Construction Vessels. Their research also investigated the combination of main vessel dimensions and introduced the Relative Rate of Operation (RRO) concept, further exploring susceptibility to weather-related delays.

Later, Gutsch et al. (2020) renamed Integrated Operability Factor (IOF) to Operability Robustness Index (ORI). Both Integrated Operability Factor (IOF) and Operability Robustness Index (ORI) represent the same analysis, evaluating the ratio between the two areas mentioned previously. Gutsch et al. (2020) used Operability Robustness Index (ORI) as a key performance indicator for the seakeeping performance of Offshore Construction Vessels, investigating the influence of vessel length, beam, draught, and metacentric height during summer and winter operations in the North Sea and North Atlantic on the Operability Robustness Index (ORI) value of RMS Roll. The $OP_{tot\,max}$ used was 2°, which was compared to the widely known percentage operability (PO). From Gutsch et al.'s (2020) study, it can be concluded that Operability Robustness Index (ORI) is a more robust performance indicator for assessing the seakeeping performance of various vessel types. The higher Operability Robustness Index (ORI) value is most affected by the initial steepness of the percentage operability curve and the choice of maximum limitation ($OP_{tot\,max}$) for the selected criterion (Sandvik et al., 2018). Although Operability Robustness Index (ORI) can assess single criteria of seakeeping performance, such as roll motion, it is not related to ship stability analysis.

One of the ship motion responses obtained from seakeeping analysis is roll, which is related to ship stability, defined as the ship's ability to return to its original position after being displaced from its original position. Ship accidents, such as capsizing, often occur due to stability failures, caused by insufficient training for ship operators regarding ship stability, leading to errors in decision-making (Davis et al., 2019). To address this issue, Caamaño et al. (2018) proposed a methodology to automatically assess ship stability, minimizing crew-system interaction. This method estimates the natural frequency of roll motion and the metacentric height throughout the vessel's voyage. Later, Caamaño et al. (2019) proposed real-time detection of changes in ship stability, informing the crew of the proximity to safety limits.

In a stability assessment, the loading condition scenario is determined at the beginning to describe ship operations during the voyage. The characteristics of the stability curve for each loading condition are evaluated using standard criteria for fishing vessels based on the Intact Stability Code from IMO (2008b). Mantari et al. (2011) investigated intact stability on fishing vessels, considering fishing gear, beam waves, and wind. Their results indicated that the heeling moment produced by fishing gear is more critical than that from adverse weather scenarios. Errors in selecting the dimensions of fishing gear and machinery were also identified as factors contributing to stability failures in fishing vessels.

However, the stability criteria may not accurately account for some dynamic phenomena related to stability-related accidents (Mata-Álvarez-Santullano and Souto-Iglesias, 2014). The stability curve and criteria recommended by IMO do not consider wave height and ship size. To address this, Deakin (2005) experimentally determined the minimum wave height required to capsize a ship for each configuration, producing a formula linking the stability curve's range (angle distance that has a positive *GZ*) and maximum Righting Moment (*GZ* max × displacement) with vessel size (length and beam). Deakin (2006) refined this formula to determine the critical significant wave height or sea state, though it did not include the influence of ship speed and wave direction. The current study presents significant wave height limitations, considering vessel speed and wave headings.

Additionally, Mata-Álvarez-Santullano and Souto-Iglesias (2014) investigated the stability and operability of several sunken fishing vessels and similar existing vessels, analysing stability and operability separately without direct correlation. Stability was assessed using the stability index (ratio of KG to the maximum allowed KG) to meet stability criteria, while operability was analysed using short-term analysis in two typical sea states, excluding Wave Scatter Diagram. Their operability calculation differed from percentage operability, employing Boolean operators to assign values of 0 or 1 for each ship speed and wave direction.

The aforementioned research attempted to relate ship stability to operability analysis but did not do so directly which is a key gap in the literature. Therefore, present thesis aims to directly link seakeeping performance, especially roll motion, to a vessel's static stability. For small boats, this relationship is crucial because the natural period of roll is small and may coincide with the wave period, leading to roll resonance. The novel indicator for seakeeping performance, Operability Robustness Index (ORI), was employed to calculate not only RMS roll motion but also the expected maximum roll.

2.3. Parametric Roll

The stability of ships in calm water has long been a subject of maritime research. Paulling and Rosenberg (1959) studied this topic, examining the influence of non-linear second-order terms and coupling terms in the equation of motion. They identified instability caused by non-linear coupling by solving the Mathieu Equation, a second-order linear differential equation with periodic coefficients. Their experimental tests, which coupled heave and roll motion, confirmed these findings, though they suggested that the coupling effect should incorporate more than two degrees of freedom. For many years, parametric roll was considered a theoretical concern until the APL China container ship experienced parametric roll in 1998, an incident that sparked widespread scholarly interest in the phenomenon.

Neves et al. (1999) conducted experimental and numerical investigations to examine the influence of different stern shapes on parametric rolls in fishing vessels. Their study focused on two similar fishing boats with different stern shapes (transom and round). Roll damping was measured using roll decrement tests, with and without bilge keels. They used an uncoupled roll motion equation in the numerical method, incorporating non-linear damping and restoring moments. The study found that the transom stern resulted in a higher parametric roll amplitude compared to the round stern, attributed to differences in longitudinal flare distribution.

Francescutto (2001) explored the potential for parametric roll in a destroyer model sailing into head seas. Roll damping was calculated through roll decay tests conducted in calm water with forward speed, though the impact of waves on roll damping was not considered. The findings demonstrated a potential risk for ships with relatively low roll periods at heads seas.

France et al. (2003) utilised FREDYN, a nonlinear, time domain ship motion simulation program developed by MARIN based on Hooft's work (1987), and LAMP (Large Amplitude Motion Program) based on Lin and Salvesen's work (1997), to investigate the influence of stern and bow flares on parametric roll amplitude in Series 60 hull forms. The study showed that ships with stern and bow flares had higher parametric roll amplitudes than those with wall-sided bows, with the amplitude increasing as the bow flare increased. Additionally, experimental tests on a post-Panamax C11 container ship model in extreme weather conditions validated these findings, reflecting real-world incidents like the 1998 accident that caused significant loss and damage.

Spanos and Papanikolaou (2006) investigated parametric roll in fishing vessels through time-domain numerical simulations in head waves, incorporating non-linear terms in six degrees of freedom (6 DoF) with viscous effects. They classified roll motion response into parametric roll, stable, and unstable (capsize) zones based on wave amplitude. Their results indicated that vessels with low Froude numbers, *GM*, and roll damping ratios experienced high amplitude in the parametric roll zone

Spanos and Papanikolaou (2007) expanded their investigation to include both fishing boats and Ro-Ro vessels, highlighting differences in parametric roll occurrence based on ship type and wave height. Sadat-Hosseini et al. (2010) studied the ONR Tumblehome surface combatant using nonlinear dynamics, EFD, and CFD methods, revealing that CFD predictions were higher but in trend agreement with EFD results. The CFD method was used for the first time by Sadat-Hosseini (2009) to predict parametric roll, as well as other modes of stability issues, such as surf riding, broaching, and periodic motion; the simulations were conducted in calm water for resistance analysis, roll decay, and in head waves with forward speed for roll decay/parametric roll.

Ribeiro e Silva et al. (2010) presented a method to determine container ship susceptibility to parametric roll based on ABS guidelines. They used Miller's (1974) method to calculate roll damping and employed numerical simulations to predict roll amplitude. Their research confirmed the effectiveness of ABS guidelines in identifying parametric roll occurrences.

Neves et al. (2011) examined the influence of vessel speed and wave amplitude in regular head waves on roll response in fishing boats with different stern shapes. Their study concluded that vessel speed significantly influenced roll amplitude, with the maximum roll occurring at a specific Froude number. Park et al. (2013) conducted sensitivity analyses of computational results, showing good agreement with theoretical solutions and examining parameters like wave spectrum discretisation and metacentric height. The impulse-response-function (IRF) and 3D Rankine panel methods were used to simulate parametric roll in regular waves.

Galbraith and Boulougouris (2015) predicted parametric roll in the Tumblehome model using Star-CCM+ software, finding that initial heel and speed significantly influenced roll amplitude. The initial heel was determined by setting an initial angular velocity and by shifting in the transverse centre of gravity to starboard. Zhou et al. (2016) developed a hybrid method to predict parametric roll in container ships, comparing it with nonlinear dynamics and CFD simulations. Their hybrid approach showed good agreement with direct CFD results. The method involved determining the damping coefficient from experimental data and a CFD method using free and forced roll decay, which was then used to predict the parametric roll based on potential theory.

Schumacher et al. (2016) investigated parametric roll in container ships under various wave conditions, validating their nonlinear time-domain model against experimental results. Roll damping was evaluated through forced rolling tests, with both linear and nonlinear methods employed. Lu et al. (2016) expanded Mauro's (1963) theory to examine the impact of parametric roll on added resistance, finding that viscous roll damping significantly affected resistance as roll amplitude increased.

Ma et al. (2018) and Zhou (2019) furthered the understanding of parametric roll through experimental and numerical methods, highlighting the influence of draft, speed, and wave amplitude. The study also showed that the parametric roll amplitude is not a linear function of wave steepness, with an initial increase followed by a gradual decrease. Additionally, the wave steepness that results in the maximum amplitude of parametric roll varies at each Froude number.

Ghamari et al. (2020) conducted a comprehensive study on the parametric roll of Norwegian fishing vessels in regular waves, employing numerical and experimental methods. The experimental tests were performed with and without forward speed at varying wave frequencies and steepness, and roll damping was determined through roll decay tests. The numerical method involved using radiation and diffraction potentials at zero speed, followed by results obtained via the strip theory based on the Salvesen, Tuck, and Faltinsen (STF) method. The study investigated a wide range of simulation conditions, with most cases showing consistent steady roll amplitude between experimental and numerical results. However, some discrepancies were observed in cases near the instability threshold.

Liu et al. (2021) used CFD to investigate parametric roll in an ONR Tumblehome, showing negligible scale effects and effectiveness of bilge keels in reducing roll amplitudes. L. Liu et al. (2022) explored liquid sloshing effects on parametric roll. Their research found that sloshing affects the natural roll frequency, decreasing the roll amplitude when the phase difference between the ship motion and sloshing is 180°.

Zhou et al. (2022) examined parametric roll vulnerability in an Offshore Research Vessel due to extended low weather decks, using experimental and numerical approaches. They compared their findings with data from C11 and S25 container ships, also exploring non-linear water-on-deck phenomena.

The sea area and season in which a ship operates influence its vulnerability to parametric rolling. Hashimoto and Furusho (2022) investigated parametric roll vulnerability in C11-class container ships and car carriers, highlighting seasonal and regional influences on ship stability. The paper revealed that the winter season has a ten times higher failure index compared to summer.

Another of interest in parametric roll study had been investigated by Maruyama et al. (2023), who investigated how to estimate roll acceleration with probability density function. Later, Liu et al. (2023) evaluated the second level of vulnerability criteria of parametric roll for C11 container ships with stochastic stability theory. Then, the results were compared with the stability criteria proposed by IMO. The proposed method gives more accurate results compared to IMO.

The majority of existing literature has compared various numerical approaches to experimental test to predict parametric roll (PR) and has contributed to understanding its behaviour. Discussions of the advantages and disadvantages of different techniques were given. Several researchers have explored PR behaviour concerning wave steepness, wave amplitude, vessel speed, wave heading, and GM. However, there has been limited exploration of PR in the context of small fishing boats. To the best of the author’s knowledge, no research has been conducted on the parametric roll of small fishing boats using fully non-linear unsteady Reynold-Averaged Navier Stokes (RANS) CFD simulations, particularly in different loading conditions that accurately represent fishing boat operations. A part of this thesis (in Chapter 6) aims to address this gap by investigating parametric roll behaviour in small fishing vessels and identifying the factors influencing its amplitude.

2.4. Seakeeping Optimisation

Seakeeping optimisation has been a key focus in ship hydrodynamics for decades, ensuring vessels operate safely, comfortably, and efficiently. The primary goal is to minimise ship resistance and enhance seakeeping performance. Researchers often employ multi-objective optimisation to address these goals simultaneously.

Bales (1980) optimised seakeeping for a destroyer ship. He introduced an operability index encompassing pitch, roll, deck wetness, slamming, and accelerations at critical points. Using linear strip theory based on the potential theory, Bales employed non-linear programming alongside regression formulas to correlate performances to form parameters.

Grigoropoulos and Loukakis (1988) embarked on optimising reefer ships. They aimed to minimise RAO peak values in head regular waves, obtained from Strip Theory Method, utilising nonlinear direct search algorithms. They obtained improved seakeeping performance by employing the Lackenby method (Lackenby, 1950) by moving the transverse sections of a hull form along the ship's length to achieve specific changes in the hull's characteristics. The result demonstrated the superior seakeeping qualities of their new ship designs in vertical acceleration and relative motion. Then the parent and optimised hull were tested experimentally to verify the seakeeping results. Both Bales (1980) and Grigoropoulos and Loukakis (1988) used ship coefficients and main dimensions as design variables in their seakeeping optimisations.

Ozmen's (1995) research on fishing vessels delved into seakeeping, added resistance, and calm water resistance indices through regression analysis. The various coefficient parameters in naval architecture were used as design variable, while displacement is fixed. The study employed strip theory and 3D source distribution techniques. The direct search method of Hooke and Jeeves (1961) revealed that optimised hulls significantly outperformed their parent forms.

Sarıöz (2009) considered vertical acceleration, heave, pitch, and slamming, both as single objectives and through a global performance measure for a motor yacht. Using a linear strip theory approach and the direct search method of Hooke and Jeeves (1961), Sarıöz (2009) found that multi-objective seakeeping optimisation can conflict in goals when optimising different degrees of freedom, posing a significant challenge. Later, Gammon (2011) used Turkish fishing vessels as a subject ship to optimise three performance indices: resistance, seakeeping (vertical motion), and stability. Utilising multi-objective genetic algorithms, his work showcased improvements across all three objectives, highlighting the potential of genetic algorithms in seakeeping optimisation. In optimisation process, length, beam, and draft of fishing vessels were used to modify hull shapes and obtain optimal hull offsets.

Bagheri et al. (2014) optimised the S60 hull and the classical Wigley hull, focusing on vertical absolute motion. His genetic algorithm reduced vertical motion by 33% and 27% in two cases, demonstrating the substantial benefits of this approach. Bagheri et al. (2014) employed ranges of ±10% for length, beam, and draft, and ±3% for hull offsets as design variables with no change in displacement.

Diez et al. (2015) optimised resistance and seakeeping for the DTMB 5415, using low-fidelity solvers and high-fidelity simulations. Their multi-objective optimisation algorithm, based on particle swarm metaheuristics, achieved approximately 10% and 9% improvements in resistance and seakeeping, respectively.

Huang et al. (2015) focused on the Series 60 hull form, applying surrogate-based methods and bee colony optimisation. Their use of the sectional area curve (SAC) and local surface modifications yielded superior hull forms with reduced drag and enhanced seakeeping performance. A ship motion program (SMP) based on the strip theory was used to solve the seakeeping performance.

Similarly, Vernengo et al. (2015) optimised a fast multihull semi-SWATH passenger ferries. By optimising global and local shape variations by varying basic curve sets, they achieved significant reductions in drag and vertical acceleration.

Miao et al. (2018) and Wang et al. (2018) used URANS and surrogate models using the Kriging method to optimise the KCS hull form. The optimum results conducted by Miao showed that the amplitude of heave and pitch can reduce up to 9.21% and 3.08%, respectively. Wang's research on trimarans utilised NSGA II for seeking the optimal outrigger layout, which can minimise heave, pitch, and roll motions. The seakeeping performances were evaluated using high-speed slender body potential flow theory (2.5D method).

Utomo and Iqbal (2020) studied the vertical motion of the S60 hull form, which they optimised the hull form through the Response Surface Method (RSM) by determine the best *L/B* and *B/T* ratios. The optimal hull form effectively reduced vertical motion up to 16.38%. The strip theory method was utilised to evaluate the seakeeping performance. Guan et al. (2021) studied Unmanned Surface Vehicle (USV) hull forms, addressing wave resistance, vertical acceleration, and pitch amplitude. By altering multiple parameters and employing CFD simulations, they utilised the Response Surface Method (RSM) in conjunction with Particle Swarm Optimisation (PSO) and Sequential Quadratic Programming (SQP) to achieve an optimised design. The optimal hull form can reduce the resistance, vertical acceleration, and roll motion up to 17%, 38%, and 35%, respectively based on RSM model.

Marín López et al. (2021) focused on optimising the small high-speed craft, targeting the index of motion sickness in accordance with ISO 2631 standards. They examined waterline length, breadth, block coefficient, deadrise angle, and longitudinal centre of gravity (*LCG*), using acceleration time histories from sea voyages to estimate passenger comfort. Their findings suggested that increasing length and deadrise angle, while moving *LCG* forward, could significantly reduce acceleration and resistance. The results suggest that a 24% increment of ship length can reduce vertical acceleration and resistance up to 20% and 4%, respectively.

Romero-Tello et al. (2022) utilised machine learning to assess the seakeeping performance for specific scenarios. They analysed cruise ships using artificial neural networks (ANN), enabling rapid assessment of a large number of cases. Their findings highlighted the benefits of larger lengths and higher block coefficients in minimising motion sickness incidence and subjective magnitude.

Both Sarıöz (2009) and Romero-Tello et al. (2022) used various naval architecture form coefficients and parameters such as length (*L*), length-breadth ratio (*L/B*), breadth-draught ratio (*B/T*), block coefficient (*CB*), midship coefficient (*CM*), waterplane coefficient (*WP*), prismatic coefficient (*CP*), and metacentric height (*GM*). Serani et al. (2022) optimised naval destroyers, employing a multi-fidelity optimisation method to achieve significant design performance improvements. Their work demonstrated the efficacy of various CFD solvers in enhancing seakeeping performance.

Guan et al. (2022) explored the optimisation of SWATH hull forms for resistance and seakeeping performance. By utilising commercial software AQWA based on potential flow theory and Non-dominant Sorting Genetic Algorithm (NSGA), they successfully obtained hull forms with better hydrodynamic performance. They altered certain control points of the contour line of the hull form that significantly impacted only resistance, determined through sensitivity analysis.

Most optimisation methods in engineering problems use approximation modelling (surrogate model), which can replace the actual complex model with a simple function

(Xiaobo, 2017). The approximation modelling builds a function expressing the relationship between design variables and the system responses using statistical techniques or regression. The researcher can reduce the number of tests when observing the unknown relationship between design variables and responses using a set of sample data and applying DoE, random number, or experimental data (Guan et al., 2021). Once the system responses, in this case, the seakeeping performance from each design variable, have been determined, a statistical approach is used to create the mathematical model.

DoE involves arranging the number of design variables needed and the number of experiments/tests that must be conducted to create a systematic sample. This is based on a fractional factorial experiment, which enables the execution of experiments with only a subset of the potential combinations of design variables or design factor values (Roy et al., 2008).

For low-order nonlinear problems and when design variables are fewer, Central Composite Design and Box-Behnken can be used as DoE for two and three design variables, respectively. Both DoE are suitable when modifying a hull form globally by shifting method, such as the Leckenby method. On the other hand, when many design variables are needed, such as control points to deform the hull form, Latin Hypercube Sampling (LHS) can be used as an alternative DoE as used by Guan et al. (2021) and Huang et al. (2015).

Different DoE will result in different mathematical model functions. There are some methods in approximation modelling, such as the Responses Surface Method, Kriging Method, and Neural Network. While RSM and the Kriging method need DoE as a sample test to build the mathematical model, Artificial Neural Network (ANN) can use any sample data informally as the model that is built from ANN is not based on regression analysis. The result is more accurate than the regression model because all data is used to build the model. In contrast, the less significant terms in the regression model are not included in the model (Bezerra et al., 2008).

Generally, optimisation techniques can be divided into conventional and non-conventional. Non-conventional techniques use either direct search or gradient-based methods. The direct search needs several iterations to find the optimal solution, such as a nonlinear direct search technique (Ozmen, 1995; Sarıöz, 2009) and gradient-based methods, such as steepest descent/ascent (Iqbal et al., 2019; Utomo and Iqbal, 2020).

Non-conventional approaches are inspired by nature, such as Genetic Algorithm which is carried out by Bagheri et al. (2014), Gammon (2011), Guan et al. (2022), Miao et al. (2018), Vernengo et al. (2015), and Wang et al. (2018). Other examples are Bee Colony, used by Huang et al. (2015), and Particle Swarm Optimisation (PSO), used by Guan et al. (2021). However, the details of optimisation techniques are outside the scope of this thesis.

As mentioned in the literature above, the numerous objective functions, parameters, and optimisation techniques in seakeeping optimisation make the process complex, necessitating the use of multi-objective functions. Researchers often compromise between many objective functions to determine the best solution. This thesis addresses that gap by demonstrating the use of new objective functions (R_y and GM ratio) in the seakeeping optimisation process to indirectly determine seakeeping performance. With only one objective function in the proposed framework, seakeeping optimisation becomes less complex. Consequently, the optimisation can be solved quickly, and a simple optimisation technique, such as the response surface method, can be used.

2.5. Summary and Identified Gaps

Based on the literature review, the following gaps have been identified:

1. To date, no studies have analysed the operability of small vessels considering changes in loading conditions. Seakeeping analyses on fishing vessels are mostly comparative studies and typically consider only one loading condition (full load). In this thesis, a single fishing boat under varying loading conditions is analysed, reflecting the nature of fishing vessel operations where cargo constantly changes underway (Chapter 2.2).
2. Although some researchers have used the GM parameter in actual conditions to relate to the ship's roll response, for the same hull, the GM value depends on the KM value, which varies with the ship's displacement. The ship's response differs with the same GM value if the KM varies. Thus, the actual GM value cannot directly determine the ship's response if KM varies. The present thesis uses the GM/KM ratio to assess how changes in GM and KM influence operability (Chapter 2.2).
3. While several researchers have attempted to link ship stability with operability, none have done so directly. In this thesis, a novel approach is proposed which directly links ship stability and operability. The Angle of Vanishing Stability (AVS) and Down flooding Angle (DFA) in the stability curve are used as the maximum limitation ($OP_{tot\,max}$) of the expected maximum roll, evaluated using Operability Robustness Index (ORI). This idea is based on the premise that if the maximum roll motion exceeds AVS, the ship becomes unstable due to a negative GZ value, potentially leading to capsizing. Moreover, when the maximum roll motion exceeds DFA, seawater is likely to enter the deck, posing additional risks (Chapter 2.2).
4. The percentage of operability outcomes varies significantly due to numerous loading conditions, making it difficult to decide on the most representative operability index. Therefore, it is necessary to develop a comprehensive operability metric that considers multiple loading conditions for fishing vessels, allowing for the evaluation of performance across different vessel sizes (Chapter 2.2).
5. Existing literature has validated various numerical approaches to predict the parametric roll phenomenon and explored its behaviour in relation to wave

steepness, wave amplitude, vessel speed, wave heading, and *GM*. However, there has been limited research on this phenomenon in small fishing boats, and none using fully non-linear unsteady RANS CFD simulations, especially under varying loading conditions typical of fishing boat operations. Investigating parametric roll behaviour in small fishing vessels and identifying the factors influencing its amplitude is a gap in the literature which this thesis aims to fill (Chapter 2.3).

6. In terms of seakeeping optimisation, existing literature shows many objective functions and design variables related to deforming hull forms. For fishing vessels, where loading conditions constantly change, there is less literature using loading conditions such as *LCG* and *KG* as design variables. Furthermore, most literature uses ship responses as objective functions to be minimised. Utilising a single objective function that does not directly calculate seakeeping performance is one of the novelties in this thesis (Chapter 2.4).
7. In terms of deforming hull forms to enhance seakeeping performance, some literature uses the Lackenby method by modifying the *LCB* and *CB* of the vessel. However, obtaining the optimum hull form by involving multiple ship responses to be minimised makes the optimisation complex. This issue is identified as a gap in the literature. To address this gap, another single objective function in this thesis can simplify the optimisation process and indirectly enhance seakeeping performance (Chapter 2.4).
8. Existing literature uses multi-objective optimisation techniques to achieve hull forms with minimum total resistance and dynamic responses. This optimisation is also considered as a complex optimisation. Therefore, the final main chapter addresses this literature gap by minimising total resistance as a single objective function in hull form deformation and optimising loading conditions to minimise dynamic responses using a single objective function as well, streamlining the optimisation process (Chapter 2.4).

3. Methodology

3.1. Introduction

This chapter presents the subject ship and simulation conditions as well as the methodologies used in the following chapters. The methodologies are categorised based on the research areas investigated in this thesis: operability assessment, parametric roll, and seakeeping optimisation. Two subject fishing vessels are used in this thesis. The first vessel is used in operability and parametric roll assessments. The second vessel's geometry is used in seakeeping optimisation due to the availability of experimental data. CFD modelling and Fast Fourier Transform methods are used in both parametric roll and seakeeping optimisation. Finally, the optimisation procedure is applied in seakeeping optimisation.

3.2. Subject Ship and Simulation Condition

3.2.1. Operability Assessment and Parametric Roll Cases

A traditional small fishing boat from Indonesia was selected as the first case study. This fishing boat had been modelled by Tezdogan et al. (2018) for hull form optimisation and by Liu et al. (2019) for the design of a bilge keel. A body plan of the fishing boat is shown in Figure 3.1, and details of the main dimension are given in Table 3.1. The boat was simulated at three speeds: zero knots, half design speed (4 knots), and design speed (8 knots) with wave heading from 0° (head waves) to 180° (following waves) with 30° increments.

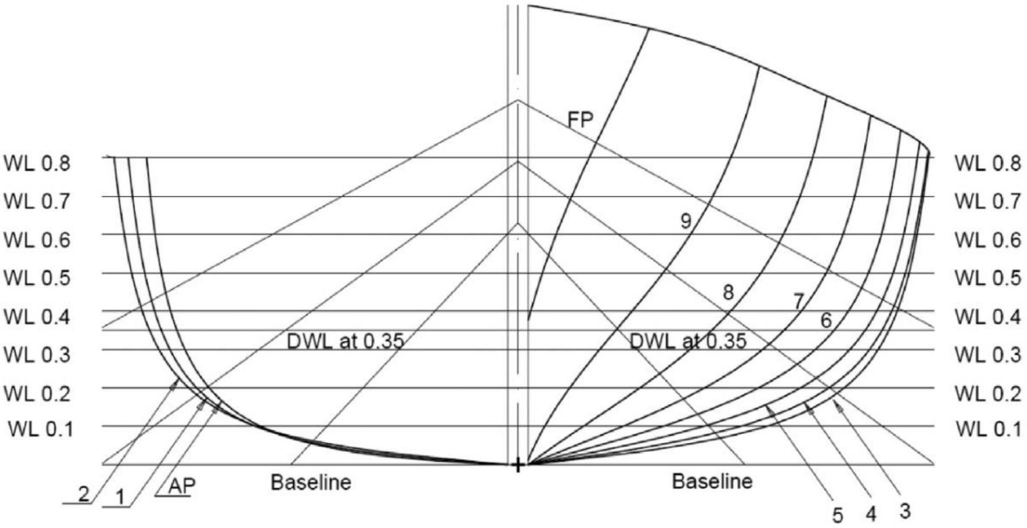

Figure 3.1. Body plan of the research object (Liu et al., 2019)

Table 3.1. Main dimension of the boat (Tezdogan et al., 2018)

Parameters	**Value**
Length between perpendicular, *LPP* (m)	5.000
Breadth at water line, *B* (m)	1.934
Depth to 1st deck, *D* (m)	1.196
Loaded draft, *T* (m)	0.350
Displacement, Δ(ton)	1.858
Block coefficient, *Cb* (-)	0.537
Mid-boat section coefficient, *Cm* (-)	0.764
Wetted surface area, *Aw* (m^2)	10.201
Froude number, F_r (-)	0.590

Aside from different velocities and wave headings, the boat was investigated with different loading conditions shown in Table 3.2 to address the gap in the literature discussed in section 2.5. Load Case 1 represents the departure condition, where the fish storage tank is still empty because no fish has been caught. In Load Case 2, it is assumed that the vessel has caught half of the fish storage tank capacity, and the catch is placed on the upper deck. For Load Case 3, the catch is placed in the fish storage tank (below deck). Load Case 4 assumes that the fish storage tank is filled to its total capacity and the catch is placed on the upper deck, while Load Case 5 models this as being below the deck. The details of Load cases 1 – 5 are shown in Table 3.2. It should be noted that the Transverse Centre of Gravity (*TCG*) is zero for all load cases since the load distribution is assumed to be symmetrical.

Table 3.2. Load scenario

Load Case	**Description**	**Ship Weight (kg)**	***LCG* (m)**	***KG* (m)**
1	Empty load of fish	712.00	1.550	0.844
2	Half load of fish, upper deck	1285.00	1.751	0.914
3	Half load of fish, below deck	1285.00	1.751	0.557
4	Full load of fish, upper deck	1858.00	1.828	1.064
5	Full load of fish, below deck	1858.00	1.828	0.57

To summarise, the vessel’s load capacity is divided into empty, half, and total capacity of fish storage with a different loading position (KG) for both half and full capacities. Therefore, the centre of gravity is changed. The different displacement and the centre of gravity will change along with the draft values for aft perpendicular, forward perpendicular, and midship locations and create the different trim conditions. The equilibrium condition of each load case is given in Table 3.3.

Table 3.3. Equilibrium condition

Parameters	**LC 1**	**LC 2**	**LC 3**	**LC 4**	**LC 5**
Displacement (kg)	712	1285	1285	1858	1858
*KM*t (m)	1.607	1.37	1.37	1.227	1.227
*GM*t (m)	0.763	0.456	0.813	0.163	0.657
Draft Amidships (m)	0.171	0.265	0.266	0.344	0.345
Draft at *FP* (m)	0.123	0.237	0.239	0.317	0.32
Draft at *AP* (m)	0.219	0.293	0.292	0.372	0.37
Draft at *LCF* (m)	0.185	0.272	0.272	0.35	0.349
Trim (+ve by stern) (m)	0.096	0.056	0.053	0.055	0.05
Trim angle (+ve by stern) (°)	1.0959	0.6391	0.608	0.6274	0.5743

With the same *KM* (as the boat's weight is the same), the *GM* will be different and affect the ship’s response, especially roll motion. There are differences in the natural period and damping values. This difference can be seen in the graph of the ship's response in regular waves, expressed through the Response Amplitude Operator (RAO).

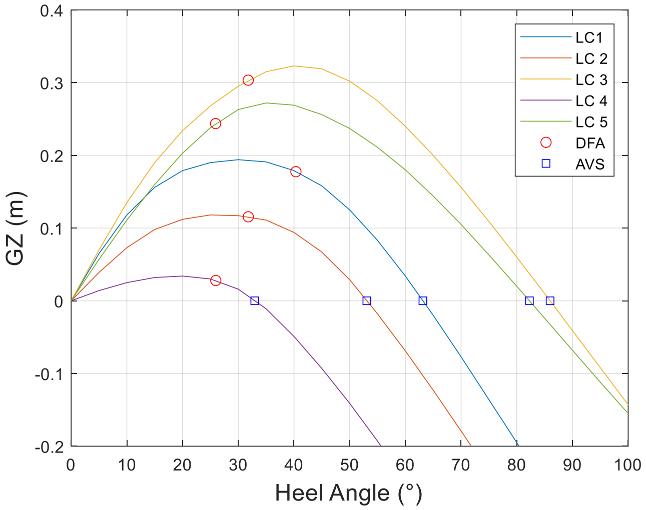

Figure 3.2. Angle of vanishing stability (*AVS*) and down flooding angle (*DFA*) of load case 1 – 5

Figure 3.2 and Table 3.4 show the Angle of Vanishing Stability (*AVS*) and Down Flooding Angle (*DFA*) for Load Case 1 – 5 in the stability curve, calculated by Maxsurf Stability Software. *AVS* is a static angle in the stability curve with zero *GZ*. In this condition, the ship is neither stable nor unstable. While *DFA* is a static angle, where the water meets any opening on the hull surface when calculating intact stability curve. The opening on the hull surface is marked with a down flooding point. However, in this study, the deck edge is defined as a down flooding point.

Table 3.4. Angle of vanishing stability (*AVS*) and down flooding angle (*DFA*) for load case 1 - 5

Load Case	***AVS* (deg)**	**(*DFA* (deg)**
LC 1	63.15	40.35
LC 2	53.09	31.80
LC 3	85.98	31.80
LC 4	32.96	26.00
LC 5	82.27	26.00

A different displacement such as empty (LC 1), half (LC 2 & 3), and full load (LC 4 & 5) results in different *DFA*. The vertical shift of centre of Gravity (*KG*) with the same displacement does not influence the *DFA*. It only influences the *AVS*. However, even if *AVS* is the same, the *GZ* value for the same displacement is different. These results will influence the roll responses and operability performance.

3.2.2. Seakeeping Optimisation

The fishing boat geometry studied herein is the FAO-01 geometry based on Pérez-Arribas et al. (2022). The main dimensions of the vessel are detailed in Table 3.5 and the 3D model based on the reference offset table is shown in Figure 3.3. The experimental data at F_r =0.33 in calm water, available in Díaz-Ojeda et al. (2023) are compared to the CFD-based results obtained here. Once the optimal loading conditions is determined, the CFD-based seakeeping simulations were conducted according to Table 3.6.

Table 3.5. Main dimensions of FAO-01 fishing vessel

Parameter	**Value**
Length overall, *LOA* (m)	9.232
Breadth moulded, *B* (m)	3.00
Depth moulded, *D* (m)	1.14
Loaded draft, *T* (m)	0.983
Volume Displacement, Δ(m^3)	5.846
Block coefficient, C_b (-)	0.267
Mid-boat section coefficient, *Cm* (-)	0.525
Wetted surface area, *Aw* (m^2)	23.914

Table 3.6. Simulation condition in waves

Parameter	**Value**
Scale Factor	4.00
Froude Number, F_r	0.33
wavelength ratio, λ/Lbp	1.15 to 3.0
wave height ratio, Hw/λ	0.06

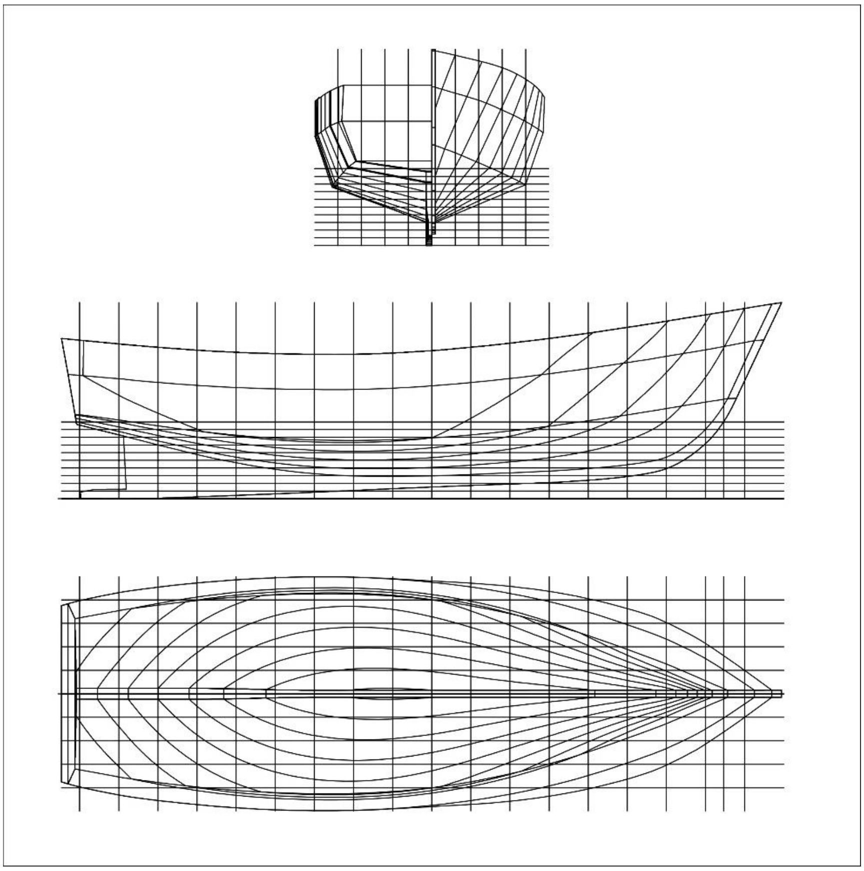

Figure 3.3. Lines plan of subject ship (Pérez-Arribas et al., 2022).

3.3. Seakeeping Analysis

From Figure 4.3, calculating a ship response in regular waves (RAO) is important to determine the operability analysis. The literature offers a wealth of seakeeping techniques which can be used to predict an RAO curve. One of the methods used to predict the motion responses of a ship is the 2-D Strip theory method which was introduced by Salvesen et al. (1970). This method splits the underwater part of the ship into several strips. Analytical or numerical methods are used to solve the two-dimensional hydrodynamic problem for each strip. Three-dimensional effects are ignored assuming there is no interaction between the strips, reducing computational time. The forces and moments from each two-dimensional cross-section can be integrated along the ship length to calculate the total force. This method is widely used because it is fast and is sufficiently accurate for conventional hulls. Even though strip theory is widely used, it has some limitations. The boat must be slender, and sail at low Froude numbers in relatively small waves, assuming first-order wave frequency motions only.

The development for solving the seakeeping problem evolved from 2-D to 3-D when computers become more advanced. The 3-D Panel Method can be used as an alternative to circumvent many of the assumptions made in the 2-D strip theory, for example, Datta et al. (2011). They investigated the fishing boat motion, where the hull form is not slender in the time domain. The 3-D Panel method requires the discretisation of the wetted surface into panels and some parts of the adjacent free surface. The hydrodynamic problem in each panel is solved using either the free-surface Green-function or Rankine panel method (He and Kashiwagi, 2014). This method can solve the ship motion in the time domain, for example, Liapis and Beck (1985) used the green-function method for a constant forward speed and Beck and Liapis (1987) for a zero-speed problem. For Rankine panel method was initially presented by Nakos and Sclavounos (1991).

The Computational Fluid Dynamics (CFD) technique is another method used in seakeeping analysis. A ship can be simulated in regular waves to determine its motion response characteristics. The time-series results of ship responses are converted to the frequency domain results using Fourier Transform to obtain the RAO values (Tezdogan et al., 2016, 2015). One of the advantages of the CFD method is that the full-scale ship simulation for seakeeping performance and ship resistance can be modelled presented by several researchers, such as Tezdogan et al. (2015), Niklas and Pruszko (2019), and Ozturk et al.(2021). The CFD method is not only powerful to model regular waves but also irregular waves as described by Romanowski et al (2019) and Zhang et al. (2021).

In this study, VERES, a plug-in of the ShipX software package was used to determine the ship RAOs. This method is based on the 2-D linear strip theory. The ship responses are assumed to vary linearly with incident wave amplitudes which are assumed to be small compared to the vessel dimensions. The wave steepness is also assumed to be small, so the waves are far from breaking. To determine the hydrodynamic forces, a potential theory is employed. The fluid is assumed as inviscid, irrotational, and incompressible. The viscous roll damping is determined from an empirical formula for roll motions. The components of this formula are frictional shear stress on the hull surface (Kato, 1957), eddy damping (Ikeda et al., 1977), lift damping (Himeno, 1981) and the bilge keel damping (Ikeda, 1979). As the ship geometry considered in this study has no bilge keel, the latter component is not included.

3.3.1. Ship Responses in Regular and Irregular Waves

The RAO of a ship in regular waves is described as the ratio between the response output (S_j) to the wave excitation input (ζ) for the six degrees of freedom (6DOF) in j

mode (for $j = 1 - 6$), as a function of encounter wave frequency (ω_e), and wave heading (β), as shown in Eq. (3.1). For rotational motion RAO, the wave excitation input (ζ) is multiplied by wave number (k).

$$RAO_j(\omega_e;\beta) = \frac{S_j\,(\omega_e;\beta)}{\zeta} \tag{3.1}$$

This thesis employs two methods to determine ship responses in regular waves. The first method is based on strip theory, which is relies on potential flow theory. The ShipX software, which utilises this method, was used to support the operability assessments in Chapters 4 and 5.

ShipX applies the strip theory method to solve seakeeping performance, making several assumptions. One key assumption is the linear relationship between ship responses and the incident wave amplitude. It should be noted that the Wave Scatter Diagram (WSD) for the Java Sea (Table 4.2) shows that the waves are relatively small compared to the size of the vessel, justifying the use of first-order wave theory in this method. The significant wave height (*Hs*) of 0.0 – 1.0 m has an 84.8% probability, which increases to 98.1% when an additional 13.3% is considered for *Hs* of 1.0 – 1.5 m. This indicates that the Java Sea is typically in Sea State 3 (Slight). However, using the most frequently occurring *Hs* of 84%, the wave amplitude is 0.5 m, which is close to the vessel's draft of 0.35 m and freeboard of 0.846 m.

Furthermore, potential flow theory is employed, meaning that viscous effects are not accounted for. To enhance accuracy, particularly in predicting roll amplitude, ShipX incorporates an empirical viscous roll damping calculation by Ikeda et al. (1977), lift damping (Himeno, 1981) and the bilge keel damping (Ikeda, 1979). Another assumption is that the vessel is slender, meaning the length of the hull must be significantly greater than the breadth. In this case, the fishing vessel under study is not slender, representing a limitation that must be acknowledged. Nevertheless, this method was chosen for its ability to save computational time to generate multiple RAOs in different speeds, wave headings, and loading conditions compared to using CFD (Computational Fluid Dynamics) for assessing the operability index.

The second method for determining ship responses in regular waves uses CFD simulations. This method includes viscous effects, which are particularly important for seakeeping results, especially concerning roll motions. A detailed discussion of this method is provided in Section 3.4.

After the calculation of the responses of the ship in regular waves, short-term responses in irregular seas should be calculated. An irregular seaway is defined as the sum of the regular waves in which each wave has a random height and period (St Denis and Pierson, 1953). A wave spectrum is used to represent a particular sea state. A short-term spectral analysis is used to predict the ship motions in a specific sea state. This analysis combines the transfer functions and the selected wave spectrum.

There are many standard wave spectra recommended by the International Towing Tank Conference (ITTC) (2002), such as spectra formulations given by Pierson Moskowitz (Pierson-Moskowitz (1964), ISSC (1964), ITTC (Mathews, 1972), and Liu (1971)), JONSWAP (Hasselmann et al., 1973), Scott (1965), and Ochi-Hubble (1976). In this present study, a JONSWAP spectrum is used. The wave spectrum multiplied by the square of the RAO gives the response spectrum. The area under the response spectrum can be used to determine the variance of the motions in question.

The JONSWAP Spectrum was used in this study because it suits the conditions of the boat's operational area (the Java Sea, Indonesia), which is closed waters or an archipelago (Hasselmann et al., 1973), (Djatmiko, 2012). The JONSWAP spectrum formula is shown in Eq. (3.2).

$$S_\zeta(\omega) = \left[\frac{\alpha g^2}{\omega^5} exp\left\{-\frac{5}{4}\left(\frac{\omega_p}{\omega}\right)^{-4}\right\}\right]\gamma^{exp\left\{-\frac{(\omega-\omega_p)^2}{2\sigma^2\omega_p{}^2}\right\}} \tag{3.2}$$

where $\alpha = 5.061(2\pi)^{-4}H_s^2\omega_p^4[1-0.287\ln(\gamma)]$ is the normalisation factor, ω_p is modal wave frequency $\left(\frac{2\pi}{T_p}\right)$, ω is incident wave frequency, $\sigma = 0.07$ is spectrum width parameter for $\omega \leq \omega_p$ and $\sigma = 0.09$ for $\omega > \omega_p$, and γ is peakedness parameter which varies between 1.0 – 7.0. For Indonesian waters, $\gamma = 2.0 - 2.5$ (Djatmiko, 2012). In this study peakedness parameter, $\gamma = 2.5$, was selected to calculate the highest sea condition.

The wave spectrum in incident wave frequency should be converted to a wave spectrum in encounter wave frequency-based by using (3.3). Then a response spectrum $S_r(\omega_e)$ was required to analyse the ship's response in irregular waves. The wave spectrum $S_\zeta(\omega_e)$ multiplied by the RAO squared gives the response spectrum $S_r(\omega_e)$, as shown in Eq. (3.4). The area under the response spectrum curve is expressed by m_n or the n-th moment (Eq. (3.5)), where $n = 0$ for displacement, $n = 2$ for velocity, and $n = 4$ for acceleration. The square root of m_n is called the Root Mean Square (RMS) or standard deviation, as shown in Eq. (3.6) (Bhattacharyya, 1978).

$$S_\zeta(\omega_e) = S_\zeta(\omega)\frac{g}{g - 2\omega U cos\mu} \tag{3.3}$$

$$S_r(\omega_e) = RAO^2 \times S_\zeta(\omega_e) \tag{3.4}$$

$$m_n = \int_0^\infty \omega^n S_r(\omega_e) d\omega \tag{3.5}$$

$$RMS = \sqrt{m_n} \tag{3.6}$$

Ship responses are usually calculated at the Centre of Gravity (*CoG*). However, ship responses at other points of interests, such as the fore peak (FP) for deck wetness and slamming probability, should also be investigated. Both heaving and pitching responses at the *CoG* can be used to determine ship responses at the FP. This response is called absolute vertical motion at FP (Z_{FP}), as shown in Eq. (3.7) (Bhattacharyya, 1978).

$$Z_{FP} = (Z_{FP})_a \cos(\omega_e t + \varepsilon_{FP}) \tag{3.7}$$

$$(Z_{FP})_a = \sqrt{(Z_a)^2 + (x_{FP}\theta_a)^2 - 2x_{FP}Z_a\theta_a \cos(\varepsilon_\theta - \varepsilon_Z)}$$

$$\varepsilon_{FP} = tan^{-1}\left(\frac{Z_a sin(\varepsilon_Z) - x_{FP}\theta_a \sin(\varepsilon_\theta)}{Z_a cos(\varepsilon_Z) - x_{FP}\theta_a \cos(\varepsilon_\theta)}\right)$$

where $(Z_{FP})_a$ is amplitude of absolute vertical motion at FP, ε_{FP} phase angle of absolute of vertical motion at FP, Z_a and θ_a are the amplitude of heaving and pitching motions, x_{FP} is longitudinal distance from *CoG* to FP, ε_Z and ε_θ are the phase angle of heaving and pitching motions.

After the absolute vertical motion at FP has been determined, this response is calculated relative to wave amplitude at the FP to generate the RAO curve. This response is called relative vertical motion (S_{FP}), as shown in Eq. (3.8) (Bhattacharyya, 1978).

$$S_{FP} = (S_{FP})_a \cos(\omega_e t + \varepsilon_s) \tag{3.8}$$

$$(S_{FP})_a = \sqrt{((Z_{FP})_a)^2 + (\zeta_a)^2 - 2(Z_{FP})_a\zeta_a \cos(kx_{FP} - \varepsilon_{FP})}$$

$$\varepsilon_s = tan^{-1}\left(\frac{(Z_{FP})_a sin(\varepsilon_{FP}) - \zeta_a \sin(kx_{FP})}{(Z_{FP})_a cos(\varepsilon_{FP}) - \zeta_a \cos(kx_{FP})}\right)$$

where $(S_{FP})_a$ is the amplitude of relative vertical motion at *FP*, ε_s is the phase angle of relative of vertical motions at *FP*, ζ_a is the wave amplitude, k is the wave number.

Based on Eq. (3.8), a different encounter frequency (ω_e) will produce different relative vertical motions at *FP* (S_{FP}). All encounter frequencies will generate another RAO graph, which is RAO for relative vertical motion at *FP*. Based on Eq. (3.5), the response spectrum of motion and velocity (m_0, m_2) can be determined. Eq. (3.9) and Eq. (3.10) are used to calculate the Probability of Slamming and Deck Wetness (Bhattacharyya, 1978). Here, T is the draft in meters, V_{cr} is the velocity threshold in m/s where $V_{cr} = 0.093\sqrt{Lpp \times g}$ (Faltinsen, 2005; Ochi, 1964), Fb is the freeboard in meters, m_0 and m_2 are area under displacement and velocity response spectrum, respectively.

$$P_{slamming} = exp\left\{-\left(\frac{T^2}{2m_0}+\frac{V_{cr}^2}{2m_2}\right)\right\} \tag{3.9}$$

$$P_{deckwetness} = exp\left\{-\frac{Fb^2}{2m_0}\right\} \tag{3.10}$$

3.4. CFD Modelling

When the viscous term is important, the CFD method must be employed to accurately capture the behaviour of the flow. While the method provides high accuracy, it can also entail considerable computational cost. This thesis utilised the CFD method to simulate the parametric roll of the fishing vessel. Moreover, in seakeeping optimisation chapters, this method effectively generates the RAO curve of heave, pitch, and added resistance. However, the CFD simulation was not involved in the optimisation process, as the novel objective function, R_y and GM ratio, in this study can be determined easily and quickly without CFD. This approach helps to reduce the need for CFD simulation in the optimisation process. Consequently, the CFD simulations in the seakeeping optimisation chapters are limited to a few cases: the initial and optimal loading conditions.

The present thesis uses three types of simulations: 1) parametric roll simulation, 2) calm water resistance simulations, and 3) seakeeping simulations. The CFD simulations were performed using the commercial CFD software, Siemens Star CCM+ version 17.04. To solve the unsteady RANS equations, the software discretised the governing equations by using the finite volume method (FVM). First-order discretisation is used for the time term and second order for the convective term of the Unsteady Reynold-Average Navier Stokes (URANS) equations.

3.4.1. Governing Equation

Reynold Averaged Navier Stokes (RANS) equation models the fluctuating velocity field in an averaged manner. The averaged continuity and momentum equation for incompressible flow with surface forces without body force are shown in Eq. (3.11) and (3.12), respectively.

$$\frac{\partial(\rho\bar{u}_i)}{\partial x_i} = 0 \tag{3.11}$$

$$\frac{\partial(\rho\bar{u}_i)}{\partial t} + \frac{\partial}{\partial x_j}\left(\rho\bar{u}_i\bar{u}_j + \rho\overline{u_i'u_j'}\right) = -\frac{\partial\bar{p}}{\partial x_j} + \frac{\partial\bar{\tau}_{ij}}{\partial x_j} \tag{3.12}$$

Where ρ is fluid density, $\bar{u}_i\bar{u}_j$and $\bar{p}$ are mean velocity vector and mean pressure in Cartesian x_i. $\rho\overline{u_i'u_j'}$ is the Reynolds stresses. For the eddy-viscosity model is shown in Eq. (3.13). $\bar{\tau}_{ij}$ is mean viscous stress tensor, as shown in Eq.(3.14).

$$-\rho\overline{u_i'u_j'} = 2\mu_t S_{i,j} - \frac{2}{3}\rho\delta_{ij}k \tag{3.13}$$

$$\bar{\tau}_{ij} = \mu\left(\frac{\partial\bar{u}_i}{\partial x_j} + \frac{\partial\bar{u}_j}{\partial x_i}\right) \tag{3.14}$$

μ_t is the turbulent (or eddy) viscosity, $S_{i,j}$ is the mean strain-rate tensor in which $S_{i,j} = \frac{1}{2}\left(\frac{\partial\bar{u}_i}{\partial x_j} + \frac{\partial\bar{u}_j}{\partial x_i}\right)$, μ is the dynamic viscosity, δ_{ij} is Kronecker delta, where $\delta_{ij} = 1$ if $i = j$ otherwise $\delta_{ij} = 0$. Finally, k is the turbulent kinetic energy, as shown in Eq. (3.15).

$$k = \frac{1}{2}\overline{u_i'u_i'} = \frac{1}{2}\left(\overline{u_x'u_x'} + \overline{u_y'u_y'} + \overline{u_z'u_z'}\right) \tag{3.15}$$

During the iteration process, the pressure and velocity values were calculated in segregated manner. To handle the pressure-velocity coupling, the Semi-Implicit Method for Pressure Linked Equation (SIMPLE) algorithm was utilised.

3.4.2. Turbulence Model and Near-Wall Modelling

Based on the non-dimensional wall distances (y^+), the boundary layer is divided into three regions, namely, the viscous sublayer ($y^+ < 5$), the buffer layer, ($5 < y^+ < 30$), and the log layer ($y^+ > 30$). The buffer layer, which is typically avoided, is transitional between the viscous sublayer and the log layer. Neither the wall function nor the near-wall treatment can be used in this region. The all y^+ treatment scheme in Star CCM+ package was used in this simulation to treat the boundary layer region either in low y^+grids (when $y^+ < 5$) or in high y^+ grids (when $y^+ > 30$).

The Shear-Stress Transport (SST) (Menter, 1994) model was used, which combines a k-ε model in the far field with a k-ω model near the wall for parametric roll chapter. Additionally, the $k - \varepsilon$ turbulence model was selected to model turbulence for seakeeping optimisation chapters. To capture the turbulence effect accurately, the log layer law was implemented, ensuring that the wall distance (y^+) remained below 1 for parametric roll chapter and between 30-100 in seakeeping optimisation chapters.

The no-slip wall is a boundary condition that is a source of vorticity in most flow problems (Siemens, 2022). The ship hull is defined as the wall for all CFD simulations in the naval architecture field. There is a region near the wall called the boundary layer. It is important to predict the fluid flow and turbulence in this region as accurately as possible.

Determining the number of near-wall layers is essential to obtain the desired y^+ effectively. The procedure to determine the number of these layers in this study was based on Terziev et al. (2022). By initially computing the friction coefficient, C_f, using ITTC correlation line (Eq. (3.16)), the shear wall stress, τ_w can subsequently be ascertained (Eq. (3.17)). Here Re denotes the Reynolds number and V denotes the vessel's forward speed. Afterwards, the first layer thickness ($2\Delta_y$) can be calculated using Eq. (3.18), where v is the kinematic viscosity and $u_t = \sqrt{\frac{\tau_w}{\rho}}$ is friction velocity. It should be noted that Δ_y is the distance between the wall to the first cell centre. Thus, the first layer thickness is equal to $2\Delta_y$.

Finally, the number of prism layers, n, can be calculated using Eq. (3.19), where S is the stretch factor, expressing the ratio of the thickness of any two adjacent cell layers, and δ is the distance over which near-wall layers are distributed. The current research reported in this research used the stretch factor of 1.2. The specific distance, δ, was determined by modelling a fraction of the flat plate equivalent turbulent boundary thickness $\delta = \frac{0.382L}{Re^{\frac{1}{5}}}$.

$$C_f = 0.075/(\log_{10} Re \ - 2)^2 \tag{3.16}$$

$$\tau_w = 0.5\rho V^2 C_f \tag{3.17}$$

$$\Delta_y = y^+ v/u_t \tag{3.18}$$

$$n = \log\left(1 - \frac{\delta(1-S)}{2\Delta_y}\right)/\log(S) \tag{3.19}$$

3.4.3. Capturing Free Surface

The present study employs the Volume of Fluid (VoF) method. This technique included as the family of surface capturing method, as stated in Siemens (2022). The VoF approach, first introduced by Hirt and Nichols (1981), differentiates between the two fluid phases (water and air) by assigning a scalar value between 0 and 1 to each cell, representing the volume fraction (α_i) of a particular fluid in that cell. The volume fraction α_i is defined as $\frac{Vol_i}{Vol}$, where Vol_i is volume of phase i and Vol is the volume of the cell. For instance, if water is represented by one and air by zero, then a cell containing 50% water and 50% air would have a scalar value (volume fraction) of 0.5, indicating the location of the air-water interface. Furthermore, the fifth-order waves were selected for all simulations in waves.

For multiphase simulations, the interface between two phases can be captured using different techniques. There are three methods that is available in most of CFD code nowadays, which are: 1) surface fitting / mesh deformation, 2) surface capturing, and 3) level set (Wackers et al., 2011). For example, a cell that contains only water, α_i is be assigned as 1. Likewise, a cell that contains only air, α_i is be assigned as 0. Based on this scalar value, the interface between two fluid phases (the cells contain water and air) can easily be defined as the collection of cells with a volume fraction α_I of 0.5. The High-Resolution Interface Capturing (HRIC) scheme in the software package proposed by Muzaferija (1998), was employed to maintain a sharp interface between the fluid phases. This scheme is suitable for tracking sharp interfaces such as those formed between water and air.

3.4.4. Simulation of Ship Motion

The employed solver, Star CCM+, uses the Dynamic Fluid Body Interaction (DFBI) module to simulate the motion of a rigid body. This module allows a body to respond to forces and moments applied by the physics continuum or any additional user-defined force or moment (Siemens, 2022).The restoring arm variation is not only influenced by the waves themselves, but also by the coupling between heave, pitch, and roll (Neves and Rodríguez, 2006). Thus, the DFBI module was utilised in this study to capture three degrees of freedom of the boat when moving on the wave, which is pitch, roll and heave. The DFBI module also computes exciting forces, moments, and the gravitational force acting on the hull and solves the governing equation of motion to determine the new position of the rigid body at each time step.

3.4.5. Computational Domain

For parametric roll simulations, the computational domain size for KCS model ranges from $-2.5LOA < x < 2LOA$ in length and $-1LOA < z < 0.4LOA$ for height, and $-1LOA < y < 1LOA$ in width. There is a difference in hull shape between the KCS and the fishing boat, namely, the KCS is more slender than the fishing boat. Specifically, the L/B ratio of the KCS is 7.14, whereas that of the fishing boat in Chapter 6 is 2.59. As the ratio of the fishing boat is lower, a larger computational domain is required than for the KCS, specifically $-3.0LOA < x < 2.5LOA$ in length and $-1.5LOA < z < 1.0LOA$ for height, and $-1.5LOA < y < 1.5LOA$ in breadth.

Figure 3.4 displays the computational domains for both the KCS model and the fishing boat. The size of computational domains for other similar CFD studies in the literature is shown in Table 3.7. It should be noted that the domain size was reversed for LC4. In this case, the downstream was positioned behind the boat, while the upstream was situated in front of the boat.

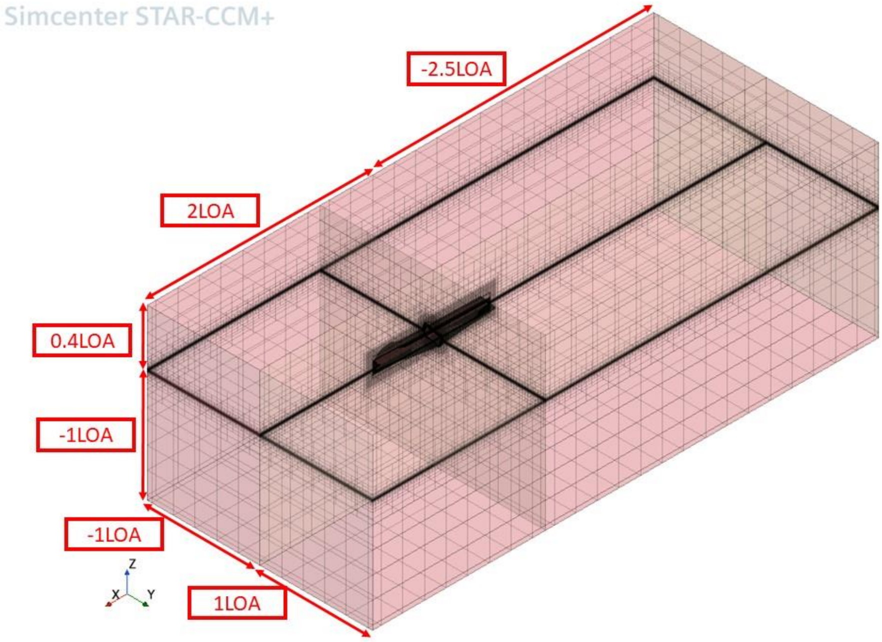

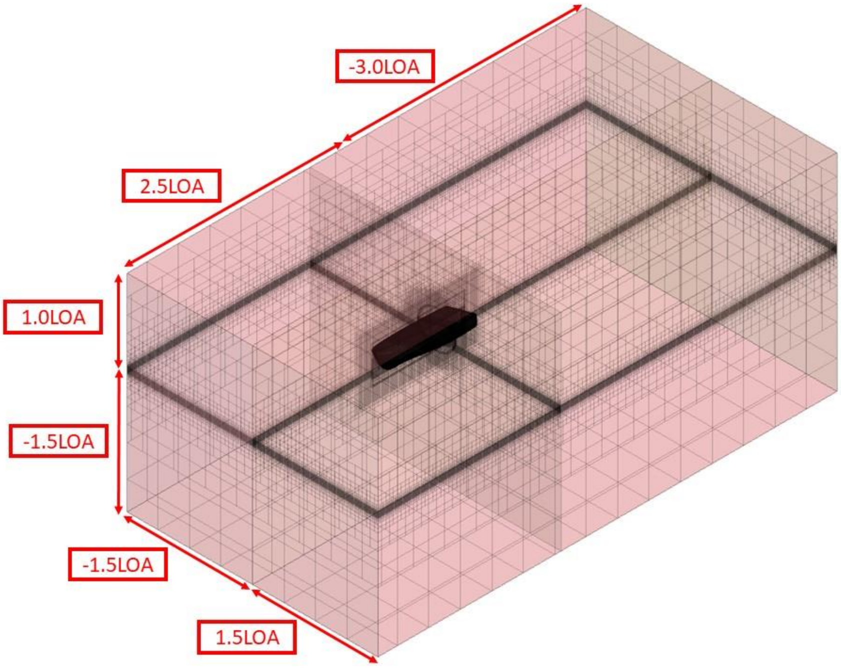

Figure 3.4. Computational domain of the KCS model (top) and the fishing boat (bottom)

All the coordinate system in this thesis is defined such that the X direction aligns with the longitudinal axis, parallel to the ship length, with the zero-point coinciding with the AP and the positive direction oriented towards the FP. The Y axis aligns with the transversal direction, with the zero-point situated at the ship's centre line and the positive direction oriented towards the port side. The vertical direction corresponds to the Z axis, with the zero-point located at the calm water free surface. The positive direction is upward, and the negative direction is downward.

Table 3.7. Computational domain size of the similar previous studies

Reference	Upstream	Downstream	Top	Bottom	Transverse
(Sadat-Hosseini et al., 2010)	0.5 L	2.0L	0.25L	1.0L	1.0L
(Ma et al., 2018)	2.0λ	4.5λ	1.5λ	2.5λ	2.5λ
(Liu et al., 2021)	1.0L	3.0L	0.4L	1.0L	1.0L

For the FAO-01 fishing boat used in Chapter 7-9, a slightly different domain size was used due to its distinct dimensions compared to the KCS, as shown in Figure 3.5. The domain for the FAO-01 fishing boat ranges from -3.0LOA to 2.5LOA in length and -1.5LOA to 1.0LOA in height, and 0 to 1.5LOA in width. However, the method for determining the grid size, time step and physics model remains the same as that used for the KCS.

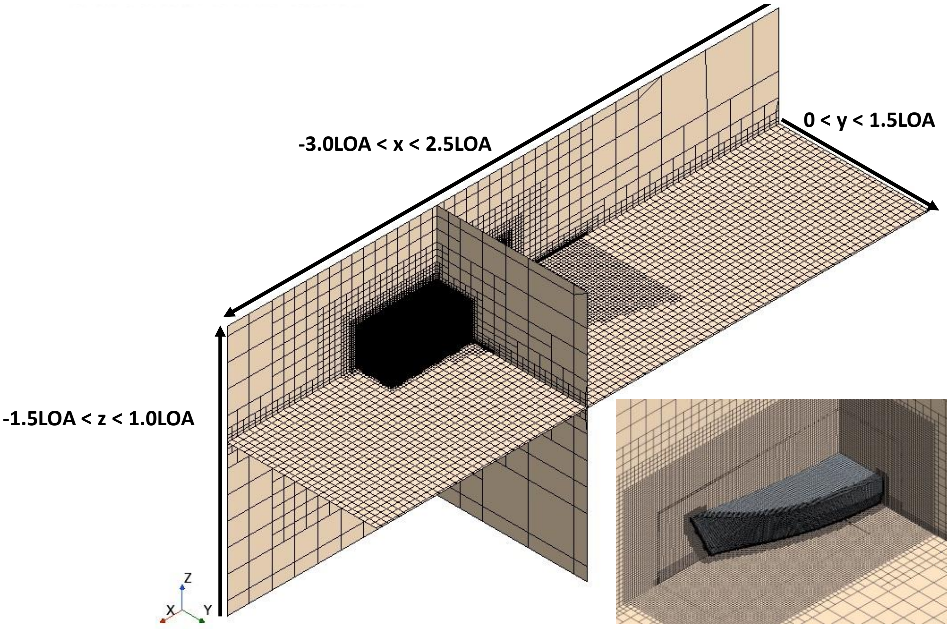

Figure 3.5. Computational domain size and the result of mesh for fishing boat

3.4.6. Boundary Conditions

The hull surface is set as a no-slip wall. All boundary conditions on the rectangular domain sides are set as velocity inlet, except for the downstream side, which is the pressure outlet. This boundary type was the same as (Galbraith and Boulougouris, 2015), (Ma et al., 2018), (Liu et al., 2021), where the downstream boundary was set as pressure outlet, and remains boundary as velocity inlet. These boundary conditions are reversed for LC4.

For the inlet boundary, the fifth order VOF Wave modules were used to represent fluid in the computational domain with the wave. The forcing method was applied on the Inlet, outlet, and right and left side boundaries. This method forces the fluid properties and the volume fraction of water in the forcing zone to be what the user input in the boundary condition. In this case, the forcing zone is forced to produce the fifth-order wave defined in the inlet boundary condition. Technically, the free surface contour in the forcing zone is not affected by the ship's speed and motion. This means that the wave reflection from the boundaries can be avoided. The forcing length was set as 1 LOA (2.415 m) from inlet and outlet boundaries and 1.0 m from the left and right-side boundaries.

On the other hand, the computational domain for all seakeeping optimisation chapters bisects the ship for calm water resistance and seakeeping simulations, using a symmetrical boundary condition applied on the domain surface where the centreline of the ship is located. The remaining boundary conditions remain consistent, where all other domain surfaces in the computational domain are set as velocity inlet, except for the surface at the rear of the ship, which was a pressure outlet.

Inlet boundaries maintain the velocity of water and air, while the pressure outlet maintains hydrostatic pressure. Wave damping and forcing functions were applied for resistance and seakeeping simulations, respectively. These conditions act at a distance of 1LBP from the inlet and the outlet, and 1.0 metre or 0.3LBP from the side boundary for the KCS, and 0.5LBP for fishing boat.

3.4.7. Mesh Resolution

The automatic meshing facility in Star CCM+ was used to generate mesh based on the cartesian cut-cell method. The trimmed cell mesher and surface remesher are applied to generate a volume grid consisting of hexahedral cells and refine it to be a high resolution of rectangular mesh on a surface. For each region (background and overset), two types of refinement are used: boundary layer refinement and refinement at the free surface (for seakeeping) or Kelvin's wave refinement (for calm water resistance). The boundary layer refinement has been explained in section 3.3.2.

The Star CCM+ software offers three mesh configurations to simulate rigid body motion: moving mesh, morphing, and overset mesh. Moving mesh involves moving all the mesh in the domain based on the body's movement, while morphing deforms the mesh around a moving body without moving the domain. Overset mesh, on the other hand, consists of two regions, the background and overset, where the overset mesh moves while the background remains static. A comparison of these three methods on the resistance of planning hull was described in Yulianti et al. (2022). The overset mesh module was used in this thesis. Mesh refinements were set in the free surface region.

For the verification study in parametric roll chapter, the influence of two different y^+ values on the amplitude of parametric roll were compared, namely $y^+ < 1$ and $30 < y^+ < 100$. Twelve layers of prismatic cells were used with the first grid distance of 4.579×10^{-5} m for 2.3 m KCS model to ensure the averaged $y^+ < 1$ over wetted surface area (WSA).

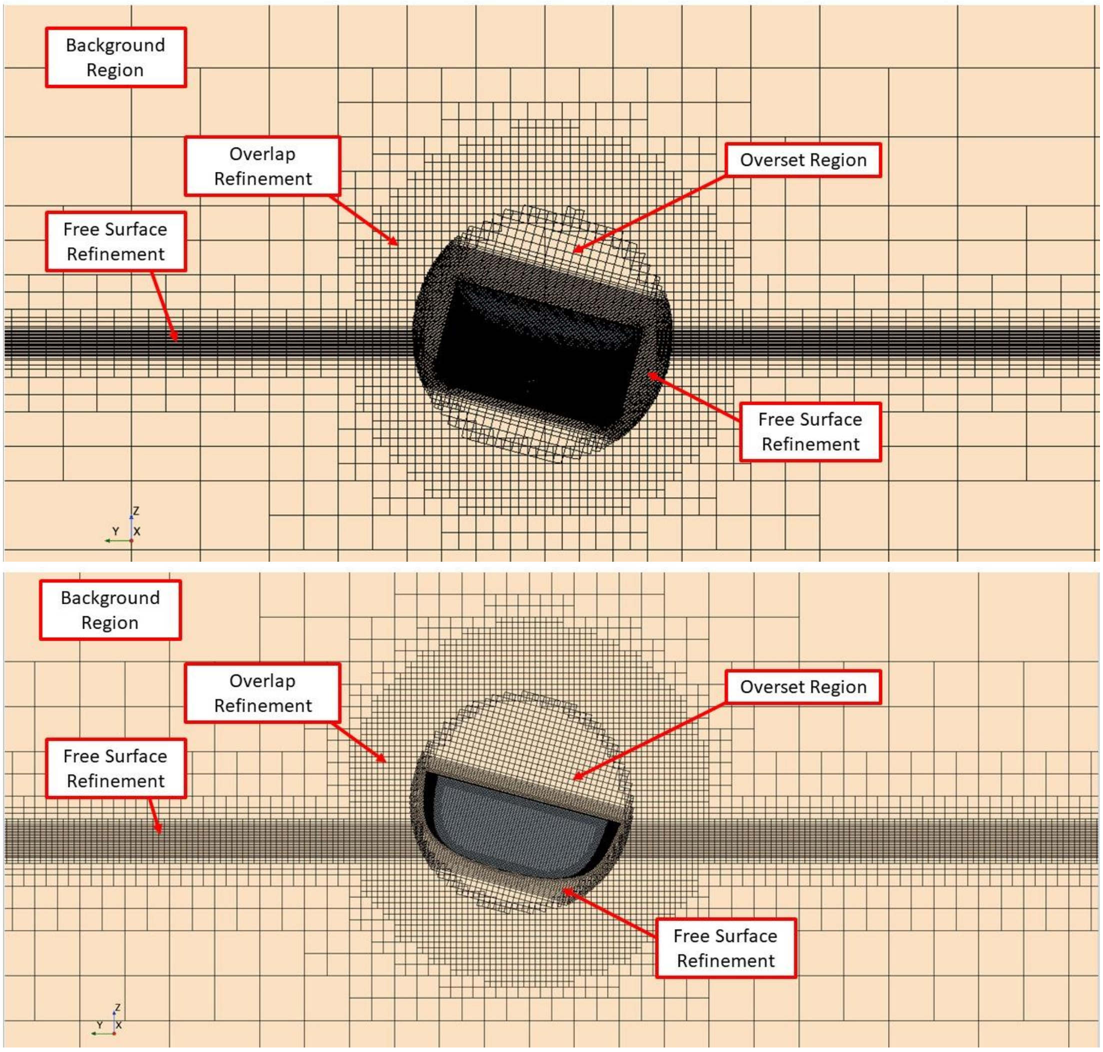

Figure 3.6. Regions and refinements for the KCS model (top) and the fishing boat (bottom) for parametric roll simulation

On the other hand, to set a targeted $y^+ = 30\text{-}100$, one layer of the prismatic cell was used with the first grid distance of 3.625×10^{-3} m. The hull boundary layer for the fishing boat simulations was set to 17 layers for the highest Reynolds number (LC 3) to ensure $y^+ < 1$. This same number of layers was used for all load cases except for LC 4, which used 15 layers since its Reynolds number was the lowest among all load cases.

All wave simulation settings used in this thesis followed the ITTC (2011) recommendation, where for both longitudinal and transversal refinement at the free surface region are λ/80 and Hw/20 for the horizontal and vertical direction, respectively. The same mesh refinements were also applied to fishing boat simulations. Figure 3.6 shows the visualisation of two regions and mesh refinement of for both the KCS model and the fishing boat in parametric roll chapter.

For all seakeeping optimisation chapters, the determination of the first layer height was calculated based on the targeted y^+, between 30 – 100, which is sufficient when using the log layer region using the method described in Terziev et al. (Terziev et al., 2022). The Kelvin wake at the free surface for resistance simulations was determined based on the predicted transverse wavelength (shown in Eq. (3.20)). Here, k represents the wave number and g represents gravitational acceleration. The area affected by the Kelvin wave has an ingress angle of 20° and extends up to 1L behind the vessel.

$$\lambda = \frac{2\pi}{k} = \frac{2\pi}{\left(\frac{g}{V^2}\right)} \tag{3.20}$$

To ensure accurate representation of the Kelvin wake, 24 cells are distributed per wavelength which establish the cell length and width. As the amplitude of the tranverse wave is unknown, the cell's height within this zone is determined by its length. The height cell (z- direction) is 1/8 of the cell length (x-direction). The refinement for free surface in the whole computational domain was determined by multiplying the cell size in Kelvin’s wave region by a factor of 2.

3.4.8. Determination of the Time Step

According to the ITTC recommendations (ITTC, 2014), for calm water resistance simulations, the time step is determined using Eq. (3.21), where L corresponds to the ship length in metre and V corresponds to ship speed in m/s. For seakeeping simulations, ITTC stipulates that the minimum time step is $T_e/100$. However, this study used $T_e/2^8$, which is smaller than ITTC recommendation, following the approach by Cho et al. (Cho et al., 2023).

$$\Delta t = (0.005{\sim}0.01)\,\frac{L}{V} \tag{3.21}$$

3.5. Optimisation Process

3.5.1. Design of Experiment (DoE)

The initial step before conducting the optimisation is to identify the objective function and design variables. The comprehensive discussion regarding this is explained in each chapter for seakeeping optimisation chapter, Chapter 7 – 9.

The Central Composite Design (CCD) method was chosen as the Design of Experiment (DoE) for two design variables, as shown in Figure 3.7. The code of ± 1.414 corresponds to fractional factorial designs, specifically tailored for two-level factorial experiments involving two design variables. These designs are augmented by several centre points and other chosen runs. To apply this DoE, each design variable is converted into a code, where the minimum and maximum values are assigned as -1 and 1, respectively, while the original model is assigned as 0. In this study, the range between the minimum and maximum values of the design variables is determined as $\pm 5\%$ from the original value.

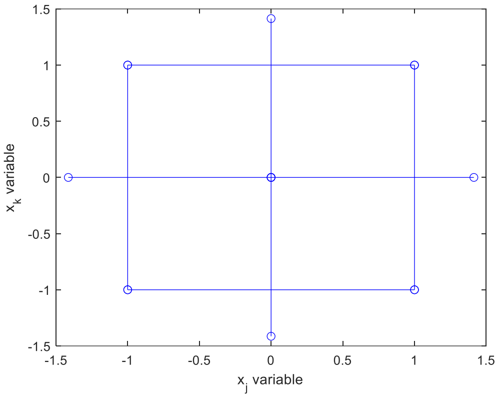

Figure 3.7. Nine designs of experiment using central composite design (CCD)

3.5.2. Approximate Mathematical Model

Utilising the Central Composite Design method illustrated in Figure 3.7, the total number of design experiments for each scenario is nine, with each yielding a distinct result. All of these results are used to construct the mathematical model, which in this case is a quadratic polynomial. The regression equation for two variables is shown in Eq. (3.22).

$$y(x_j, x_k) = a + bx_j + cx_k + dx_j{}^2 + ex_k{}^2 + fx_jx_k \tag{3.22}$$

Here, $y_i(x_j, x_k)$ represents the response or objective function that is dependent on the design variables x_j and x_k. The response (y) corresponds to $R_y(x_1, x_2)$. Then, j

and k take values of the input parameters, LCG and KG. The coefficients a to f are determined through linear regression.

3.5.3. Optimal Solution

The subsequent step in this optimisation process involves achieving the objective functions. The minimum response can be ascertained once a mathematical equation for each response has been established. According to the Response Surface Method, there are three potential shapes for a response, 1) Maximum, 2) Minimum, and 3) Saddle shape, wherein one variable tends towards a maximum while the other tends towards a minimum.

For maximum and minimum responses, the optimal solution can be determined based on the first derivative of the response with respect to each variable (j, k), as depicted in Eq. (3.23). Then, two linear equations containing two variables need to be solved to identify the stationary point (x_j, x_j) which corresponds to either a maximum or a minimum response (y_i).

$$
\begin{aligned}
y_{i\,max/min}(x_j, x_k) &= \frac{dy_i(x_j, x_k)}{dx_j} \\
y_{i\,max/min}(x_j, x_k) &= \frac{dy_i(x_j, x_k)}{dx_k}
\end{aligned}
\tag{3.23}
$$

The minimum or maximum surface location may be significantly distant from the initial point, making it challenging or even infeasible to implement. Therefore, it is necessary to impose constrains to ensure the feasibility of the optimum condition. In this case, the maximum and minimum code for each variable is set as ± 2.5 or $\pm 12.5\%$. These maxima and minima constitute the aforementioned constraints.

3.6. Summary

The subject ship and simulation conditions used in this thesis are presented, covering the operability assessment and parametric roll chapters for a 5-meter fishing boat, and the FAO-01 fishing vessel for seakeeping optimisation chapters. The repeated methodologies used throughout the thesis are also outlined.

4. Operability Analysis of Traditional Small Fishing Boats in Indonesia with Different Loading Conditions

4.1. Introduction

The operation of fishing vessels is different from that of a merchant ship. The net cargo of merchant ships tends to remain unchanged during the voyage. The cargo will be loaded onto the ship before departure from the fishing location(s) and released after arriving at the destination port. For fishing boats, the net cargo, which is fish caught, will be zero at departure. When underway, the cargo will be filled gradually. For this reason, the boat's loading conditions alongside its centre of gravity will change during its operation at sea.

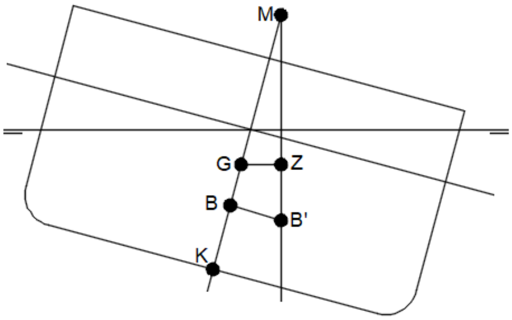

Figure 4.1. Position of *KM*, *KG*, and *GM*

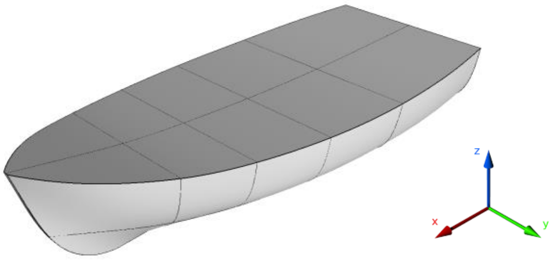

Figure 4.2. Coordinate system of the boat

Figure 4.1 shows the position of Vertical Centre of Buoyancy (*KB*) and Gravity (*KG*). Each displacement (draught) has a unique vertical buoyancy (*KB*). From this condition, we also can calculate *BM* as a volume displacement function *(BM = I/Vol)*. The total of both heights is *KB*+*BM* = *KM*. In this research, the influence of loading conditions (empty, half, and full load) is examined, as it can change the *KM*. Different *KG* was also examined and resulted in different *GM*, as *GM* = *KM* – *KG*. Changes in the load will affect the stability points such as *KG*, *KM* and *GM*, and alter the natural frequencies and damping coefficients in the roll and pitch motions of the ship. As a result, the ship's motion responses will also change. The coordinate system used in this study is shown in Figure 4.2.

An operability analysis with a fishing boat was carried out to determine how the boat can operate safely and comfortably in its operational area, ensuring that the boat does not exceed the pre-determined seakeeping criteria. This investigation aims to inform the fishers how long a boat should be kept on standby on the shore until the weather conditions permit the boat to operate. A 5-metre-long traditional fishing boat operating in the Java Seas, Indonesia, was used as a case study. Five configurations of loading conditions were employed to represent the operation of the fishing boat in question. Each condition was then examined for its seakeeping performance and operability based on a 2-D linear potential theory using ShipX VERES Software.

ShipX is a hydrodynamic software platform developed by SINTEF for ship design and performance analysis. It integrates tools for hull geometry handling, ship motion simulations, and power performance predictions. Specialised plug-ins cover areas like seakeeping (VERES), station-keeping, and ship manoeuvring (SIMAN), as well as speed loss in waves. It also features animation and report generation for testing outcomes. The operability calculation in this thesis used VERES plug-in.

Two types of operability assessment were utilised in this study, namely Percentage Operability (PO) developed by Fonseca and Soares (2002) and Operability Robustness Index (ORI) developed by Gutsch et al. (2020). PO was assessed corresponding to seakeeping criteria for fishing vessels. ORI was applied to evaluate the RMS roll response and the expected maximum roll amplitude of the boat, which were observed as key to preventing stability failure. The stability curve is used to relate the ship stability analysis to the seakeeping analysis.

The present chapter aims to determine the effect of changes in load on a traditional fishing boat’s operability in Indonesia, considering the ship’s intact stability. In addition, the work presented herein highlights the response of the ship roll motion to prevent stability failure. The stability curve is used to relate ship stability analysis to seakeeping analysis. Percentage operability and Operability Robustness Index are used to assess the root mean square (RMS) roll response and the ship's expected maximum roll motion.

4.2. Methodology

4.2.1. Overview of Operability Analysis

Sea conditions always change with time and depend on the location. To ensure the ship can be well-operated within these conditions, long-term analysis is used, also called ship operability analysis. Ship operability is the percentage of time in which the ship can operate in an area by meeting selected seakeeping criteria based on an existing wave scatter diagram (WSD). WSD is statistical data of waves in a particular location that records the number of occurrences of significant wave heights (H_s) and wave peak periods (T_p) within certain time ranges, such as daily, weekly, monthly, seasonal, and annually.

Figure 4.3 describes an overview of the operability analysis procedure. The red colour indicates an input for calculation, and the green colour is the result. First, vessel data and the conditions are required to calculate response amplitude operators (RAOs), that is, the boat responses in regular waves. The combination between RAOs and selected wave spectrum will result in responses spectrum (short-term analysis), boat responses in irregular waves. The variance of the motions, such as root means square (RMS) and the probability, can be determined from the response spectrum. Then, the selected seakeeping criteria will result in operability limiting boundary, the limit of significant wave height and wave period that make the boat responses do not surpass the seakeeping criteria. Lastly, a particular wave scatter diagram of a specific sea area (the location where the boat operates) is used to calculate the percentage operability.

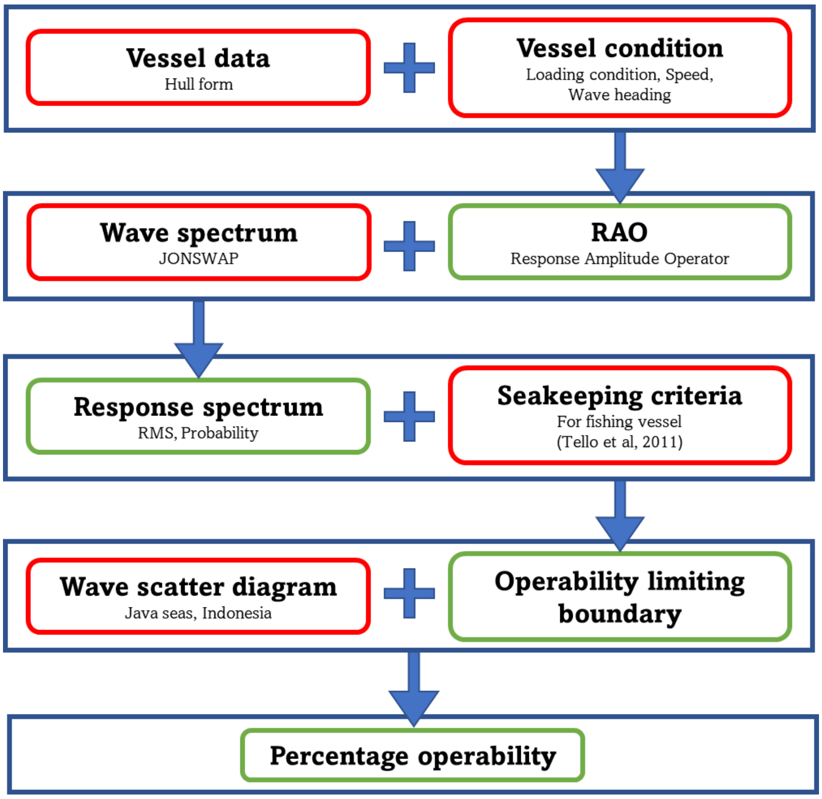

Figure 4.3. Overview of the operability analysis procedure

4.2.2. Operability Limiting Boundary

Seakeeping criteria are used to evaluate the vessels' performance based on short-term spectral analysis. These criteria are essential as they can be used to determine a ship's operability in a certain period by combining them with a Wave Scatter Diagram (WSD). Various types of seakeeping criteria exist today. These criteria are used according to the type of ships, such as the Nordic cooperative research project on the seakeeping performance of ships (NORDFORKS) for a merchant ship, naval vessel, and fast small craft (Nielsen, 1987) and NATO Standardization Agreement (STANAG) 4154 for naval vessels (Eriksen et al., 2000). For passenger ships, the criteria are more focused on passenger comforts, such as Motion Induced Interruption (MII) (Baitis et al., 1995) and Motion Sickness Incident (MSI) (O'Hanlon and McCauley, 1973). Details for different types of seakeeping criteria can be found in Ghaemi and Olszewski (2017).

Sariöz & Sariöz (2006) investigated the seakeeping performance of high-speed displacement vessels (HSDVs) using typical seakeeping performance criteria. The pitch and roll motions, vertical and lateral accelerations, and the number of slamming events and deck wetness per hour were found to be significant in determining the seakeeping criteria. For a high-speed passenger ship, Tezdogan et al (2014) used human comfort as limiting criteria which are MII, MSI, vertical and lateral accelerations. In the current study, the limiting criteria are selected for fishing vessels listed in Table 4.1 (Tello et al., 2011).

Table 4.1. Seakeeping criteria for fishing vessel (Tello et al., 2011)

No	Criteria	Limit
1	RMS roll	6.00°
2	RMS pitch	3.00°
3	Probability of green water (GW)	0.05
4	Probability of slamming (SL)	0.03
5	RMS vertical acceleration at working area / bridge deck (VA)	0.20 g
6	RMS lateral acceleration at working area / bridge deck (LA)	0.10 g

Each criterion has a different operational limit, meaning that each criterion has a different maximum significant wave height as a limitation for the vessel to operate for a certain peak wave period. Nevertheless, all criteria must be met to set the limits of the vessels' operation.

The ship response per meter of significant wave height (g_x) can be written as in Eq. (4.1) where σ_x is ship response and H_s is significant wave height. For displacement/motion criteria, Eq. (4.2) is used to determine the limiting significant wave height (H_s^{lim}), where σ_x^{lim} is the limiting value of the specific motion criterion (Fathi, 2018).

$$g_x = \frac{\sigma_x}{H_s} \tag{4.1}$$

$$H_s^{lim}(T_p) = \frac{\sigma_x^{lim}}{g_x} \tag{4.2}$$

For the slamming criterion, Eq. (4.3) based on Ochi (1964) is used to determine the limiting significant wave height (H_s^{lim}), where Ps is a probability of slamming criterion (Ps =0.03), g_r and g_{rv} are RMS–value of relative vertical motion and velocity per meter significant wave height, respectively. Here, T is the draft in meters. The limiting significant wave height (H_s^{lim}) for green water criterion is shown in Eq. (4.4) based on Fathi (2018), where Pgw is a probability of green water criterion (Pdw =0.05).

$$H_s^{lim}(T_p) = \sqrt{-\frac{1}{2\ln Ps}\left(\frac{T^2}{(g_r)^2} + \frac{V_{cr}^2}{(g_{rv})^2}\right)} \tag{4.3}$$

$$H_s^{lim}(T_p) = \frac{Fb}{g_r\sqrt{-2\ln Pdw}} \tag{4.4}$$

4.2.3. Percentage Operability

The operational area of a fishing boat is the Java Sea, located in the north of Java Island, Indonesia (Figure 4.4). The Annual WCS data can be seen in Table 4.2 obtained from metoceanview (https://app.metoceanview.com/hindcast/). As shown in Table 4.2, the highest percentage of wave period occurrences is 3-4 seconds with a percentage of 35.3% and 4-5 seconds with a percentage of 37.0%. The highest percentage for a significant wave height is 0.5-1.0 m with 45%, followed by 0.0-0.5 m with 39.8%, and 1.0-1.5 m with 13.3%. These waters can be categorised as sea state 3. In these conditions, a ship must have an operational limit over 1.5 m for all criteria to operate at least 98% of the time.

Figure 4.4. Location of wave scatter (www.bing.com/maps)

Table 4.2. Wave scatter diagram of Java Sea (https://app.metoceanview.com/hindcast/)

***Hs* (m) \ *Tp* (s)**	**0 – 1**	**1 – 2**	**2 – 3**	**3 – 4**	**4 – 5**	**5 – 6**	**6 – 7**	**7 – 8**	**8 – 9**	**9 – 10**	***Hs* Occurrence**
0.0 – 0.5	6	139	8192	25249	7677	518	48	21	3	0	39.8%
0.5 – 1.0	0	0	3	11863	28587	6764	88	6	0	0	45.0%
1.0 – 1.5	0	0	0	0	2650	10558	801	13	0	0	13.3%
1.5 – 2.0	0	0	0	0	0	840	830	32	0	0	1.6%
2.0 – 2.5	0	0	0	0	0	4	188	77	0	0	0.3%
2.5 – 3.0	0	0	0	0	0	0	6	52	1	1	0.1%
3.0 – 3.5	0	0	0	0	0	0	0	4	6	0	0.0%
3.5 – 4.0	0	0	0	0	0	0	0	0	0	0	0.0%
4.0 – 4.5	0	0	0	0	0	0	0	0	0	0	0.0%
4.5 – 5.0	0	0	0	0	0	0	0	0	0	0	0.0%
***Tp* Occurrence**	0.0%	0.1%	7.8%	35.3%	37.0%	17.8%	1.9%	0.2%	0.0%	0.0%	**100%**

The percentage operability for a particular wave heading, seakeeping criteria, and ship speed is obtained by Eq. (4.5) (Fathi, 2018). P_{Op}^{β} is percentage operability for a particular wave heading, seakeeping criterion, and ship speed. $P_{jk}\left(H_{s j_j} < H_{s_{cr}}, T_k\right)$ is the probability of occurrence of a significant wave height in interval j below the limiting significant wave height with a wave period in interval k.

$$P_{Op}^{\beta} = \sum_{j=1}^{N_{Hs}} \sum_{k=1}^{N_{Tp}} P_{jk}\left(H_{sj} < H_{s_{cr}}, T_k\right) \tag{4.5}$$

The percentage operability for all headings with a certain seakeeping criterion and ship speed is obtained by Eq. (4.6) (Fathi, 2018). P_{Op} is percentage operability for all headings with a certain seakeeping criterion and ship speed. $P_{Op_i}^{\beta}$ is the percentage operability for the ith wave heading. $P(\beta_i)$ is the probability of occurrence of the ith wave heading βi. If $P(\beta_i)$ has an equal probability, then Percentage Operability for all heading can be calculated as average of Percentage Operability for all heading βi.

$$P_{Op} = \sum_{i=1}^{N_\beta} P_{Op_i}^{\beta}\, P(\beta_i) \tag{4.6}$$

4.2.4. Operability Robustness Index for Roll Motion

Operability Robustness Index (ORI) can be described as a ratio of the area below the curve of Percentage Operability of Roll motion criteria from 0° to 6° ($P_{op}(OP_{tot})$ or Area A) to the area of maximum theoretically possible operability ($OP_{tot\,max} \times 100$ or Area A + Area B), as described in Eq. (4.7) and Figure 4.5. $OP_{tot\,max}$ in this case is set as 6°, which is a limiting criterion of RMS Roll motion for a fishing vessel, as described in Table 4.1. The Operability Robustness Index figure is shown in Figure 4.5-a.

$$ORI = \frac{\int_0^{OP_{tot\,max}} P_{op}\,(OP_{tot})\; d(OP_{tot})}{OP_{tot\,max}100} = \frac{Area\ A}{Area\ A + Area\ B} \tag{4.7}$$

An RMS roll motion of 6° as a seakeeping criterion is a limitation to ensure the boat is safe and comfortable to be operated. Nevertheless, it is unknown if the boat will remain safe upon surpassing this limit. This present study utilises Angle of Vanishing Stability and Down Flooding Angle to relate ship operability analysis to ship stability and to indicate whether the boat remains safe.

The expected maximum is defined as the maximum roll response that can be reached by vessel in a particular range of time, operated in a particular sea state. Rayleigh probability function is employed as an approximation to the probability density function for the maximum of the responses. Eq. (4.8) based on Fathi (2018) is used to determine the single amplitude of the expected maximum of Roll Motion.

$$E_{max_{Roll}} = \sqrt{m_{0_{Roll}}}\left[\sqrt{2\ln N} + \frac{0.5772}{\sqrt{2\ln N}}\right] \tag{4.8}$$

$$N = \frac{T\,.3600}{T_{z_{Roll}}}$$

$$T_{z_{Roll}} = 2\pi\sqrt{\frac{m_{0_{Roll}}}{m_{2_{Roll}}}}$$

where $E_{max_{Roll}}$ is expected maximum roll motion, T is duration in hours. In this research, $T = 3$ hours to illustrates the boat operate. $T_{z_{Roll}}$ is the zero–up crossing period of the roll response.

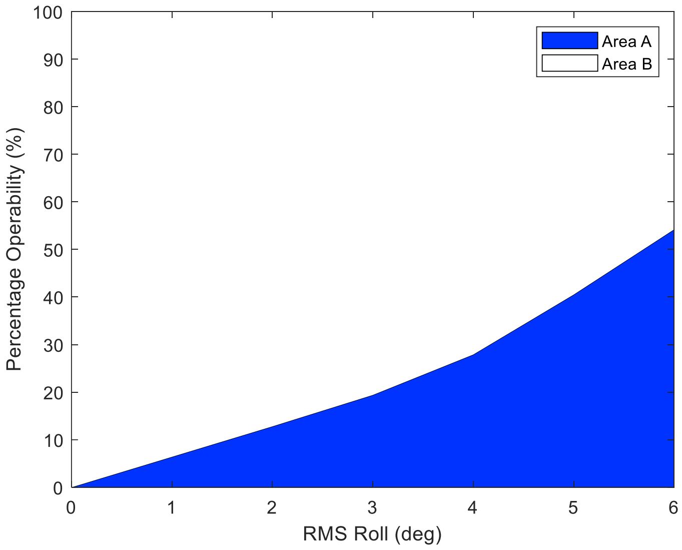

(a)

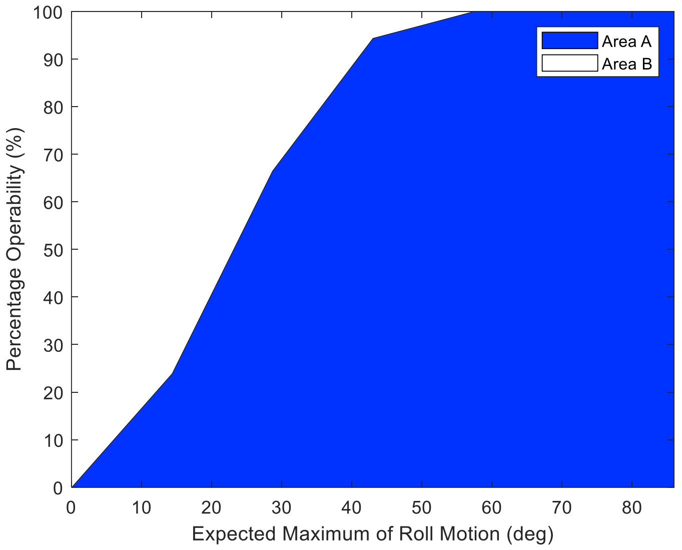

(b)

Figure 4.5. Definition of ORI for RMS roll motion (a), and expected maximum of roll (b)

According to Figure 4.5-b, the vessels must have 100% operability, at least at maximum limitation angle, $OP_{tot\,max}$. In this case $OP_{tot\,max}$ is Angle of Vanishing Stability (*AVS*), which is 85.98°. If the boat has not been capable of being operated 100%, there is a chance for a boat to reach an angle of roll response higher than $OP_{tot\,max}$. The boat will have a negative *GZ*. It will be better if the vessel has 100% operability at the angle lower than $OP_{tot\,max}$. The value of ORI will increase excessively since area A in Figure 4.5 increases.

4.3. Results and Discussion

4.3.1. Response Amplitude Operator

Each wave heading and boat speed results in a different RAO. Figure 4.6 shows the heave RAO graph at 0, 4, and 8 knots for head seas. It is known that the vertical motions are more pronounced in this heading. It should also be noted that in this study 0° wave heading corresponds to a head wave condition. The RAO reported in here covered all loading conditions, which are LC 1 (empty fish tank), LC 2 (half capacity of the fishtank with higher *KG*), LC 3 (half capacity of the fishtank with lower *KG*), LC 4 (total capacity of a fishtank with higher *KG*), and LC 5 (total capacity of a fishtank with lower *KG*).

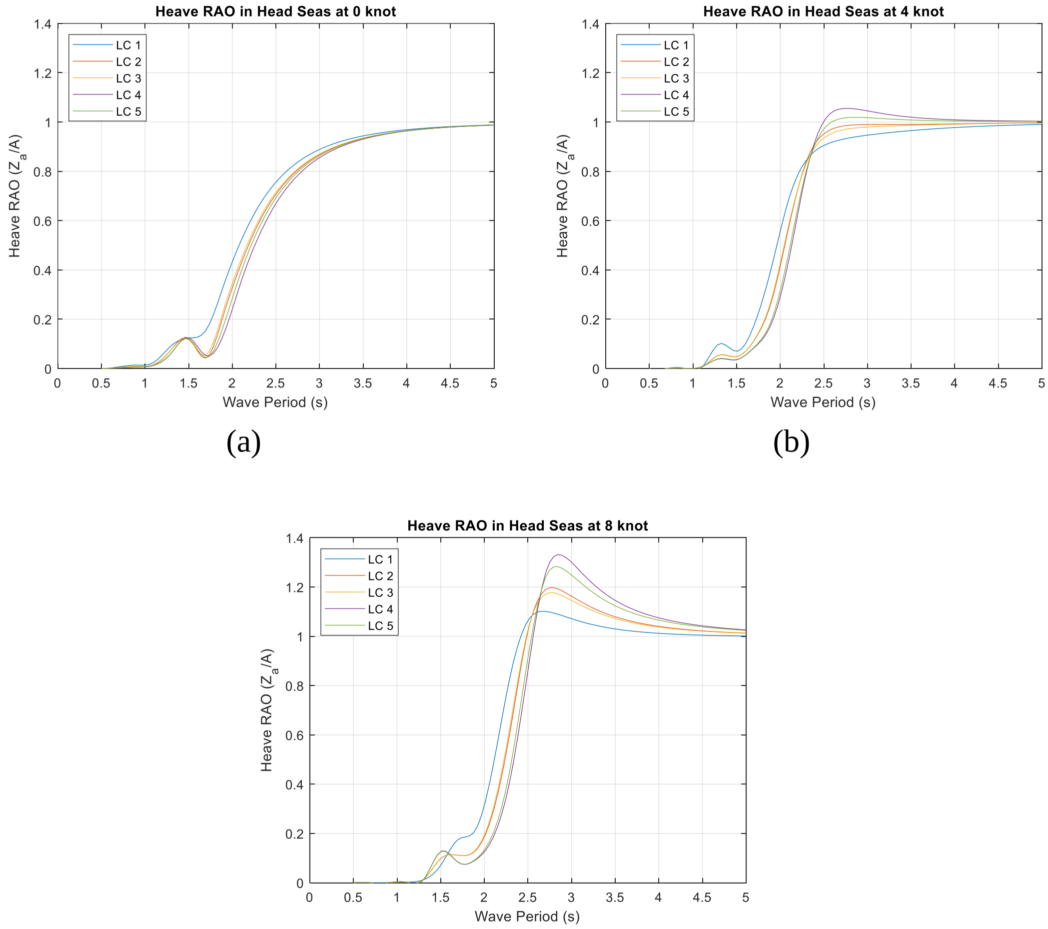

(a) (b)

(c)

Figure 4.6. Heave RAO in head seas (0°) at 0 knot (a), 4 knot (b), and 8 knot (c)

As shown in Figure 4.6, the peak of RAO increases along with the boat speed. The trend of curves is also similar to the boat displacement and Longitudinal Centre of Gravity (*LCG*). The highest peaks of RAO belong to the load cases with the highest displacements (LC 4 and LC 5) and so for the next lower peak. When the displacement is constant (LC 4 and LC 5), the peak of LC 4 RAO is higher than LC 5 as the LC 4 has higher *KG* (low *GM*) due to difference in moment of inertia. This phenomenon can be seen for LC 2 and LC 3 which have the same displacement. It can be inferred that the boat displacement as well as the *CoG* position influence the heave damping, resulting in different heave motions.

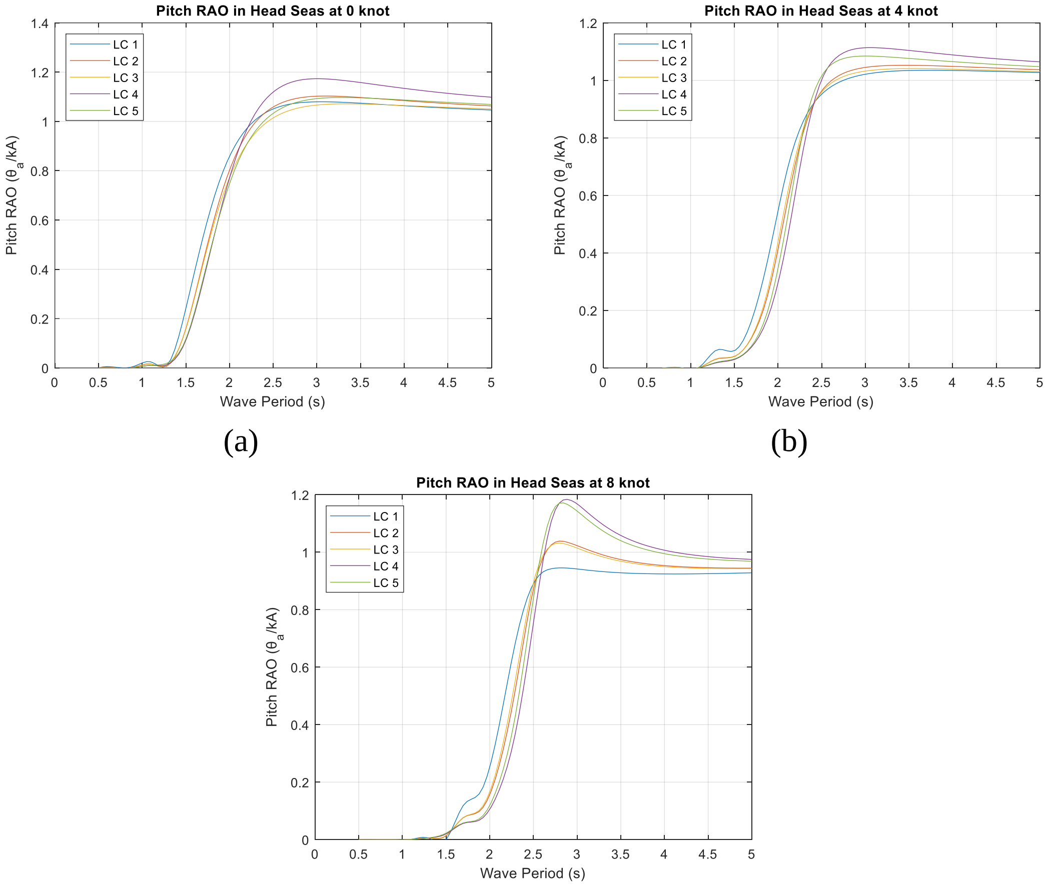

(a)

(b)

(c)

Figure 4.7. Pitch RAO in head seas (0°) at 0 knot (a), 4 knot (b), and 8 knot (c)

The natural period of heaving motion also can be seen in Figure 4.6, where the period at the abscissa reaches the peak of the curve. For all load cases, the natural periods are similar to each other. This happens for a wave period between 2 seconds and 3 seconds. Examining the Wave Scatter Diagram data in Table 4.2, the most frequent periods are 3-4 seconds and 4-5 seconds. However, 2-3 seconds wave periods have a 7.8% probability, indicating heave resonance is possible in the operational area.

The pitch RAO can be seen in Figure 4.7 for the three speeds: 0, 4, and 8 knots. LC1 at zero speed has a higher peak than the 4-knot speed at a wave period of about 3 seconds. LC 4 is the highest peak at zero speed, but it is not the only one for 4 and 8 knot speed; LC 5 is the highest too for both speeds.

However, the trend of the pitch RAO peaks at 4 and 8 knots are likely similar to those of heave. The two highest are LC 5 and LC 4, and the lowest is LC 1. The pitch

RAO peaks represent the effect of the damping coefficient. It can be concluded that the trend of damping coefficients for both speeds is similar to that of heave but not at zero speed. From Figure 4.7, we can also see that the natural period in pitch is similar to that in heave. The natural period for each speed and load case is about 2-3 seconds, which will also cause resonance in pitch, especially when the pitch damping is low. The pitch response will be significantly increased.

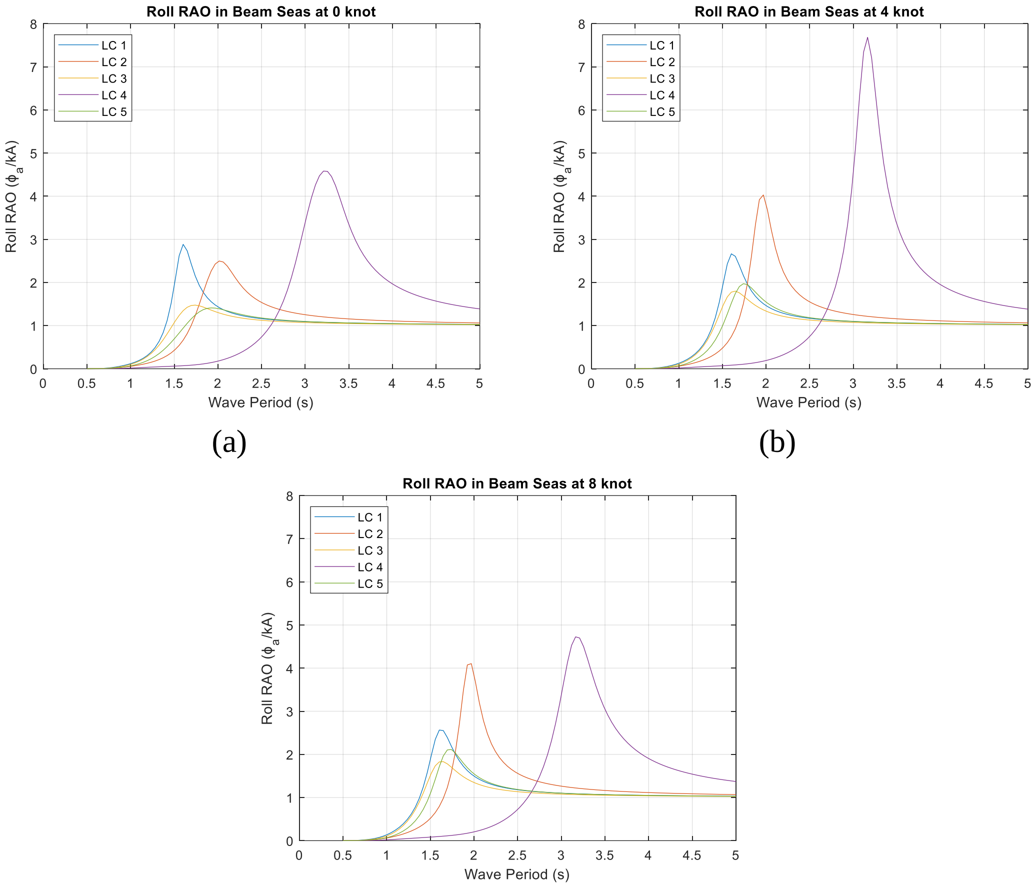

(a)

(b)

(c)

Figure 4.8. Roll RAO in beam seas (90°) in 0 knot (a), 4 knot (b), and 8 knot (c)

Figure 4.8 illustrates the roll RAO at 0, 4, and 8 knots. In this RAO, the beam sea (90°) was chosen since this heading most affects the ship's roll response. The peak of roll RAO varies with speed. LC 4 shows that the highest peak occurs at 4 knots, not at 8 knots. However, the higher the *KG* position, the higher the RAO peak, meaning a decrease in roll damping and an increase in roll response. It can be inferred that the determination of *KG* position is essential since it directly influences the roll response.

Based on the occurrence of *Hs* and *Tp* in wave scatter diagram in Table 4.2, Java Sea can be categorised as Sea State 3 (slight), which may be a safe sea for a large ship but not for a small fishing boat. Due to small in size, the peak roll RAO shows that the resonance occurs at low period, between 1-4 seconds. The wave scatter diagram shows that the *Tp* in Java Sea lies between 2-7 seconds. The most occurrence is at 3-5 seconds, which covers 72.3%. When the natural roll period has the same value with wave period, it results in resonance conditions, making the excessive responses.

On the other hand, changing the speed and wave heading also changes the peak of encounter period (*Te*). When Te is close to half of natural period (Tn), there is a possibility that parametric roll can occur for a small fishing boat that is operated in Java Sea. The further investigation regarding the parametric roll on small fishing boat is investigated in Chapter 6.

The limitations of the ShipX software have been described in Section 3.3.1. Therefore, it is essential to compare the roll amplitudes based on ShipX and CFD simulations, given the differences in roll damping ratios. The roll damping ratio from CFD was determined from a roll decay simulation, which is described in detail in Chapter 6.3.2. The speed of the boat is 0.2 m/s and the wave frequency is 3.51 rad/s. The amplitude of the roll motion was calculated by using (4.9).

$$\phi_a = \frac{M_0/K}{\sqrt{(1-r^2)^2 + (2\zeta r)^2}} \tag{4.9}$$

here M_0 is the amplitude of roll excitation moment, K is roll stiffness, r is the ratio between the incident wave frequency and the natural roll frequency (ω/ω_n), and ζ is the roll damping ratio. Then, the roll amplitudes were converted to be a transfer function value. Table 4.3 shows the comparison of the roll transfer function between two different roll damping ratios. M_0, K were taken from ShipX calculation.

Table 4.3. The roll transfer function (ϕ_a/kA) comparison between two different roll damping ratios

Load Case	**r (ω/ω_n)**	**ϕ_a/kA**		**Difference (%)**
		ζ from ShipX	**ζ from CFD**	
1	1.12	3.826	4.128	-7.31
2	1.12	4.816	4.554	5.76
3	0.89	2.997	2.758	8.67
4	2.44	0.638	0.641	-0.47
5	0.88	2.691	2.836	-5.10

It can be seen in Table 4.3 that the difference between ShipX and CFD is larger when the r value is close to 1, under the resonance conditions. However, for r values greater than 1, such as in load case 4 ($r = 2.44$), the transfer function shows a smaller difference. This comparison indicates that the roll amplitude from ShipX is less accurate under resonance conditions.

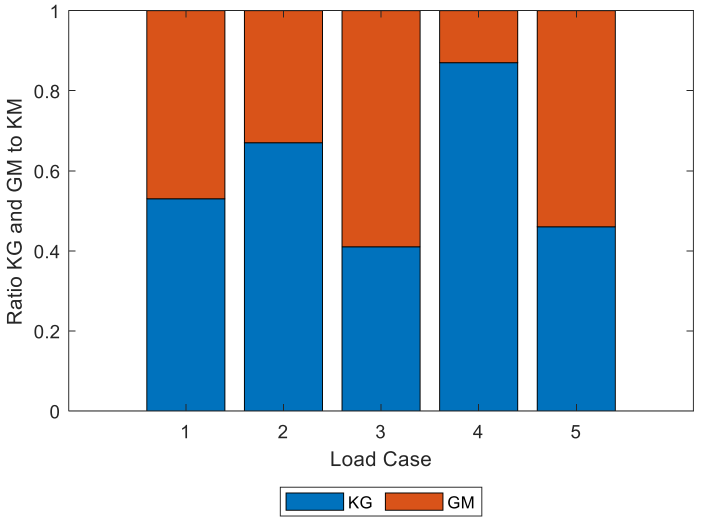

Figure 4.9. Ratio *KG* and *GM* to *KM*

Each displacement has a different *KM* value. Different *KG* positions will result in different *GM* values with the same *KM* ($GM = KM - KG$). This is shown for LC 2 with LC 3 (half load) and LC 4 with LC 5 (full load). If we compare *GM* with each *KM* value, we can calculate the ratio of *GM* to *KM*, as shown in Figure 4.9.

Based on Figure 4.8, LC 4, LC 2, and LC 1, a few different *KG* values (about 0.1 m) will result in a different ratio *GM*/*KM* because those LCs have a different *KM*. The *GM*/*KM* ratio value aligns with the RAO peak. So, the higher *GM*/*KM* ratio is, the lower RAO peak.

Unlike heave and pitch, Figure 4.8 shows that loading conditions, due to the change in the *KG* position, affect the natural roll period of the vessel. The natural roll period for LC 4, around 3 seconds, is considerably different from the other load cases, which show a natural roll period of 1-2 seconds. From Wave Scatter Diagram shown in Table 4.2, it can be seen that LC 4 is dangerous in roll resonance. The natural roll period is the same as the second most frequent period, 3-4 seconds, whose probability of occurrence is 35.3%. Other load cases (natural period of 1-2 seconds) do not significantly influence the roll resonance because the probability of occurrence is only 0.1%.

4.3.2. Operability Limiting Boundary

The combination of RAOs (Response Amplitude Operators) and the selected wave spectrum results in a response spectrum (short-term analysis), illustrating the boat's behaviour in irregular waves. The variance of the motions, such as root mean square (RMS) and probability, can be determined from the response spectrum. The chosen seakeeping criteria will then establish an operability limiting boundary, defining the significant wave height and wave period limits beyond which the boat's responses do not meet the seakeeping criteria.

In Figure 4.10, the results of the operability limiting boundary for five load cases in wave heading of 60° at 8 knots are given. VA, LA, GW, and SL refer to Vertical and Lateral Acceleration, Green water, and Slamming. In the figure, the horizontal axis is the peak period. The vertical axis is a limit of significant wave height, where the boat responses do not exceed the seakeeping criteria. Each peak period has a different limitation of significant wave height. The "No Wave" line is a border showing the breaking wave limit. This theoretical limit of breaking waves is shown in Eq. (4.10) (Myrhaug and Dahle, 1994).

$$H_{BW} = 0.105{T_p}^2 \tag{4.10}$$

where H_{BW} is limit of breaking wave (m), T_p is peak period (sec).

According to Figure 4.10, for all load cases, the limit of significant wave height for green water and slamming probability criteria are above the "No Wave" line. This means, the boat would not surpass these two seakeeping criteria for all wave periods and significant wave height combinations and can be fully operated (PO is 100%).

On the other hand, the trough of the other four criteria lies below the "No Wave" line when $Tp > 2$ s. Between 2-4 seconds, some criteria have the limits of significant wave height of one meter, while the others are a half meter. From Wave Scatter Diagram data in Table 4.2, it can be seen that the probability of occurrence for *Hs* with no more than a half meter is 39.8 % for the total peak period. This result suggests that the boat has a low PO. Details of the results of percentage operability are described in the following section.

Examining Figure 4.10, the limiting significant wave heights are different for each load case. Overall, all load cases have a limiting significant wave height below one metre. Referring to the limiting significant wave height based on the formula from Deakin (2006, 2005), the boat in this study has a limiting significant wave height under one metre. It means that the boat can safely operate only if the *Hs* of operational area is under 1 metre. The results from this study are in line with Deakin's. However, this study reveals which wave period results in low limiting significant wave height.

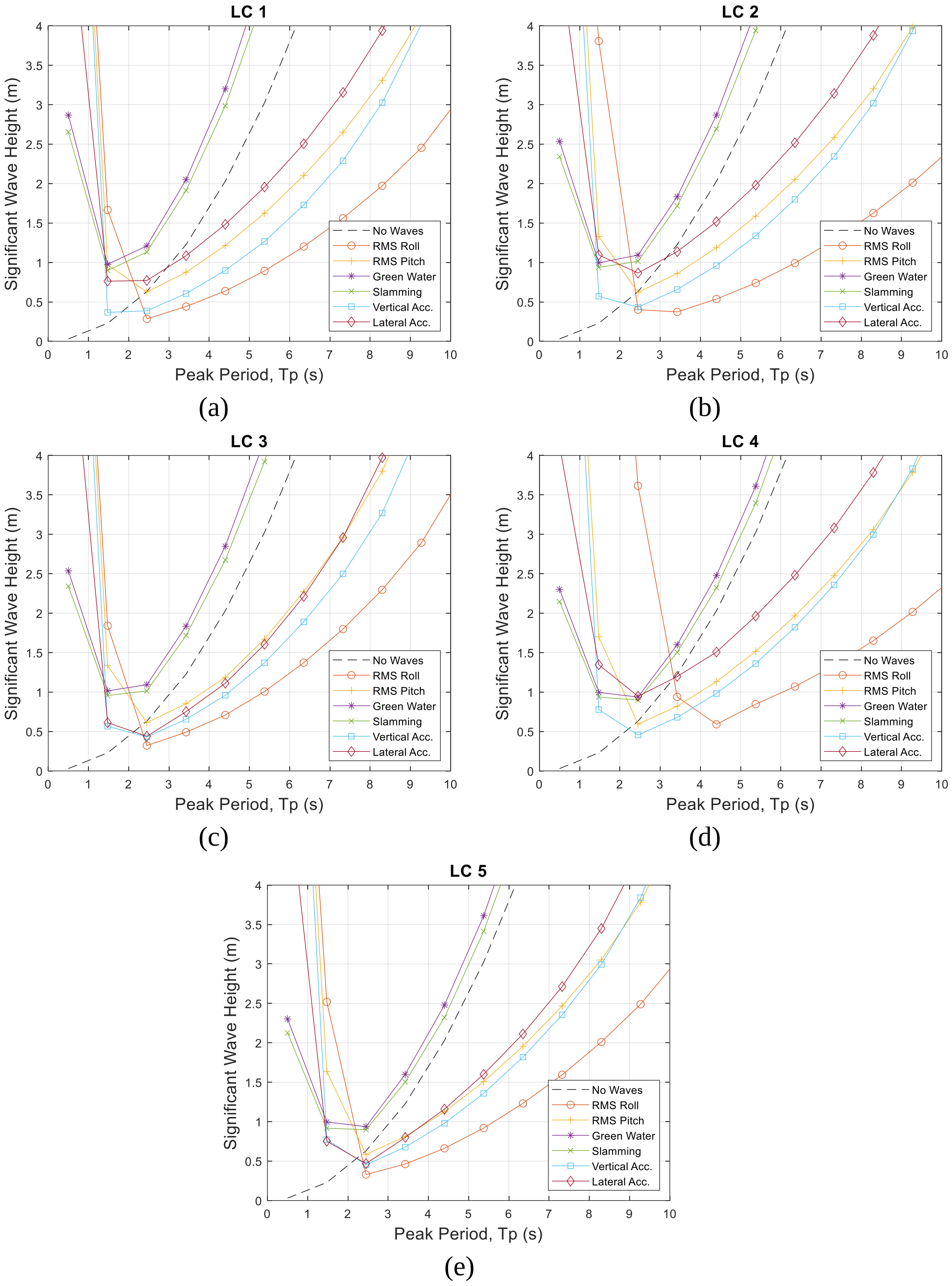

(a) (b)

(c) (d)

(e)

Figure 4.10. Operability limiting boundary in wave heading 60°, at 8 knots for load case 1 (a), load case 2 (b), load case 3 (c), load case 4 (d), load case 5 (e)

4.3.3. Percentage Operability

The operability limiting boundary restricts the boat from operating in certain wave periods (T_p) and significant wave heights (H_s). Based on the wave scatter diagram, information about the frequency of occurrence for different combinations of T_p and H_s is provided. By combining this data with the operability limits, the percentage of time the boat can operate within the T_p and H_s conditions that meet the seakeeping criteria is determined. This outcome is referred to as the percentage operability.

Percentage Operability results for three speeds, seven wave headings, and five load cases are listed in Figures 12 - 15. The probability of occurrence for each wave heading is considered equal. Thus, based on Eq. (4.6), an average of all wave headings is defined as the Percentage Operability for all headings.

Figure 4.11 shows the percentage operability for Criterion 1 (RMS Roll) and Criterion 2 (RMS Pitch). The Percentage Operability for Criterion 1 reaches low values in wave heading of 60°, 90°, and 120° for all speeds except at 8 knots, which can be operated well (100%) at 120°. Load Case 4 is the worst operability at zero speed and 4 knots. Contrary to 8 knots, Load Case 2 is the lowest value for the RMS roll criterion. According to Figure 4.9, Load Cases 2 and 4 have a minimum GM/KM ratio than other load cases, meaning that the roll damping is low, and hence the roll response is higher than in other cases.

The low Percentage Operability for pitch criterion belongs to wave heading of 0°, 30°, 150° and 180° (head, quarter, and following waves). For 8 knots and 4 knots, the lowest Percentage Operability occurs in following waves (180°) and quarter-following waves (150°), while the opposite is true in the zero-speed case where this occurs in head waves (0°). For every speed, an average of PO for each load case has a similar value.

Figure 4.12 illustrates the Percentage Operability for Criterion 3 (Probability of Green Water) and Criterion 4 (Probability of Slamming). It can be concluded that almost all speeds and load cases have excellent operability. A 100% operability is found at zero ship speed. At 4 knots, Load Cases 4 and 5 have the lowest operability value in a heading wave (0°), which is around 97-98%. For maximum speed, the lowest operability value does not occur at the heading wave but quarter following waves (150°) and following waves (180°). However, the value is no less than 89.9%. For both criteria, this value is sufficiently high for safe operations.

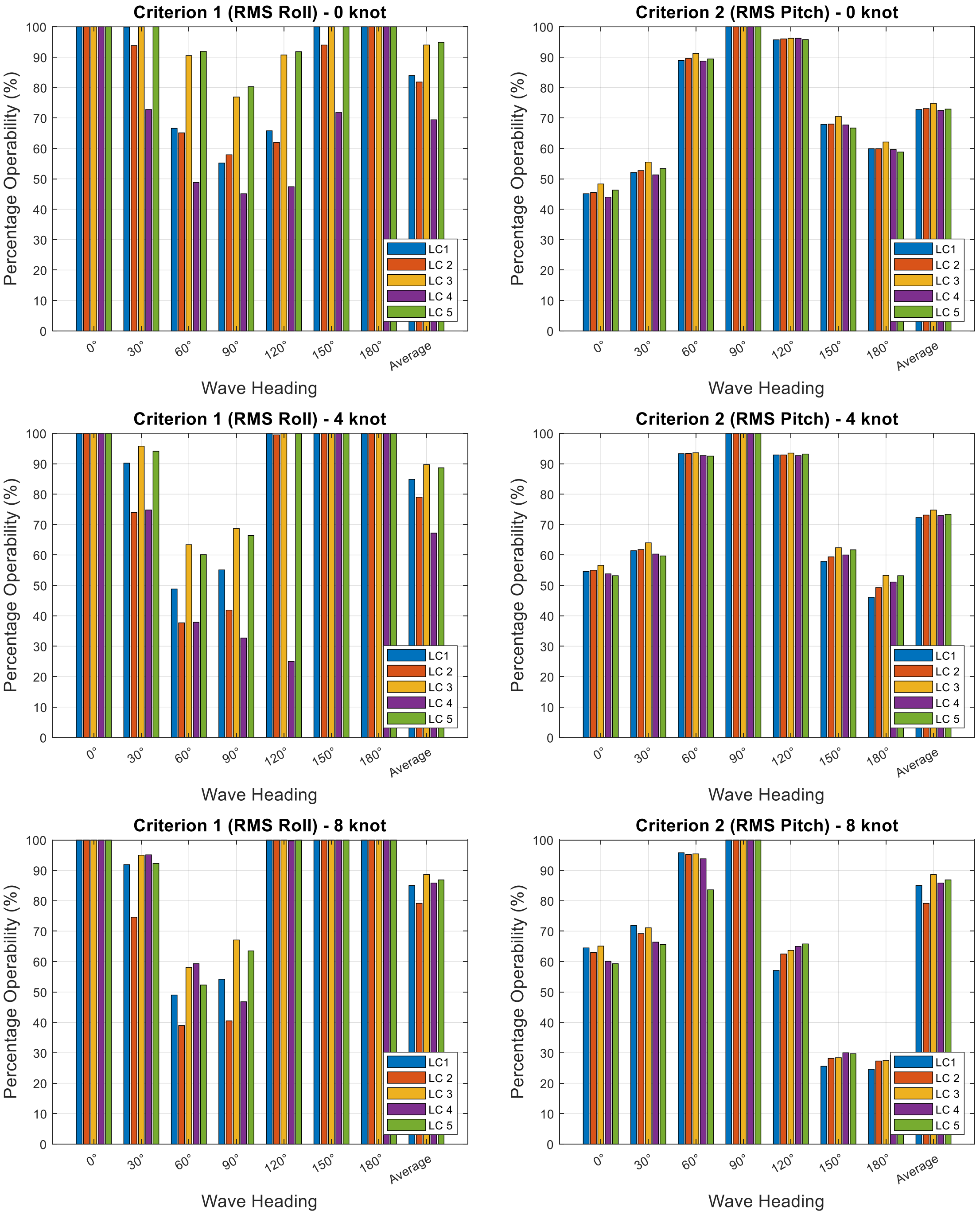

Figure 4.11. Percentage operability for criterion 1 and criterion 2

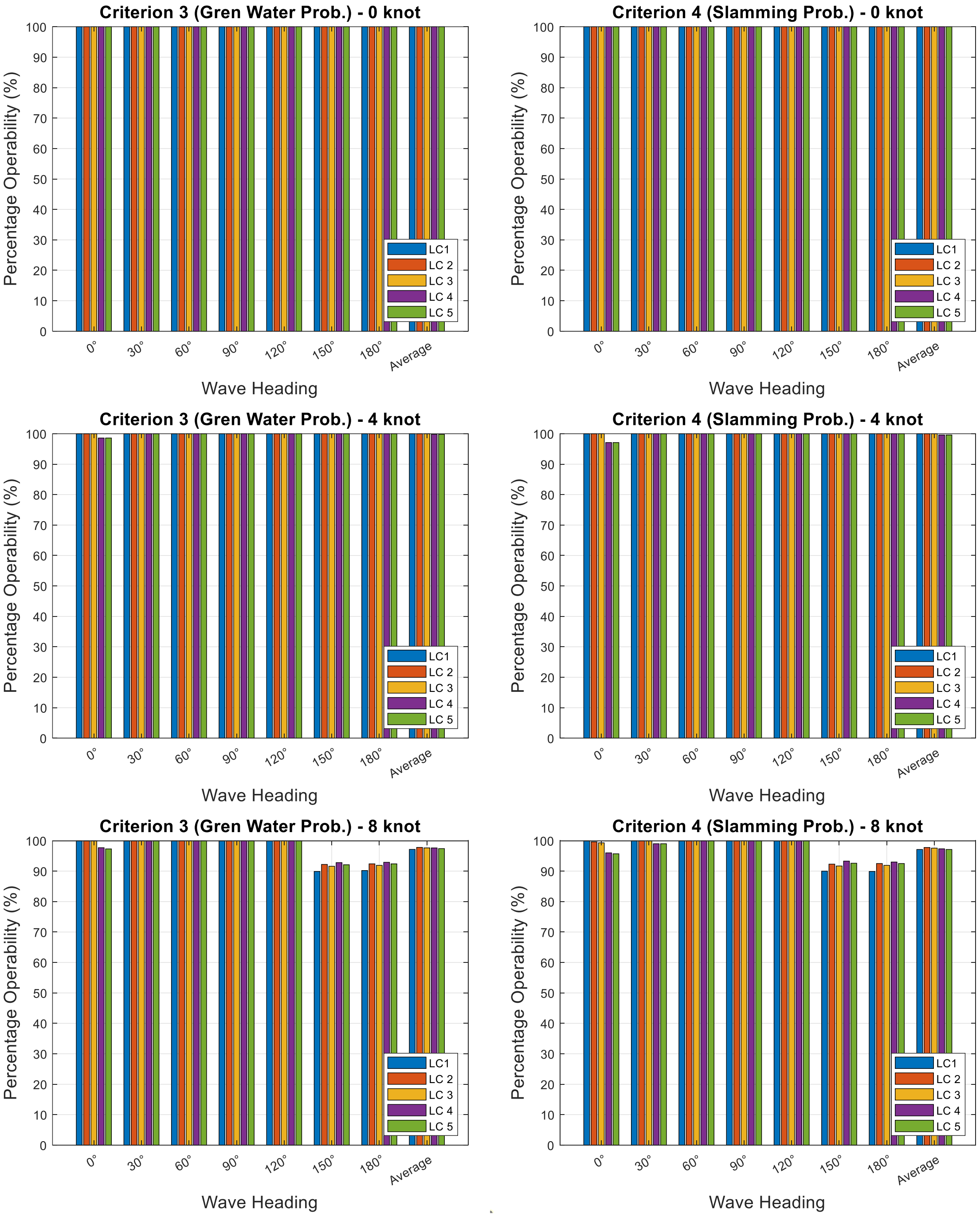
Criterion 3 (Gren Water Prob.) - 0 knot

Criterion 4 (Slamming Prob.) - 0 knot

Criterion 3 (Gren Water Prob.) - 4 knot

Criterion 4 (Slamming Prob.) - 4 knot

Criterion 3 (Gren Water Prob.) - 8 knot

Criterion 4 (Slamming Prob.) - 8 knot

Figure 4.12. Percentage operability for criteria 3 and criteria 4

Percentage Operability for Criterion 5 (vertical acceleration) and Criterion 6 (lateral acceleration) are shown in Figure 4.13. According to Criterion 5, the boat can be operated well for all load cases at zero speed. For Criterion 6, the lowest operability value is around 99%, occurring at head waves. The Percentage Operability for criterion 5 in wave heading 0° and 30° have the lowest value in maximum speed, varying from 35% to 63%. This value is not high enough to operate the boat safely. For a 60°

heading, the Percentage Operability value is around 78% to 87%, whereas in the case of criterion 6, the lowest operability value occurs in heading 60° and 90°, above 91.9%.

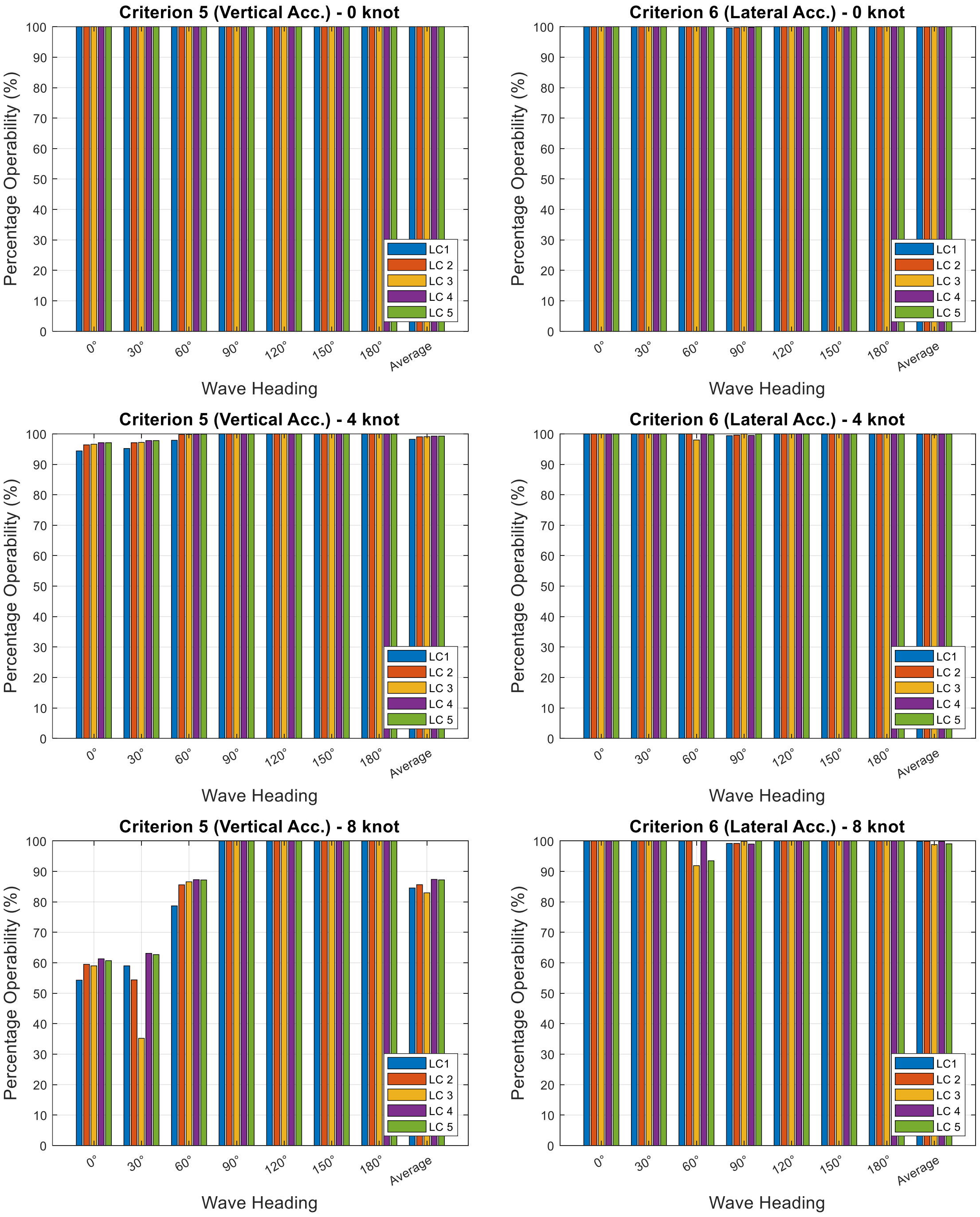

Figure 4.13. Percentage operability for criteria 5 and criteria 6

The minimum Percentage Operability values between criteria 1 and 6 are selected as the Percentage Operability for all criteria, as shown in Figure 4.14. For wave headings of 60° and 90°, RMS roll is selected as Percentage Operability for all criteria. For other wave headings, RMS Pitch is selected. For the highest speed, the operability for all load cases varies from 61% to 64%. For medium speed and zero speed, the operability is around 67% to 74%. Overall, the Percentage Operability of this boat is relatively small. The boat cannot be operated safely in the Java Sea because some combinations of significant wave heights and wave peak periods do not meet the RMS roll and pitch limiting criteria. Based on Figure 4.11, the RMS roll is predicted to surpass 6°, as none wave heading of 30°, 60°, and 90° reach the percentage operability of 100%. However, the maximum roll response experienced by the boat is still unknown until the analysis of the expected maximum roll is carried out.

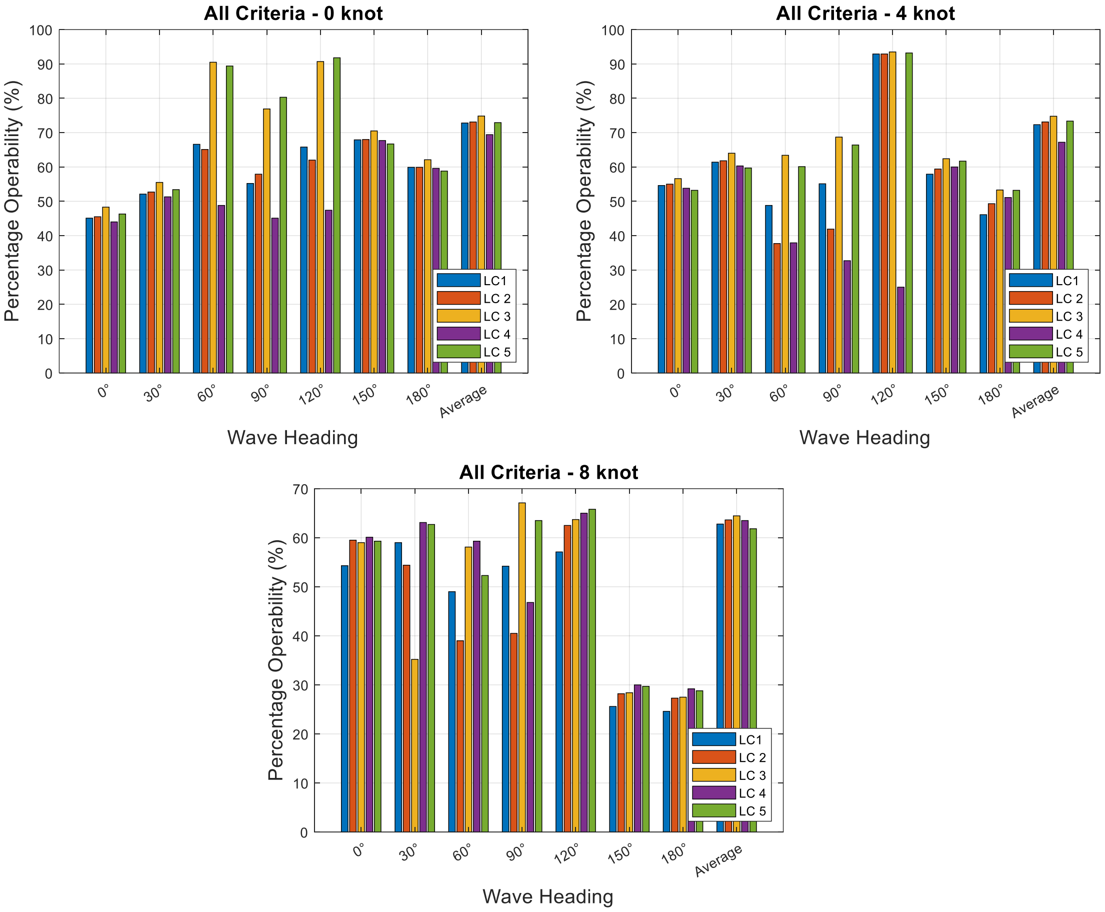

Figure 4.14. Percentage operability for all criteria

Figure 4.15 presents the Percentage Operability for the expected maximum of roll motion, with Angle of Vanishing Stability (left-hand side) and Down Flooding Angle (right-hand side) as a limiting angle. The left-hand side shows that almost all load cases have 100% Percentage Operability, except LC 4. Based on these results it can be concluded that the boat can operate well in all cases except under the condition of LC 4. It should be noted that 100% of Percentage Operability here means that the boat can operate without having a negative *GZ*, as the roll response is predicted not to exceed Angle of Vanishing Stability. From this case, the different limiting angle (Angle of

Vanishing Stability) does not give a clear difference between the load case to the Percentage Operability value.

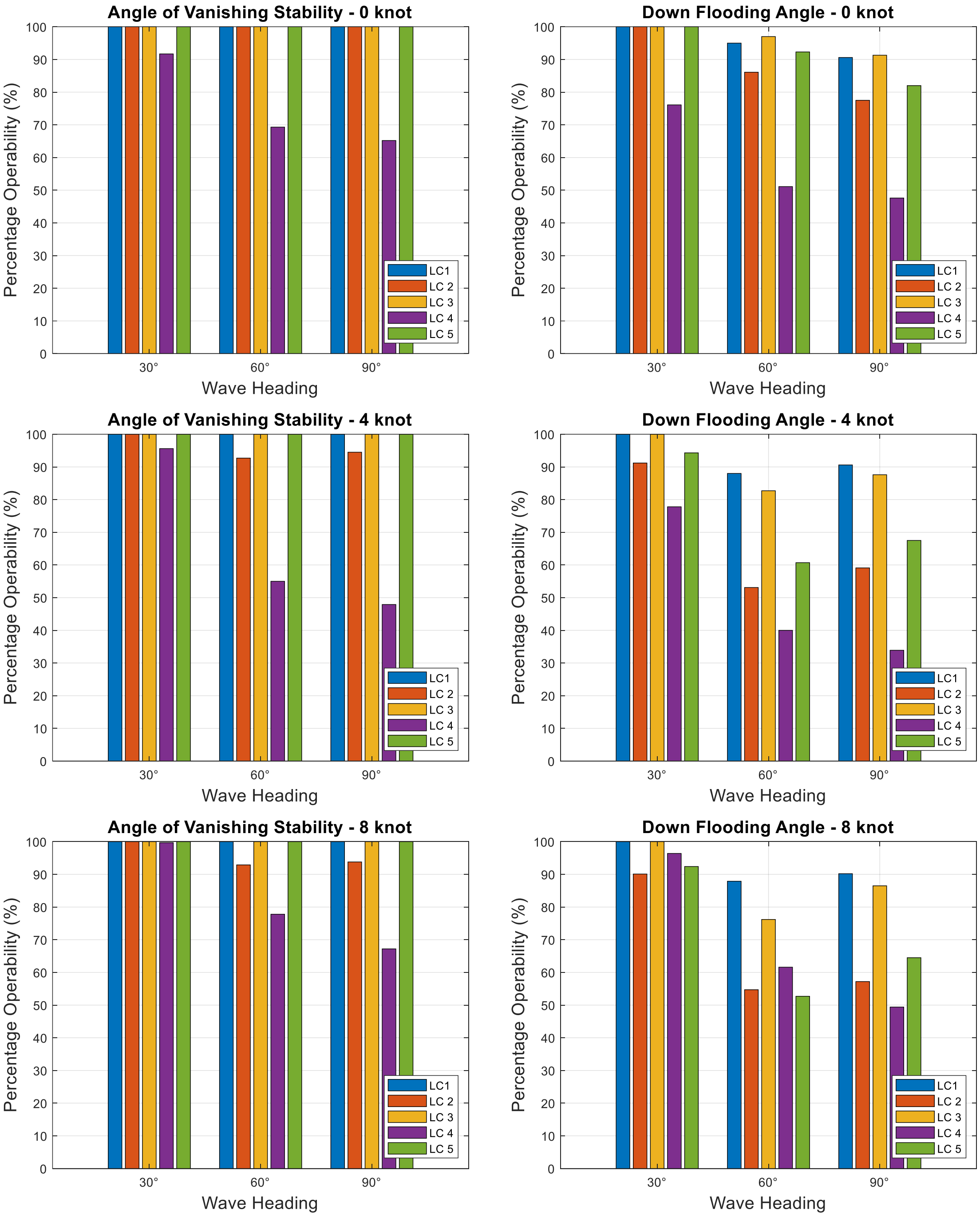

Figure 4.15. Percentage operability for expected maximum of roll with a different limiting angle.

On the right-hand side of Figure 4.15 (with Down Flooding Angle as a limiting angle), it can be observed that each loading case results in a unique Percentage Operability value. Since the Down Flooding Angle is lower than Angle of Vanishing

Stability, the calculation of Percentage Operability becomes more sensitive to loading conditions even if the same limiting angle is used. This makes the distinction between load cases clearer.

Consequently, as LC 1 has the highest limiting angle (Down Flooding Angle), the Percentage Operability of LC 1 is the highest. With Down Flooding Angle as a limiting angle, LC 1, LC 3, and LC 5 no longer have 100% operability like those from Angle of Vanishing Stability. From this comparison, the choice of Down Flooding Angle as a limiting angle to calculate Percentage Operability is better than Angle of Vanishing Stability because this angle is more sensitive and clearly shows the distinction between the load case. It also should be noted that 100% of Percentage Operability, in this case, means that the boat can operate without the edge of the deck meeting the water.

4.3.4. Operability Robustness Index

4.3.4.1. Operability Robustness Index for RMS Roll Motion

Operability Robustness Index is an operability index to assess a particular criterion. In this study, the chosen maximum limiting angle ($OP_{tot\ max}$) criterion for RMS roll is referred to Tello et al. (2011), which is 6°, as shown in Table 4.1. For each angle, the Percentage Operability was calculated and plotted as a curve. The area below the curve is calculated as shown in Eq. (4.7). In this research, angles from zero to the maximum limitation angle ($OP_{tot\ max}$) are divided into six angles to employ Simpson Rule for calculating the area below the curve. This area is then compared to the maximum area of the possible Percentage Operability ($100\% \times OP_{tot\ max}$).

In Figure 4.16, the Operability Robustness Index results of RMS roll motion for all load cases in wave heading 30°, 60°, and 90° are presented. All loading condition attain their highest Operability Robustness Index value for a wave heading of 30°. This heading does not influence the roll motion as much as the others. Overall, LC 2 and LC4 have the lowest value compared to other load cases, except for LC 4 at maximum speed with a wave heading 60°. It can be concluded that it will be perilous for the fisherman to put the caught fish above the deck during the operation under the LC 2 and LC 4 conditions, especially when they catch the fish in large quantities at once, as it will suddenly influence the roll response of the boat.

If the Operability Robustness Index results in Figure 4.16 are compared with the PO for the RMS roll in Figure 4.11, it can be seen as a clear view of why the Operability Robustness Index results are more objective than the Percentage Operability results. Percentage Operability values for LC 2 and LC 4 at 4 knots with a wave heading of 30° are similar, 74% and 74.80%, respectively. However, the Operability Robustness Index values for both load cases are different, 0.31 and 0.38. For the wave heading of 60°, Percentage Operability values for LC 2 and LC 4 are also similar, specifically 37.70% and 37.90%. However, the Operability Robustness Index results are different, 0.17 and 0.21. From that example, it can be concluded that Operability Robustness

Index approaches its maximum value slower than the Percentage Operability value, and, therefore, allows boat designers and operators to rank performance more independently of the chosen limitation criterion with a similar Percentage Operability.

As explained by Gutsch et al. (2020), in comparison to Percentage Operability, Operability Robustness Index accounts for the development of the Percentage Operability value on its complete course of its behaviour between zero and the chosen maximum motion limitation. Gutsch et al. further conclude that "therefore, the Operability Robustness Index behaves qualitatively similar but approaching its maximum possible value of 1.0 slower. Consequently, the Operability Robustness Index allows vessel performance assessment to be more independent of the chosen environmental condition and level of limitation criteria."

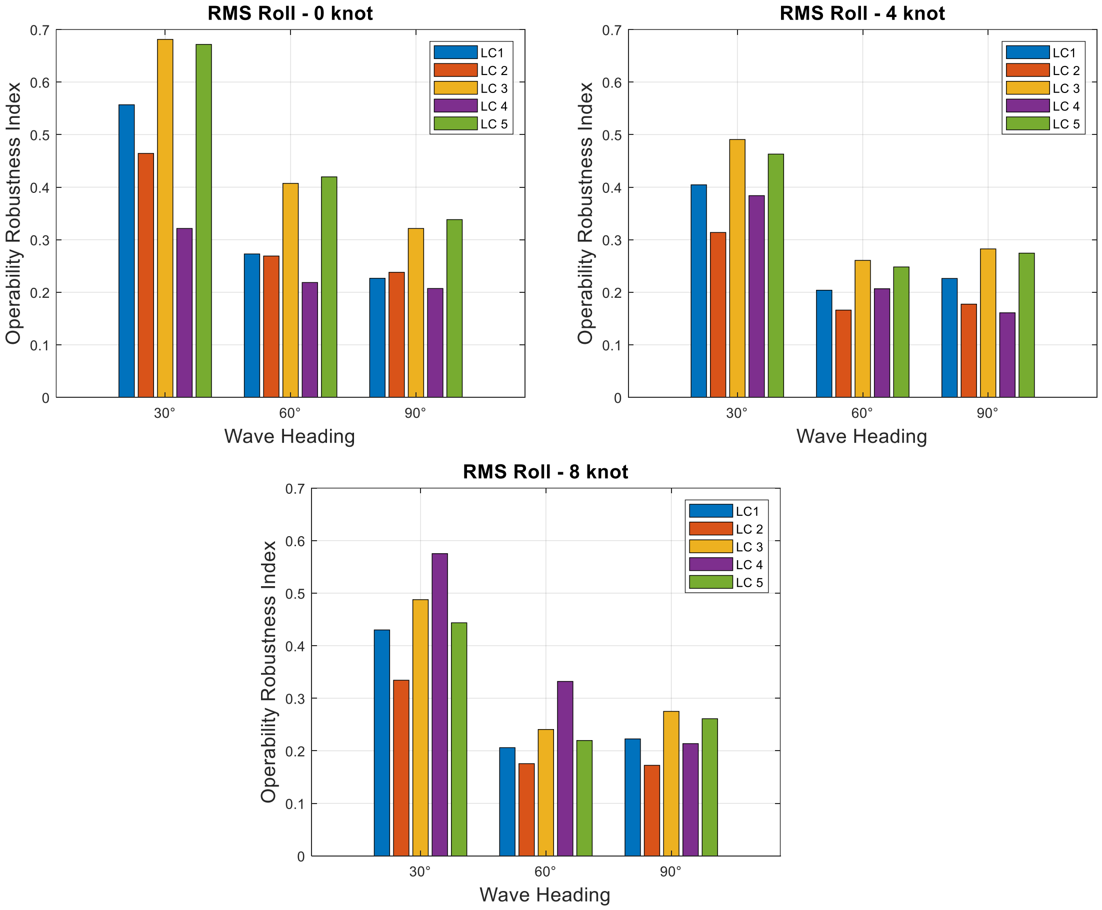

Figure 4.16. Operability Robustness Index (ORI) value for RMS roll motion

4.3.4.2. Operability Robustness Index for Expected Maximum of Roll Motion

The Operability Robustness Index of the expected maximum of roll motions are presented in Figure 4.17 for all load cases and speeds with wave headings of 30°, 60°, and 90°. Different $OP_{tot\ max}$, Angle of Vanishing Stability and Down Flooding Angle. Angles from zero to maximum limitation angle ($OP_{tot\ max}$) are also divided into six angles to employ Simpson Rule for calculating the area below the curve.

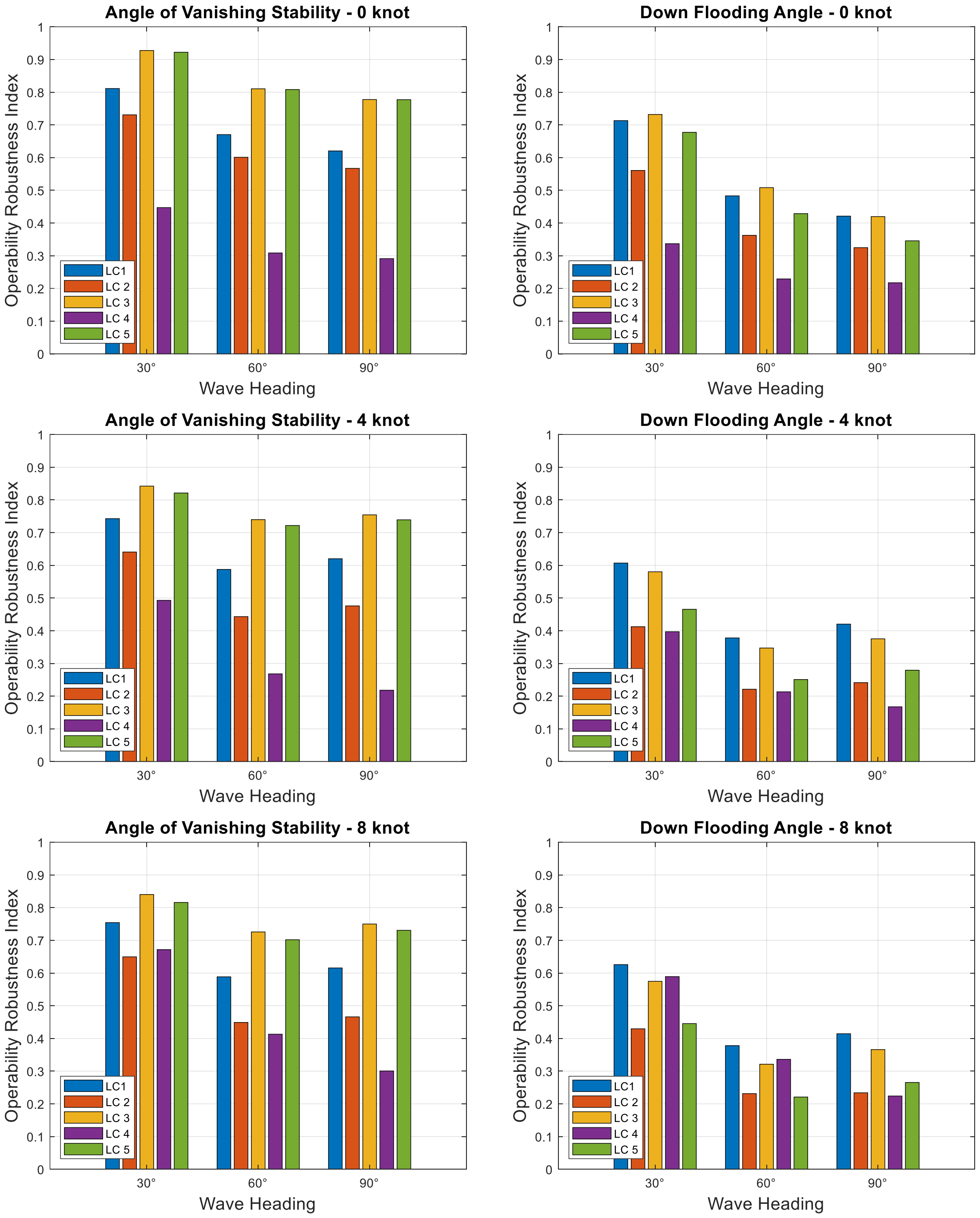

Figure 4.17. Operability Robustness Index (ORI) value for expected maximum roll motion with different maximum limiting angle

Angle of Vanishing Stability as a $OP_{tot\,max}$ is presented on the left-hand side of Figure 4.17. Each load case has a different AVS which results in a different Operability Robustness Index. This difference cannot be seen by examining Percentage Operability results (Figure 4.15). Based on the figure, for almost all conditions, the ranking of Operability Robustness Index values from best to worst is LC 3, LC 5, LC 1, LC 2, and LC 4. The order is different for 8-knots speed with a wave heading of

30°, where Operability Robustness Index for LC 4 is higher than LC 3 with a slight difference. The order of Operability Robustness Index results from the left-hand side of Figure 4.17 is aligned to *GM*/*KM* ratio in Figure 4.9 and the AVS. Specifically, higher *GM*/*KM* ratios give better Operability Robustness Index values.

The Operability Robustness Index indicator gives a new perspective to better assess better Load Cases in seakeeping performance, especially in roll motion with the same Percentage Operability of 100% (LC1, LC 3, and LC 5). When using Angle of Vanishing Stability as a limiting angle, LC 3 is the best scenario for other load cases. This load case also has the highest *GM*/*KM* ratio, namely 59%. Under these conditions, the response of the roll motion becomes low, as seen from the Roll RAO in Figure 4.8.

On the other hand, when Down Flooding Angle is set as a $OP_{tot\,max}$ (right-hand side of Figure 4.17), all Operability Robustness Index values become lower than Angle of Vanishing Stability. The reason is that the Down Flooding Angle is lower than Angle of Vanishing Stability. In these cases, the limiting criterion became stricter, so the Percentage Operability value also decreased (Figure 4.14). From the right-hand side of Figure 4.15, the PO of expected maximum of roll for LC 1 and LC 3 with a wave heading of 30° is 100%. The Operability Robustness Index results also allow boat designers or boat operators to distinguish and rank them. For zero speed, LC 3 is better than LC 1. For medium and maximum speed, LC 1 is better than LC 3.

As shown in Figure 4.17, even though Operability Robustness Index can rank all load cases, with different $OP_{tot\,max}$ (Angle of Vanishing Stability and Down Flooding Angle) the order of load cases is different from top to bottom. This becomes clearer at the medium and maximum speeds. For example, Figure 4.18 explains why there is a different order of Operability Robustness Index values between LC 4 and LC 5 at maximum speed with a wave heading of 60°.

Based on Figure 4.18-a, the maximum limiting angle (Angle of Vanishing Stability) of LC 4 (32.96°) is lower than LC 5 (82.27°). At the low limiting angles, the Percentage Operability of LC 4 is higher than LC 5. However, because LC 5 has a higher limiting angle and 100% Percentage Operability at last limiting angles, LC 5 has a higher Operability Robustness Index that LC 4. When Angle of Vanishing Stability is employed as a maximum limiting angle (Figure 4.18-b), which is 26° for both load cases, the Operability Robustness Index results show that LC 4 is higher than LC 5.

This comparison shows that the Operability Robustness Index value is not only influenced by the maximum limiting angle ($OP_{tot\,max}$) but also the value of Percentage Operability in each limiting angle. The lower $OP_{tot\,max}$ does not always make the Operability Robustness Index value lower. The Percentage Operability value in each limiting angle also contributes to increasing the Operability Robustness Index value because the area below the curve is calculated from the Percentage Operability value.

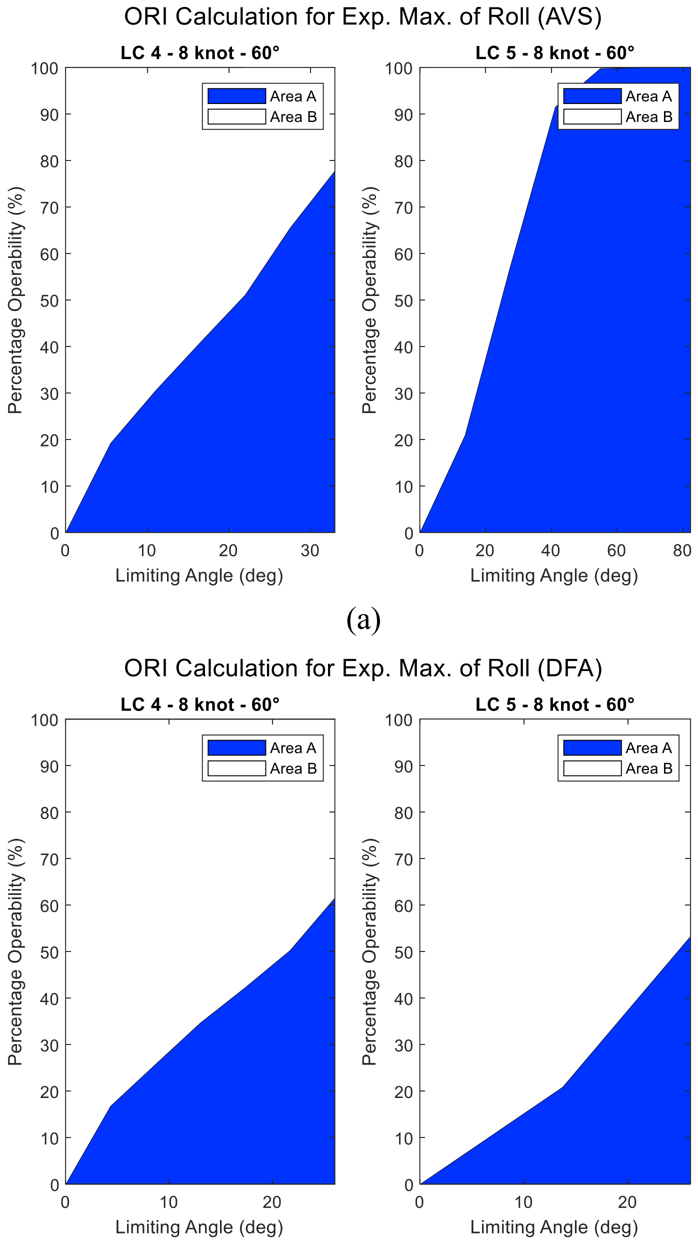

(a)

(b)

Figure 4.18. Operability robustness index calculation for same load case with different maximum limiting angle (angle of vanishing stability and angle of vanishing stability)

4.4. Summary

An operability assessment, both in Percentage Operability and Operability Robustness Index, was carried out under different loading conditions. Different loading conditions give different *GM*/*KM* ratios as the position of *KG* changes. This ratio influences the roll responses and dampings, as shown in roll RAOs, but does not noticeably affect heaving and pitching motion, as the LCG is not influenced significantly.

The operational area of the boat, which can be categorized as sea state 3, gives low Percentage Operability, especially in the peak period of 1 to 3 seconds. The Percentage Operability of the boat for all criteria is not high, varying from 61% to 74%. Among all criteria, the limiting boundary for Criteria 1 (RMS Roll motion) and Criteria 2 (RMS Pitch Motion) renders the Percentage Operability value low.

The Percentage Operability for RMS roll motion is low because it exceeds 6° as a maximum limitation. This situation might make the crew uncomfortable on board, but it does not mean that the boat is unsafe. Therefore, an expected maximum of roll motion investigation was carried out to ensure the roll responses do not surpass the Angle of Vanishing Stability. Thus, the GZ value is always positive. Once the GZ value becomes negative, the boat will be unstable and capsize. Down Flooding Angle was also employed as another limiting angle to investigate whether the expected maximum of roll will exceed Down Flooding Angle. If so, the deck edge will meet the seawater, and the water is assumed to be on the deck.

Based on the Percentage Operability for the expected maximum of roll motion, LC 4 is the worst scenario for all speeds and headings (for AVS chosen as $OP_{tot\,max}$). LC 2 is the same for medium and maximum speeds with wave headings of 60° and 90°. While other load case has 100% operability, which means the maximum roll response do not surpass the Angle of Vanishing Stability. The boat is predicted to be stable and has a positive GZ.

On the other hand, the Percentage Operability results are different for Down Flooding Angle as $OP_{tot\,max}$. Some load cases no longer have 100% operability like those from Angle of Vanishing Stability. The expected maximum roll of the boat was predicted will exceeding Down Flooding Angle. From this comparison, the choice of Down Flooding Angle as a limiting angle to calculate Percentage Operability is better than Angle of Vanishing Stability because this angle is more sensitive and clearly shows the distinction between the load cases. Among load cases with 100% operability for the expected maximum of roll motion, an Operability Robustness Index investigation was carried out to assess which Load Case is better. A different $OP_{tot\,max}$ will give different results of Operability Robustness Index.

A loss of stability due to restoring moment variations when the wave profile is taken into account, such as parametric roll and pure loss of stability, is a part of our future work. The roll responses of a fishing boat from the head and following waves will be investigated using an unsteady Reynolds-Averaged Navier Stokes-based Computational Fluid Dynamics (CFD) technique. This technique will enable researchers to include the effect of the full nonlinearity and coupled heave, pitch, and roll motions.

5. Development of Single Operability Assessment for Small Fishing Vessels

5.1. Introduction

Operability index assessment is used to assess the seakeeping performance based on the operational area (represented in Wave Scatter Diagram data) in a certain period (monthly, seasonally, or annually). Operability assessment is essential, especially for fishing vessels, to assess the safety and comfort of the fishing vessels.

Regardless of the ship speed and wave direction, the operability assessment is typically used in one loading condition, i.e., full load. This condition is suitable for merchant ships whose loading condition is usually unchanged during the voyage. However, this is not suitable for a fishing vessel. The loading condition of a fishing vessel changes during her voyage. Then, the operability assessment should be carried out by involving many loading conditions.

The influence of changes in loading condition, such as the displacement and longitudinal and vertical centre of gravity position, towards the percentage operability of small fishing boat was investigated by Iqbal et al. (2023) in Chapter 4. Due to changes in loading conditions, the natural period of the boat is altered. Certain loading conditions result in a low percentage of operability, as they lead to high response levels that exceed the seakeeping criteria limits.

However, altering the loading condition is not the sole method of modifying the natural period of vessels. The size of the vessel also plays a role in determining the natural period, which subsequently impacts the percentage of operability. The current chapter investigates the degree to which vessel size modifications improve the fishing boat's seakeeping performance, leading to an increase in the operational effectiveness expressed as a percentage operability.

On the other hand, the percentage operability based on Fonseca and Soares (2002) outcomes vary significantly due to the presence of numerous loading conditions. Therefore, deciding on the most representative value of the operability index is not straightforward. The recent operability index, Operability Robustness Index based on Gutsch et al. (2020), focus only one criterion. Thus, that index cannot fully cover all fishing vessel operation in indexing ship operability.

The objective of this chapter is to develop a comprehensive operability metric that considers multiple loading conditions for fishing vessels. Additionally, it aims to evaluate the performance of three fishing vessels, obtained by scaling up the original hull form to three different sizes.

The present chapter demonstrates the extent to which vessel size influences the improvement in percentage operability. Moreover, based on each operability index of different vessel size, this research can assess the seakeeping performance among many options and provides information to the stakeholders on the best size suitable for the same operational region, in this case, the Java Sea.

5.2. Methodology

The main dimensions of the fishing vessel used in this research are shown in Table 5.1. The initial hull then was scaled up twice to create two other vessels. The study compares the operability index assessments of the three boats proposed in this research.

Table 5.1. Three main dimension of fishing vessels

Parameters	**Initial,**	**2x Scale,**	**4x Scale,**
Length between perpendicular, *LPP* (m)	5.000	10.000	20.000
Breadth at water line, *B* (m)	1.934	3.868	7.736
Loaded draft, *T* (m)	0.350	0.70	1.40
Displacement, Δ(ton)	1.858	14.864	118.912
Block coefficient, *Cb* (-)	0.537	0.537	0.537
Mid-boat section coefficient, *Cm* (-)	0.764	0.764	0.764
Froude number, F_r (-)	0.590	0.590	0.590

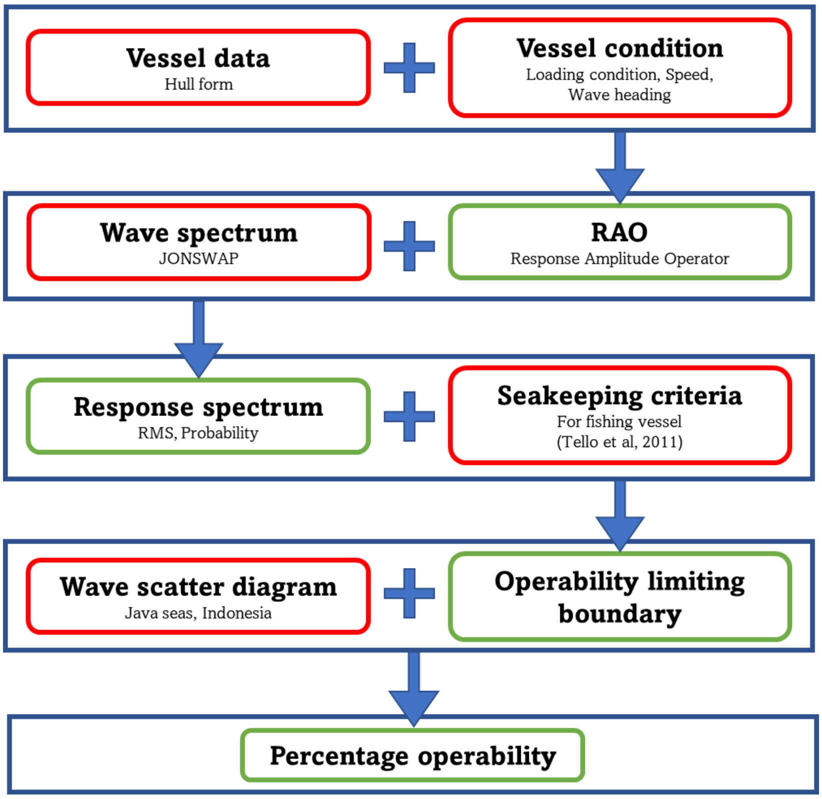

Figure 5.1. Overview of percentage operability analysis procedure

Figure 5.1 shows the overview of the operability analysis procedure. The first step in the procedure is to determine the Response Amplitude Operator (RAO) from vessel data (wave heading and vessel speed) and the loading condition. The RAO was determined using VERES, the plugin from ShipX Software, which used linear potential theory that is solved using strip theory method. The method was introduced by Salvesen et al. (1970).

Then the response spectrum is obtained by using the combination of RAO's and wave spectrum for a single significant wave height (*Hs*) and wave peak period (*Tp*). This study used the JONSWAP spectrum (Hasselmann et al., 1973) in Eq. (5.1) with γ = 2.5, which represents the Java Sea where the boat is operated.

$$S_{\zeta}(\omega) = \left[\frac{\alpha g^2}{\omega^5} exp\left\{-\frac{5}{4}\left(\frac{\omega_p}{\omega}\right)^{-4}\right\}\right]\gamma^{exp\left\{-\frac{(\omega-\omega_p)^2}{2\sigma^2{\omega_p}^2}\right\}} \tag{5.1}$$

The operability limiting boundary can be determined in each response spectrum using the seakeeping criteria based on Tello et al. (2011), as shown in Table 5.2. The responses spectrum calculation is iterated by changing *Hs* and *Tp* according to the wave scatter diagram data of Java Sea in Figure 5.2. Lastly, the percentage operability for each load case is selected based on the minimum percentage from all criteria.

Table 5.2. Seakeeping criteria for fishing vessels.

No	**Criteria**	**Limit**
1	RMS roll	6.00°
2	RMS pitch	3.00°
3	Probability of green water (GW)	0.05
4	Probability of slamming (SL)	0.03
5	RMS vertical acceleration at working area / bridge deck (VA)	0.20 g
6	RMS lateral acceleration at working area / bridge deck (LA)	0.10 g

Based on Figure 5.1, one vessel condition (loading condition and ship speed) produces a single percentage operability. In this research, each loading condition is characterised by a weighting factor $\boldsymbol{w(LC_i)}$, which is obtained from the percentage of the total duration of the operation. The speed used in each loading condition is different and is characterised by the maximum vessel speed. Details of the different loading conditions are shown in Table 5.3. Finally, a single percentage operability $P_{op}(LC)$ from the combination of different loading conditions is shown in Eq. (5.2).

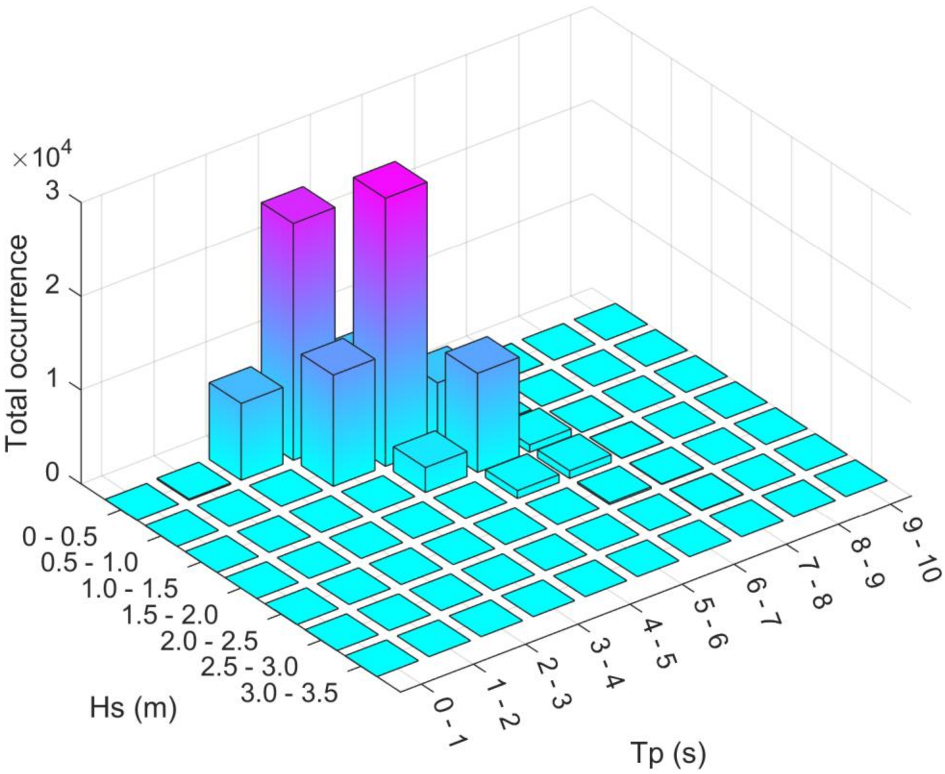

Figure 5.2. Wave scatter diagram of Java Sea (https://app.metoceanview.com/hindcast/)

Table 5.3. Loading condition of fishing vessel

Loading condition	**Departure**	**Fishing activity**			**Arrival**
	LC 1	**LC 2**	**LC3**	**LC 4**	**LC 5**
Ship weight (kg)	712	1285	1285	1858	1858
LCG (m)	1.550	1.751	1.751	1.828	1.828
KG (m)	0.844	0.914	0.557	1.064	0.57
$\boldsymbol{V_i}$	Vmax	0.3*Vmax	0.3*Vmax	0.3*Vmax	Vmax
$\boldsymbol{w(LC_i)}$	35%	10%	15%	10%	30%

$$P_{op}(LC) = \sum_{i=1}^{N_{LC}} P_{op}(\beta, V_i) w(LC_i) \tag{5.2}$$

where $P_{op}(LC)$ is Percentage Operability that considers many different load cases, $P_{op}(\beta, V_i)$ is Percentage Operability for all wave headings (β) at a particular speed (V_i) in each load case. $w(LC_i)$ is the weighting factor that is taken from the percentage of total duration of fishing vessel operation.

5.3. Results and Discussion

5.3.1. RAO for Various Fishing Boats Sizes and Load Cases

Based on the wave scatter diagram of the Java Sea in Figure 5.2, the highest occurrences of *Hs* are observed between *Tp* values of 3 and 5 seconds. When the RAO peak is situated in that region, the boat exhibits a significant response. As a result of this condition, there is a decrease in the percentage operability, as the boat's responses exceeded the limit of the seakeeping criteria.

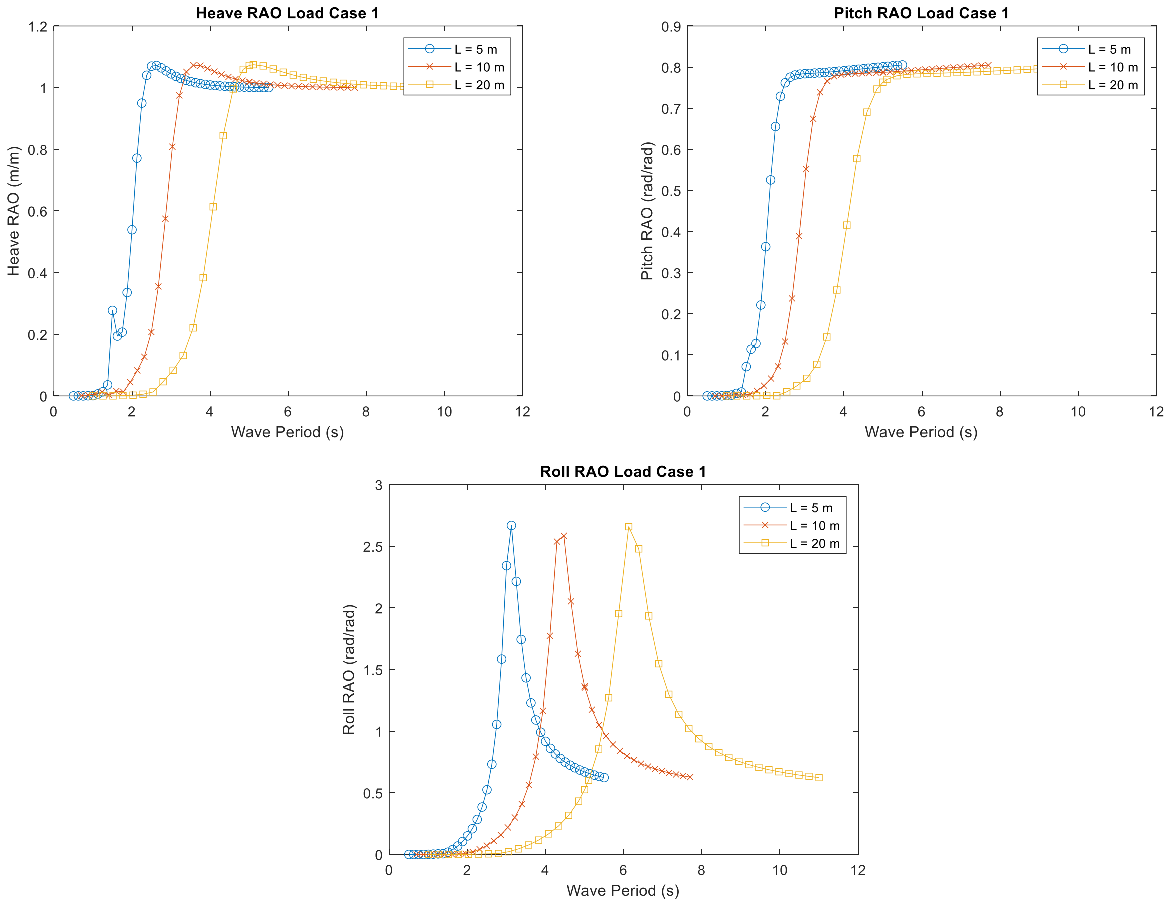

Figure 5.3. RAO of heave, pitch, and roll of load case 1 for various fishing boat sizes at a wave heading of 30°.

Figure 5.3 displays the RAO curves of heave, pitch, and roll for various boat sizes. All calculations were performed with a wave heading of 30° and under the same load case, LC 1. The figure clearly illustrates how the size of the boat affects the peak values of the RAO. The RAO curve and the position of its peak are influenced by a combination of factors, including speed, wave heading, and loading conditions. Changes in these factors result in alterations to the RAO curve and the position of its peak.

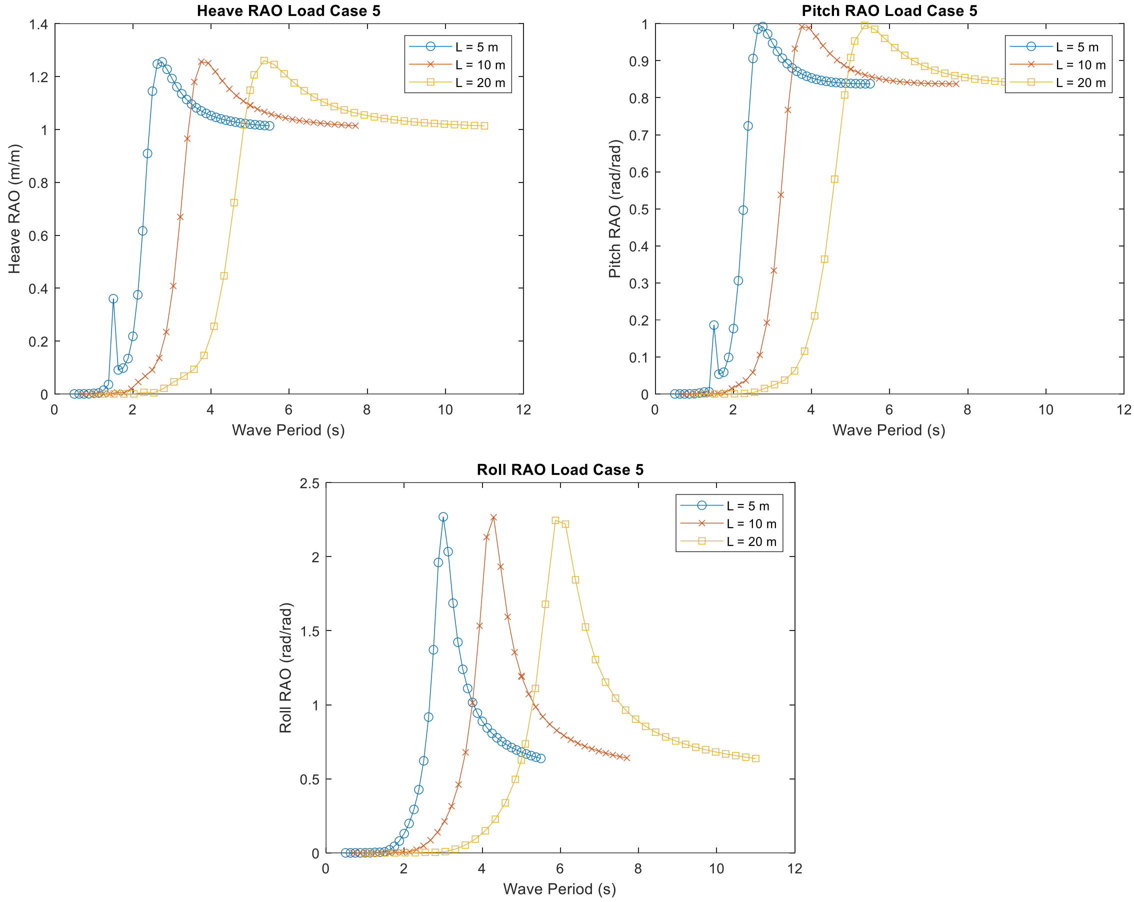

Figure 5.4. RAO of heave, pitch, and roll of load case 5 for various fishing boat sizes at a wave heading of 30°.

Figure 5.4 shows the RAO curve with the same wave heading as Figure 5.3 but under a different load case, LC 5. A comparison between both figures reveals that changes in loading conditions impact the characteristics of the RAO curve, whereas the size of the boat primarily alters the peak location without significantly affecting the shape of the curve. The next subsection will discuss the influence of loading conditions and boat size on the percentage operability.

It clearly shows that make the vessel larger alter the RAO peak to be a larger period. Based on the wave scatter diagram, the occurrence of wave period (*Tp*) at 6-7 seconds is 1.9% and become lower for higher *Tp*. Making the vessel larger is one of solutions to enhance the safety of fishing vessels, as it can operate well due to meeting all the seakeeping criteria for fishing boat.

5.3.2. Percentage Operability for Different Criteria

Figure 5.5 displays the percentage operability, categorised by ship size, for different criteria. The definition of criteria 1 – 6 can be seen in Table 5.2. Based on this figure, it is shown that criteria 1-3 (RMS roll, RMS pitch, and Probability of Green Water) have low values compared to other load cases. However, the operability values increases when the ship size increases.

The percentage operability values were obtained from 12 wave headings, from 0°-360° in 30° increments and have the same weight factor. Each load case has a different speed, as shown in Table 5.3.

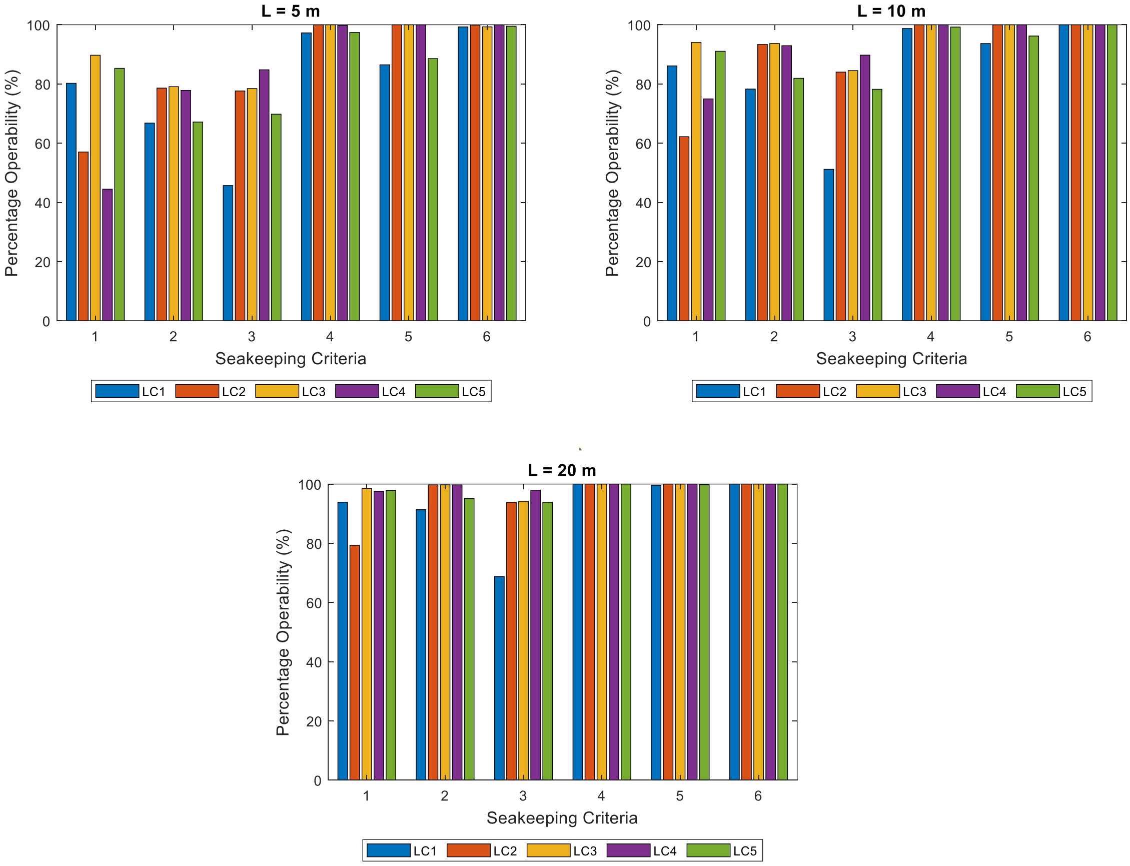

Figure 5.5. Percentage operability for different criteria

In Figure 5.5, it is evident that among all criteria, criterion 3 (probability of green water) for Load Case 1 and a boat size of L=5m has the minimum value of 45.67%. The minimum value obtained, 45.67%, was selected as the percentage operability for Load Case 1. The same method was applied to determine the percentage operability for each load case.

Figure 5.5 also illustrates the areas of percentage operability that require improvement for each criterion. By addressing the criterion with the lowest value, the operability for all load cases can be enhanced. For instance, if the percentage operability for the probability of green water (criterion 3) is low, the vessel can be improved by increasing the freeboard to prevent green water from impacting the vessel.

5.3.3. Percentage Operability for Different Load Cases

Based on Figure 5.5, the percentage operability for each load case can be determined by choosing the lowest value among all criteria. Figure 5.6 shows the results of percentage operability in each load case. Based on the figure, each load case has a different percentage operability. The trend varies for each load case depending on the size, even though the shape of the boat remains the same.

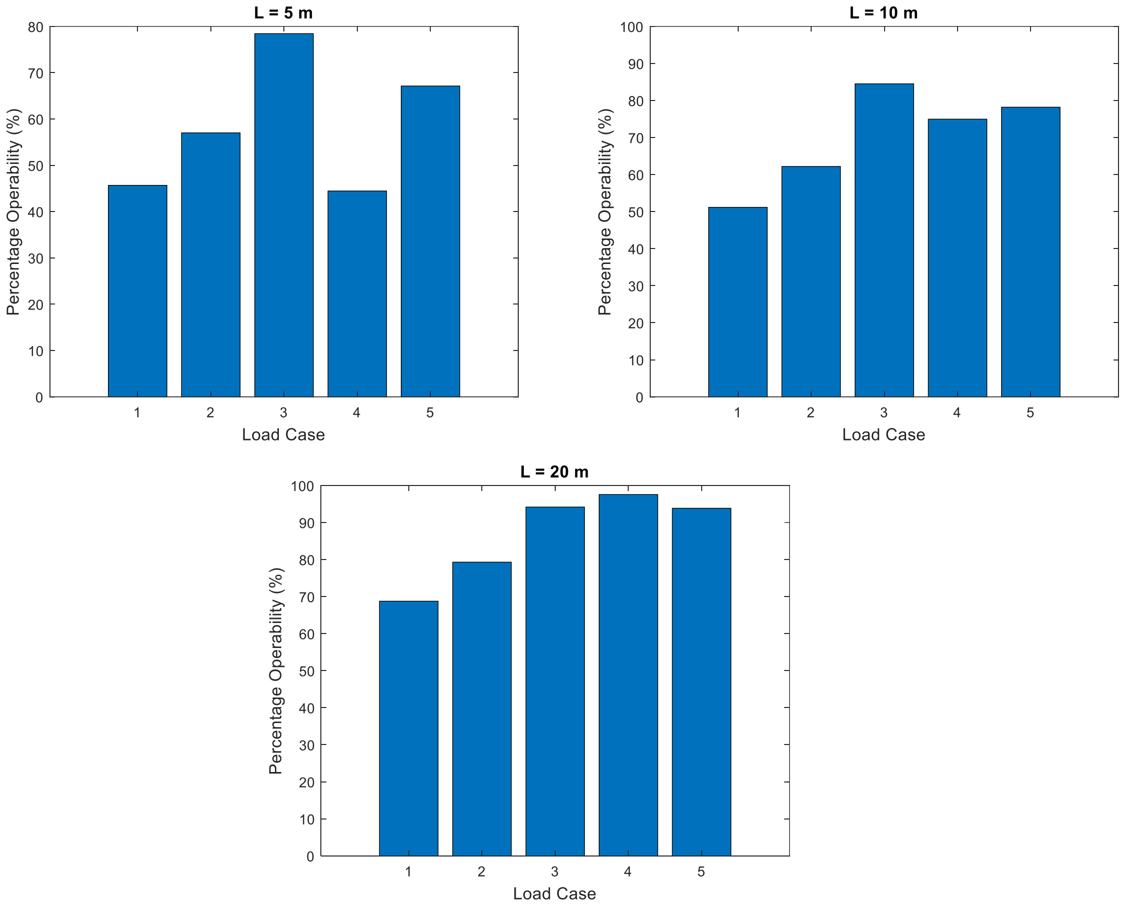

Figure 5.6. Comparison of the operability percentage of fishing boats across various sizes and load cases

In Iqbal et al. (2023) (Chapter 6), the percentage operability for each load case was calculated at the same speed value to observe the influence of loading condition and assess the worst loading condition during the operation. However, as the speed is the same for each load case, it is challenging to determine a single operability index of the vessel that considers all load cases. The operability cannot simply be averaged, as the speed for each load case is dependent on the activity in each load case.

The boat used in the present research was the same as Iqbal et al. (2023). However, the boat speed used in the calculation for each load case was adjusted according to three categories: departure, fishing activity, and arrival, as outlined in Table 5.3.

Despite this condition, each load case still yields varying percentages of operability, similar to the findings reported by Iqbal et al. (2023). It is challenging to straightforwardly average the percentage operability for each load case due to the differing time durations associated with them. Consequently, this issue is addressed by converting the duration of each load case into a percentage of the total duration. This percentage is then taken into account in the overall operability index calculation for a single fishing boat in question.

5.3.4. Percentage Operability for Different Ship Sizes

The procedure used to calculate the percentage operability of a vessel typically ends at Figure 5.7, where percentage operability for a specific load case is successfully determined. However, the loading conditions for fishing vessels during operation constantly change. As a result, there are numerous percentages of operability for a single vessel, each depending on the total number of loading conditions.

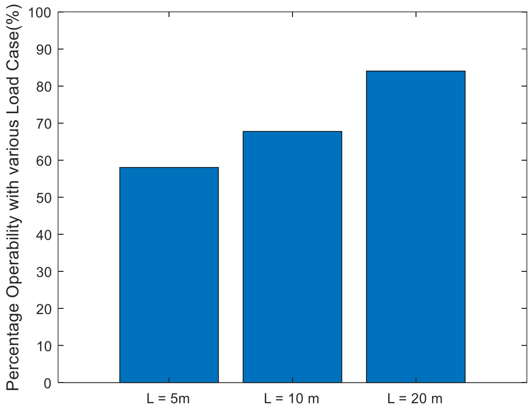

Figure 5.7. Percentage operability for different vessel size

In contrast, comparing the operational effectiveness of different vessels solely based on percentage operability poses challenges. To address this issue, the present study aimed to consolidate the various loading conditions into a single value of percentage operability, as illustrated in Table 5.3 and described by Eq. (5.2). By obtaining this consolidated value, it becomes possible to better compare it with other vessels and determine the most suitable choice.

Figure 5.7 shows the results of the percentage operability with various load cases for a different vessel size, starting from initial size ($L = 5$ m) which was then multiplied by two ($L = 10$ m) and then multiplied again by two ($L = 20$ m). The percentage operability for $L = 5$ m is 58.04%, while $L = 10$ m is 67.75% and $L = 20$ m is 84.03%.

Based on the above finding, the percentage operability of the boat increases consistently with the boat size. The larger size alters the natural frequency, keeping one's distance from the most frequent peak wave period of the Java Sea and avoiding the resonant responses. As the boat responses are low, the percentage operability becomes higher by satisfying the seakeeping criteria.

The size of the boat exerts a greater influence on the percentage operability compared to variations in the loading conditions for each size. The work carried out within the present chapter reaffirms the appropriate size for fishing boats operating in the Java Sea. In general, fishing boats with a length of 20 metres or greater have a substantial natural period that exceeds the most common wave periods in the Java Sea. While loading conditions can affect the natural period, the impact of these changes is less significant compared to the alterations in boat size.

The single percentage operability resulted in this study can be a tool to assess the seakeeping performance of fishing vessels and select the best one among many vessel options. This single percentage operability has included the change in loading condition, which is a typical feature of fishing vessels during operation.

5.3.5. Determination of Vessel Length with 100% Operability

Once a single operability index for different vessel lengths has been determined, polynomial regression can be used to analyse how the operability index changes as vessel length varies. The regression equation can then be used to estimate the minimum vessel length required to achieve a 100% operability index by extrapolating the data. A second-order polynomial was fitted to the data, yielding an R^2 value of 1, indicating that the equation accurately represents the data. The regression equation is presented in Eq. (5.3), and the corresponding regression graph is shown in Figure 5.8.

$$P_{op}(L) = -0.0209L^2 + 2.256L + 47.283 \tag{5.3}$$

According to Eq. (5.3), a vessel must have a minimum length of 34.21 metres to achieve 100% operability, as shown in Figure 5.9. However, it should be noted that Eq. (5.3) is only valid for this hull from due to several limitations. The equation was derived from only three data points, which may not represent the majority of fishing vessels in Indonesia. Additionally, the comparison for the three different vessel sizes assumed the same hull form, Froude number, and loading conditions. In reality, vessels of different sizes may operate at different speeds and, consequently, have different Froude numbers. Loading conditions may also vary, as larger vessels are equipped with different fishing gear. Doubts can also be raised regarding the validity of extrapolating to a point far from the original data set.

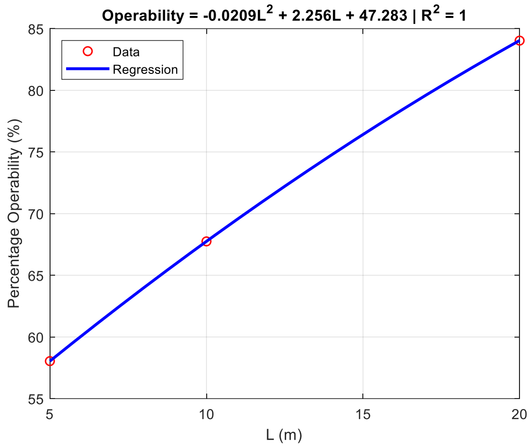

Figure 5.8. Results of the second order polynomial regression

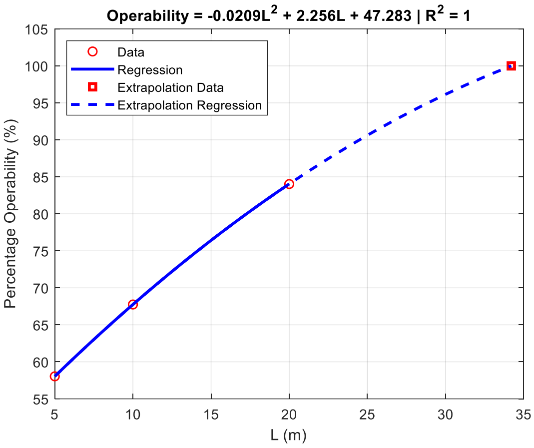

Figure 5.9. Minimum length of vessel to achieve 100% operability

However, as more extensive data becomes available in the future, this methodology could be used to determine a typical operability index for vessels of a certain length. This would allow the government to establish standards for the required operability index for different vessel sizes, based on the regression model, which could be practically applied by designers. Existing small fishing boat can still operate with limitations, as a consequence of having a low operability index.

5.4. Summary

The operation of fishing vessels is dynamic. The payload is always changed depending on the number of fish that the fishermen can catch. Starting from the empty fish tank and then gradually filling the fish tank. The way the catch is placed changes the Centre of Gravity (*CoG*). Thus, the transversal and longitudinal metacentric height (*GM*) result in a different natural period.

A comprehensive evaluation of operability was conducted on three distinct sizes of fishing boats. This assessment encompassed diverse loading conditions that simulated various fishing boat operations, considering alterations in displacement and centre of gravity. Each loading condition was accompanied by an appropriate speed corresponding to the specific fishing boat activity.

The percentage operability calculation in this research utilised seakeeping criteria for a fishing vessel. The lowest percentage operability among all the criteria was chosen as the representative operability for a single load case. As there are multiple load cases, each resulting in different percentages of operability, a weighting factor was introduced. This weighting factor was determined by considering the percentage of time spent in each load case relative to the total duration of the fishing boat's operation. By applying the appropriate weighting factors, a unified percentage operability value for a single vessel could be derived.

Based on the research findings, it was observed that increasing the size of the fishing vessels leads to an improvement in percentage operability. This improvement is attributed to the altered natural period, which moves away from the most common peak period found in the Java Sea (3-5 seconds). The largest fishing vessel examined, with a length of 20 meters, exhibited the highest percentage operability of 84.03% compared to the percentage operability of other two fishing boats with smaller sizes but the same hull form, which are 67.75% (10 meters) and 58.04% (5 meters), respectively.

This study extends by generating the regression equation from those three data points to estimate the vessel length which has 100% operability. The regression indicates that the vessel must have a minimum length of 34.21 metres to achieve 100% operability for operations in the Java Sea.

The methodology presented in this chapter offers a practical approach for selecting the most suitable vessel based on its seakeeping performance, as represented by a single percentage operability value. As more extensive data becomes available in the future, this methodology could be used to determine a typical operability index for vessels of a certain length.

6. Unsteady RANS CFD Simulation on the Parametric Roll of Small Fishing Boat under Different Loading Conditions

6.1. Introduction

Parametric roll is one of the five stability failures that should be investigated in the design phase recommended by IMO on the Second Generation of Intact Stability (SGIS). Parametric roll occurs because of the periodic variation of the restoring roll moment. When the ship moves in waves, especially in head waves, the *GM* changes considerably during one encounter period. Usually, the *GM* is low when the wave crests at the midship and high when the wave trough at the midship. These changes trigger the roll motion gradually. When the encounter frequency is twice the roll's natural frequency, parametric resonance occurs (Park et al., 2013).

The flare of the vessel plays an important role in changing the *GM* value due to heave and pitch motion in waves. For large ships, the significant flares are located on the bow and stern parts (V shape) as the middle part has a U shape. For a small fishing boat, almost their hull shapes are in V shape hull, which in trim conditions can be similar with flare and potentially change their *GM* significantly in waves.

The parametric roll phenomenon also occurs when the wavelength is close to the vessel length. Most of sea around the world has a longer wave, making the larger ships have a big chance experiencing this phenomenon. However, in Java Sea, which can be categorised as Sea State 3, have a low period, which have a short wave. This can be the bad news for a small vessel, especially for a fishing vessel which has a V shape, as the parametric roll can be occurred and experienced by small fishing boat.

The occurrence of parametric roll can be identified early in the design spiral using the relationship between the encounter wave period (Te) and the natural roll period (Tn). The phenomenon is predicted to occur where the ratio Te/Tn is close to 0.5. However, the amplitude of parametric roll should also be predicted to ensure the boat's safety, and comfort during operation. In the worst case, high roll amplitudes may lead the ship to capsize because of insufficient restoring moment.

Parametric roll studies have mostly focused on large ships, such as ONR Tumblehome surface combatant (Sadat-Hosseini et al., 2010), (Liu et al., 2021) and container ships (Park et al., 2013), (Yu et al., 2018), (Yu et al., 2019), (Zhou et al., 2016). While many researchers focused on investigating the parametric rolling of large ships, some researchers investigated fishing boats, such as (Neves, 2002), (Ghamari et al., 2017), and (Ghamari et al., 2020). Based on these publications, , it has been shown that fishing boats can experience parametric roll in the same way as merchant ships as long as the conditions triggering parametric roll are met.

However, the length of the fishing boats mentioned in the above studies investigated large vessels, approximately 25 m in length, which is not sufficiently small to represent a large portion of today's fishing boat fleet. There are considerable differences in the seakeeping behaviour between large and small vessels. Subject to the same wave at sea, the response of small boats tends to be higher than large vessels, making them uncomfortable. Moreover, to the best of the author's knowledge, no prior work has taken place in this field, investigating the parametric rolling of small fishing boats under different loading conditions using fully nonlinear unsteady RANS simulations. The present study models a typical five-metre Indonesian fishing boat to investigate its parametric roll behaviour as a case study.

Small fishing boats are the most prone to accidents compared to the large ones. Moreover, Iqbal et al. (2023) showed that the operability of small fishing boats is not high, around 60% - 70%, due to several strict seakeeping criteria, such as limits on RMS roll amplitudes. Due to the small typical boat size, the roll natural period of the small fishing boat is relatively low and might be close to the wave period. This condition may lead to the roll resonance. Also, the parametric roll is expected to occur when the encounter period is close to the half of the natural roll period.

This study aims to investigate the parametric roll characteristics of a small fishing vessel while in operation, specifically when there are changes to its loading conditions. The influence of displacement and the *GM*/*KM* ratio on the parametric roll are presented. Also, in terms of vessel shape, the influence of longitudinal flare distribution at the waterline of the boats is discussed. The information provided herein offers guidance to fishing boat operators on the optimal methods for handling the fish they catch during their operations.

The prediction of parametric roll was investigated using a commercial Computational Fluid Dynamics (CFD) software package, Star CCM+. The employed technique used in this study is based on the unsteady Reynolds-Averaged Navier Stokes Equations (URANS) method, which has been used widely by many researchers to investigate similar marine hydrodynamics-related problems. The presented CFD simulations in this study are compared against existing data using the experimental research on the parametric roll of the benchmarking KCS model as reported by Yu et al. (2019, 2018). Once an adequate simulation set-up was established for the KCS, characterised by a low comparison error with the experiment, regardless the domain size, identical numerical set-up was implemented for the fishing boat.

One of the benefits of using URANS CFD simulation is its accuracy in predicting Parametric Roll (PR), as the viscous effects are directly included in the simulation. Different wall treatment was tested to ensure the viscous terms are correctly calculated allowing a comparison of different y^+ strategies to be carried out. In addition, two methods for predicting the conditions that trigger the parametric roll were used: level 1 assessment of parametric roll on the Second Generation of Intact Stability form IMO and Susceptibility criteria of PR from the American Bureau of Shipping (ABS). Then, the direct CFD simulation for parametric roll was carried out to predict the amplitude of parametric roll. The effect of displacement and *GM*/*KM* ratio on the *GM* Ratio is observed. Also, the influence of vessel shape and the longitudinal flare distribution on the waterline are considered.

6.2. Methodology

The simulation flowchart is presented in Figure 6.1, where the steps involved in conducting a CFD simulation for the KCS model are shown on the right-hand side. The first step, a fine mesh configuration was simulated using two different y^+ strategies. Then, steady roll amplitudes obtained using low and high y^+ meshing strategy were compared to the experimental result obtained from the parametric roll test of the KCS model studied by Yu et al. (2019, 2018). This step was carried out to observe the viscous effect to the parametric roll amplitude. An estimate of the discretisation uncertainty obtained through the Grid Convergence Index (GCI) method is then used as a second step in the verification section of the present chapter. In this step, the grid spacing, and time step were systematically coarsened to quantify the error due to numerical method.

After ensuring the GCI result was low, in the third step, the set-up of CFD simulation of the KCS model was applied for both free roll decay simulation and direct CFD simulation on parametric roll simulation for fishing boats. The linear roll damping ratio was obtained through free decay test (fourth step), which is used as an input in susceptibility criteria assessment (fifth step). The linear roll damping obtained from CFD calculations was also compared to Ikeda's method, which was calculated in the ShipX software with the same conditions as CFD. The viscous roll damping in ShipX software is determined from an empirical formula for roll motions. The components of this formula are frictional shear stress on the hull surface (Kato, 1957), eddy damping proposed by Ikeda et al. (1977), lift damping (Himeno, 1981) and the bilge keel damping (Ikeda, 1979). The latter component is not included because in this study the boat has no bilge keel.

The left-hand side of the flowchart starts by determining the loading conditions. The loading condition was described in Chapter 3.2.1, which represents the operation of fishing boat. In the second step of the left-hand side, the ABS (2019) recommendation is used to determine the design wave and vessel speed for a given loading condition. This design wave is then used to calculate the GM variation as the wave crest moves from the bow to the stern (the third step of left-hand side). The resulting GM Ratio, the ratio between the amplitude GM in wave and GM in calm water, is then used to perform the Lv1 Parametric Roll Assessment of Second Generation of Intact Stability (SGIS) and to assess the susceptibility criteria, following the ABS' (2019)method. Finally, after determining the design wave and boat speed in each load case and having done the CFD setup, CFD simulations of the fishing boat to investigate a parametric roll can be carried out.

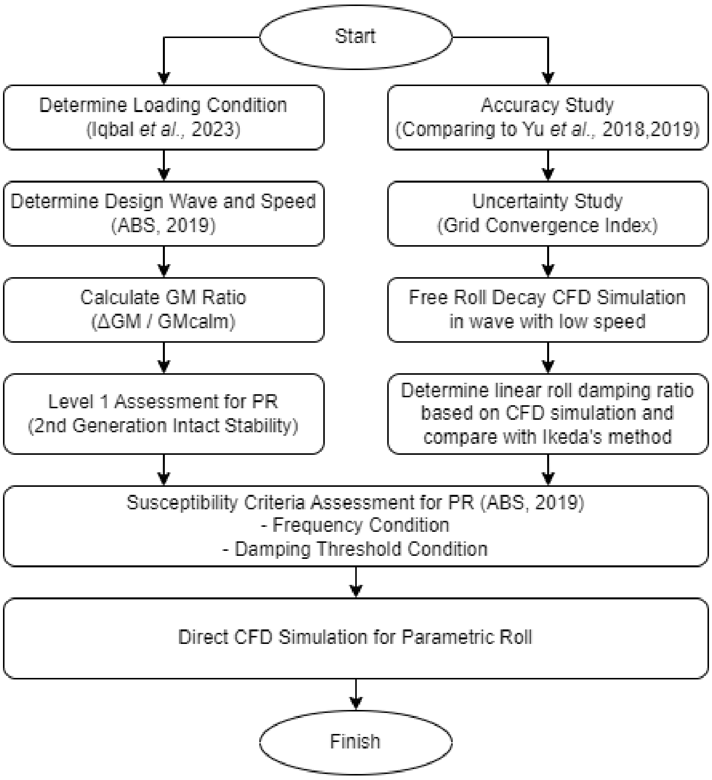

Figure 6.1. Simulation flowchart

6.2.1. Determination of the Design Wave and Vessel Speed

The ABS (2019) guidelines recommend using a wavelength equal to the ship length and to determine the wave height based on the relationship with its length. The table shows that the wave steepness ratio, H_w/λ (where H_w is the wave height and λ is the wavelength), increases when the wavelength decreases. In this particular study, the fishing boat's length is 5 m, so the wavelength λ is also 5 m. According to the Table 6.1, the H_w/λ ratio used was supposed to be 0.12 (for the lowest wavelength), resulting in a wave height of 0.6 m. However, this ratio is too high for a 5-metre fishing boat, and it would cause wave breaking. Therefore, a lower H_w/λ ratio of 0.06 was used, resulting in a wave height of 0.3 metres.

Eq. (6.1) from ABS (2019) was employed to determine the velocity of the boat (V_{PR}, in knots) that leads to a parametric roll. In Eq. (6.1), If $2\omega_m > \omega_w$ (where ω_w is the wave frequency and ω_m is the mean frequency) the parametric roll phenomenon will be expected in head waves. Conversely, if $2\omega_m < \omega_w$ the parametric roll will be expected in stern waves, which can be determined based on the wavelength. ω_m is the mean frequency that obtained from GM_m by calculating the stability in longitudinal wave, explained in the following subsection.

Table 6.1. Wave height information according to the wave scatter data from IACS recommendation

Wavelength, λ (m)	50	100	150	200	250	300	350	400	450
Wave height, H_w (m)	5.9	11.6	14.2	15.1	15.2	14.6	13.6	12.0	9.9
H_w/λ	0.12	0.12	0.09	0.08	0.06	0.05	0.04	0.03	0.02

$$V_{PR} = \frac{19.06 \times |2\omega_m - \omega_w|}{{\omega_w}^2} \tag{6.1}$$

6.2.2. Calculation of the *GM* Ratio and Level 1 Assessment of PR

Using the design wave determination procedure described earlier, the wave crest location (referred as x in Figure 6.2) was shifted along the ship length (LBP) to calculate the *GM*. Maxsurf Stability software was employed to calculate this step, resulting in $GM_{\max}$, GM_{min}, GM_m, and GM_a, as shown in Figure 6.2. Here, GM_{max} and GM_{min} are the maximum and minimum *GM* values, while GM_m is mean of *GM*, where $GM_m = 0.5(GM_{max} + GM_{min})$, and GM_a is the amplitude of *GM* calculated as $0.5(GM_{max} - GM_{min})$. GM_a is also referred to as ΔGM and is used to calculate Level 1 vulnerability criteria of Parametric Roll in the Second Generation of Intact Stability (SGIS), as shown in Eq. (6.2).

$$\frac{\Delta GM}{GM_{calm}} \leq R_{PR} \tag{6.2}$$

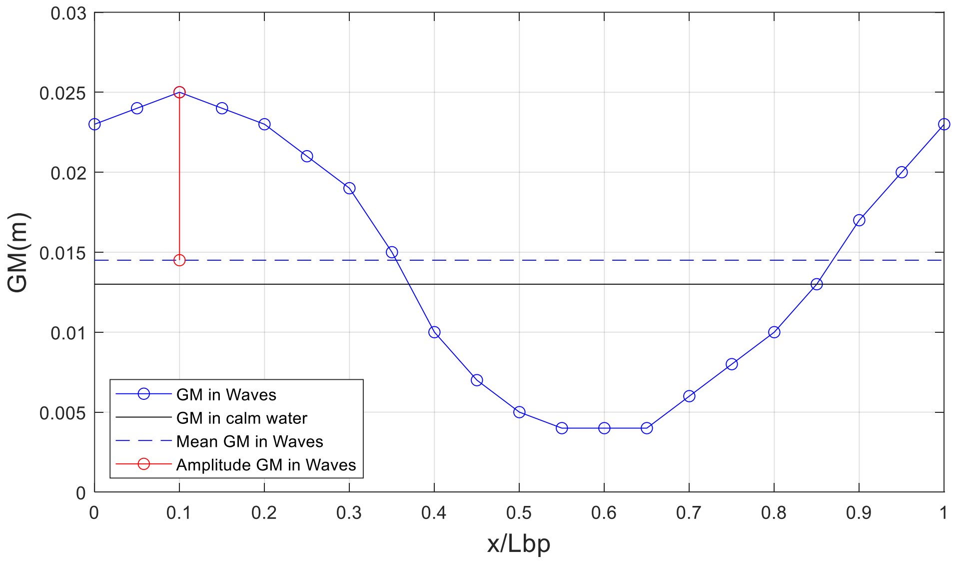

Figure 6.2. *GM* value of 2.3 m KCS model in waves

Table 6.2. Result of vessel speed and wave direction for λ = 5.0 m and Hw = 0.3 m based on Eq. (6.1)

Load Case	T_n **(s)**	**Boat Speed, V_{PR} (m/s)**	**Wave Direction**	T_e **(s)**	T_e/T_n
1	2.00	2.37	Head waves ($2\omega_m > \omega_w$)	0.968	0.48
2	2.00	1.33	Head waves ($2\omega_m > \omega_w$)	1.212	0.61
3	1.60	2.85	Head waves ($2\omega_m > \omega_w$)	0.886	0.55
4	4.38	0.35	Following waves ($2\omega_m < \omega_w$)	2.046	0.47
5	1.57	2.36	Head waves ($2\omega_m > \omega_w$)	0.970	0.62

Table 6.3. The results of level 1 SGIS based on Eq. (6.2)

Load Case	ΔGM	GM_{calm}	$\Delta GM/GM_{calm}$	R_{PR}	**Status**
1	0.419	0.763	0.261	0.17	Failed
2	0.252	0.456	0.184	0.17	Failed
3	0.145	0.813	0.106	0.17	Pass
4	0.271	0.163	0.221	0.17	Failed
5	0.071	0.657	0.058	0.17	Pass

A ship is predicted to experience parametric roll if $\frac{\Delta GM}{GM_{calm}} > R_{PR}$, where R_{PR} is a semi-empirical factor based on the basic geometrical characteristics of a vessel, such as *L, B*, and midship coefficient (*C_m*). The equation is stated in IMO (2008a), which is highly sensitive to bilge keel area, Ak. When there is no bilge keel installed on the vessel, R_{PR} is set as 0.17. In the present investigation, the computation proceeds to the Direct Stability Assessment (DSA) stage instead of Level 2, in the event of a failure in Level 1 assessment, when $\frac{\Delta GM}{GM_{calm}} > R_{PR}$. This decision is taken considering the utilisation of the Computational Fluid Dynamics technique to simulate the amplitude of parametric roll.

The result of Eq. (6.1) (vessel speed) and Eq. (6.2) (Lv 1 assessment of parametric roll) are shown in Table 6.2 and Table 6.3, respectively. As Table 6.2 indicates, the speeds at which parametric roll is triggered vary for each load case. The wave direction for all load cases is head waves, except for load case 4, which involves following waves. In Table 6.3, all load cases except LC3 and LC5 failed to satisfy the Level 1 assessment for parametric roll, thereby necessitating progression to Level 2 assessment. Nonetheless, this study undertakes a direct stability assessment, which leverages Computational Fluid Dynamics simulation to estimate the amplitude of parametric roll, instead of Level 2 assessment.

6.2.3. Susceptibility Criteria of Parametric Roll

Prediction of parametric roll in regular waves can be accomplished using the Mathieu equation. This equation can be deconstructed by considering a ship moving in waves with forward speed. As the ship moves through the waves, the *GM* of the ship changes in response to the location of the wave crest and trough.

The change of GM can be simplified with the sinusoidal waves as shown in Eq. (6.3). By substituting Eq. (6.3) to the equation of 1 DOF of damped free roll motion, one arrives at Eq. (6.4), where ${\omega_m}^2 = \frac{\Delta.GM_m}{I_{xx}+I_{A.xx}}$ and ${\omega_a}^2 = \frac{\Delta.GM_a}{I_{xx}+I_{A.xx}}$. Then, the parameter $\omega_e t$ can be replaced with τ, a notation to normalise Eq. (6.4) by dividing it by ${\omega_e}^2$ resulting in Eq. (6.5). The ζ symbol in Eq. (6.4) is the defined as a damping ratio, the ratio between the linear damping coefficient of the roll (B) to its critical damping (B_c).

The present study determines the linear roll damping for every load case from free roll decay simulation. A speed of 0.2 m/s was selected in the simulation to produce τ or $\omega_e t$. High speeds were avoided as they may increase the roll damping coefficient (B) and reduce the roll motion.

The condition of fishing vessels when determining the roll damping using CFD simulation is that the vessel is non-stationary and in waves. The first reason for this is to obtain the roll damping as realistic as possible. When the fishing boat experiences parametric roll, it occurs in waves (not in calm water) and at non-zero speed condition. The second reason is the roll damping obtained from a simulation with forward speed in waves is mostly higher than in calm water case, as reported by Rodríguez et al. (2020). Therefore, linear roll damping would be overestimated if we use the roll damping based on calm water values.

The result of linear roll damping was subsequently compared to that obtained from Ikeda's method, which was computed using ShipX software under the same conditions as the CFD simulation. To eliminate the second term (linear damping) in Eq. (6.5), the solution of 1 DOF of damped free roll motion (Eq. (6.6)) is used and results in Eq. (6.7). This equation is referred to as the Mathieu equation. The common form of the Mathieu equation is shown in Eq. (6.8), as explained in ABS (2019).

$$GM = GM_m + GM_a \cos(\omega_e t) \tag{6.3}$$

$$\frac{d^2\phi}{dt^2} + (2\zeta\omega_n)\frac{d\phi}{dt} + \left({\omega_m}^2 + {\omega_a}^2 cos(\omega_e t)\right)\phi = 0 \tag{6.4}$$

$$\frac{1}{{\omega_e}^2}\frac{d^2\phi}{dt^2} + \left(2\frac{\zeta\omega_n}{{\omega_e}^2}\right)\frac{d\phi}{dt} + \left(\frac{{\omega_m}^2}{{\omega_e}^2} + \frac{{\omega_a}^2}{{\omega_e}^2}\cos(\omega_e t)\right)\phi = 0 \tag{6.5}$$

$$\frac{d^2\phi}{d\tau^2} + \left(2\frac{\zeta\omega_n}{\omega_e}\right)\frac{d\phi}{d\tau} + \left(\frac{{\omega_m}^2}{{\omega_e}^2} + \frac{{\omega_a}^2}{{\omega_e}^2}\cos(\tau)\right)\phi = 0$$

$$\phi(\tau) = x(\tau).\,e^{-\mu\tau} \tag{6.6}$$
$$\text{where } \mu = \zeta\omega_n/\omega_e$$

$$\frac{d^2\phi}{d\tau^2} + \left(\frac{{\omega_m}^2}{{\omega_e}^2} - \frac{(\zeta\omega_n)^2}{{\omega_e}^2} + \frac{{\omega_a}^2}{{\omega_e}^2}\cos(\tau)\right)\phi = 0 \tag{6.7}$$

$$\frac{d^2x}{d\tau^2} + \big(p + q\cos(\tau)\big)x = 0 \tag{6.8}$$
$$\text{where } p = \frac{{\omega_m}^2}{{\omega_e}^2} - \frac{(\zeta\omega_n)^2}{{\omega_e}^2} = \frac{{\omega_m}^2}{{\omega_e}^2} - \mu^2$$
$$q = \frac{{\omega_a}^2}{{\omega_e}^2}$$

There are two susceptibility criteria based on ABS after p and q are determined. First, the frequency of parametric excitation (encounter wave frequency) should be about double of natural roll frequency ($\omega_e \approx 2\omega_n$) or the encounter wave period should be about a half of natural roll period ($T_e \approx 0.5T_n$). The frequency condition of susceptibility criterion is shown in Figure 6.3 and Eq. (6.9). The boundary line in Figure 4 is determined from Eq. (6.9) and is sourced from ABS (2019). Based on these, the ship is considered susceptible to parametric roll if the point obtained from the combination of p and q lies inside the unstable zone.

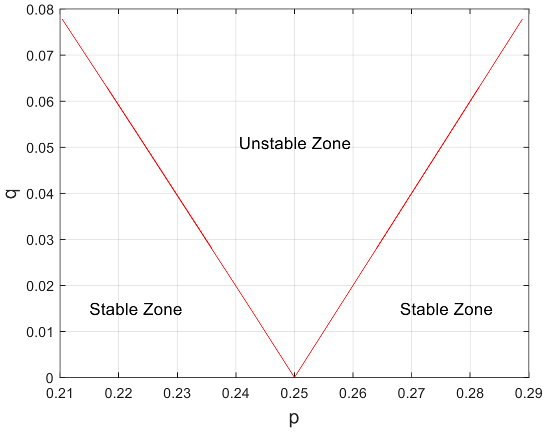

Figure 6.3. Frequency condition of susceptibility criterion

Even though the first criterion is satisfied, parametric roll can be triggered because roll damping plays an important role. If the roll damping is sufficiently high, parametric roll caused by changing stability in waves will not develop. However, if the roll damping is insufficient to reduce the roll amplitude significantly, then parametric roll will develop. Therefore, the second susceptibility criterion from ABS (2019) is about the roll damping threshold. The ship is susceptible to parametric roll if the effective damping ($\zeta\omega_n/\omega_e$) of the ship is smaller than the damping threshold ($q.k_1.k_2\sqrt{1-{k_3}^2}$), as shown in Eq. (6.10), based on ABS (2019).

$$\frac{1}{4}-\frac{1}{2}q-\frac{1}{8}q^2+\frac{1}{32}q^3-\frac{1}{384}q^4 \leq p \leq \frac{1}{4}+\frac{1}{2}q \tag{6.9}$$

$$\frac{\zeta\omega_n}{\omega_e} < q.k_1.k_2\sqrt{1-{k_3}^2} \tag{6.10}$$

$$\text{where } k_1 = 1-0.1875q^2$$
$$k_2 = 1{,}002p + 0.16q + 0.759$$
$$k_3 = \frac{q^2-16+\sqrt{q^4+352q^2+1024p}}{16q}$$

6.3. Results and Discussion

6.3.1. Accuracy and Numerical Uncertainty of the CFD Model

The accuracy of the CFD model was established by comparing the CFD-based results to the experimental data. To conduct the accuracy study, the experimental results from the KCS model, such as the parametric roll amplitude or seakeeping results are needed. Then, the CFD set-up applied for KCS can be used for the fishing vessel with the slight adjustment due to different size between KCS and Fishing vessel.

For parametric roll accuracy study, the 1:100 scale KCS model was used with L_{bp} = 2.3 m in parametric roll condition (v= 0.4 m/s, λ/Lbp = 1.0, and H/λ = 0.02). The reference is made to Yu et al. (2018) and Yu et al. (2019), since they provided the experimental data that can be used to compare the numerical results obtained in this study with their experimental results. The body plan of KCS is shown in Figure 6.4. The main dimension of KCS model and simulation conditions are shown in Table 6.4.

The Grid Convergence Index (GCI) method was used to conduct the uncertainty study. This approach is based on the Richardson extrapolation (1911) as described by Celik et al. (2008). At least three solutions should be evaluated in terms of convergence behaviour. In this research, both grid and time uncertainty were conducted in the same simulation with different refinement, namely coarse, medium, and fine configurations. This approach aligns with recommendations made by Burmester et al. (2020) and ensures that the achieved Courant number remains consistent across the solution triplet. In addition, the number of near-wall layers remains constant across the solution triplet while the distance over which near-wall layers are distributed is magnified accordingly to maintain the cell aspect ratio of all cells. The fine configuration was coarsened in terms of both for grid and time step simultaneously through the refinement ratio of $r_{21} = 1.23$ and the medium configuration was coarsened again into the coarse configuration by multiplying by the refinement ratio $r_{32} = 1.24$, following to Ravenna et al. (2022). It should be noted that the remaining simulations in this study used the fine configuration.

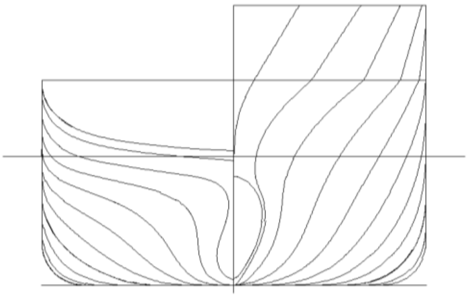

Figure 6.4. Body plan of the KCS

Table 6.4. Main dimensions of the KCS model (1:100) and simulation conditions

Parameters	**Value**
Length between perpendicular, L_{bp} (m)	2.3
Breadth at water line, *B* (m)	0.322
Depth, *D* (m)	0.19
Loaded draft, *T* (m)	0.108
Displacement (kg)	52.31
Longitudinal Centre of Buoyancy (*LCB*) From *AP* (m)	1.116
Height of Centre of Gravity, *KG* (m)	0.1366
Metacentric height, *GM* (m)	0.0127
K_{xx}/B, K_{yy}/L_{bp}, K_{zz}/L_{bp}	0.3242, 0.2495, 0.2465
Roll natural period, T_n (s)	2.16
Simulation Condition	
V (m/s)	0.40
Wavelength, λ/L_{bp}	1.00
Wave height, H_w/ wavelength, λ	0.02
T_e/T_n	0.464

Once three solutions are obtained, the difference between medium-fine and coarse-medium can be obtained using Eq. (6.11) and Eq. (6.12), where S_1, S_2, and S_3 are the solution for fine, medium, and coarse configurations, respectively. Then, the convergence ratio, R, can be calculated using Eq. (6.13). The value of convergence ratio categorizes the behaviour of the simulation with refinement into three types, monotonic convergence (0<R<1), oscillatory convergence (-1<R<0), and divergence (|R|>1). The order of accuracy, p, then can be calculated using Eq. (6.14) iteratively, where r_{21} and r_{32} represent the medium-fine and coarse-medium refinement ratios, respectively. Finally, the GCI can be estimated based on Celik et al. (2008) by using Eq. (6.15).

$$\varepsilon_{21} = S_2 - S_1 \tag{6.11}$$

$$\varepsilon_{32} = S_3 - S_2 \tag{6.12}$$

$$R = \frac{\varepsilon_{21}}{\varepsilon_{32}} \tag{6.13}$$

$$p = \frac{1}{\ln r_{21}} \left| \ln \left| \frac{\varepsilon_{32}}{\varepsilon_{21}} \right| + q(p) \right| \tag{6.14}$$

where $q(p) = \ln\left(\left(r_{21}^{p} - s\right)/\left(r_{32}^{p} - s\right)\right)$, and $s = \operatorname{sgn}(\varepsilon_{32}/\varepsilon_{21})$

$$GCI = 1.25 \left| \frac{S_1 - S_2}{S_1} \right| / \left(r_{21}^{p} - 1\right) \tag{6.15}$$

6.3.1.1. Accuracy Study Results

A different wall treatment was used to investigate the viscous effect's influence on the amplitude of roll during parametric roll motions. Two y^+ values were used, y^+ = 30-100 and y^+<1. A varying number of near-wall layers, including a single layer and 12 layers, were implemented on the hull to obtain the different y^+ values. The fine mesh configurations for two different total number of layers are shown in Figure 6.5.

The averaged y^+ values obtained for the wetted surface area of the hull are presented in Figure 6.6. The single layer configuration resulted in a range of y^+ values between 40-55, while the 12-layer configuration produced values of y^+ less than 1. The distribution of y^+ the wetted surface area is presented in Figure 6.6. As stated previously, selecting different y^+ value can affect the wall function implemented for turbulence resolution. Specifically, when y^+ was between 30 -100, the logarithmic law region was employed to solve the boundary layer around the hull. In contrast, a viscous sublayer region was used when y^+ was less than 1.

The time series results of the roll amplitude obtained from the CFD simulation are shown in Figure 6.7-a. Different y^+ configurations were also compared to the experimental data from (Yu et al., 2019, 2018). The comparison with the experimental data is only based on the roll amplitude, as no time series data is available for other modes of motion for this test simulation. Then, the last three cycles from the present CFD results were used to determine the amplitude and frequency of the harmonic responses, as shown in Figure 6.7-b. The last three cycles were selected where the oscillations are periodically repeating.

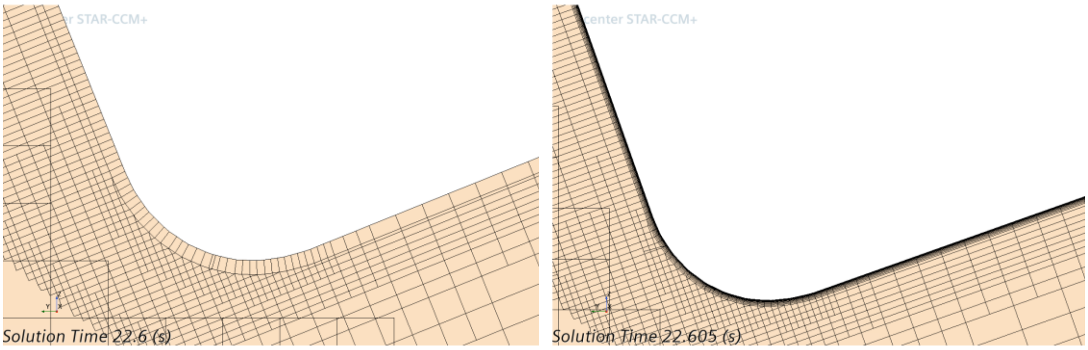

Fine Configuration – 1 Prism Layer

Fine Configuration – 12 Prism Layers

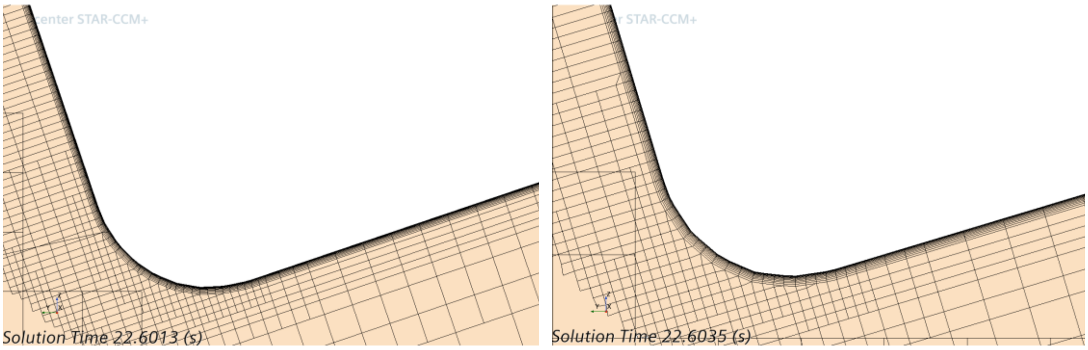

Medium Configuration – 12 Prism Layers

Coarse Configuration – 12 Prism Layers

Figure 6.5. Near wall prism layer for different configuration set-up

Table 6.5. Comparison of roll amplitude for different y^+ values

Parametric Roll Results	**$y^+ > 30$**	**$y^+ < 1$**
CFD	28.77°	23.77°
EFD (Yu et al., 2018) and (Yu et al., 2019)	24.68°	24.68°
Error (%)	16.33	-3.66

The comparison results are shown in Table 6.5 which reveals that viscous effects influence the roll amplitude. The steady roll amplitude of $y^+ < 1$ configuration is more accurate compared to y^+ values between 30 – 100 with a difference from the experimental result of only –3.66%. In contrast, a significant difference from the experimental results is shown when y^+ is between 30 -100, which is 16.33%. Based on these results, it can be concluded that the parametric roll is sensitive to the y^+value. Therefore, the $y^+< 1$ configuration was used for all fishing boat simulation in this study.

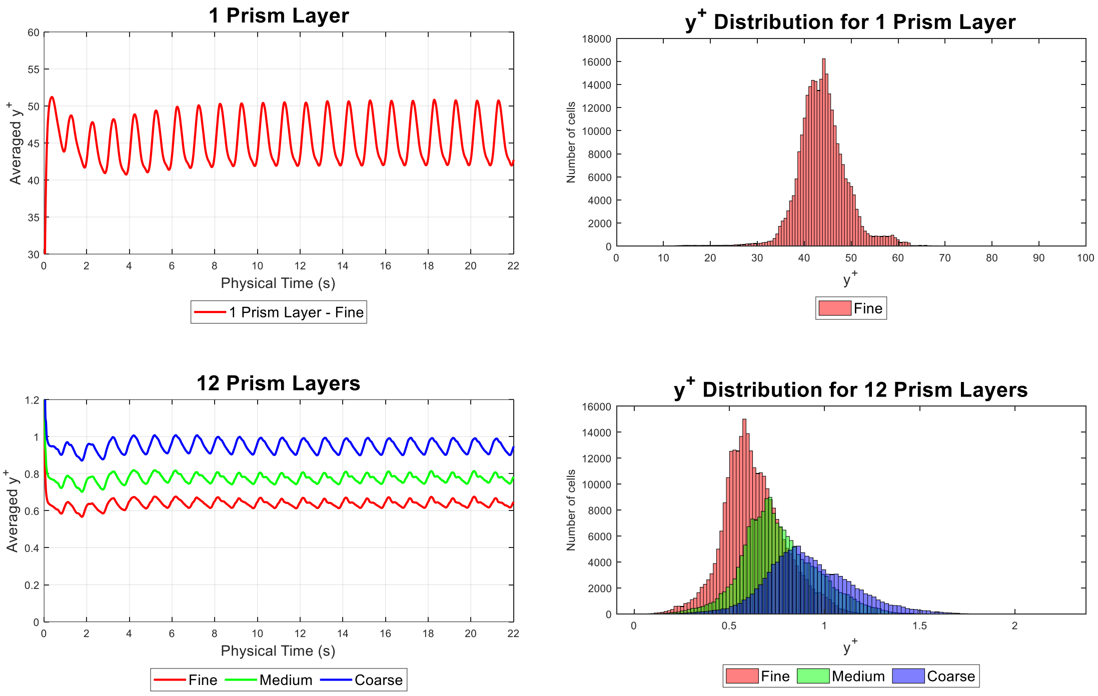

(a) (b)

Figure 6.6. The results of average y^+ and y^+ distribution on wetted surface for different configuration set-up

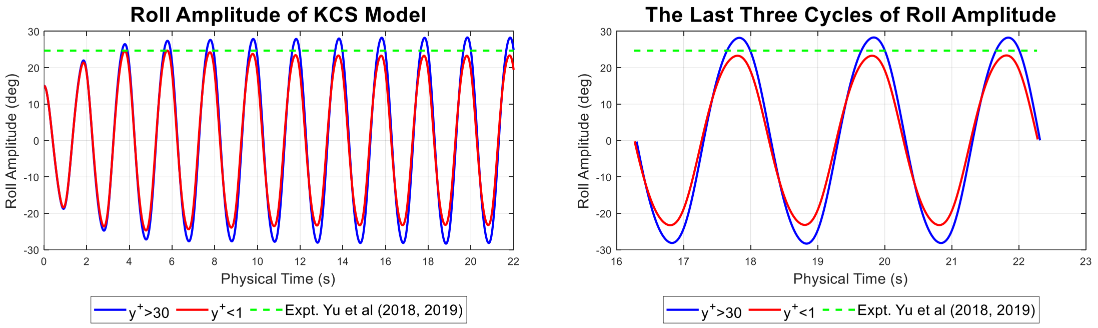

(a) (b)

Figure 6.7. Roll amplitude of 2.3 m KCS model under parametric roll (a) and the last three cycles of steady roll amplitude (b)

6.3.1.2. Numerical Uncertainty Study Results

In order to perform the Grid Convergence Index (GCI) for uncertainty study, the fine mesh configuration with 12 prism layers was coarsened in mesh size and time step to create the medium and coarse configurations. The roll amplitude was calculated for each configuration and used in the GCI calculation. Figure 6.5 shows the result of the mesh near the hull surface. With the same number of prism layers, the coarsening of the mesh size resulted in an increase in the y^+ value, as demonstrated in Figure 6.6. However, the y^+ value for the coarse configuration remained below 1. The last three cycles for all configurations are presented in Figure 6.8. The roll amplitude for all configurations is described in Table 6.6 and was used in the verification study for GCI calculation.

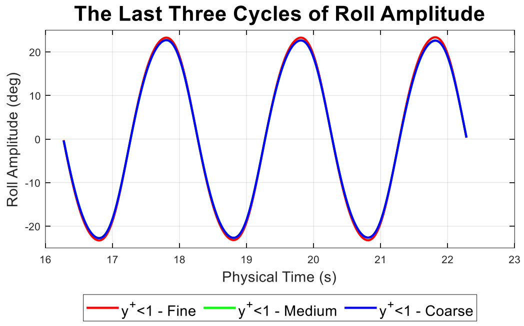

Figure 6.8. The last three cycles for all configurations

Table 6.6 presents the results of the verification study, which involved coarsening both the mesh and time step. With $s = 1$, $q(p)$ can be obtained after three iterations and resulted in $q(p) = -0.0562$. The GCI value obtained from this study was 2.76%, which is considered small since it is below the threshold of 5%. The numerical error was found to be -3.66% when compared to the experimental results as indicated in Table 6.5. Therefore, the verification and error comparison studies demonstrated that the numerical error was within acceptable limits. Consequently, the numerical set up was used to perform a parametric simulation of a small fishing boat in this study.

Table 6.6. Uncertainty study results

Parameter	**Symbol**	**Value**
Fine Configuration	N_1	Total mesh = 13,305,894; Time step = 0.005000
Medium Configuration	N_2	Total mesh = 8,479,668; Time step = 0.006150
Coarse Configuration	N_3	Total mesh = 5,544,893; Time step = 0.007626
Refinement ratio	r_{21}	1.23
Refinement ratio	r_{32}	1.24
Fine solution	S_1	23.7698°
Medium solution	S_2	23.1206°
Coarse solution	S_3	21.5843°
Medium-Fine	ε_{21}	−0.6492°
Coarse-Medium	ε_{32}	−1.5363°
Convergence ratio	R	0.4226 (Monotonic, 0<R<1)
Order of accuracy	p	3.8893
GCI	GCI	2.76%

6.3.1.3. The Viscous Effect

A qualitative analysis of the CFD results following the quantitative discussion in the previous section is presented next. Figure 6.9 displays the wave elevation contour from different CFD configurations at the same physical time (22.6 s) and scale (-0.0623 m to 0.126 m). The impact of different y^+ values on the fine configuration is evident from the figure. Despite a higher roll amplitude for $y^+ > 30$, water on the deck did not appear. Conversely, water on the deck was observed when y^+ less than 1 was used for the medium and coarse configurations. The viscous effect near the hull surface, particularly on the deck, were prominently noticeable between different y^+ values.

Figure 6.10 illustrates the velocity magnitude of each configuration at the same physical time (22.6 s) and the same scale, ranging from 0 m/s to 0.5 m/s. It is evident that the total number of near-wall layers significantly impacts the velocity magnitude close to the hull. Specifically, for $y^+ < 1$ with 12 layers, the velocity is smoothly captured, particularly near the bilge area. On the other hand, the thickness of the colour layer around the hull for $y^+ > 30$ (single prism layer) is greater, dominated by a single value, and the degradation of velocity cannot be accurately captured despite using a logarithmic law region in that single near-wall layer.

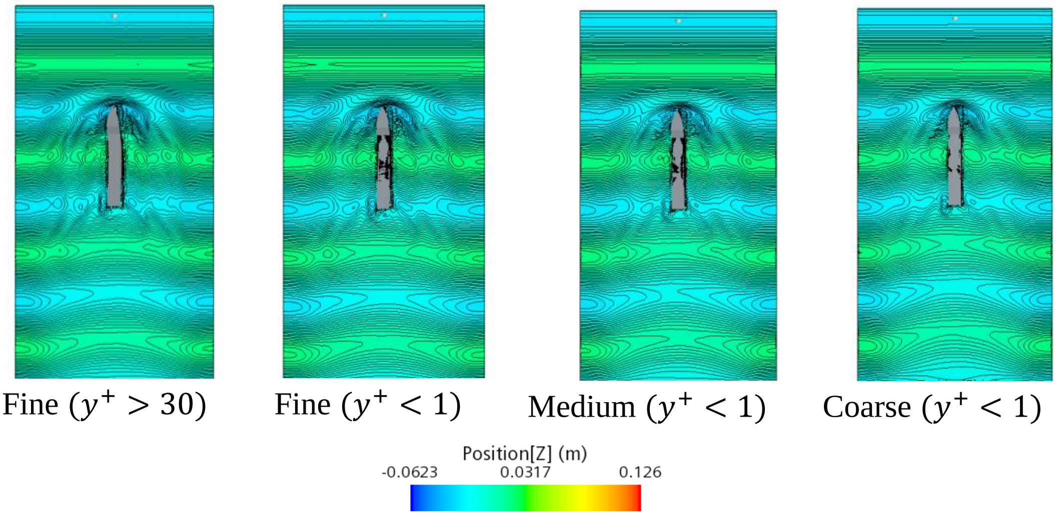

Fine ($y^+ > 30$) Fine ($y^+ < 1$) Medium ($y^+ < 1$) Coarse ($y^+ < 1$)

Figure 6.9. Wave elevation contour for different configuration. In all cases, the solution time is equal to 22.6s.

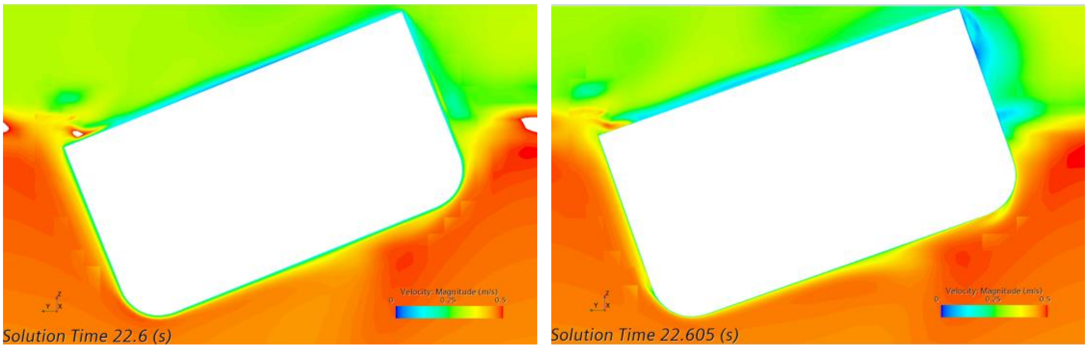

Fine (y^+>30) Fine (y^+<1)

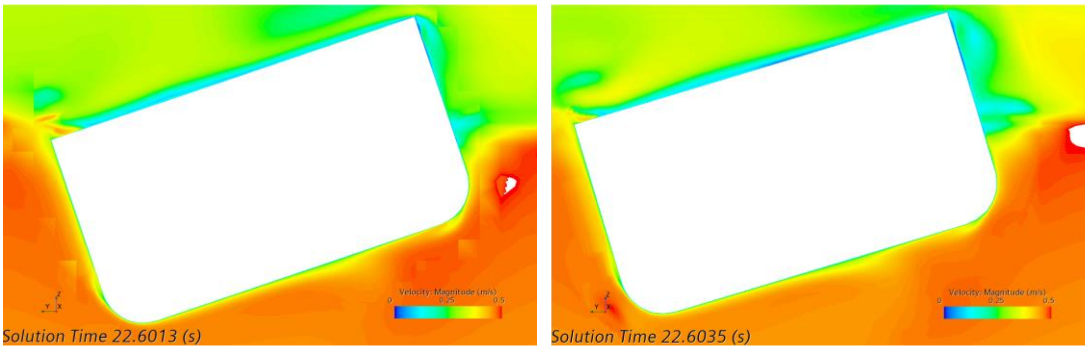

Medium (y^+<1) Coarse (y^+<1)

Figure 6.10. CFD results of velocity magnitude for different configuration

When 12 prism layers were applied, the low velocity area near the no-slip boundary condition of the hull thins and exhibited a greater variation in velocity values. This means the different velocities around the hull can be captured well. The low y^+ approach yields a better agreement with the experimental results, as shown in Table 6.5. Therefore, it is important to maintain $y^+ < 1$ to produce the good result in the CFD simulation. As explained earlier in Figure 6.1 (flow chart) in this study, this fine configuration was applied to other CFD simulations which are roll decay simulations to determine the ratio of linear roll damping and direct CFD simulations of small fishing boat on parametric roll.

6.3.2. Susceptibility Assessment Results

6.3.2.1. Roll Damping Results

Figure 6.11 shows the result of roll decay simulations in each load case. The linear roll damping ratio (B/B_c), which is the ratio of roll damping to critical roll damping, was determined from the roll amplitude decrement. This can be described in the exponential equation $(e^{-\zeta\omega_n t})$, which is similar to μ in Eq. (6.6). The term μ in Eq. (6.6) consists of $\zeta\omega_n$, where ζ is the ratio between the linear roll damping and critical roll damping $(B/B_c)$and ω_n is natural roll frequency in rad/s. Once μ is determined from the regression, which is shown in Figure 6.11, the ratio of linear roll damping, ζ can be determined by dividing μ by ω_n.

The present study provides the linear roll damping ratio results in Table 6.7. To benchmark the numerical results, these values were compared with those obtained from the Ikeda's method, which is an empirical method provided in the ShipX software. As seen in Table 6.7, the comparison between the CFD and the Ikeda's method results shows a sufficient similarity, considering the approximate nature of the Ikeda's method.

The ratio of roll damping, ζ from ShipX, was calculated using the critical roll damping, B_c, which is defined as $B_c = 2(I_{xx} + (I_{xx})_a)f_n$ (kg.m/s), where I_{xx} is the moment of inertia of roll and $(I_{xx})_a$ is added moment of inertia of roll, and f_n is the natural roll frequency (1/s). Both moment of inertia values as well as the roll damping, B are taken from ShipX. As shown in Table 6.7, irrespective of the vertical load position, the roll damping, B, increased with displacement (LC 1, LC2 -LC3, and LC4-LC5).

However, the values of the linear roll damping ratio, ζ, varied for each load case, indicating that the vertical load position impacted the critical damping, B_c. As shown in Table 6.7, the moment of inertia of roll, I_{xx}, differed in each load case, while the added moment of inertia, $(I_{xx})_a$, was the same for the same displacement. This implies that the ratio of the linear roll damping, ζ, was affected by the different loading conditions, with the vertical load position playing a crucial role in this change. Unlike B and $(I_{xx})_a$, which are only influenced by displacement, the vertical loading position influenced the roll radius of gyration, k_{xx}, resulting in varying values of the moment of inertia of roll, I_{xx}, even when the displacement was the same.

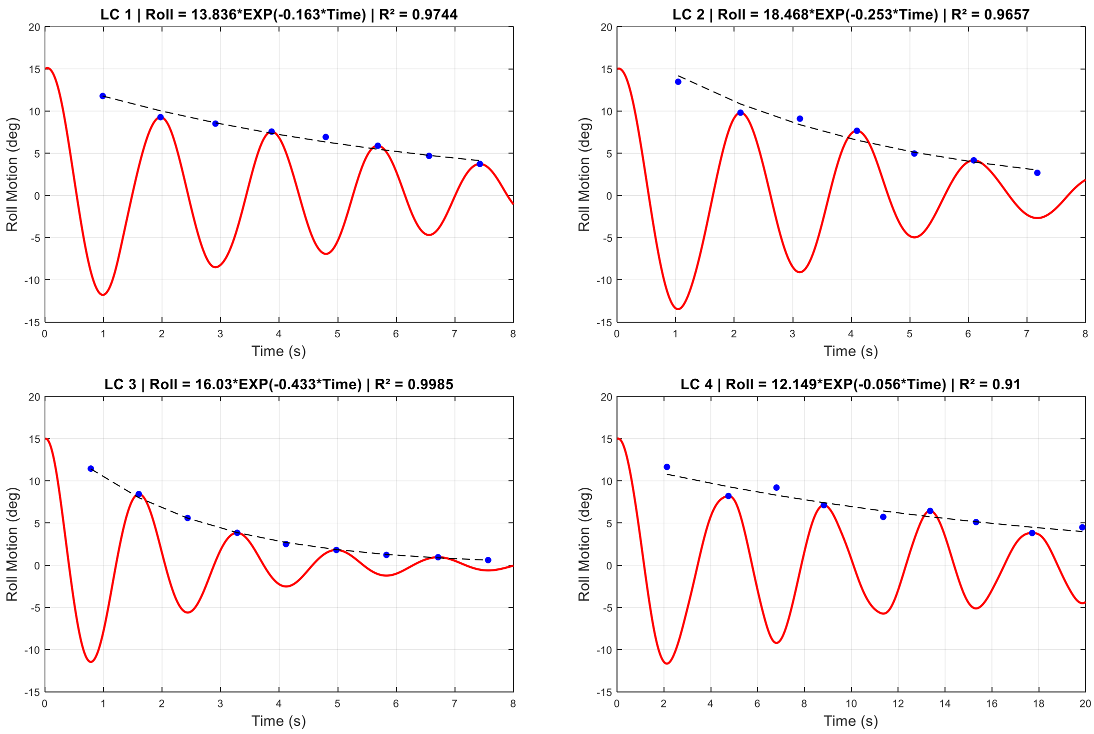

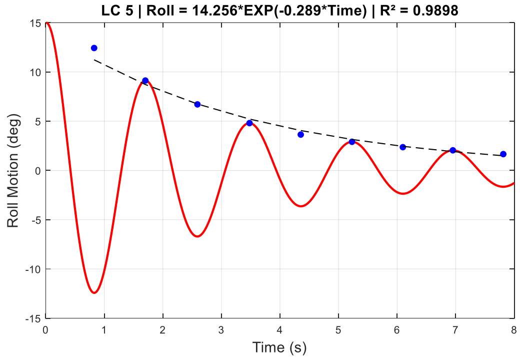

Figure 6.11. Exponential equation in determining the damping ratio (ζ) for all load cases

Table 6.7. Comparison of the linear roll damping between the CFD and Ikeda's method

Load Case	**ShipX Calculation (Ikeda's method)**			**Roll Damping Ratio Calculation**			**CFD Linear Roll Damping Ratio**			**Difference (%)**
	Ixx (kg.m^2)	**Ixx$_{add}$ (kg.m^2)**	**B (kg.m^2/s)**	**fn (1/s)**	**Bc (kg.m^2/s)**	**ζ (B/Bc)**	μ (Figure 6.11)	**ωn**	**ζ (μ/ωn)**	
1	637.00	337.00	692.28	4.93	9608.12	0.07	0.163	3.14	0.05	-27.8
2	1160.00	441.00	1064.80	4.93	15793.23	0.07	0.253	3.14	0.08	20.1
3	509.00	441.00	1067.30	6.17	11729.14	0.09	0.433	3.93	0.11	20.9
4	2130.00	456.00	1241.10	2.26	11698.79	0.11	0.056	1.44	0.04	-63.2
5	675.00	456.00	1243.40	6.28	14212.57	0.09	0.289	4.00	0.07	-17.7

The ratio of roll damping value obtained from the CFD simulation was used to assess the susceptibility criteria of parametric roll according to ABS' rules (2019). If the ratio is unknown, the ABS guidelines recommend using the following range of roll damping ratios: $\mu = 0.03, 0.05, 0.075, 0.10$. However, the values obtained from the roll decay CFD simulation in this study were found to be better than using the range of μ recommended by ABS. The accuracy in determining this coefficient is important for assessing the susceptibility criteria, especially in criterion 2 (Eq. (6.10)), where the effective roll damping is evaluated to determine whether it exceeds the threshold.

6.3.2.2. Susceptibility criteria assessment results

Table 6.8 shows the results of the susceptibility criteria analysis for the vessel. Criterion 1 is satisfied for all load cases, as shown in Figure 6.12, indicating that the vessel has the potential to experience parametric roll. However, the vessel's behaviour depends on the effective damping, as shown in Criterion 2. If the effective damping is lower than the damping threshold (Eq. (6.10) is satisfied), then parametric roll is expected to occur.

Referring to the Susceptibility Criteria in Table 6.8, load cases 3 and 5 have a higher effective damping roll than the damping threshold, which means that the parametric roll is not expected to occur in these load cases. Other load cases (LC 1, LC 2, and LC 4) are predicted to experience parametric roll because Criterion 2 was satisfied. In these conditions the roll damping in each load case is lower than that damping threshold. Because the roll damping is below the threshold, the roll damping is not high enough to reduce the roll motions significantly caused by the periodic variation of the restoring roll moment.

The prediction of PR occurrence in the early stage has been carried out by using two different methods. First, level 1 assessment of PR from Second Generation of Intact Stability IMO and second, the Susceptibility Criteria of Parametric Roll from ABS. Both assessment methods give the same results, whereas LC 3 and LC 5 do not result in parametric roll. Nevertheless, the amplitude of parametric roll of suspected load case is still to be confirmed by carrying out the CFD simulations. The following sub-section will discuss the results of direct CFD simulation of PR for the small fishing vessel.

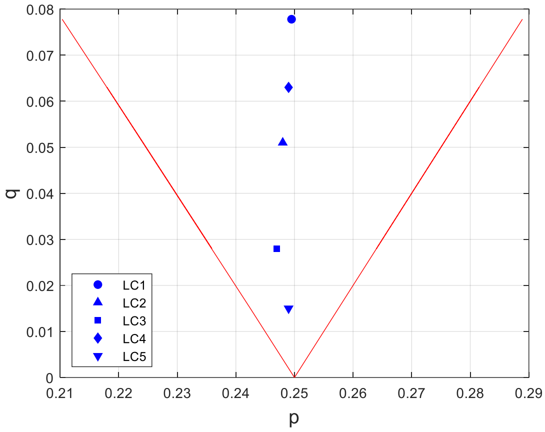

Figure 6.12. Result of criterion 1 of susceptibility criteria

Table 6.8. The results of the susceptibility criteria

Load Case	**Criterion 1**			**Criterion 2**		
	p	**q**	**Eq. (6.9)**	**Effective Damping**	**Damping Threshold**	**Eq. (6.10)**
1	0.249	0.078	Satisfied	0.025	0.079	Satisfied
2	0.248	0.051	Satisfied	0.049	0.052	Satisfied
3	0.247	0.028	Satisfied	0.061	0.028	Not Satisfied
4	0.249	0.063	Satisfied	0.017	0.064	Satisfied
5	0.249	0.015	Satisfied	0.037	0.015	Not Satisfied

6.3.3. CFD Results for Parametric Roll Simulation

6.3.3.1. Results of Averaged y^+

Figure 6.13 shows the results of averaged y^+ on the wetted surface area for all load cases. As can be seen in the figure that all averaged y^+ are below 1. The determination of the total number of layers was successful in achieving the targeted y^+ value

($y^+_{target} = 0.7$) which was also used when studying the KCS hull performance. This is used as an indication that the velocity gradient near the wall is captured. The determination of the total number of layers for all load cases (except LC 4) used the highest speed only (speed for LC 3) and resulted in 17 layers. Then, with the same total number of layers, the averaged y^+ in each load case are varying because the different speeds result in different y^+. The lower speeds resulted in a lower averaged y^+. Nevertheless, the average values are always y^+<1.

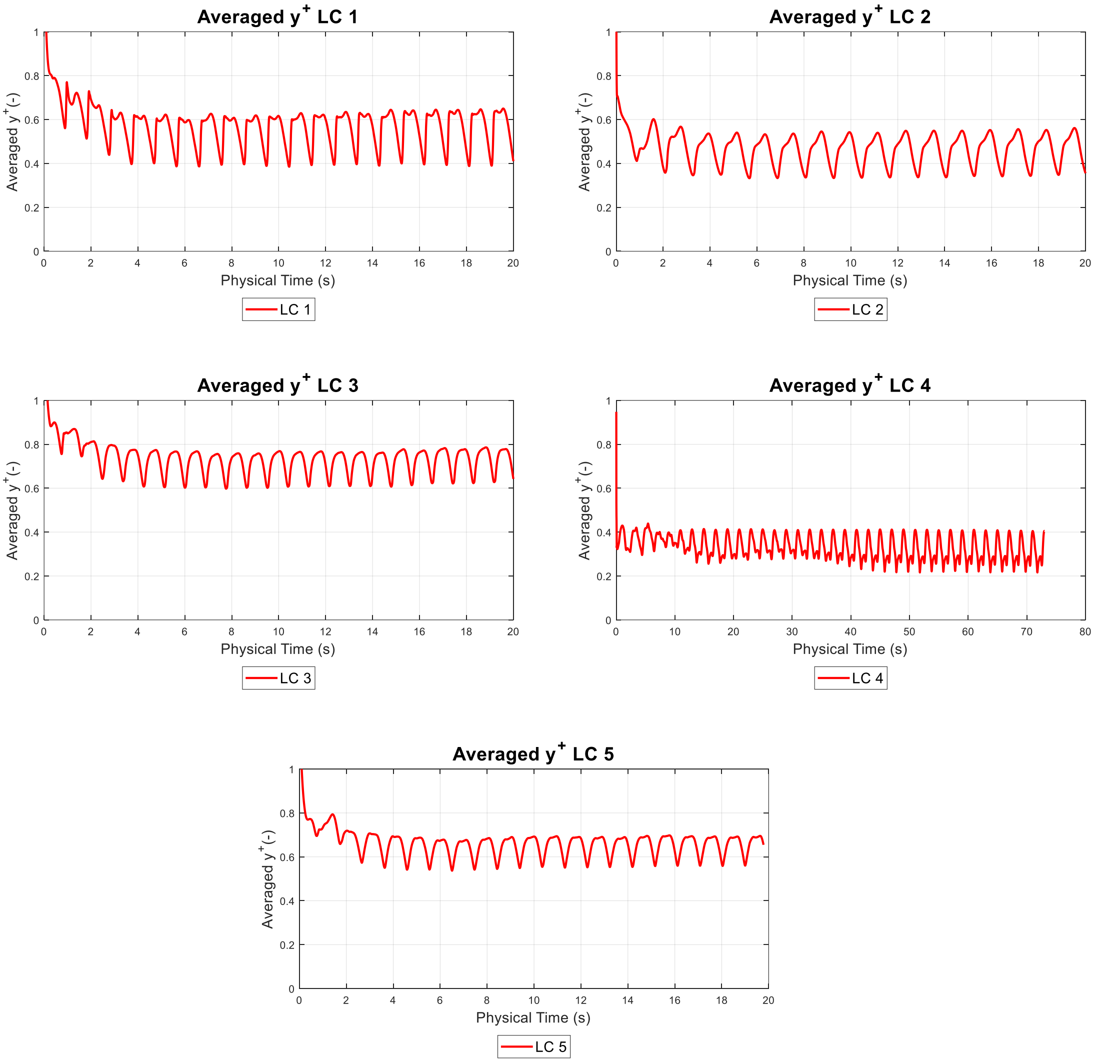
Averaged y^+ LC 1

Averaged y^+ LC 2

Averaged y^+ LC 3

Averaged y^+ LC 4

Averaged y^+ LC 5

Figure 6.13. Results of averaged y^+ for different load cases

6.3.3.2. Parametric Roll Amplitude

Figure 6.14 and Figure 6.15 present the outcomes of CFD modelling for the various load cases (LC 1 to LC 5) under a presumed state of parametric roll. To hasten the occurrence of the roll phenomenon, the vessel was initially inclined at 15° and sailed under specific wave and velocity conditions as detailed in Table 6.3. It should be noted that the initial roll angle did not impact the parametric roll amplitude results obtained, as reported by (Liu et al., 2021).

It is evident that LC 3 and LC 5 did not undergo parametric roll, as evidenced by the level 1 Second Generation of Intact Stability results in Table 6.3 and the susceptibility criteria presented in Table 6.8. The roll amplitude in these cases decreased rapidly and dissipated after 10 seconds of physical time. By contrast, for LC 2 and LC 4, parametric roll persisted with a small amplitude. Initially, after the boat was tilted 15°, there was some parametric roll with higher amplitude than in the previous cycles. However, once the roll amplitude became steady, LC 2 did not exhibit parametric roll, while LC 4 did. The highest roll amplitude was observed in LC 1. After the boat was released, the roll amplitude of LC 1 decreased very slowly, indicating that the roll amplitude did not differ significantly from the initial values.

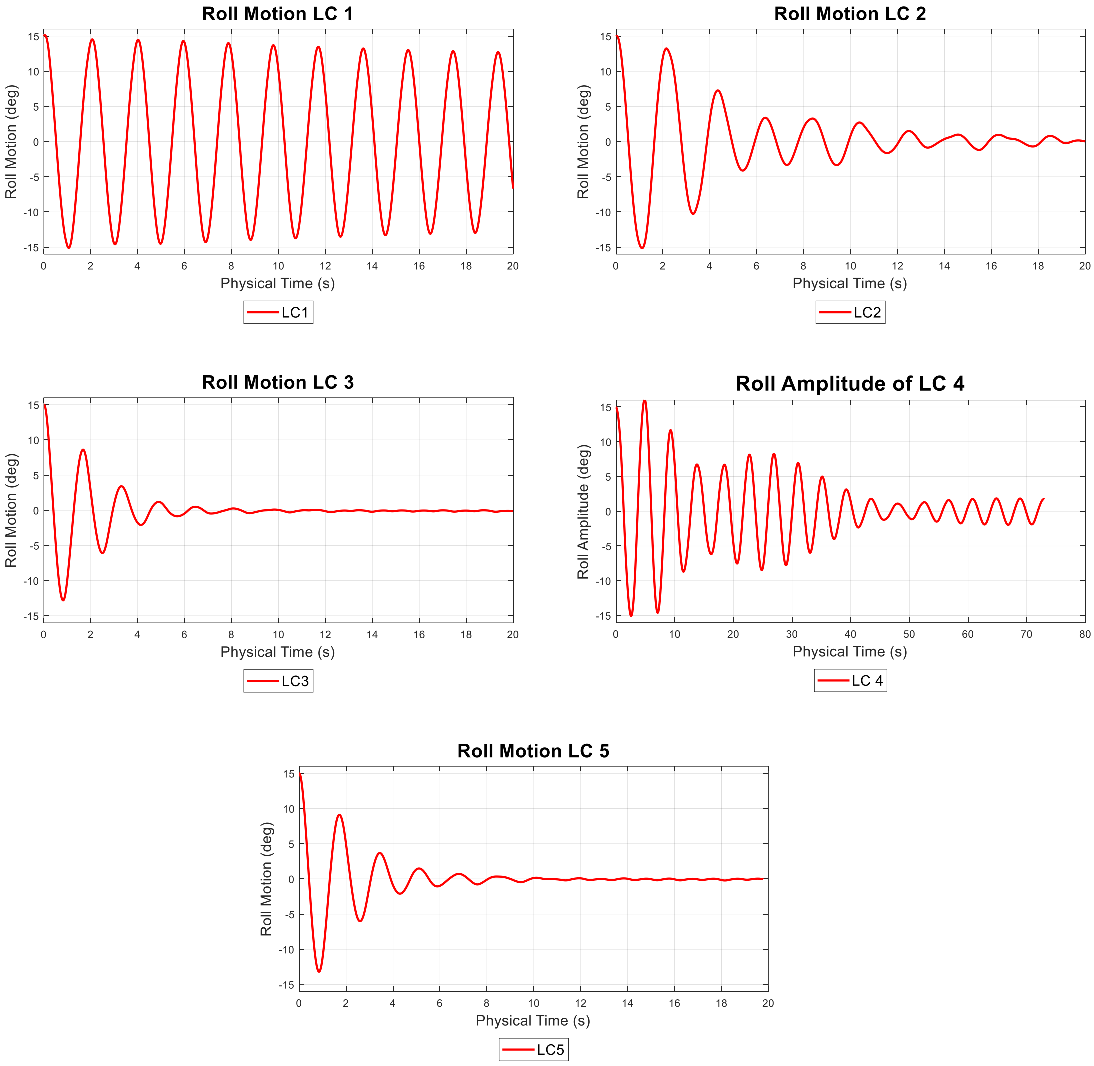

Figure 6.14. Results of roll amplitude on different loading condition

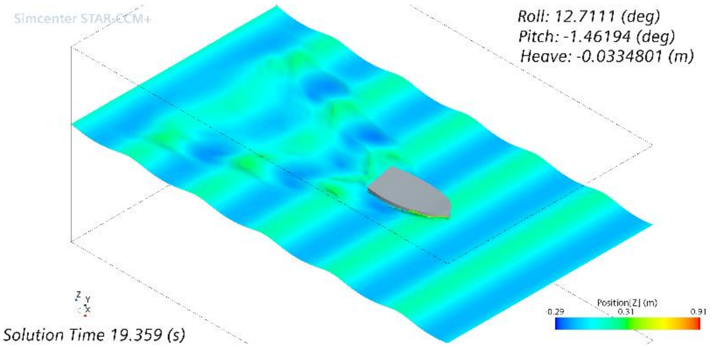

Load Case 1

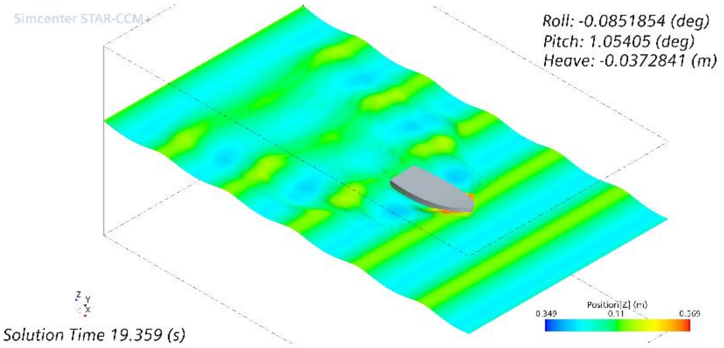

Load Case 2

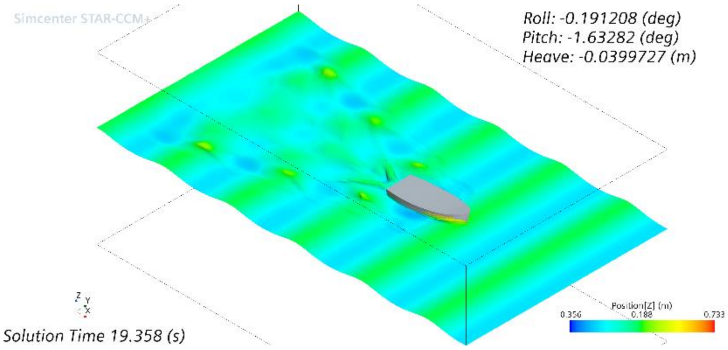

Load Case 3

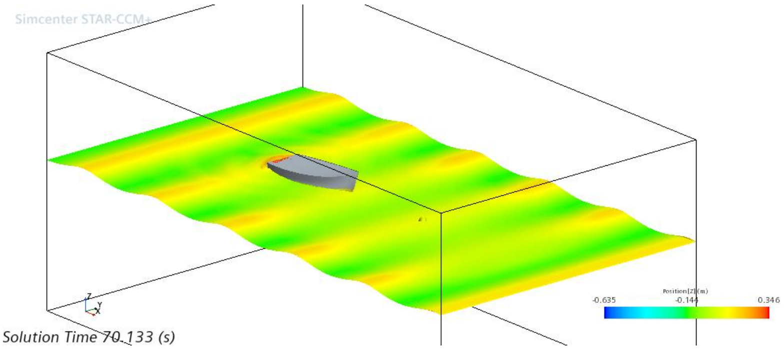

Load Case 4

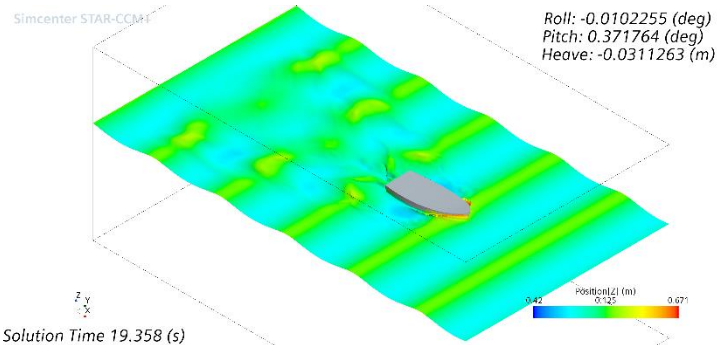

Load Case 5

Figure 6.15. The wave elevation results from CFD simulation

6.3.3.3. Roll, Pitch, and Heave Motions

The present chapter utilised a coordinate system, where the X-direction coincides with the length of the boat. A positive X-direction represents the direction towards the bow. With regards to rotational motion, the positive value is equivalent to a clockwise direction. For X-direction rotational motion (roll motion), a positive value indicates that the boat is rolling towards the starboard side. Conversely, in the case of pitch motion, a positive Y-direction represents the direction towards the port side, and a negative Y-direction represents the starboard side. Thus, when the boat rotates in a positive Y-direction, it will pitch downwards from the bow.

The results of roll, pitch, and heave amplitude are shown in Table 6.9. Based on the results, it can be inferred that the largest parametric roll amplitude occurs in LC 1, which is 12.7556°. The second one is LC 4 which has a roll amplitude of 1.8376°. The other load cases are considered to have no parametric roll, as their roll amplitude is close to 0°.

Table 6.9. Results of roll, pitch, and heave motion

Load Case	**Roll (deg)**		**Pitch (deg)**		**Heave (m)**	
	Mean	**Amplitude**	**Mean**	**Amplitude**	**Mean**	**Amplitude**
1	-0.11644	12.7556	-3.0536	1.9458	-0.017479	0.029679
2	0.15217	0.7756	-1.5018	2.9968	-0.00756	0.038771
3	-0.094458	0.031794	-2.6677	1.1569	-0.038993	0.014939
4	-0.022276	1.8376	-0.98283	5.0395	-0.009717	0.056559
5	-0.063592	0.024213	-0.70197	1.2305	-0.021113	0.018813

Among the five load cases, only LC 1 can be considered dangerous due to the occurrence of parametric roll. Table 6.3 indicates that all load cases are simulated with similar relative wave conditions, and that the speeds for LC 1, LC 3, and LC 5 are also similar at around 2 m/s. Despite these similarities, there are differences in the roll motion response among these load cases. Specifically, LC 1 shows a considerable roll amplitude, while LC 3 and LC 5 do not. This implies that the different loading conditions are sensitive to the parametric roll behaviour.

Based on Table 6.9, there is no correlation between the amplitude of roll to the pitch motion. The highest roll amplitude (LC 1) has the lowest pitch motion amplitude (1.94°), while LC 4 results in a pitch angle of 5.04°. This shows no correlation between roll and pitch motion amplitudes when the boat moves in head waves. The roll-heave correlation is similar to the roll-pitch correlation. It can also be seen in Table 6.9 that the order from the highest to the lowest for heave motions is the same as for pitch motions. LC 4, which results in the highest heave motions, also results in the highest pitch motions and so for the lowest heave and pitch that occurred on LC 3.

The correlations between roll, and pitch/heave motions during parametric roll phenomenon can be explained by examining the cycles of each mode of motion. Specifically, pitch and heave motions complete two cycles for each roll cycle. The total number of cycles roll, and pitch/heave can then be used to establish their relationship. Figure 6.16 shows that parametric roll occurs when the total cycle of pitch/heave is approximately twice that of roll.

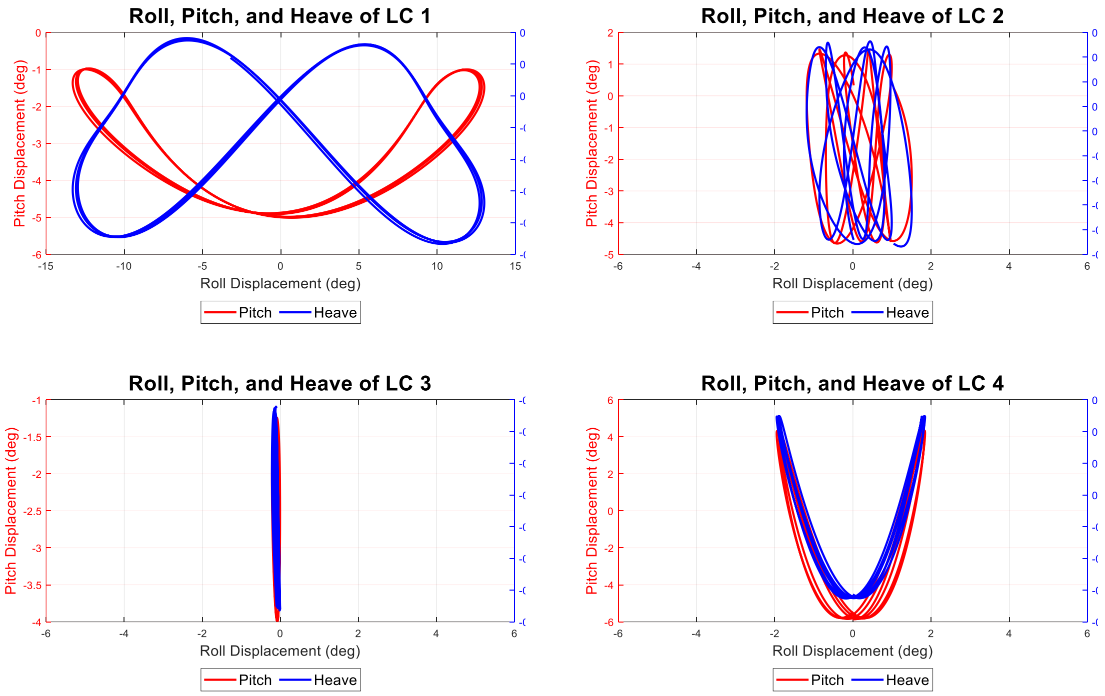

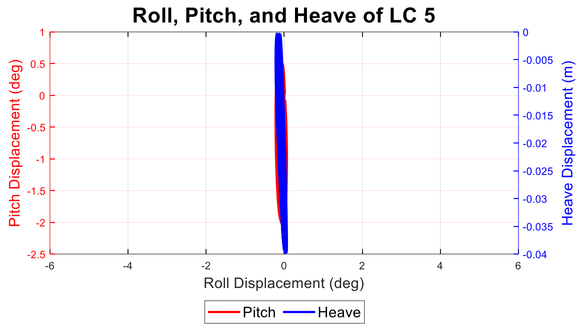

Figure 6.16. Roll, pitch, and heave displacement of all load cases

Figure 6.16 illustrates a comparison between the motion of roll-pitch and roll-heave for LC 1 to LC 5. The graph presents a vertical line for the load cases, such as LC 3, LC 5, and LC 2, where the boat did not experience parametric roll. In contrast, for LC 1 and LC 4, which experienced the parametric roll, it can be observed that pitch and heave underwent two cycles during one cycle of roll motion. This is a typical feature of parametric roll, where the encounter wave period is twice as roll natural period. Heave and pitch have the same period as the encounter waves in head waves.

Examining Figure 6.16 for LC 1, it can be seen that with the same roll angle, there are two different displacement values for both heave and pitch, but this does not mean that the boat experienced two different heave and pitch displacements simultaneously. It should be noted that Figure 6.16 only compares the displacement behaviour between roll-pitch and roll-heave and the figure is not time-dependent. This can be explained well in Figure 6.17 when the time series of roll-pitch and roll-heave of LC 1 are shown. Based on Figure 6.17, it is clearly shown that with the same roll angle (5°), the displacement of heave and pitch are different because there is a different physical time in the same roll angle (5°). Each physical time has a different displacement for both heave and pitch.

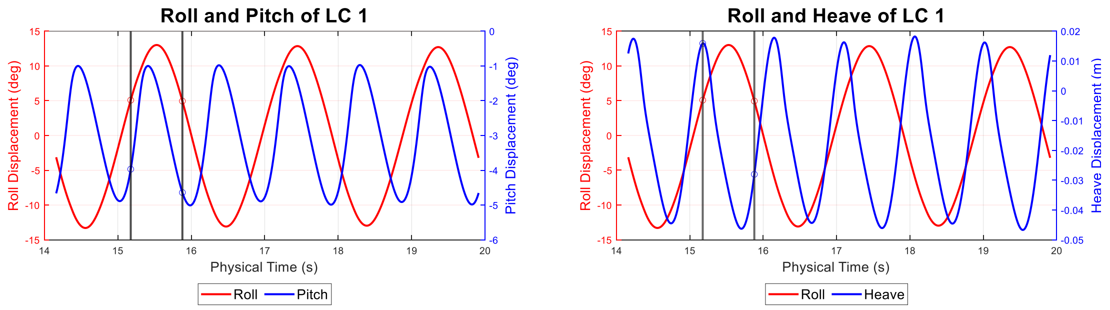

Figure 6.17. The comparison of roll-pitch and roll-heave in time series

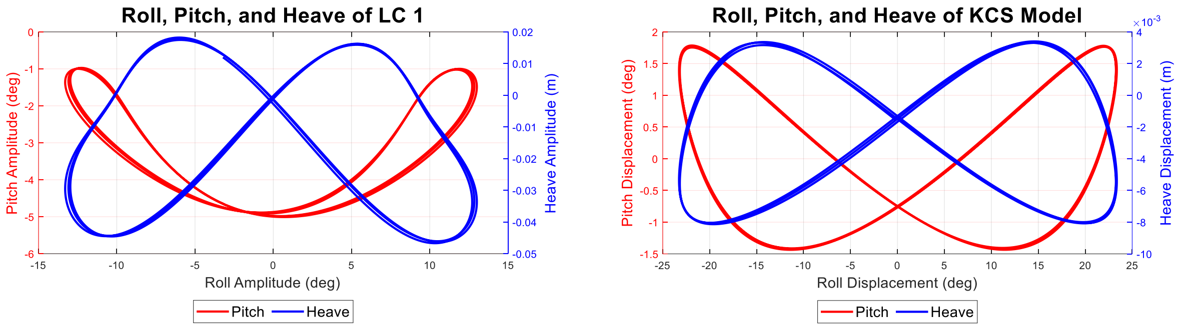

Figure 6.18. The comparison of Roll, Pitch, and Heave motion of LC 1 and KCS model

Figure 6.18 shows the phase portrait of the roll, pitch, and heave motion between LC 1 and the KCS model, which serves as the verification study. Both conditions demonstrate the parametric roll phenomenon, with two cycles of pitch and heave in each cycle of the roll. The heave motion of LC1 and KCS model attain their highest and lowest values at half and maximum roll. For example, LC 1's highest and lowest heave occurred at a roll of around 6° and 12°, respectively. In comparison, the KCS model's highest and lowest heave occurred at a roll of approximately 12° and 24°, respectively. However, the pattern for the pitch motion is different. The KCS model follows the same pattern as the heave motion for the maximum and minimum pitch. In contrast, the fishing boat exhibits a distinct minimum pitch pattern, which appears at a roll of less than about 6°.

6.3.4. The Influence Loading Condition

Changes in the loading condition of a fishing vessel often occur during operation. As discussed in the background section, various factors can affect parametric rolling, including *GM* Ratio and flare shape. The subsequent subsection investigates the extent to which changes in loading condition impact *GM* Ratio and flare shape, ultimately affecting seakeeping and parametric rolling behaviour.

6.3.4.1. Flare Distribution

The *GM* Ratio is also influenced by the stern shape and the flare of stern and bow, as stated by Neves et al. (1999) and France et al (2003). Different loading conditions applied to a certain ship will result in a change in the draught of the boat. Thus, the submerged hull shape also changes significantly, especially for the V-shape hull, which is mostly common in fishing boats. This condition makes a different longitudinal distribution of half breadth (*Y*) and flare (*dY/dZ*) at the water line, as shown in Figure 6.19.

Figure 6.19 describes the longitudinal distribution of the half breadth and flare at the water line for LC 1 and LC 5. LC 1 is the lightest weight and has the highest parametric roll amplitude. Conversely, LC 5 is the heaviest and has no parametric roll. Based on the figure, the half breadth distribution for both load cases is entirely different. Moreover, the V-shaped of hull form results in a significant change in flare distribution because of the low draught due to low displacement. As can be seen from Figure 6.19, the longitudinal position of LC 1 is characterised by a flare (dY/dZ) of more than 1. Unlike LC 5, which only has a flare of more than 1 at X/L_{bp} 0.6-0.85.

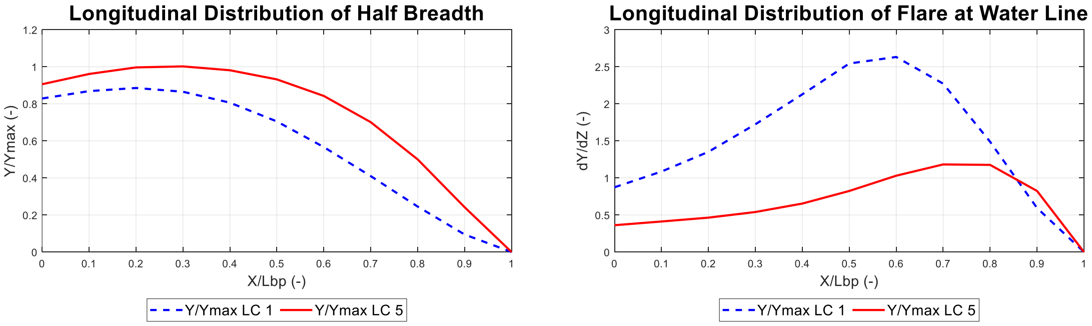

Figure 6.19. Longitudinal distribution of breadth and flare for different load case

As stated by Neves et al. (1999), the significant difference in the longitudinal distribution of flare influences the parametric roll amplitude. Furthermore, France et al. (2003) clarified this influence by comparing the flare angle from one station in the bow started from 0° to 40°. The value of 0° which means when there is no flare curve there is no PR, while the flare angle of 40° results in the highest PR amplitude. The results show that the hull shape above the water line significantly influences the PR. When the vessel is pitching and heaving, the high flare angle changes the buoyancy compared to the straight case which results in a GM variation.

6.3.4.2. GM Ratio

Figure 6.20 depicts the influence of displacement change on the KM value. The lowest displacement corresponds to LC 1, which indicates 100% fish tank capacity. Subsequently, the displacement decreases to 50% fish tank capacity for LC 2 and LC 3, and full load condition for LC 4 and LC 5. The graph illustrates a decreasing trend of KM with increasing displacement. LC 1 exhibits a GM/KM ratio of more than 0.4, while LC 2 and LC 3 are approximately 0.4 and 0.6, respectively. LC 4 and LC 5 show a GM/KM ratio of less than 0.2 and 0.6, respectively.

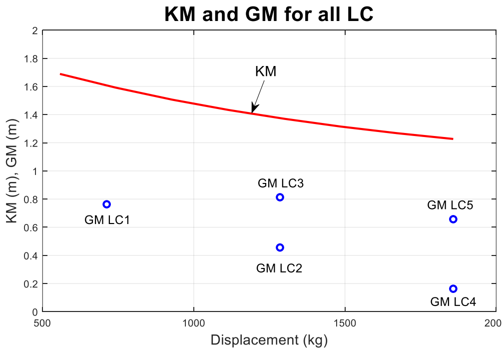

Figure 6.20. *KM* and *GM* change of small fishing boat regarding the displacement

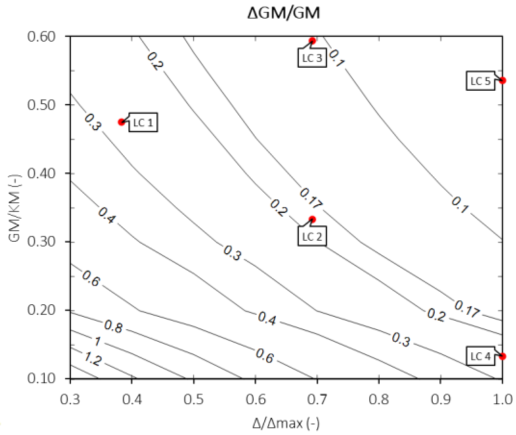

Figure 6.21. The influence of different loading conditions through the *GM* Ratio

Based on Figure 6.20, it can be seen that the actual *GM* between LC 1, LC 3, and LC 5 are relatively similar, but they are characterised by a different *GM*/*KM* ratio. The higher displacement cases have the higher *GM*/*KM* ratios. Following this, the *GM* Ratio ($\Delta GM/GM_{\mathrm{calm}}$), which is known as level 1 assessment of PR, was calculated from the combination of *GM*/*KM* ratios and displacement change (relative to the maximum displacement) to observe the influence of the loading conditions. The impact of changes in both the vertical loading position (*GM*/*KM* ratio) and displacement on *GM* Ratio is illustrated in Figure 6.21.

Figure 6.21 illustrates the impact of different loading conditions on *GM* Ratio in head waves with a wavelength of $\lambda = 5.0$ m and a wave height of Hw = 0.3 m. *GM* Ratio is a Level 1 assessment of parametric roll in the Second Generation of Intact Stability, as described in Eq. (6.2). The ratio of displacement to the maximum displacement represents the change in displacement, and the *GM*/*KM* ratio represents the change in vertical loading condition. The *GM* Ratio threshold (Rpr) for the ship without a bilge keel is 0.17. The figure also shows the *GM* Ratios for all load cases, which are taken from Table 6.3.

The trend in Figure 6.20 shows that at the same *GM*/*KM* ratio, the lowest displacement has the highest *GM* Ratio. On the other hand, observing each displacement, the lower *GM*/*KM* ratio, the higher *GM* Ratio. Referring to loading condition and Figure 6.20 (*KM* and *GM*), the *GM* for LC 1 and LC 5 are quite similar (0.763 m and 0.657 m), but both *GM* Ratio results are different, as both *GM*/*KM* ratios are different. This indicates that the *GM*/*KM* ratio is more essential than the actual *GM*. The *KM* for each load case should be considered as well in a parametric roll.

6.3.4.3. Relationship Between GM Ratio to the Amplitude of Roll, Pitch and Heave

When the *GM* Ratio is linked to the parametric roll amplitude, it may be concluded that a higher a *GM* Ratio is associated with a greater roll amplitude, as depicted in Figure 6.22. The aforementioned figure indicates that the roll amplitude commences to increase when the *GM* Ratio surpasses the threshold of 0.17, which is attributed to LC 2, LC 4, and LC 1. This discovery aligns with SGIS's evaluation of parametric roll, which requires the identification of the roll motion amplitude in the event of level 1 failure (i.e., *GM* Ratio exceeding the threshold) and proceeding to level 2 or direct stability analysis.

The present investigation examines not only LC 3 and LC 5, which passed level 1 SGIS assessment for Parametric Roll, but also other load cases that failed, by utilizing fully nonlinear URANS CFD simulation to assess their parametric roll amplitudes. Of all the load cases considered, LC 1, which has the lowest weight, poses the greatest danger to fishing boats due to its elevated parametric roll amplitude. As the displacement and *GM*/*KM* ratio increase, the *GM* Ratio decreases, leading to a reduction in parametric roll amplitude. Regardless of the boat's speed or wave direction, the operator should not run the vessel with an empty load and should lower the vertical load's position to prevent parametric roll from occurring during operation.

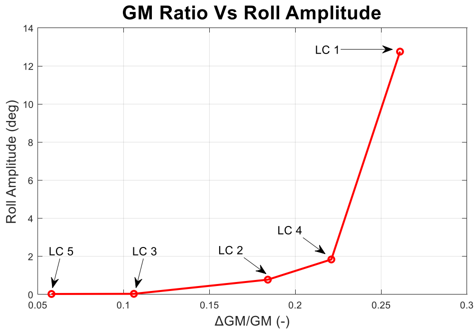

Figure 6.22. The relationship of *GM* Ratio to the parametric roll amplitude

In the previous study (Iqbal et al., 2023), in Chapter 4, the heave, pitch, and roll motions of the same fishing vessel modelled herein were predicted by using the linear strip theory. Based on these findings, both vertical load position and displacement change the roll motions. The roll natural frequency as well as roll damping are changed when the displacement and *GM* are altered. Based on this, the influence of *GM* Ratio on the pitch and roll amplitude can be observed with the same displacement.

Figure 6.23 shows the correlation between *GM* Ratios and the pitch and heave amplitudes. The figure shows why there exists a discrepancy between the amplitude of roll and pitch and heave. A higher roll amplitude does not necessarily entail that pitch and heave amplitudes are also high. In fact, with the same displacement, variations in *GM* play a significant role in increasing pitch and heave amplitudes.

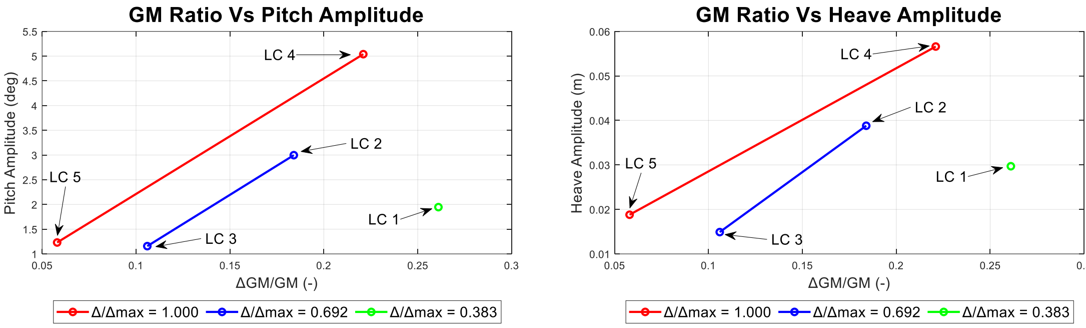

Figure 6.23. The relationship between *GM* Ratio and pitch and heave amplitudes

The red line in Figure 6.23 is the full load displacement, consisting of LC4 and LC5. As the *GM* Ratio increases, the amplitude of pitch increases from 1.23° to 5.03°. This change was replicated in LC 2 and LC3, where the fish tank capacity was 50% full. It can be seen that the pitch amplitudes increased from 1.15° to 2.99° in these cases. As there is no vertical loading position change in LC1, it is not possible to observe the influence of *GM* Ratio on the pitch and heave amplitudes. However, based on two different displacements, both amplitudes will increase if the *GM* increases. All trends observed for pitch were similar in the case of heave.

The above findings show that the parametric roll amplitudes do not influence the pitch and heave amplitudes. The *GM* Ratio, which is the level 1 assessment of SGIS form IMO, is the only one that affects the amplitude of roll, pitch, and heave. In this research, the *GM* ratio was determined from different loading conditions, which are the vertical load position (*GM*/*KM*) and displacement (Δ/Δmax). Both of these parameters change the amplitudes of parametric roll. On the other hand, the influence of *GM* ratio on the amplitudes of pitch and roll can be observed with the same displacement. This means, the *GM* ratios that change the amplitudes of pitch and heave motions are based on vertical load position only.

The level 1 assessment of SGIS from IMO is a reliable tool to detect the parametric roll in the early design stages. Through the utilisation of fully nonlinear Computational Fluid Dynamics (CFD) simulation, the present chapter showed how the pitch and heave amplitudes are influenced by the independent increase of *GM* ratio, regardless of the roll amplitude. This research imparts vital information to the ship operator, specifically, the significance of maintaining the *GM* ratio below the predetermined threshold, set at 0.17. To meet this criterion, the placement of the fish tank should be as low as possible to ensure a high *GM*/*KM*, and the vessel should be laden as heavily as possible by avoiding an empty fish tank.

6.4. Summary

Parametric roll simulations for the KCS model and a small fishing boat were carried out using a commercially available URANS solver. The result from fine configuration of mesh and time step was 3.66% lower compared to the available experimental test. The Grid Convergence Index showed an acceptable level of discretisation uncertainty of 2.76%. It was demonstrated that keeping the y+ value below unity is important to ensure the effect of viscous damping on the amplitudes of parametric roll is modelled accurately. The results showed that the fine configuration with the high y^+ (30-100) resulted in high roll amplitudes, overestimating the experimental results taken from the open literature by 16.33%

Two assessments to detect the parametric roll occurrences in early design stages were carried out by using the level 1 assessment of Parametric roll on Second Generation of Intact Stability from IMO and the Susceptibility criteria of Parametric roll from ABS. Both returned the same results, where LC1, LC2, and LC 4 are predicted to exhibit parametric roll. The susceptibility criteria from ABS were also used to determine the design wave and vessel speed that was suspected to trigger parametric roll, which is useful in reducing the total number of CFD simulations.

Level 1 assessment is based on *GM* Ratios, while the susceptibility criteria is based on the frequency condition and the ratio of linear roll damping $\left(\frac{B}{B_c}\right)$. With the damping threshold, the last criterion from ABS revealed that if the effective roll damping was sufficient the parametric roll motions were going to be very low. However, the accurate prediction of roll damping is necessary. To achieve this, low speed CFD roll decay simulations in head waves were carried out.

Linear roll damping ratios obtained from CFD simulations were compared with those obtained from Ikeda's method using the ShipX software. It was revealed that the displacement of the vessel influenced the roll damping coefficient and added roll moment of inertia. Meanwhile, the displacement and vertical load position influenced the roll moment of inertia. All of these change the linear roll damping ratio. Even though the prediction of PR occurrence in the early stage has been carried out using two different methods, the amplitude of parametric roll of suspected load case still needs to be confirmed through the CFD simulations.

Based on the CFD simulations, LC1, surprisingly was the load case that had the highest parametric roll amplitude (12.76°) followed by LC4 (1.84°) and LC 2 (0.78°). Meanwhile, LC 3 and LC 5, as predicted, did not result in parametric roll. It was also revealed that the parametric roll amplitude did not directly influence the amplitude of pitch and heave motions. A higher parametric roll amplitude does not indicate high pitch and heave amplitudes. The changes in loading conditions during operation also changed the longitudinal distribution of flare shape at the water line. The flare shape contributed to the occurrence of parametric roll, as it can significantly change the buoyancy as well as the *GM* when the boat is pitching and heaving in waves.

The *GM* Ratio (level 1 assessment of PR on SGIS from IMO) had a crucial role in changing the amplitudes of parametric roll, pitch, and heave. The roll amplitudes were increased when the *GM* Ratio caused by vertical load position (*GM*/*KM*) and displacement (Δ/Δmax) increased. With the same displacement, the amplitude of pitch and heave motions will also increase when the *GM* Ratio increased due to the change of vertical load position (*GM*/*KM*).

This chapter gives the information to the ship operator that it is important to keep the *GM* Ratio of the boat below the threshold, which is, in this case 0.17, to avoid the parametric roll occurrence and increase in pitch and heave motions during its operation. This can be achieved by placing the fish as low as possible (making the *GM*/*KM* high) and keeping the boat as heavy as possible (making the displacement high) by not keeping the fish tank empty.

Future work should focus on minimising power requirements while considering the boat's loading condition, as larger displacements can be used to avoid parametric roll occurrence. Still, that may result in higher resistance in calm water and waves. Additionally, as the boat operates at high Froude numbers, it may enter the semi-planning modes of motion.

7. Minimising Radius of Gyration to Enhance Seakeeping Performance of Small Fishing Vessel

7.1. Introduction

Fishing at sea is the main source of fish and seafood, where many accidents occur during. The mortality and fatality rate among fishers are the highest compared to other occupations (FAO, 2000). The main causes of accidents can be classified into two categories: human factors (Obeng et al., 2022a), and environmental conditions, including poor weather, strong winds, and high waves (Jin and Thunberg, 2005). These conditions lower the operability index of fishing boats. A significant proportion of reported accidents occur on small fishing vessels and an even larger proportion of accidents on such small vessels are never reported (Ugurlu et al., 2020; Wang et al., 2005). Therefore, increasing the operability index by enhancing the seakeeping performance can minimise the risk of accidents.

Conducting seakeeping optimisation is one solution to enhance the safety and seakeeping performance of ships during operation. The way fishermen locate the fish also changes the centre of gravity, longitudinally (LCG) and/or vertically (KG). As the loading conditions of fishing vessels change during operation, arranging and managing the centre of gravity is essential for maintaining stability, improving seakeeping, ensuring overall safety, and reducing fuel consumption.

Similar work related to managing centre of gravity involves trim and ballast optimisation to minimise total resistance, as evidenced by the work of Reichel et al. (2014) and Hüffmeier et al. (2020). Even though the optimum trim and ballast condition can reduce the resistance, it can influence the seakeeping performance, such as heave, pitch, and added resistance, as demonstrated by Shivachev et al. (2020) for the KCS model.

Unlike resistance optimisation which its objective function is minimising the resistance, there are many objective functions in seakeeping optimisations to be minimised, such as vertical acceleration, heave, pitch, roll, slamming and deck wetness. The optimisation process is therefore complex, time consuming, and must use multi objective optimisation (Miao et al., 2018; Vernengo et al., 2015; Wang et al., 2018) or converting to be single solution, such as the seakeeping index (Bales, 1980; Ozmen, 1995; Sarıöz, 2009), the combination of multiple responses, such as vertical motions or acceleration (Bagheri et al., 2014; Diez et al., 2015) to achieve the best compromise solution.

The present chapter introduces the radius gyration in the y direction (R_y) as a novel objective function for seakeeping optimisation in managing the centre of gravity (CoG) location. This value relates to pitch damping coefficient and pitch moment of inertia. Because a single objective function is required, it is possible to simplify the optimisation process. R_y is chosen as an objective function stem from the nature of fishing vessel operations, where their loading conditions are dynamic. Namely, the fish tank is empty at the beginning and is gradually filled by fish, changing the displacement and loading position. Changes in loading position and displacement influence the R_y. Therefore, it is essential to find the best location of *LCG* and *KG* that minimise R_y.

The aim of this chapter is to enhance the seakeeping performance of a fishing boat by using a novel objective function, R_y. The research considers changes in loading conditions, which is characteristic of fishing vessel operation. The original and optimal conditions are then simulated using URANS CFD to compare the Response Amplitude Operators (RAO) of heave, pitch, and their added resistance performance. A spectral (short-term) analysis is then carried out using three different peak periods (*Tp*) and significant wave heights (*Hs*), which collectively represent a majority of annual wave occurrences in the Java Sea. The JONSWAP spectrum is employed to quantify the seakeeping performance of the initial and optimal conditions.

7.2. Methodology

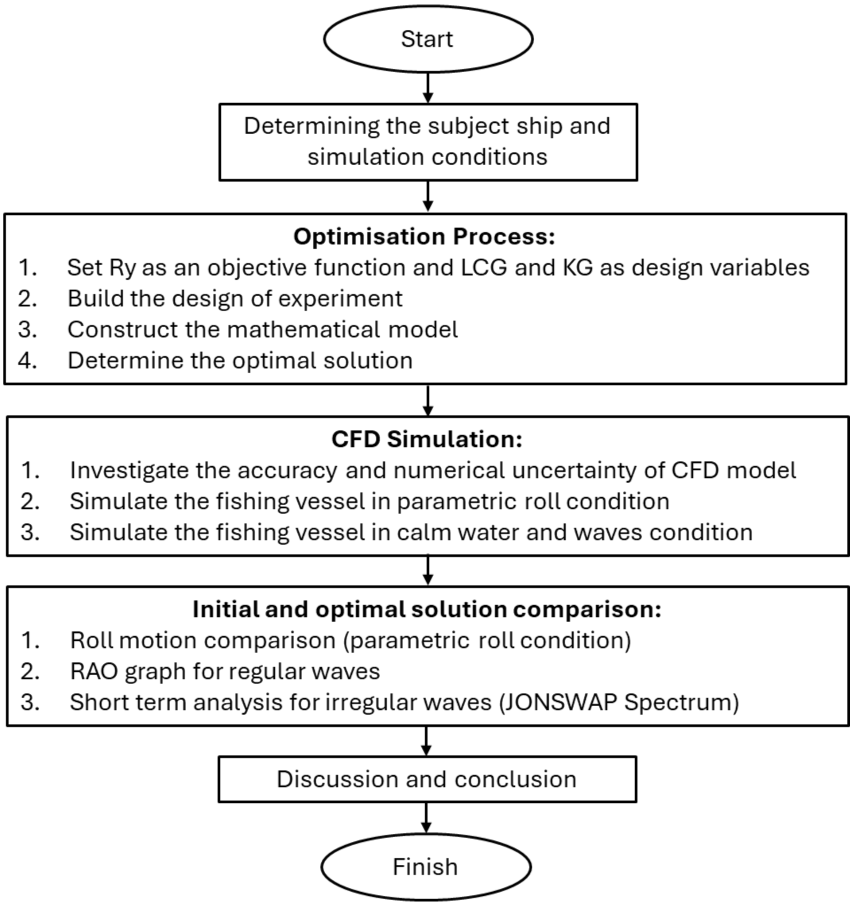

Figure 7.1. Research flowchart

Figure 7.1 shows the flowchart of the remainder of the study. The research begins by determining the subject ship and the simulation conditions, which are discussed in subsection 3.3.2. The study then continues with the optimisation process. In this case, the response surface methodology is employed, as explained in subsection 3.6. Once the optimum solution is determined, the research proceeds to simulate the seakeeping performance using CFD, the details of which are described in subsection 3.4. The results and discussion under various conditions are presented in section 7.3. Finally, the conclusion of this research is provided in section 7.4.

7.2.1. Objective Function and Design Variables

The operation of fishing vessels is dynamic as the payload always changes depending on the number of fish caught. The process begins with an empty fish tank, which gradually fills as fish are caught. More crucially, the way the catch is placed changes the position of the centre of gravity. Such changes have implications for the radius of gyration in the y-direction (R_y) even if the overall mass remains the same, which is an assumption used in this thesis. In Eq. (7.1), w_i represents the finite mass, z_i and x_i denote the vertical and longitudinal distances from the centre of the finite mass to the centre of gravity, and Δ represents the total mass. A lower radius of gyration corresponds to a lower moment of inertia (I_{yy}) for the same mass.

$$R_y = \sqrt{\frac{I_{yy}}{\Delta}} = \sqrt{\frac{\sum w_i({z_i}^2 + {x_i}^2)}{\Delta}} \tag{7.1}$$

$$\zeta = \frac{C}{C_r} = \frac{C}{2\left(I_{yy} + I_{yy(a)}\right)\omega_n} \tag{7.2}$$

Consequently, assuming no variation in hull shape, both the added moment of inertia ($I_{yy(a)}$) and the damping coefficient (C), shown in Eq. (7.2), remain identical despite changes in the centre of gravity position. The resulting change in natural frequency, ω_n, is not significant compared to the change in I_{yy}. Therefore, vessels with a lower radius of gyration exhibit a lower critical damping (C_r), resulting in a higher damping ratio (ζ), as shown in Eq. (7.2). When the damping ratio is high, the motion amplitude will be low. This phenomenon—the influence of loading condition on roll damping ratio and parametric roll amplitude for fishing vessels—has previously been investigated by Iqbal et al. (2024), as described in Chapter 6.

Seakeeping performance encompasses several aspects to be minimised, including heave, pitch, roll, and added resistance. Consequently, the objective function for optimising seakeeping performance is inherently complex. In this study, heave, pitch, and roll are not calculated directly or used as objective functions in the seakeeping optimisation process. Instead, this study proposes a novel objective function to assess seakeeping performance indirectly, thereby simplifying the optimisation process. This approach allows for improved seakeeping performance without directly calculating the seakeeping characteristics of the ship.

The objective function utilised in this study is Radius Gyration in the Y direction (R_y). It is also well known that the pitch moment of inertia (I_{yy}) depends on R_y. With the same displacement, when the radius gyration R_y is low, the pitch moment of inertia will be low. Thus, as explained previously, the pitch damping ratio is expected to be high, lowering the pitch amplitude. However, the R_y value depends on the location of the centre of mass of the ship. A change in centre of mass is common for a fishing vessel as the amount of caught fish is variable during fishing. Therefore, determining its optimum location of is essential to produce a low R_y.

7.3. Results and Discussion

7.3.1. Optimisation Results

Table 7.1 shows the R_y 's values to FAO-01 fishing vessel by shifting LCG and KG. All R_y values were used to determine the mathematical model and generate the response surface for R_y. The mathematical model based on Table 7.1 is shown in Eq. (7.3) and achieves an R^2 value of 0.9998. Notably, the coefficient x_1x_2 in Eq. (7.3) is zero, indicating that the equation accurately explains the influence of LCG and KG.

The response surface of R_y is shown in Figure 7.2-a, where the rectangle represents the constraint, and the point indicates the location of the lowest response within the constraint. Figure 7.2-b shows the plot of actual R_y based on the calculation versus predicted R_y based on Eq. (7.3). A mathematical model is considered to produce good results if the predicted and actual data align closely with the fitted line, $y = x$, the black line in Figure 7.2-b (Abdulkadir et al., 2021). It is shown in Figure 7.2-b, as the R^2 value is high, the predicted and actual value in this case is close.

Table 7.1. Responses of R_y for FAO-01

Loading Condition	**X_1**	**X_2**	***LCG***	***KG***	**R_y**
Initial	0	0	0.945	0.379	0.5533
LC 1	1	1	0.992	0.398	0.5570
LC 2	1	-1	0.992	0.360	0.5539
LC 3	-1	1	0.898	0.398	0.5575
LC 4	-1	-1	0.898	0.360	0.5543
LC 5	-1.414	0	0.878	0.379	0.5577
LC 6	1.414	0	1.012	0.379	0.5570
LC 7	0	-1.414	0.945	0.352	0.5517
LC 8	0	1.414	0.945	0.406	0.5563

$$Ry = 0.5533 - 0.0002x_1 + 0.0016x_2 + 0.0020{x_1}^2 + 0.0003{x_2}^2 \qquad (7.3)$$

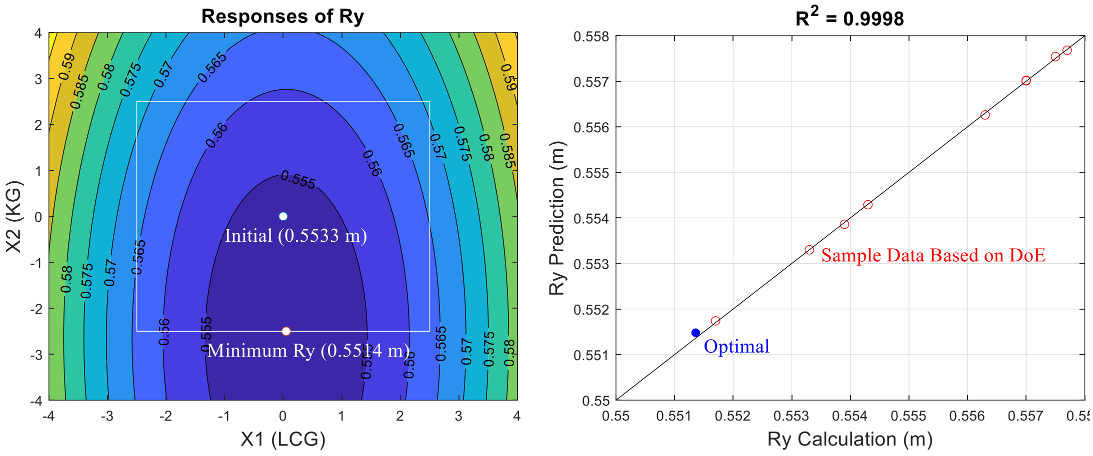

(a) (b)

Figure 7.2. The responses surface of R_y Influenced by *LCG* and *KG* with the constrains and optimal location (a) and the comparison between Actual and Prediction of R_y

Table 7.2. The comparison between the original and optimum results in R_y for FAO-01

Loading Condition	x_1	x_2	***LCG* (m)**	***KG* (m)**	**R_y Cal (m)**	**R_y Eq. (7.3)(m)**
Initial	0.00	0.00	0.945	0.379	0.55330	0.55330
Optimal	0.05	-2.50	0.947	0.332	0.55136	0.55147
Difference (%)					**-0.351%**	**-0.332%**

In Figure 7.2, it is evident that both *LCG* and *KG* influence the R_y values for the FAO-01 model. The alteration in the centre of gravity longitudinally and vertically for the small fishing vessel is essential in R_y variations due to vessel size. On the other hand, vertical movement may have less influence in R_y for the long ship. However, the level of change due to *LCG* in this study is notably more significant than *KG*. This observation may be explained by the coefficient of ${x_1}^2$, which is higher than ${x_2}^2$ in Eq. (7.3). A comparison of R_y between the original condition and the optimum loading condition is shown in Table 7.2. The optimum loading condition can reduce the R_y value by up to 0.351% from the initial condition according to calculation and by up to 0.332% according to the mathematical model in Eq. (7.3).

7.3.2. Accuracy and Numerical Uncertainty of the CFD Model

The accuracy of the CFD model was established by comparing the CFD-based results with experimental data. Since there was no experimental data available for the seakeeping values of the FAO-01 fishing vessel, the well-known benchmark for seakeeping tests, the KRISO container ship (KCS), with seakeeping data provided by Simonsen et al. (2013) at a 1:52.667 scale and Shivachev et al. (2020) at a 1:75 scale, was employed to test the accuracy of the CFD set-up. The main dimensions of the KCS in full scale are presented in Table 7.3. The aforementioned studies include seakeeping tests for the KCS, covering heave, pitch, and added resistance in head waves characterised by $\lambda/Lbp = 1.15$, $H/\lambda = 1/60$, and $Fr = 0.26$. The CFD set-up applied for the KCS can then be used for the fishing vessel with slight adjustments due to the size differences between the KCS and fishing vessel.

Table 7.3. Main dimensions of KCS

Dimensions	Value
Length between perpendicular, L_{bp} (m)	230
Breadth at water line, B (m)	32.2
Depth, D (m)	19.0
Loaded draft, T (m)	10.8
Block Coefficient	0.651

The comparison results between the CFD and experimental data is shown in Table 7.4. The present CFD shows excellent performance compared to the experiment, with approximately 1% deviation. In wave conditions, the CFD models shows a difference of less than 5% compared to the experimental transfer function (TF) for heave and pitch, which is deemed acceptable. In the case of added resistance, two sets of experimental data were compared, as shown in the calm water resistance comparison. It is observed that the present CFD exhibits a 5.03% difference when compared to Simonsen et al. (2013) and -2.21% when compared to Shivachev et al. (2020).

The accuracy study of the KCS demonstrates good agreement with the EFD results across all parameters of interest. Consequently, the CFD setup was adopted for the simulations of the FAO-01 fishing boat, with the exception of computational domain size. The choice of physics model, the determination of mesh setup, and the time step remain unchanged.

Table 7.5 shows the comparison of the total resistance of the FAO-01 fishing boat in calm water at $F_r = 0.33$, obtained from CFD calculations, with that obtained from measurements (Díaz-Ojeda et al., 2023) which shows that the CFD result has a -0.97% difference compared to experimental data. This present CFD has the same low difference with CFD conducted by Díaz-Ojeda et al. (2023), which is below 1%.

Table 7.4. Results comparison between present CFD and experimental data of the KCS at $F_r = 0.26$

	Calm Water	**Wave Condition (λ/Lbp = 1.15)**		
	CT (*10^3)	**Heave TF**	**Pitch TF**	**Added Resistance TF**
EFD (Simonsen et al., 2013)	4.31	0.950	0.693	9.106
Present CFD	4.36	0.954	0.727	9.564
Difference (%)	**1.06%**	**0.43%**	**4.89%**	**5.03%**
EFD (Shivachev et al., 2020)	4.41	-	-	9.78
Present CFD	4.36	0.941	0.735	9.173
Difference (%)	**-1.23%**	**-**	**-**	**-6.21%**

Table 7.5. Results comparison between present CFD and experimental data of FAO-01 Fishing Boat at $F_r = 0.33$.

	RT (N)	**Difference (%)**
EFD (Díaz-Ojeda et al., 2023)	15.31	
Present CFD	15.162	**-0.97%**
CFD (Díaz-Ojeda et al., 2023)	15.250	**-0.40%**

Table 7.6. Numerical Uncertainty Results for the KCS

	Calm Water	**Wave Condition (λ/Lbp = 1.15)**		
	CT (*10^3)	**Heave TF**	**Pitch TF**	**Added resistance TF**
Fine Configuration	total cell = 3,591,024, time step = 0.01845 s	total cell = 4,330,069, time step = 0.00360 s		
Medium Configuration	total cell = 1,396,929, time step = 0.02609 s	total cell = 1,889,342, time step = 0.00509 s		
Coarse Configuration	total cell = 561,609, time step = 0.03690 s	total cell = 923,707, time step = 0.00720 s		
Fine solution, S_1	0.00436	0.9541	0.7269	9.5638
Medium solution, S_2	0.00444	0.9550	0.7265	9.8579
Coarse solution, S_3	0.00458	0.9650	0.7131	15.2748
Medium-Fine, ε_{21}	0.00008	0.0009	-0.0004	0.2941
Coarse-Medium, ε_{32}	0.00014	0.0100	-0.0134	5.4169

Convergence ratio, R	0.57143	0.0900	0.0299	0.0543
Order of accuracy, p	1.61471	6.9479	10.1322	8.4062
GCI Method (%)	**3.05810**	**0.0117**	**0.0021**	**0.2207**
CF Method (%)	**3.66972**	**0.1793**	**0.1084**	**5.9737**
FSRE Method (%)	**0.00019**	**0.0038**	**0.0008**	**0.9140**

To estimate the discretisation error, the CFD setup used to compare against experimental data above is the fine configuration. This configuration underwent a coarsening process in mesh size and time step with a refinement factor $\sqrt{2}$ for the KCS model and 1.23 for FAO-01 fishing boat, thereby creating a medium configuration. Subsequently, the medium configuration was further coarsened, resulting in a coarse configuration for the KCS model and factor of 1.24 for FAO-01 fishing. The results from these three configurations were used to estimate the numerical uncertainties, employing three methods: Grid Convergence Index (GCI) based on Roache (1998), Correction Factor (CF) based on Stern (2001), and Factors of Safety for Richardson Extrapolation (FSRE) based on Xing & Stern (2010). Following the recommendations of Burmester (2020), the time step and grid dimension are magnified simultaneously, thus, the percentage uncertainty reported in Table 7.6 is the total spatiotemporal discretisation error.

Table 7.7. Numerical uncertainty results for FAO-01 fishing vessel

	RT Calm Water	**Wave Condition (λ/Lbp = 1.5)**		
		Heave TF	**Pitch TF**	**Added resistance TF**
Fine Configuration	total cells = 1,715,717, time step = 0.0131 s	total cell = 3,536,648, time step = 0.0026 s		
Medium Configuration	total cells = 1,010,918, time step = 0.0161 s	total cell = 1,419,264, time step = 0.0037 s		
Coarse Configuration	total cells = 577,607, time step = 0.0200 s	total cell = 512,760, time step = 0.0052 s		
Fine solution, S_1	15.1616 N	1.1177	0.6884	1.9716
Medium solution, S_2	15.5010 N	1.1157	0.6837	1.9473
Coarse solution, S_3	16.2236 N	1.0937	0.6657	1.8631
Medium-Fine, ε_{21}	0.33939	-0.00200	-0.0047	-0.0243
Coarse-Medium, ε_{32}	0.72260	-0.02200	-0.0180	-0.0842
Convergence ratio, R	0.46969	0.09091	0.2611	0.2886
Order of accuracy, p	3.39085	6.91886	3.8745	3.5857
GCI Method (%)	**2.7495**	**0.0224**	**0.3016**	**0.6250**
CF Method (%)	**6.7463**	**0.3400**	**1.1242**	**1.9650**
FSRE Method (%)	**4.5490**	**0.0084**	**0.0282**	**0.1440**

Table 7.6 shows the results of numerical uncertainty for the KCS. Overall, the uncertainty results from the three methods are low (below 5%), except for added resistance transfer function with the correction factor method, which yields a value of 5.97%. Based on these numerical uncertainty results, all the CFD setups of the KCS for seakeeping simulations were applied to the FAO-01 fishing boat and considered to possess the same accuracy and uncertainty as the KCS. Table 7.7 shows that the numerical uncertainty for FAO-01 fishing vessel also yields favourable results, with values up to 1% across all three different methods for seakeeping and below 5% in calm water resistance, except with CF method.

7.3.3. Seakeeping Performance in Parametric Roll Condition

As reported by Iqbal et al. (2024) (Chapter 6), different loading conditions alter the natural roll period and roll damping. Consequently, certain combinations of speed and wave period can trigger parametric roll. The influence of loading conditions between the initial and optimum states is compared under parametric roll conditions to demonstrate that the optimal centre of gravity can prevent parametric roll and capsize. To ensure an equal comparison with seakeeping simulations without parametric roll (discussed in the following subsection), the wave conditions and the forward speed of the fishing vessel were kept consistent.

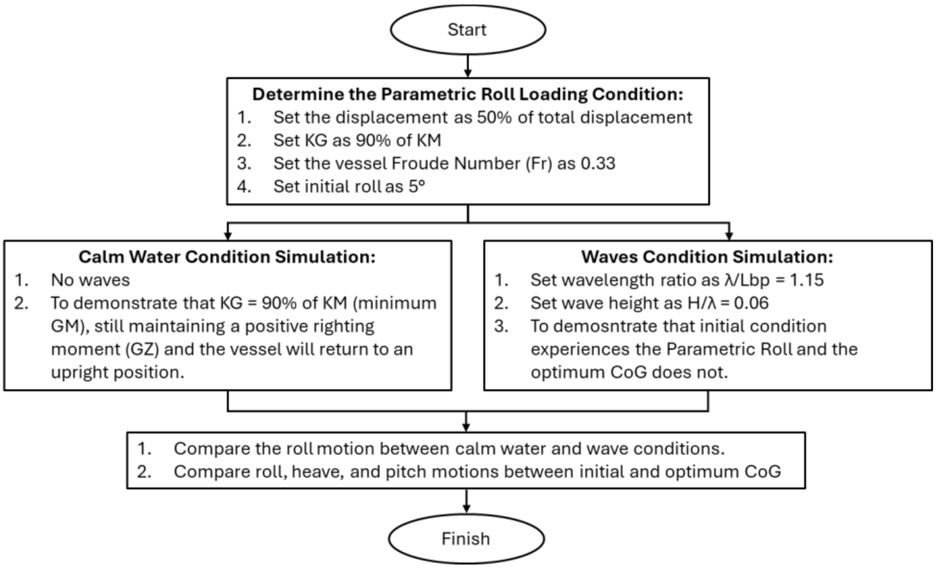

Figure 7.3. Flowchart of parametric roll simulation

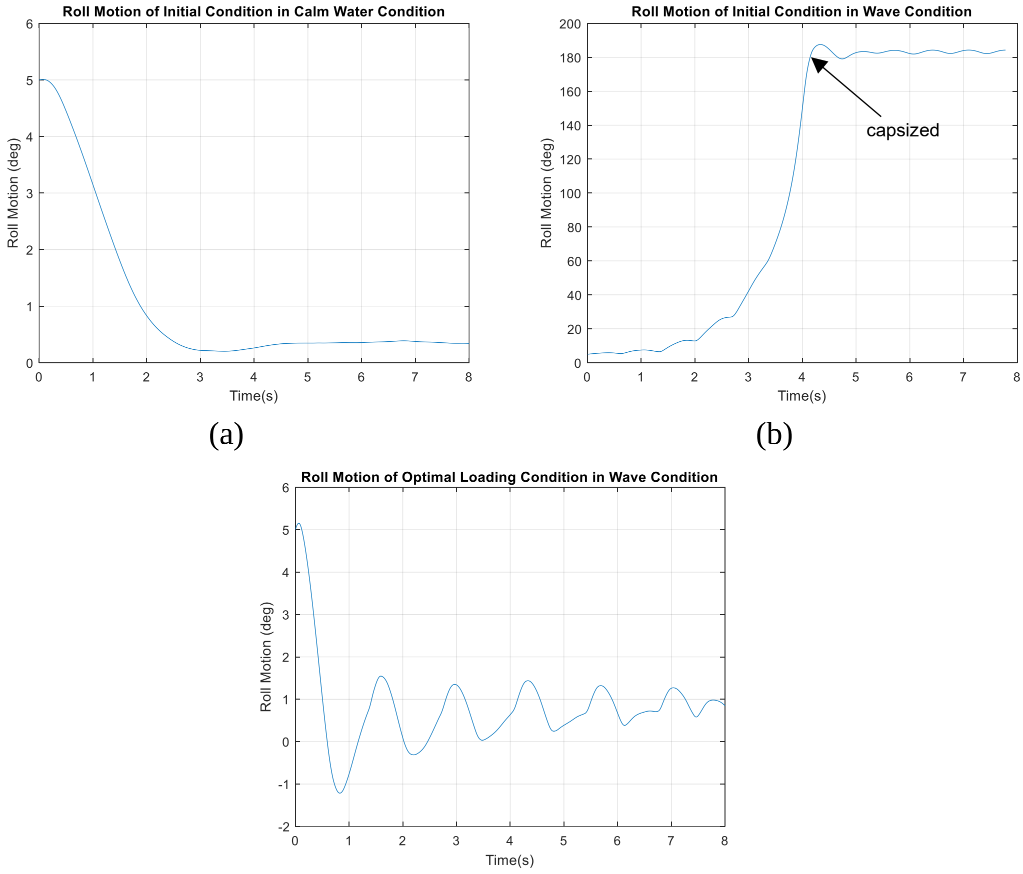
Roll Motion of Initial Condition in Calm Water Condition

Roll Motion of Initial Condition in Wave Condition

Roll Motion of Optimal Loading Condition in Wave Condition

(a) (b) (c)

Figure 7.4. The comparison of roll motion

Figure 7.3 shows the flowchart of the parametric roll simulation in this study. Firstly, to induce parametric roll, the loading condition must be set. This is achieved by setting the displacement to 50% of the total displacement and the *KG* to 90% of the *KM*, with a Froude Number (F_r) of 0.33. Then, the vessel is rotated to 5° in roll as an initial condition. According to the previous findings in Chapter 6 (Iqbal et al., 2024), a low displacement with a high *KG* increases susceptibility to parametric roll. Following this, the loading condition is simulated under two scenarios: calm water and wave conditions.

According to the *GZ* curve, this loading condition allows the vessel to return to the upright position from a heel of 5°. Then, the CFD simulation in calm water was conducted to demonstrate that the minimum *GM* condition still has a positive righting moment (*GZ*), which returns the vessel to the upright position. The wave condition (λ/Lbp = 1.15, H/λ = 0.06) is simulated to demonstrate that the initial arrangement of *LCG* and *KG* triggers parametric roll, while the optimum arrangement is safe from parametric roll.

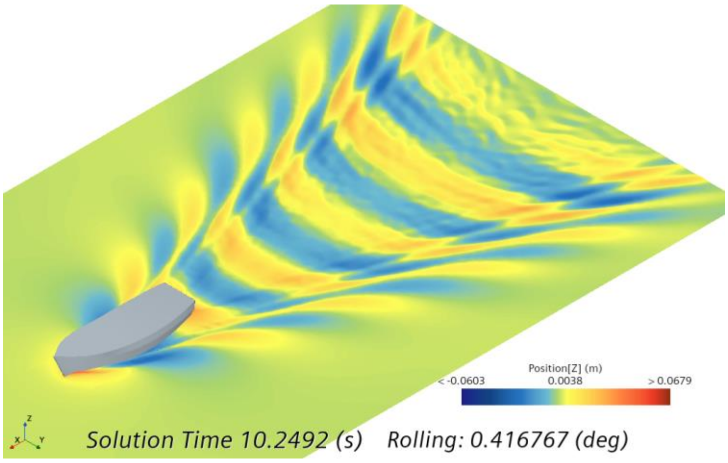

(a) Initial loading condition in calm water (not capsized)

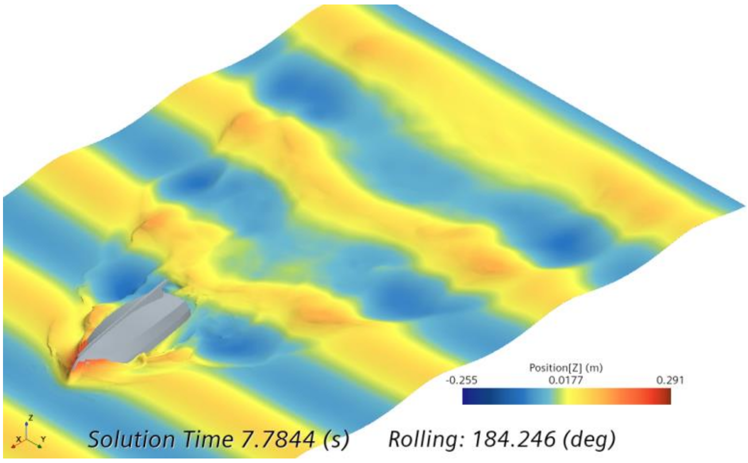

(b) Initial loading condition in waves (capsized)

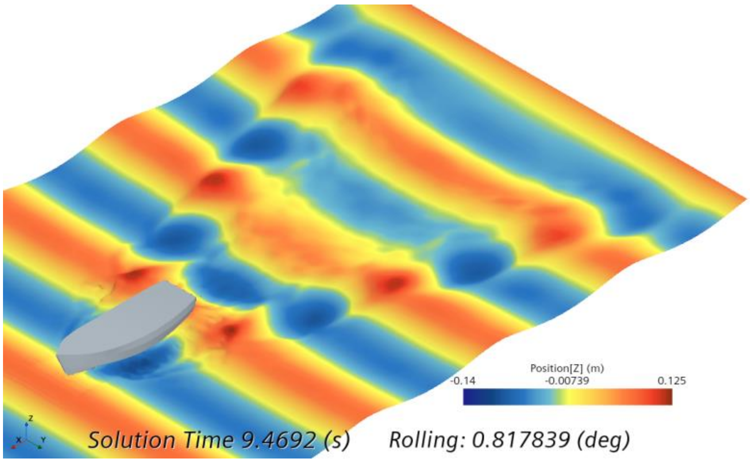

(c) Optimal loading condition in waves (not capsized)

Figure 7.5. The results of CFD-based simulation in parametric roll condition

Figure 7.4-a and -b show the roll motions of the initial condition both in calm water and wave conditions, with the same initial roll, forward speed, and loading condition. The figures illustrate that the initial loading condition capsized due to parametric roll. In contrast, the vessel did not experience parametric roll when operating in calm water conditions, where the roll motion decreases. This comparison highlights that specific wave conditions can trigger the most severe parametric roll condition, ultimately capsizing the vessel.

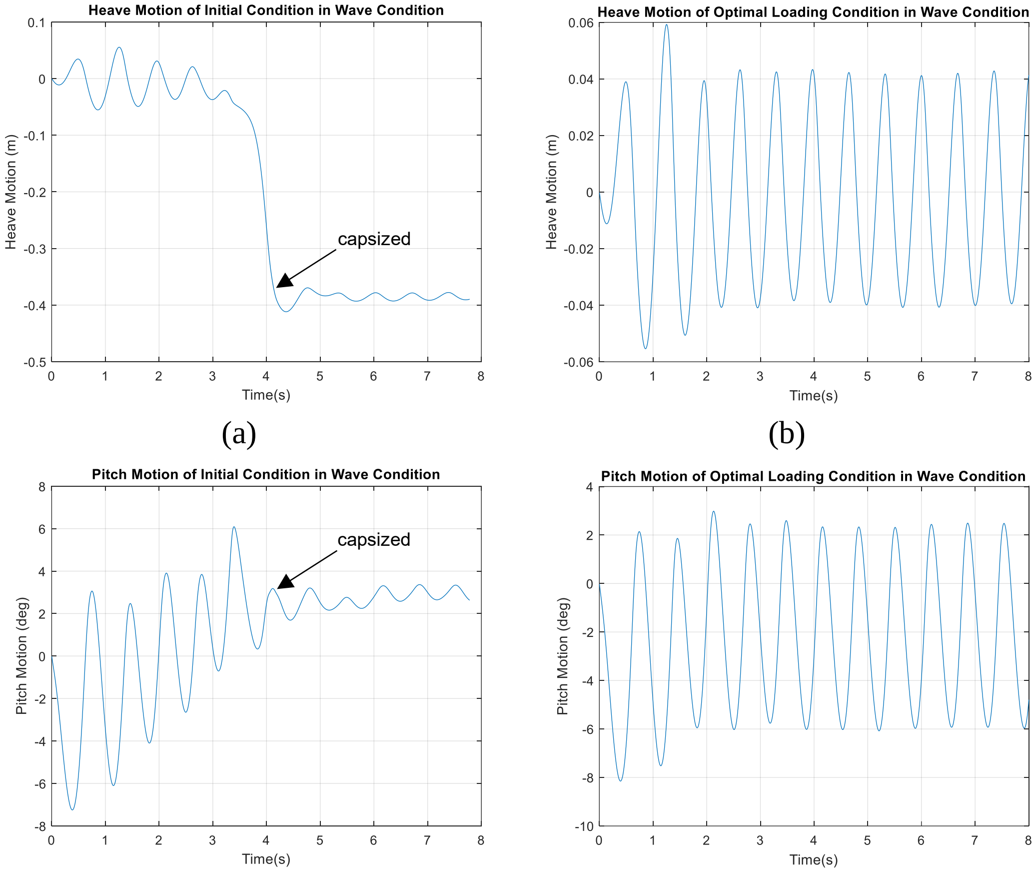

(a) (b)

(c) (d)

Figure 7.6. The comparison of heave and pitch motions of fishing vessel between initial and optimal loading conditions

Figure 7.4-c shows the results of roll motions of optimal loading condition. It is shown that roll motion of optimal loading condition decreased from initial roll of 5°. This demonstrates that optimal loading condition can prevent this hazardous incident by minimising R_y. Illustrations of the capsizing phenomenon for the initial loading conditions are shown in Figure 7.5-b, while the condition of optimal loading condition without the parametric roll phenomenon are also presented.

Having observed parametric roll, it is informative to study the heave and as pitch responses under the same condition. Figure 7.6-a and -b show the heave responses of the initial and optimum condition heave response. As the initial condition resulted in capsize, the heave response was lower due to different hull shape below the water line before and after capsizing. The same trend is observed for pitch response in Figure 7.6-c and -d. For the initial condition, the pitch amplitudes change from negative values (trim by stern) before capsizing to positive values (trim by bow) after capsizing. Both heave and pitch motions of optimum loading condition remain small by comparison. Changes in LCG and KG have proved that they affect the R_y which affects the pitch moment inertia. Having a low inertia moment of pitch can further reduce the pitch amplitude, as the pitch damping ratio becomes higher.

7.3.4. Seakeeping Performance in Regular Waves

The seakeeping performance of initial and optimum conditions were carried out to calculate the heave and pitch responses as well as the added resistance in maximum displacement. The simulations used five wavelength ratios, ranging from λ/L =1.15 to λ/L =3.0. All CFD results for heave, pitch, and roll motions, as well as the resistance in waves, exhibit periodic time dependence. A Fourier Transform algorithm was used to determine the motion amplitudes for each wavelength ratio (λ/L) in order to establish the RAO curves. This was achieved by using Eq. (7.4) for translational and rotational motions, respectively, while the RAO values for added resistance were obtained by using Eq. (7.5).

$$RAO = \frac{z_a\ (m)}{\zeta\ (m)};\ RAO = \frac{\theta_a\ (rad)}{k\zeta\ (rad)} \tag{7.4}$$

$$RAO = \frac{Mean\ RT_{wave} - RT_{calm}\ (N)}{\rho g \zeta^{\,2} \left(\frac{B^2}{L}\right) (N)} \tag{7.5}$$

The RAOs, determined based on the model scale, were converted to the full scale to conduct short-term (spectral) analysis. The Spline Interpolation method was used to interpolate the RAOs obtained from CFD simulations. This analysis was carried out to predict the seakeeping performance of the fishing boat in the Java Sea. The nondimensional RAOs for pitch were multiplied by the full-scale wave number, k, to determine dimensional RAO (deg/m).

Meanwhile, the nondimensional added resistance RAO values were multiped by the full scale $\rho g \left(\frac{B^2}{L}\right)$ value to produce dimensional RAOs of added resistance (N/m^2). Based on Eq. (7.5), the added resistance is determined by subtracting the total resistance in calm water from the total resistance in waves. Table 7.8 shows the results of total resistance in calm water for both the initial and optimal loading conditions. According to Table 7.8, the total resistance in calm water for both loading conditions is quite similar.

Figure 7.7 displays the comparison between the mean total resistance in waves and total resistance in calm water. The difference between them is referred to as added resistance. It can be seen that the optimal loading condition does not have a significant impact on the total resistance in calm water. However, it affects the mean total resistance in waves, resulting in different added resistance. The optimal loading condition has a lower added resistance at higher wavelength ratio, as shown in Figure 7.7.

Table 7.8. The RT comparison

Loading Condition	x_1	x_2	***LCG* (m)**	***KG* (m)**	**RT CFD (N)**
Initial	0.00	0.00	0.945	0.379	15.162
Minimum R_y	0.050	-2.50	0.947	0.332	15.165
				Difference (%)	**0.020**

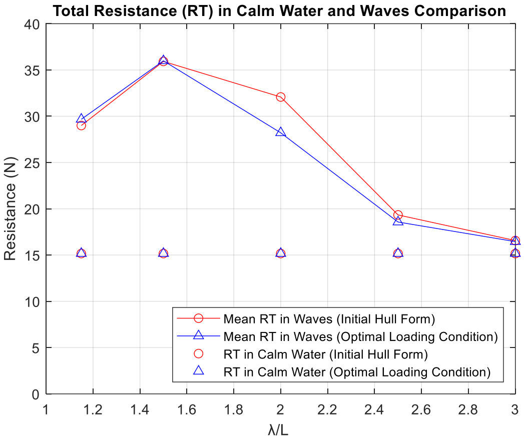

Figure 7.7. Total Resistance in calm water and mean total resistance in waves

Table 7.9 shows the comparison of RAOs between the initial and optimal loading conditions. The RAO curves for heave and pitch motions, as well as the added resistance coefficients are shown in Figure 7.8. Based on the heave RAO curve shown in Figure 7.8-a, it can be concluded that minimising R_y leads to a reduction in the heave RAO at the resonance condition (λ/L = 2.00). For wavelength ratio below 2, the heave RAO is slightly higher than the original condition, although the difference is small. This indicates that the optimisation procedure, along with a single objective function (minimising R_y) in this study, was successful in reducing heave motion.

The same trend as for heave is observed for pitch RAO (Figure 7.8-b). The original condition exhibits a peak RAO when the wavelength ratio, λ/L = 2.5. Optimum loading condition shows a lower value compared to the original condition starting from this wavelength ratio (λ/L = 2.5). However, for wavelength ratios below 2.5, optimum loading condition displays a slightly higher pitch RAO compared to the original.

Table 7.9. Response amplitude operator comparison

λ/L	Initial			Optimal		
	Heave TF	**Pitch TF**	**C_{AW}**	**Heave TF**	**Pitch TF**	**C_{AW}**
1.15	0.320	0.225	1.035	0.339	0.246	1.085
1.5	0.917	0.570	1.553	0.950	0.614	1.558
2	1.387	1.105	1.265	1.263	1.115	0.976
2.5	1.069	1.153	0.312	1.033	1.055	0.255
3	0.983	1.075	0.105	0.973	0.994	0.096

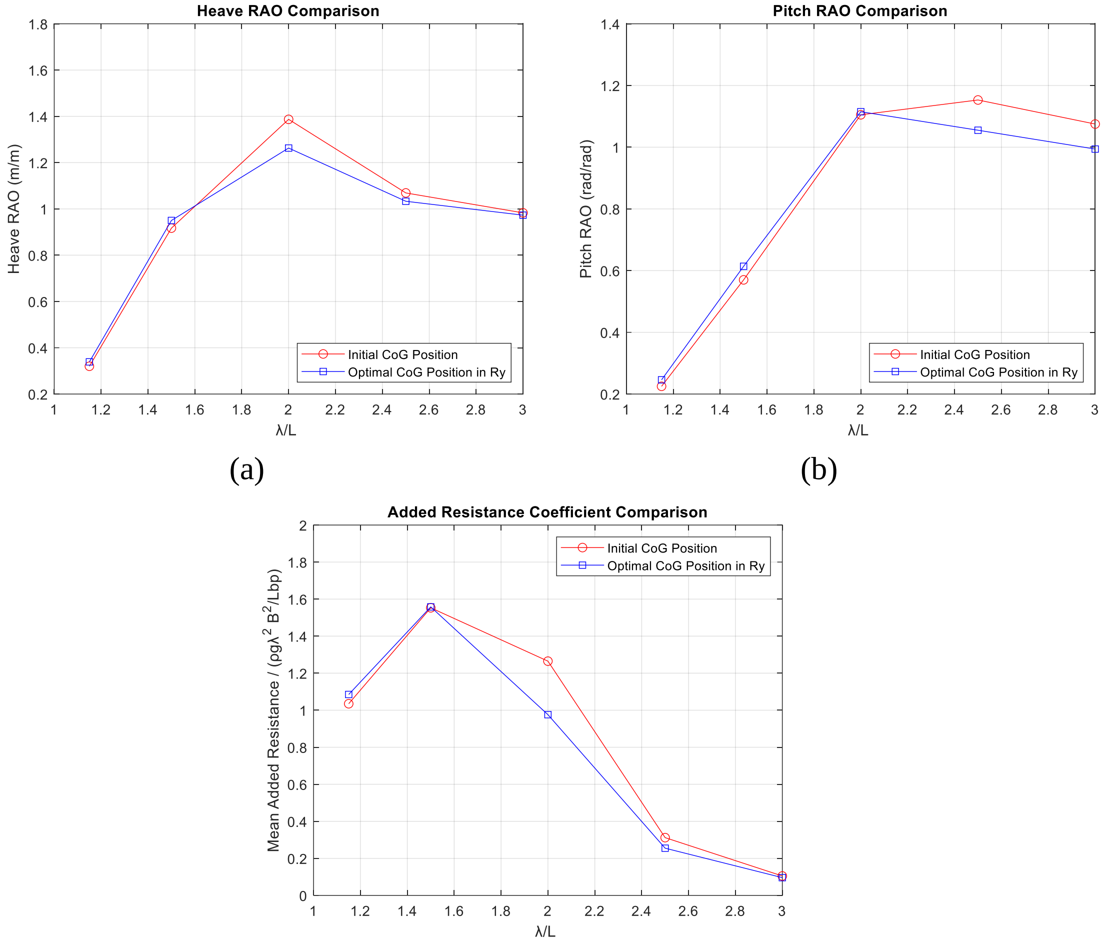

(a)

(b)

(c)

Figure 7.8. Heave, pitch RAO and added resistance coefficient comparison

Figure 7.8-c shows the added resistance coefficient in the initial and optimal loading conditions. The peak curve of the initial condition is located at *λ/L* = 1.5. However, unlike the trends observed in heave and pitch, the optimal loading condition demonstrates a lower added resistance value compared to the initial loading condition when the peak in added resistance is surpassed at *λ/L* = 1.5. In other words, the optimal loading condition exhibits a marginally higher added resistance coefficient in resonance conditions or at smaller wave lengths. Nevertheless, although optimal

loading condition shows a higher added resistance value than the original condition, the difference is not significant, as shown in Figure 7.7. The optimal loading condition also demonstrates an important trend: in resonance condition and lower wavelength ratio, the added resistance value is close to the initial one.

Overall, the optimisation method using only a single objective function in this study offers improved seakeeping performance by reducing heave and pitch motions, as well as added resistance coefficients. Figure 7.8 demonstrates that solely employing a single objective function, minimising R_y, can enhance seakeeping performance. The approach demonstrated here is simpler than existing methodologies due to the use of a single objective function to address all seakeeping issues.

The combination of simple optimisation with a single objective function represents a significant contribution of this thesis to fishing vessel designers and operators, enabling them to enhance the seakeeping performance of fishing vessels and thereby improve safety. For existing fishing vessels, minimising R_y can be an option to consider when arranging the caught fish during fishing.

7.3.5. Seakeeping Performance in Irregular Waves

Comparing the RAOs to assess the seakeeping performance cannot definitively determine superiority of one design over another. Ultimately, the response and added resistance amplitude operators combined with the wave spectra of the location where a vessel operates will determine the performance of a vessel. If the vessel operates in an area characterised by waves with periods close to one of its natural frequencies, resonance conditions may occur, leading to high response amplitudes.

In this subsection, RAO values will be used to conduct spectral analysis to assess the seakeeping performance of both initial and optimum conditions. The JONSWAP spectrum is used with $\gamma = 2.5$. The n^{th} moment calculation is used to determine the displacement (motion), velocity, and acceleration spectrum as well as the RMS result has been described in Chapter 4.

The FAO-01 fishing boat is assumed to be operating in Java Sea, Indonesia. Therefore, a wave scatter diagram representing the sea is required. However, not all peak periods (Tp) and significant wave height (Hs) are considered. This study focuses on three of the most frequently occurring Tp and Hs combinations to investigate their effect on fishing boat responses. Table 7.10 shows a partial wave scatter diagram of the Java Sea, highlighting the most prevalent condition. The selected Hs-Tp combinations account for 89.2% of the recorded conditions in the Java Sea in the course of one year.

Since the wave scatter data is provided in actual data (full-scale), the RAOs of the fishing vessel in model scale were scaled up to full scale by using Eq. (7.4) and Eq. (7.5). It is assumed that the scaling of all responses is linear. Spline interpolation was used to gather data between the five wavelength ratios used in CFD simulations when obtaining the RAOs.

Table 7.10. The highest occurrence of *Tp* and *Hs* in Java Seas, Indonesia

***Hs* (m) \ *Tp* (s)**	**3 – 4**	**4 – 5**	**5 – 6**
0.0 – 0.5	23.99%	7.30%	0.49%
0.5 – 1.0	11.27%	27.17%	6.43%
1.0 – 1.5	0.00%	2.52%	10.03%

The seakeeping criterion used to evaluate the vertical motion in the working area is the RMS acceleration ($\sqrt{m_4}$). Given that the fishing boat is small, and most fisherman work in the centre of the vessel, it is assumed that there is no longitudinal distance creating vertical motion due to pitch. Therefore, the vertical motion in this study is assessed using heave motion only.

The result of RMS vertical accelerations in g unit is shown in Table 7.11. The criterion for vertical acceleration is that responses should remain below 0.2 g. It is observed that not all *Tp-Hs* combination results meet the vertical acceleration below the criterion. The lowest *Hs* (0.25 m) is identified as the best *Hs* for heave acceleration. For *Hs* = 0.75 m, all fishing boat meet the criterion except in *Tp* = 3.5 s. The averaged reductions of vertical accelerations for the optimum model are also presented in Table 7.11. The optimum loading condition can reduce heave accelerations on average by 3.12 %.

Table 7.11. The comparison of RMS vertical acceleration ($\sqrt{m_4}$) in g unit and its reduction

	***Tp* (s)**								
	3.5	**4.5**	**5.5**	**3.5**	**4.5**	**5.5**	**3.5**	**4.5**	**5.5**
***Hs* (m)**	**Initial**			**Optimum**			**Difference**		
0.25	0.056	0.036	0.027	0.054	0.035	0.026	-3.55%	-2.79%	-3.03%
0.75	0.168	0.109	0.080	0.162	0.106	0.077	-3.55%	-2.79%	-3.03%
1.25	0.279	0.182	0.133	0.269	0.177	0.129	-3.55%	-2.79%	-3.03%
						Average	**-3.12%**		

The seakeeping criterion for pitch motions utilises the RMS pitch ($\sqrt{m_0}$), set at 3 degrees. Thus, the spectral analysis for pitch motions in this study is presented through its motion responses. The RMS pitch results are shown in Table 7.12. In all the cases, the fishing boat can safely operate below the RMS pitch criterion in *Hs* = 0.25 m. Although the operational limit for the fishing boat is consistent across two different conditions, the optimal loading condition can diminish the RMS pitch values. The results are presented in Table 7.12. This suggests that the percentage of RMS pitch reduction is influenced by *Tp*. Overall, the optimal loading condition can decrease the RMS pitch motions by 1.72% in averaged from the initial.

Table 7.12. The comparison of RMS pitch response ($\sqrt{m_0}$) in degree

	Tp (s)								
	3.5	**4.5**	**5.5**	**3.5**	**4.5**	**5.5**	**3.5**	**4.5**	**5.5**
***Hs* (m)**	**Original**			**LC 9**			**Difference**		
0.25	1.013	0.665	0.490	0.999	0.653	0.480	-1.35%	-1.78%	-2.05%
0.75	3.038	1.994	1.471	2.997	1.958	1.441	-1.35%	-1.78%	-2.05%
1.25	5.063	3.323	2.452	4.995	3.264	2.402	-1.35%	-1.78%	-2.05%
Average							**-1.72%**		

Table 7.13. The comparison of mean added resistance in kilo Newton.

	Tp (s)								
	3.5	**4.5**	**5.5**	**3.5**	**4.5**	**5.5**	**3.5**	**4.5**	**5.5**
***Hs* (m)**	**Initial**			**Optimum**			**Difference**		
0.25	0.049	0.020	0.011	0.043	0.018	0.010	-11.88%	-10.06%	-10.67%
0.75	0.437	0.184	0.096	0.385	0.165	0.086	-11.88%	-10.06%	-10.67%
1.25	1.214	0.510	0.267	1.070	0.459	0.238	-11.88%	-10.06%	-10.67%
Average							**-10.87%**		

The final assessment for seakeeping in this study is added resistance. There is no particular criterion established for added resistance. Hence, the optimal loading condition was solely assessed based on their reduction from the initial one. The mean added resistance results ($2m_0$) and the percentage reduction in added resistance are presented in Table 7.13. As the peak period (*Tp*) varies, so does the average reduction. Even when *Hs* changes, the reduction remains consistent at the same *Tp*. This finding suggests that *Tp* also influences added resistance. The averaged reduction in added resistance for the optimal loading condition is 10.16%.

7.3.6. The Influence of Design Variables to Calm Water Resistance

In the previous section, it was established that *LCG* and *KG* affect the R_y value, which in turn impacts seakeeping performance. This study seeks to explore how these parameters influence total resistance in calm water using a similar optimisation process. In this investigation, the calm water resistance was set as an objective function to be minimised with the same design variables. The impact of *LCG* and *KG* on total resistance in calm water is evident from the derived mathematical model and the response surface figure.

Table 7.14 details the total resistance for each load case variation based on the Central Composite Design. This data was utilised to formulate the mathematical model, represented in Eq. (7.6), which boasts an R^2 value of 0.9757. It means that according to this model, *LCG* and *KG* account for 97.57% of the total resistance of FAO-01, with the remaining 2.43% attributed to an unknown factor.

Figure 7.9 shows the response surface based on the mathematical model from Eq. (7.6) and the plot of actual RT based on CFD versus predicted RT based on Eq. (7.6). It is shown that the R^2 of Eq. (7.6) is lower than that of Eq. (7.3), indicating that the predicted and actual data is not closely aligned. However, the results of the mathematical model are still considered accurate.

Table 7.14. Responses of RT for FAO-01

Loading Condition	**X_1**	**X_2**	***LCG***	***KG***	**RT CFD (N)**
Initial	0	0	0.945	0.379	15.162
LC 1	1	1	0.992	0.398	15.225
LC 2	1	-1	0.992	0.360	15.253
LC 3	-1	1	0.898	0.398	15.316
LC 4	-1	-1	0.898	0.360	15.397
LC 5	-1.414	0	0.878	0.379	15.543
LC 6	1.414	0	1.012	0.379	15.287
LC 7	0	-1.414	0.945	0.352	15.174
LC 8	0	1.414	0.945	0.406	15.160

$$RT\ (N) = 15.162 - 0.0746x_1 - 0.0161x_2 + 0.1282{x_1}^2 + 0.0042{x_2}^2 + 0.0132x_1x_2 \tag{7.6}$$

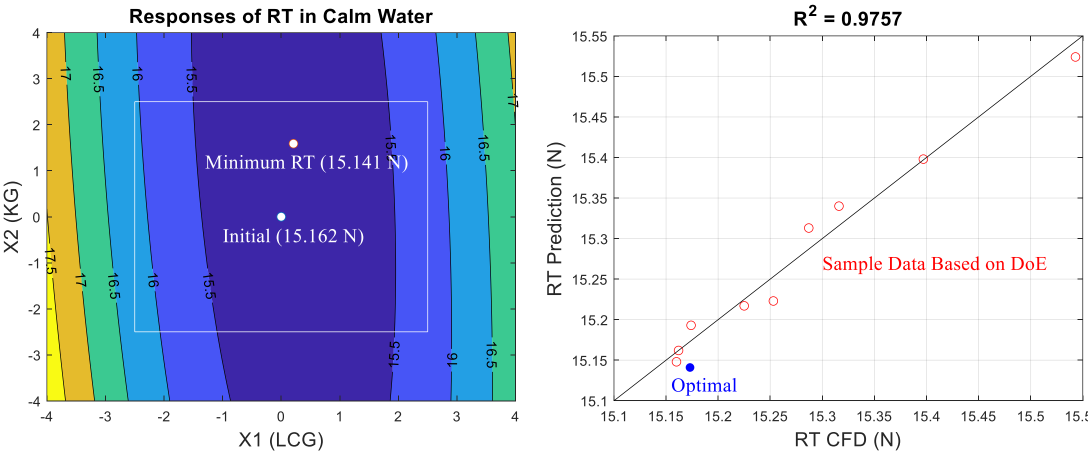

(a) (b)

Figure 7.9. The responses surface of RT Influenced by *LCG* and *KG* with the constrains and optimal location (a) and the comparison between actual and prediction of RT (b)

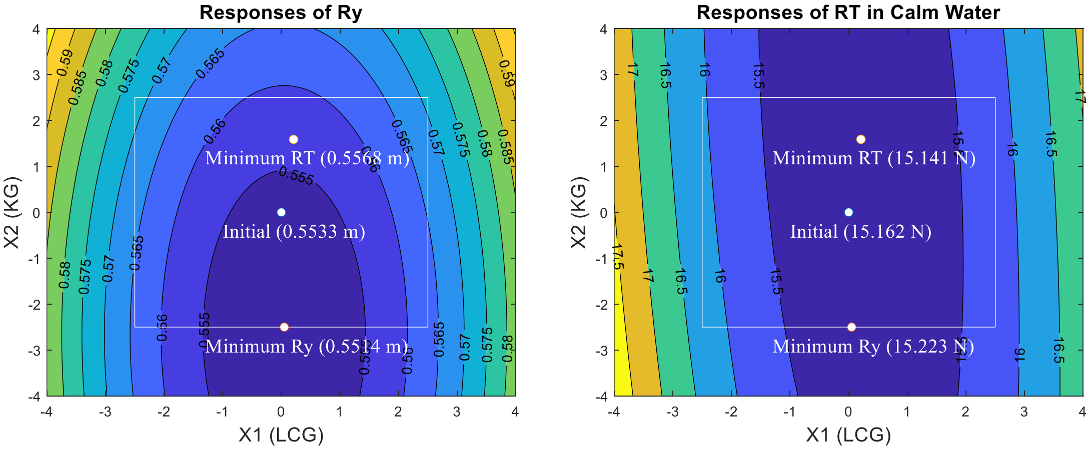

Figure 7.10. Response Surface Result for R_y (a) and RT (b) Influenced by *LCG* and *KG* with the constrains and optimal location

Figure 7.10 depicts the comparison between the optimal locations of *LCG* and *KG* for R_y and the total resistance (RT). The prediction of R_y and RT value based on the combination of the best X_1 and X_2 in R_y and RT was determined using Eq. (7.3) for R_y and Eq. (7.6) for RT. Unlike the R_y response, *KG*'s influence on RT is negligible compared to that of *LCG*. The optimal *KG* is positioned higher than the initial *KG*, whereas the optimal *LCG* is close to the initial condition. According to Eq. (7.6), optimal loading condition in R_y yields a total resistance of 15.223, which is 0.54% higher than optimal loading condition in RT and 0.4% higher than the initial condition. However, this increase in RT is not significant. Details of these comparisons are presented in Table 7.15. This suggests that the improvement in seakeeping does not significantly affect the total resistance in calm water, as the *LCG* location is not much different compared to the location for minimum RT.

Table 7.15. The RT comparison for minimum R_y and RT

Loading Condition	x_1	x_2	***LCG* (m)**	***KG* (m)**	**RT CFD (N)**	**RT Eq.** (7.6) **(N)**
Initial	0.00	0.00	0.945	0.379	15.162	15.162
Minimum R_y	0.050	-2.50	0.947	0.332	15.165	15.223
Minimum RT	0.209	1.588	0.955	0.409	15.173	15.141
Minimum R_y and initial difference (%)					**0.020%**	**0.402%**
Minimum RT and initial difference (%)					**0.073%**	**-0.136%**

Table 7.15 compares the total resistance in calm water between the initial and the optimal loading condition in RT. According to Eq. (7.6), the optimal *LCG* and *KG* in RT can reduce total resistance by up to 0.136%, a minimal reduction of less than 1%. The predicted results might differ from the actual CFD-based values due to lower accuracy compared to the R_y optimisation.

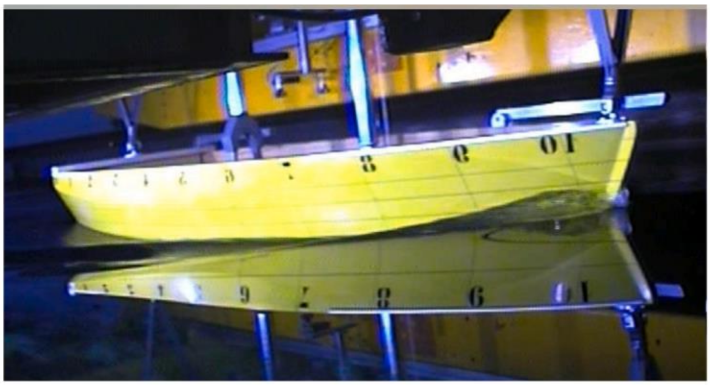

(Initial – experimental result from Pérez-Arribas et al (2022)

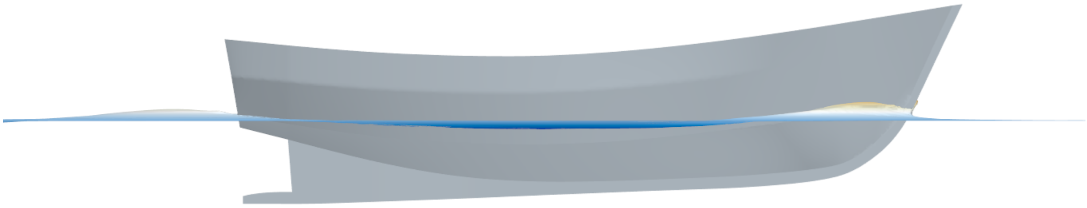

(Initial – resulting trim = 0.27°)

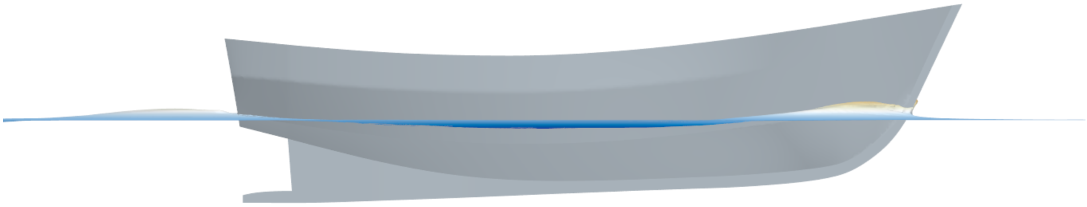

(Minimum R_y – resulting trim = 0.33°)

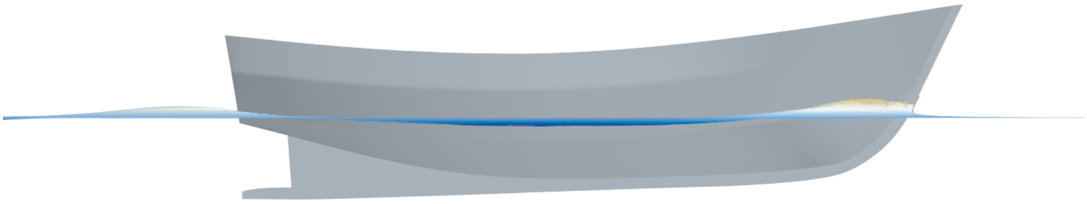

(Minimum RT – resulting trim = 0.88°)

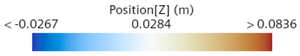

Figure 7.11. the Visualisation of free surface wave elevation on hull

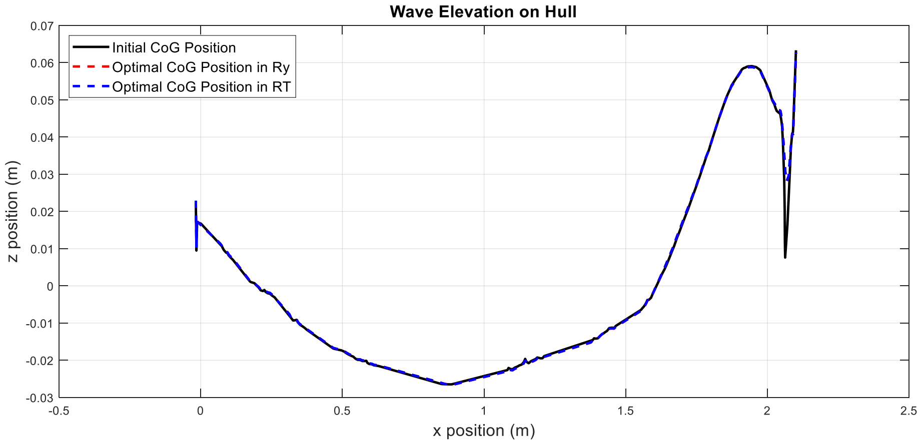

Figure 7.12. Comparison of free surface wave elevation on hull between different *CoG* position

When a CFD simulation was conducted for the optimum loading condition in RT, the result was slightly higher than the predicted value, with a difference of 0.21%. This discrepancy, considered a low error, shows that the optimal results had a marginally higher value of 0.073% compared to the initial condition. This negligible difference lies within the predicted discretisation uncertainty obtained in Table 7.7.

These findings suggest that the best position for *LCG* and *KG* in minimising R_y improving the seakeeping performance but does not significantly change total resistance. Finally, Figure 7.11 presents the CFD-based comparison between the initial and optimal *CoG* position in R_y and RT. The figure also compares the free surface elevation around hull based on experiments conducted by Pérez-Arribas et al (2022). Both optimal *LCG* for minimal R_y and RT shift to the bow, resulting in changes in trim by bow. Since the total resistance shows no significant difference, the wave amplitudes on the hull also appear similar to the initial conditions, as shown in Figure 7.12.

7.4. Summary

In this study, a single-objective function in seakeeping optimisation was successfully demonstrated for the FAO-01 fishing vessel. This objective function, the radius of gyration in the y-direction (R_y), is minimised by varying *LCG* and *KG*. The response surface method was used as the optimisation technique, and Central Composite Design was utilised as the design of experiment to construct a mathematical model of the responses. The optimal loading condition results in the minimum R_y.

The initial and optimal conditions were also compared under parametric roll conditions using CFD simulations. The initial condition was configured to induce parametric roll. Subsequently, under the same conditions, the optimal loading conditions demonstrated their ability to prevent parametric roll and the perilous phenomenon of capsizing.

Following this, CFD simulations were conducted to compare the seakeeping performance, specifically heave, pitch, and added resistance, for both the initial and optimal loading conditions. The transfer function of heave, pitch, and added resistance for the optimal one exhibited a diminished transfer function when λ/L exceeds the resonance condition.

Furthermore, the assessment of seakeeping continued with the performance in irregular waves. Three distinct *Tp* and *Hs* values, derived from the highest occurrences in the Java Sea, were utilized. The optimal loading condition demonstrated superior seakeeping performance compared to the initial condition, reducing RMS vertical acceleration, RMS pitch amplitude, and mean added resistance by up to 3.12%, 1.72%, and 10.87%, respectively.

From the above findings, it is evident that this single objective functions, minimising R_y, has proven successful and is viable for seakeeping optimisation. The improved seakeeping performance under the optimum is notably enhanced compared to the initial. This objective function is useful and applicable to simplify the complexity of seakeeping optimisation process.

The influence of the same design variables was successfully analysed by using total calm water resistance (RT) as an objective function to be minimised. As predicted by the mathematical model, the optimal loading condition in RT can reduce the total resistance by up to 0.136%. However, the CFD-based results for optimal loading condition in RT showed an increase in total resistance by 0.073%, indicating that both design variables have no significant impact on total resistance. This finding also indicates that optimal loading condition in R_y exhibits no significant difference in total resistance compared to optimal loading condition in RT (0.54% higher) and the initial condition (0.4% higher). Improving seakeeping performance by minimising R_y can enhance seakeeping indirectly without significantly increasing total resistance in calm water.

8. Minimising *GM* Ratio to Enhanced Seakeeping Performance of Small Fishing Vessels

8.1. Introduction

The presence of fishing vessels in Indonesia is crucial for ensuring the country's food security through the maritime sector, as highlighted by Bappenas (2010). These vessels not only provide a steady supply of fish, enhancing food security, but also contribute significantly to the welfare and sustenance of the local population. However, the fishing industry, particularly on a large scale, faces some challenges related to sustainability and environment. One of them is to avoid overfishing and to employ environmentally friendly fishing practices that do not involve harmful equipment. In this context, small fishing vessels offer a promising solution. They are less likely to engage in overfishing and are more adaptable to sustainable practices.

However, as mentioned in the previous chapter, there are so many accidents occurred by small fishing vessels. They frequently encounter challenges due to their size during operations. Optimising the hull forms of these small vessels can further enhance their seakeeping performance, making them safer in various sea conditions. Accidents primarily arise from two sources: human factors (Obeng et al., 2022a), and environmental conditions such as poor weather, strong winds, and high waves (Jin and Thunberg, 2005). These factors reduce the operability of fishing vessels, with small fishing boats being particularly prone to accidents (Ugurlu et al., 2020; Wang et al., 2005). Enhancing the seakeeping performance of the vessels can mitigate these risks by conducting the seakeeping optimisation.

Seakeeping optimisation can significantly enhance the safety and operational performance of ships. This process involves minimising various ship responses as objective functions such as heave, pitch, roll, vertical and lateral accelerations, slamming, and deck wetness. While the previous chapter involve the position of centre of gravity, this chapter involve deforming the hull form in seakeeping optimisation.

The hull shape affects the seakeeping performance of the vessel, including the stability and total resistance. Technique in deforming the hull form used in this chapter is the Leckenby (1950) method, which is the simplest because only adjusting the Curve of Sectional area by shifting the location of longitudinal of centre of buoyancy and determine the block coefficient. Depending on the objective functions, the resulted hull form based on both parameters can enhance the ship performance, such as minimising heave, pitch and resistance (Huang et al., 2015; Kim and Yang, 2010), minimising vertical motion (Utomo and Iqbal, 2020), and minimising vertical acceleration (Sarıöz, 2009). This chapter use the *GM* ratio as the objective function to be minimised by varying the longitudinal of centre of buoyancy and block coefficient in deforming the hull form of fishing vessels.

Fishing vessels, by their nature, experience constant changes in loading conditions, leading to continuous variations in displacement and the position of the centre of gravity during fishing operations. These changes impact the metacentric height (*GM*). In wave conditions, the *GM* value differs from that in calm water, making it essential to determine the optimal hull form with a low *GM* ratio (the ratio between *GM* in waves and calm water). Once the best hull form is identified, the optimal centre of gravity position for the best hull form is determined by minimising the radius of gyration in the y direction (R_y), as applied in Chapter 7.

The overall aim of the present work is to enhance the seakeeping performance of a fishing vessel using the novel objective functions, the *GM* ratio and R_y. The Unsteady Reynold-Average Navier Stokes CFD method is employed to compare the RAO of heave, pitch, and added resistance coefficient between the initial and optimal hull forms, without involving the optimisation process. A spectral (short-term) analysis is conducted using three different peak periods (*Tp*) and significant wave heights (*Hs*), representing the majority of annual wave conditions in the Java Sea. Finally, the JONSWAP spectrum is utilised to assess the seakeeping performance under both initial and optimised conditions.

8.2. Methodology

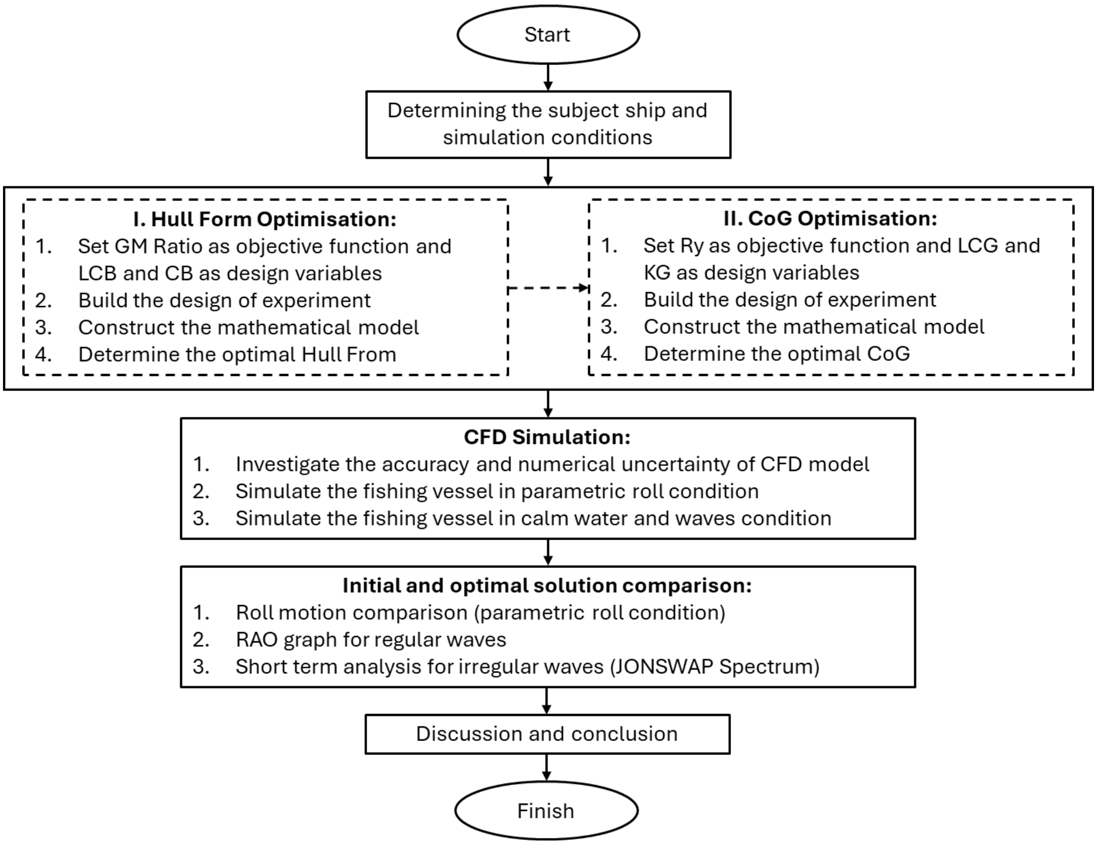

Figure 8.1. Research flowchart

Figure 8.1 illustrates the research flowchart. This study begins by determining the subject ship and simulation conditions, as described in subsection 3.1. This is followed by optimisation process, which include two types of optimisations: hull form and Centre of Gravity (*CoG*) optimisations. Once the optimal hull form is determined, the optimal *CoG* for the optimal hull form must be established, as detailed in subsection 3.2. The next step involves conducting CFD simulations, which cover parametric roll, calm water, and wave conditions. These simulations were undertaken only after completing the studies on accuracy and numerical uncertainty, with the numerical set-up described in subsection 3.3. After the results of CFD simulations are obtained, a comparison between the initial and optimal hull form is made. The results and discussion, as well as the conclusions, are presented in sections 4 and 5, respectively.

8.2.1. Objective Function and Design Variables

The dynamic loading conditions of fishing vessels, with changing displacement and centre of gravity during fishing, impact the metacentric height (*GM*). Variations in hull form result in different *KM* values, affecting *GM*, as *GM* = *KM* - *KG*. The *GM* value also differs between calm water and wave conditions, making it essential to determine the best hull form with a low *GM* ratio (the ratio between *GM* in waves and calm water).

This chapter utilises a novel single objective function, the *GM* ratio, to be minimised by deforming hull forms. The Longitudinal Centre of Buoyancy (*LCB*) and Block Coefficient (*CB*) are selected as design variables to create a new hull form, based on Lackenby (1950) method. Once the best hull form is identified, the optimal centre of gravity is determined by minimising the radius of gyration in the y direction (R_y), another novel objective function applied in Chapter 7.

The dynamic loading conditions, where the fish tank starts empty and gradually fills, shift the vessel's displacement and *CoG* both longitudinally (*LCG*) and vertically (*KG*). Minimising R_y helps find the optimal positions for *LCG* and *KG*, enhancing stability and performance.

In calm water, the transversal *GM* is crucial for static stability, allowing the ship to return to an upright condition even with a low *GM*. However, in waves, the *GM* must also be considered due to the risk of parametric roll. The Second Generation of Intact Stability (SGIS) framework uses the *GM* ratio, combining *GM* in waves (ΔGM) and in calm water (GM_{calm}), as shown in Figure 8.2 and Eq. (8.1). GM_{max} and GM_{min} represent the maximum and minimum *GM* in waves.

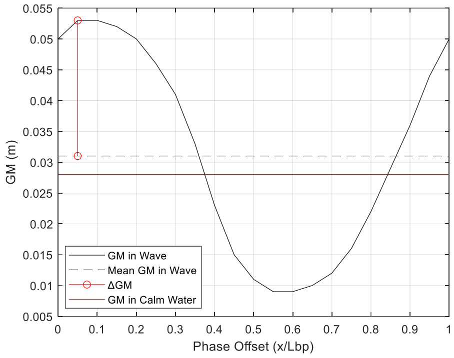

Figure 8.2. Illustration of *GM* ratio

$$GM\ Ratio = \frac{\Delta GM}{GM_{calm}} = \frac{0.5(GM_{max} - GM_{min})}{GM_{calm}} \tag{8.1}$$

The *GM* ratio serves as an initial check for parametric roll in Second Generation of Intact Stability (SGIS) from IMO. According to the Mathieu Equation, heave and pitch in certain wave periods can induce parametric roll. Based on the previous observation in Chapter 6, a low *GM* ratio indicates low amplitudes of heave and pitch, reducing the risk of parametric roll. Figure 8.3 shows that a lower *GM* ratio correlates with reduced heave and pitch amplitudes, enhancing seakeeping performance.

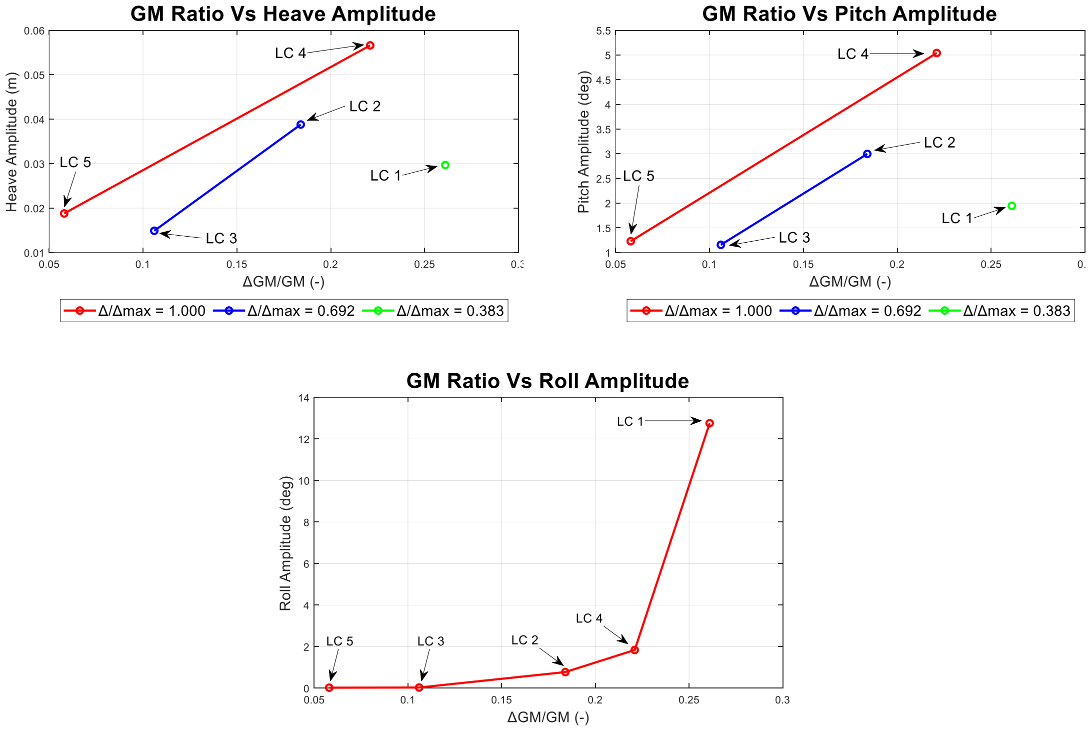

Figure 8.3. The influence of *GM* ratio to the heave, pitch, and roll amplitude (Iqbal et al., 2024).

The *GM* ratio is used as an objective function to be minimised through hull form adjustments. Variations in hull forms lead to different *KM* values, and consequently, different *GM* values. The optimisation process involves adjusting the Longitudinal Centre of Buoyancy (*LCB*) and Block Coefficient (*CB*) using the Parametric Transformation module in Maxsurf Modeler software, based on the Lackenby method (1950). Throughout this process, the ship's length (L_{BP}), draft (*T*), and displacement (Δ) are kept constant, while the breadth (*B*) is modified to achieve the desired *LCB* and *CB*. This method proves particularly useful during the design phase, enabling designers to identify the optimal configuration.

Table 8.1. Design variable and code for transforming the hull form

Design Variables	**FAO-01**		
	-1	**0**	**1**
***LCB* (%), x_1**	51.196	53.890	56.585
***CB* (-), x_2**	0.254	0.267	0.280

Table 8.1 presents the design variables and their corresponding codes for this scenario. Notably, the Longitudinal Centre of Buoyancy (*LCB*) is measured from the forward perpendicular (*FP*) as a percentage of the length between perpendiculars (L_{BP}). For each hull form, the *GM* ratio is calculated using Eq. (8.1), yielding GM_{max} and GM_{min}, the maximum and minimum *GM* values achieved in waves. Both values were computed using the Maxsurf Stability software.

During the calculation of *GM* in waves, the wave conditions employed according to ABS (2019), which are $\lambda/L_{bp} = 1.0$ and H_w/λ in this case is 0.03. *LCG* and *KG* for all hull form variations remain consistent with the initial hull form, where *LCG* is assumed to be equal to LCB in even keel conditions. *KG* is assumed to be 80% *KM* to achieve a high *GM* ratio. Once the optimal hull form is achieved, this optimisation is followed by optimising the loading condition/*CoG* of the optimal hull by changing the *LCG* and *KG* with the same procedure. Once the optimum hull form is determined, the optimum location of Centre of Gravity (*CoG*) must be determined by minimising the radius of gyration in y direction (R_y), as applied in Chapter 7.

8.3. Results and Discussion

8.3.1. Hull Form Optimisation Results

The result of *GM* ratio for each variation in design of experiment are shown in Table 8.2. Based on the table, a mathematical model was formulated to describe the influence of these two variables on *GM* ratios. The result of the mathematical model is shown in Eq. (8.2). The equation attains an R^2 value of 0.9945, indicating that changes in the *LCB* and *CB* values can account for changes in the *GM* ratio up to 99.45%.

Based on Eq. (8.2), the response surface of the *GM* ratio can be visualised, as depicted in Figure 8.4-a, enabling determination of the optimum location on the resulting surface. The rectangle represents the constraint, with the point indicating the minimum response location within it. The plot results between the predicted and actual *GM* Ratio are shown in Figure 8.4-b, to show the accuracy of mathematical model of Eq. (8.2). According to Eq. (8.2), the minimum response is 0.0541, achieved with $x_1 = -2.5$ and $x_2 = 0.342$. Upon conversion of the code to actual values, the *LCB* is determined to be 47.093% from the *FP*, and *CB* is 0.272, which determine the optimum hull form.

Table 8.2. Responses of *GM* ratio

Hull Form	**X_1**	**X_2**	***LCB* (%)**	***CB* (-)**	***GM* Ratio (-)**
Initial	0	0	53.890	0.267	0.1535
F-1	1	1	56.585	0.280	0.2500
F-2	1	-1	56.585	0.254	0.1903
F-3	-1	1	51.196	0.280	0.1237
F-4	-1	-1	51.196	0.254	0.1019
F-5	-1.414	0	50.079	0.267	0.0940
F-6	1.414	0	57.701	0.267	0.2267
F-7	0	-1.414	53.890	0.248	0.1400
F-8	0	1.414	53.890	0.286	0.1905

$$GM\ Ratio = 0.1535 + 0.0503x_3 + 0.0191x_4 - 0.0043{x_3}^2 + 0.0068{x_4}^2 + 0.0095x_3x_4 \tag{8.2}$$

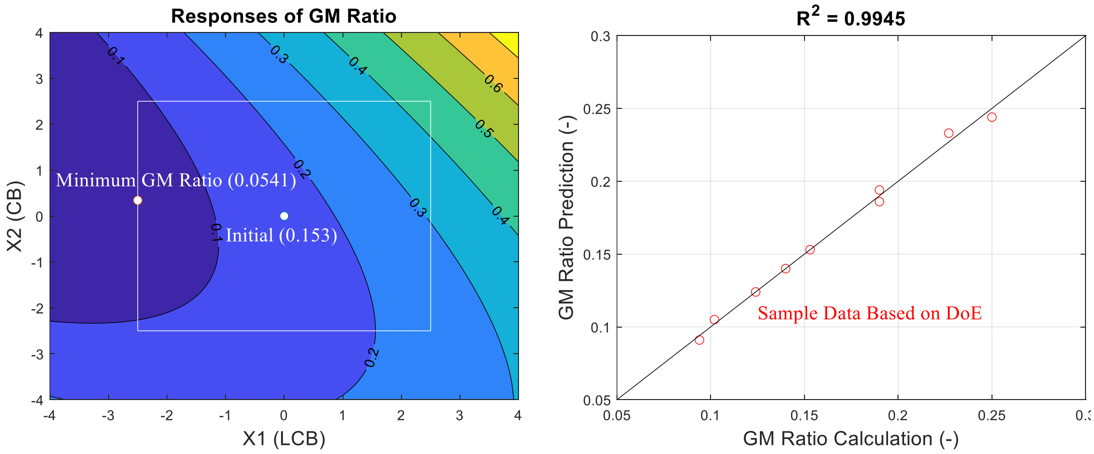

(a) (b)

Figure 8.4. The responses surface of *GM* ratio influenced by LCB and CB with the constrains and optimal location (a) and the comparison between actual and prediction of RT (b)

A comparison of the lines plan between the initial and optimum hull forms is presented in Figure 8.5. It is essential to note that to maintain the displacement, length, and draft of the fishing boat unchanged, the breadth is adjusted. With the increased optimal CB, the breadth is adjusted to be smaller, resulting in an optimal beam of 0.666 m, whereas the original breadth is 0.678 m.

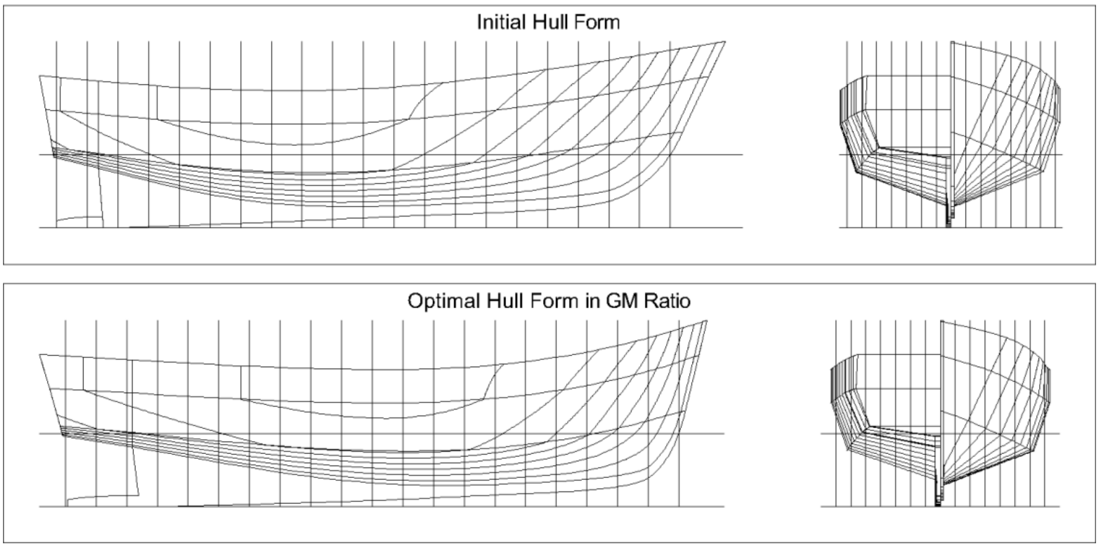

Figure 8.5. Hull form comparison between original (a) and optimal (b)

The *GM* ratio of the optimal hull form is 0.0758, marginally higher than that predicted by the mathematical model. A comparison of the *GM* ratios between the initial and optimal hull forms, as determined by calculation and the mathematical model, is presented in Table 8.3. The optimal hull form demonstrates a potential reduction in the *GM* ratio of up to 50.46% according to the calculation and 64.75% according to the prediction from the mathematical model. These findings suggest the efficacy of the optimisation process.

Table 8.3. The comparison between the original and optimum condition R_y for FAO-01 shifting load scenario.

Hull Form	x_1	x_2	**LCB (%)**	**CB (-)**	***GM* Ratio (-)**
Initial	0.00	0.00	53.890	0.267	0.1530
Optimal	-2.50	0.342	47.154	0.272	0.0758
				Difference (%)	**-50.46**

8.3.2. Centre of Gravity Optimisation Results

When calculating *GM* in waves in the previous optimisation, *LCG* and *KG* for all hull form variations were assumed to be the same as the initial hull form. Therefore, it is essential to determine the optimum *CoG* for the optimal hull form by minimising the radius of gyration in y-axis (R_y) with varying the *LCG* and *KG*. The R_y optimisation procedure is therefore applied. There are nine combinations of loading conditions, LC 1 to LC 8 plus initial loading conditions (initial LC), where *LCG* was set as the same value of *LCB* in zero trim and *KG* was set as 75% of *KM*.

Table 8.4 shows the comparison between the initial and optimal loading conditions. The optimum loading condition has a minimum R_y and can achieve a reduction of up to 1.7% compared to the initial condition. This condition causes the vessel to trim by 1.73° by the stern. The *GM* ratio of the optimum loading condition was reduced by up to 42.02% from the initial loading condition. This comparison demonstrates the success of the optimisation in achieving a low *GM* ratio. The optimal hull form, along with the optimal loading condition, will be used for CFD-based simulations for seakeeping and calm water resistance predictions and will be compared with the initial form in the following subsection.

Table 8.4. The comparison initial and optimal loading conditions for optimal hull form

Loading Condition	***LCG* (m)**	***KG* (m)**	**Trim**	**R_y**	***GM* Ratio (-)**
Initial	1.084	0.387	0.00°	0.5727	0.119
Optimal	0.994	0.339	1.73° (by stern)	0.5630	0.069
			Difference (%)	**-1.70%**	**-42.02%**

8.3.3. Results of Seakeeping Performance in Parametric Roll Condition

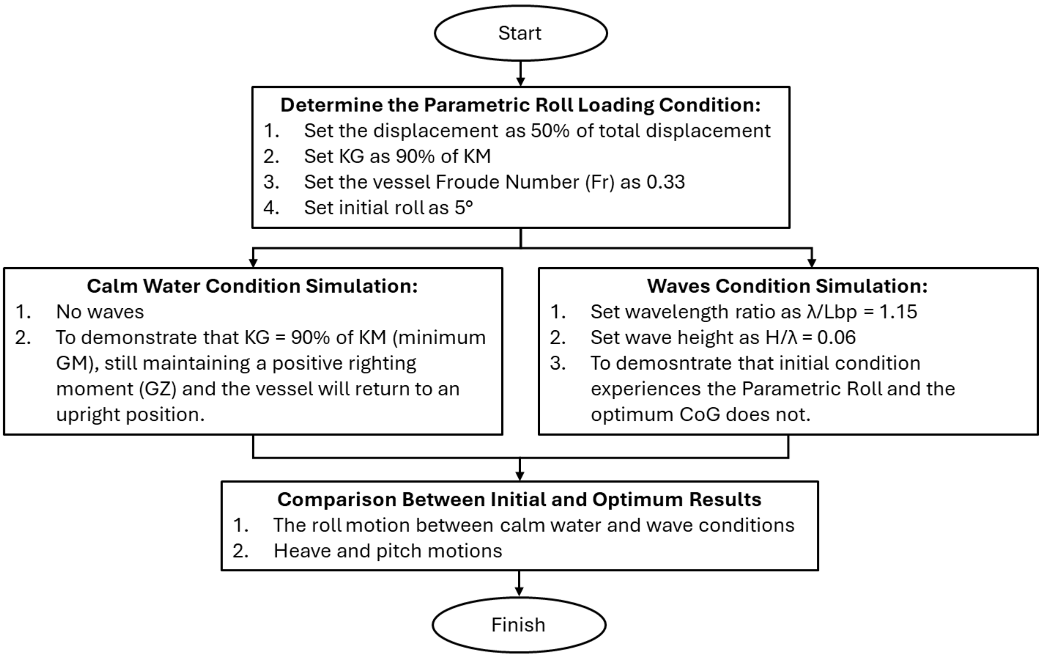

Figure 8.6. Flowchart of parametric roll simulation

Based on IMO regulations, the *GM* ratio serves as the primary indicator to assess whether a ship may experience parametric roll. This subsection aims to demonstrate that the optimisation process, addressing both objective functions (*GM* ratio and then minimising R_y), can capsize due to parametric roll. To ensure an equal comparison with seakeeping simulations devoid of parametric roll (in the following subsection), the wave condition and the forward speed of the fishing vessel remained consistent. Figure 8.6 illustrates the flowchart of the parametric roll simulation, the same procedure described in Chapter 7.

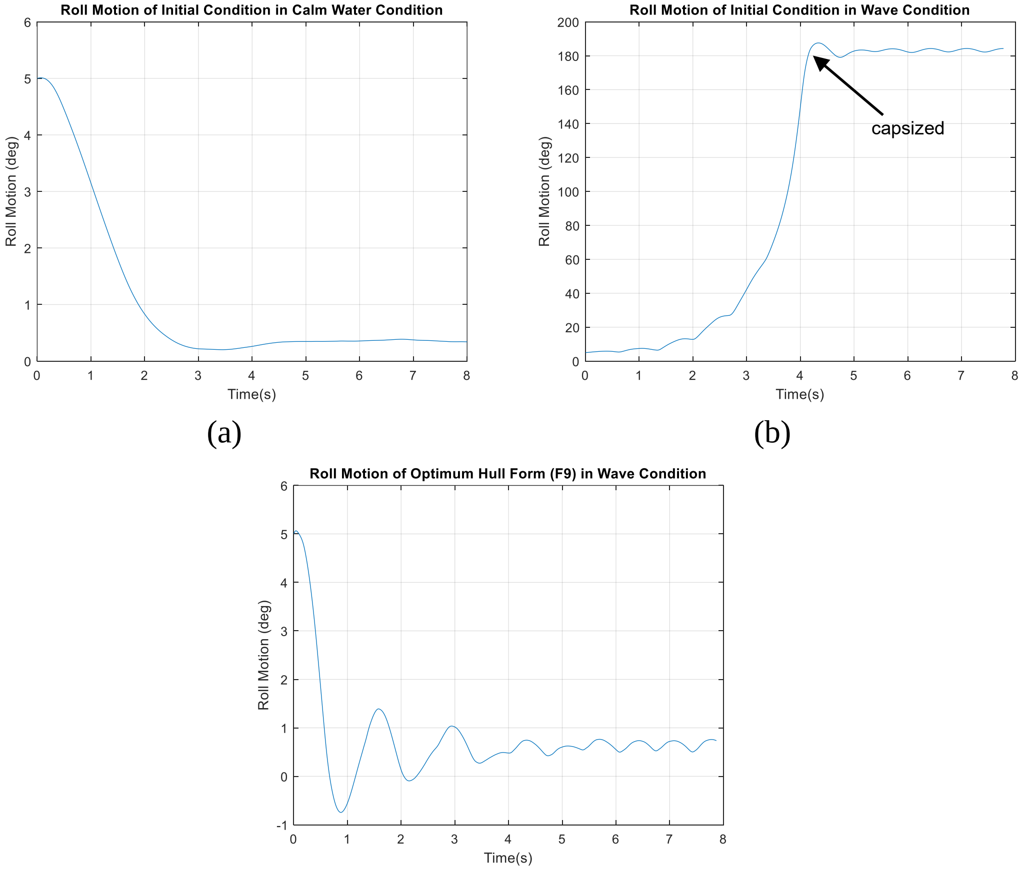

(a) (b)

(c)

Figure 8.7. The comparison of roll motion of initial condition in calm water and wave conditions and optimum condition

Figure 8.7-a and -b show the comparison of roll motion for the initial loading condition in both calm water and waves. It is evident that the combination of loading conditions and waves induces parametric roll and capsize. However, the optimal hull form, which has a minimum *GM* ratio and R_y, can prevent this accident, as shown in Figure 8.7-c.

Figure 8.8 illustrates the heave and pitch responses of both the initial and optimal hull forms. The initial hull form resulted in capsizing, leading to unstable responses due to changes in the hull shape below the waterline before and after capsizing. In contrast, the optimal hull form, which is stable and does not capsize, exhibits heave and pitch motions as expected.

Figure 8.9 presents the results of CFD simulations for three cases. In Figure 8.9-a, it is evident that the vessel can return to an upright position from its initial roll of 5° in calm water. When waves are involved, the initial hull form capsizes, whereas the optimal hull form remains safe. The illustrations of the capsize and non-capsize conditions are shown in Figure 8.9-b and -c, respectively. Based on this simulation, minimising *GM* ratio and R_y as a novel objective function in seakeeping optimisation can prevent the fishing vessel from parametric roll-driven capsize.

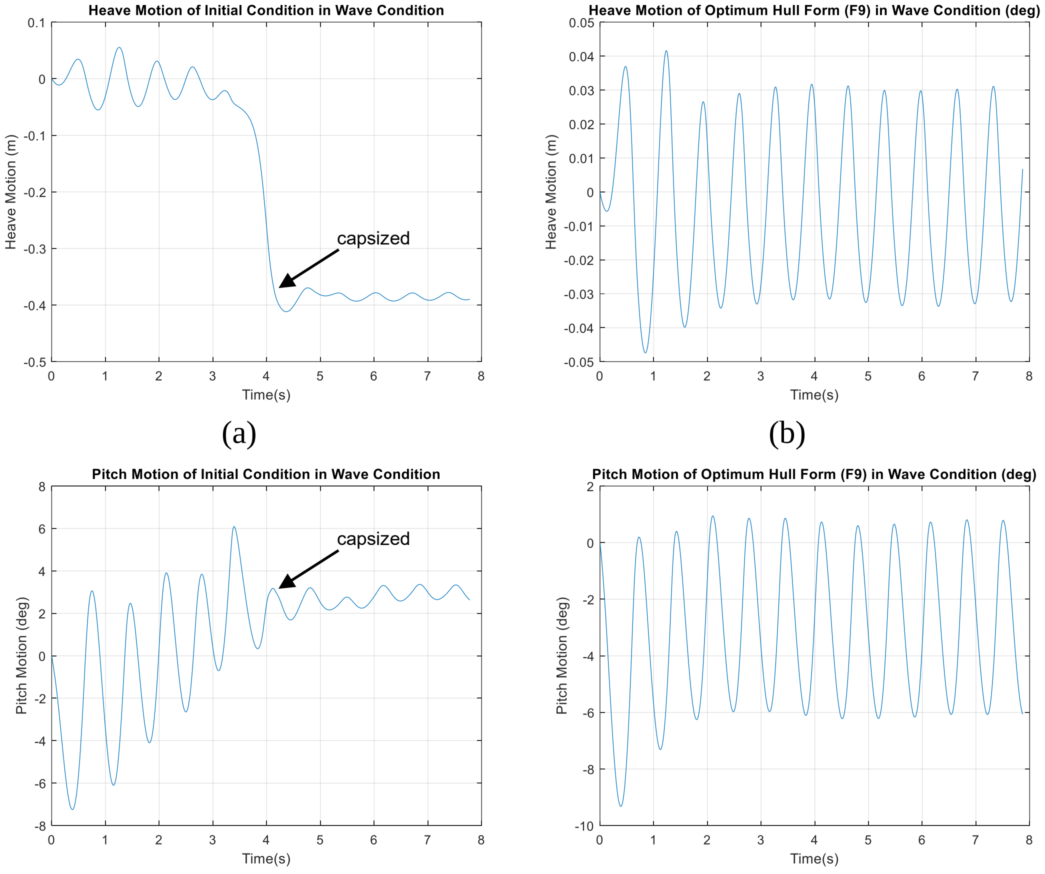

(a) (b)

(c) (d)

Figure 8.8. The comparison of heave motion of fishing vessel between original condition (left) and optimum model (right)

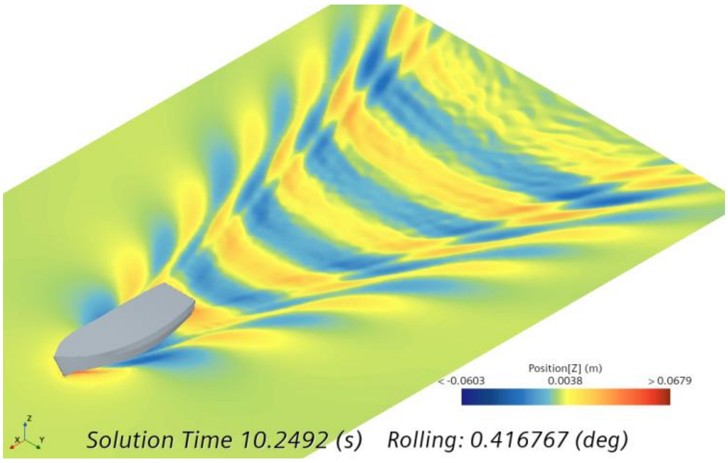

(a) Initial loading condition in calm water (not capsized)

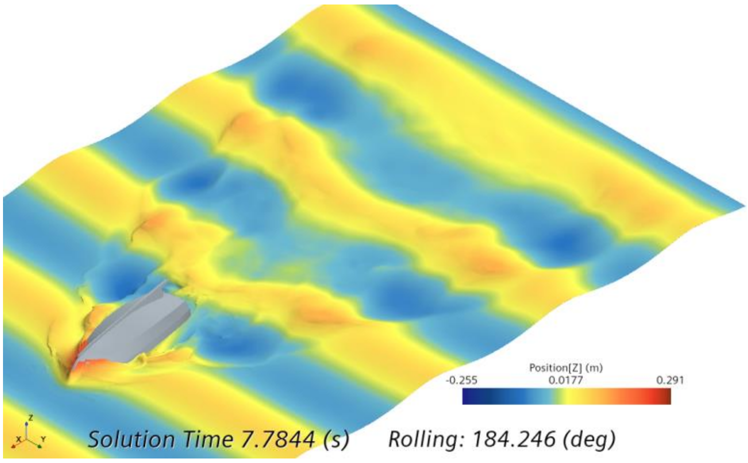

(b) Initial loading condition in waves (capsized)

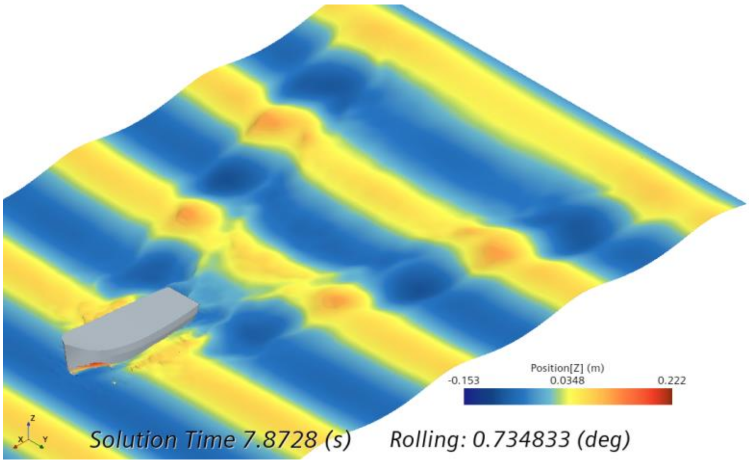

(c) Optimal hull form with optimal loading condition (not capsized)

Figure 8.9. The result s of CFD-based simulation for roll motion of fishing vessel between original condition in calm water (a) and wave conditions (b), optimum hull form with optimum R_y (c)

8.3.4. Results of Seakeeping Performance in Regular Waves

As stated in Chapter 7 to determine the added resistance, the total resistance in calm water must first be determined. Table 8.5 shows the calm water total resistance of the optimal hull form in the *GM* ratio. The results are also compared with the initial hull form to observe the differences between the two hull forms.

Based on Table 8.5, the optimal hull form in the *GM* ratio results in higher total resistance. The shape in the bow region becomes larger as a consequence of the LCB of the optimal hull form moving forward to the bow region. This change increases the pressure force, as shown in Figure 8.10, and raises the wave height on the hull, as shown in Figure 8.11 and Figure 8.12.

The CFD results for heave, pitch, and roll motions, along with the total resistance in waves, display periodic time dependencies. Consequently, Fourier Transform Analysis was employed to ascertain the motion amplitudes for each wavelength ratio (λ/L), facilitating the creation of RAO curves. Eq. (8.3) and Eq. (8.4) were utilised for this purpose, with Eq. (8.3) applied to translational and rotational motions, and Eq. (8.4) used to determine the RAO for added resistance coefficient.

Table 8.5. The RT comparison between initial and optimal hull forms

Hull Form	x_1	x_2	**LCB (%)**	**CB (-)**	**RT CFD (N)**
Initial	0.00	0.00	53.820	0.267	15.162
Optimal	-2.50	0.342	47.093	0.272	19.632
				Difference (%)	**29.49**

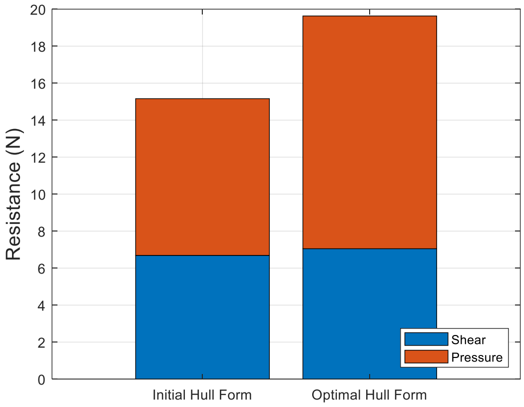

Figure 8.10. Comparison of total resistance decomposition between initial and optimal hull forms

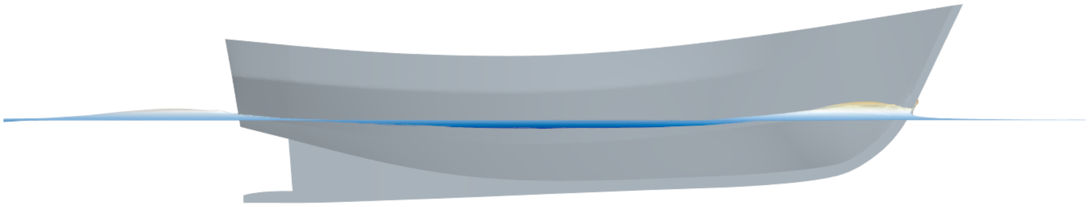

(Initial Hull Form – Resulted Trim = 0.27°)

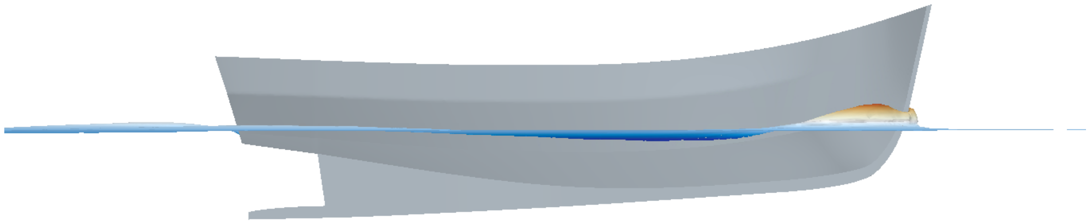

(Optimal Hull Form – resulting trim = -2.47°)

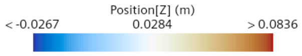

Figure 8.11. Result of CFD resistance simulation at Fr = 0.33

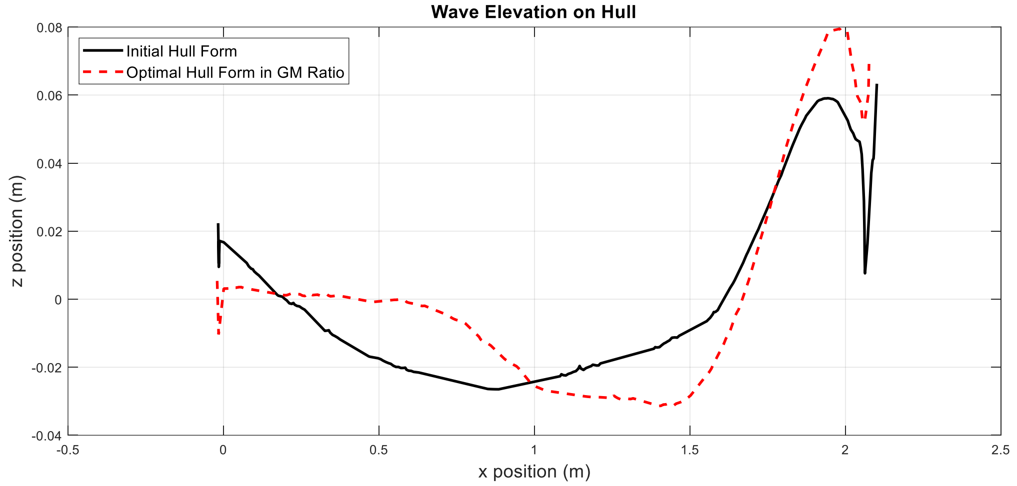

Figure 8.12. Comparison of wave elevation on the hull between different hull forms

$$RAO = \frac{z_a\ (m)}{\zeta\ (m)};\ RAO = \frac{\theta_a\ (rad)}{k\zeta\ (rad)} \tag{8.3}$$

$$C_{AW} = \frac{Mean\ RT_{wave} - RT_{calm}\ (N)}{\rho g \zeta^{\,2}(B^2/L)(N)} \tag{8.4}$$

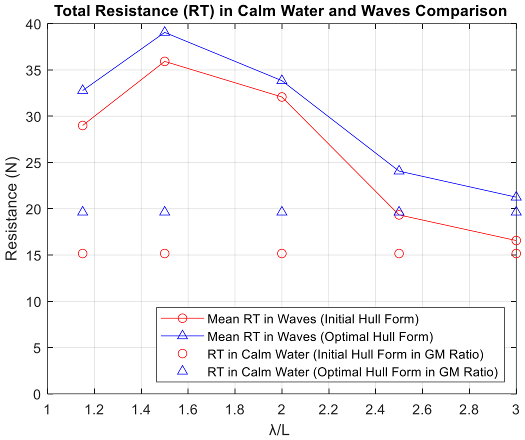

Figure 8.13. Total resistance in calm water and mean total resistance in waves

Figure 8.13 displays the mean total resistance in waves and the total resistance in calm water for both the initial and optimal hull forms. The difference between the mean total resistance in waves and the total resistance in calm water represents the added resistance. The figure indicates that the optimal hull form increases the total resistance in calm water by up to 33%, resulting in a higher mean total resistance in waves compared to the initial hull form. However, when comparing the added resistance of both hull forms, the optimal hull form performs better, as its added resistance is lower than that of the initial hull form, as shown in Table 8.6 and Figure 8.14.

Table 8.6 and Figure 8.14 compare the RAOs of the initial and optimal hull forms (with the optimal *CoG*). These results indicate that the RAOs for heave, pitch, and added resistance coefficients for the optimal hull form are lower across all wavelength ratios. This signifies a successful enhancement in seakeeping performance through the optimisation process.

Table 8.6. Response amplitude operator comparison

λ/L	**Initial**			**Optimal**		
	Heave TF	**Pitch TF**	**CAW**	**Heave TF**	**Pitch TF**	**CAW**
1.15	0.320	0.225	1.035	0.264	0.195	0.983
1.5	0.917	0.570	1.553	0.842	0.536	1.453
2	1.387	1.105	1.265	1.218	1.037	1.063
2.5	1.069	1.153	0.312	1.029	1.054	0.332
3	0.983	1.075	0.105	0.970	1.015	0.121

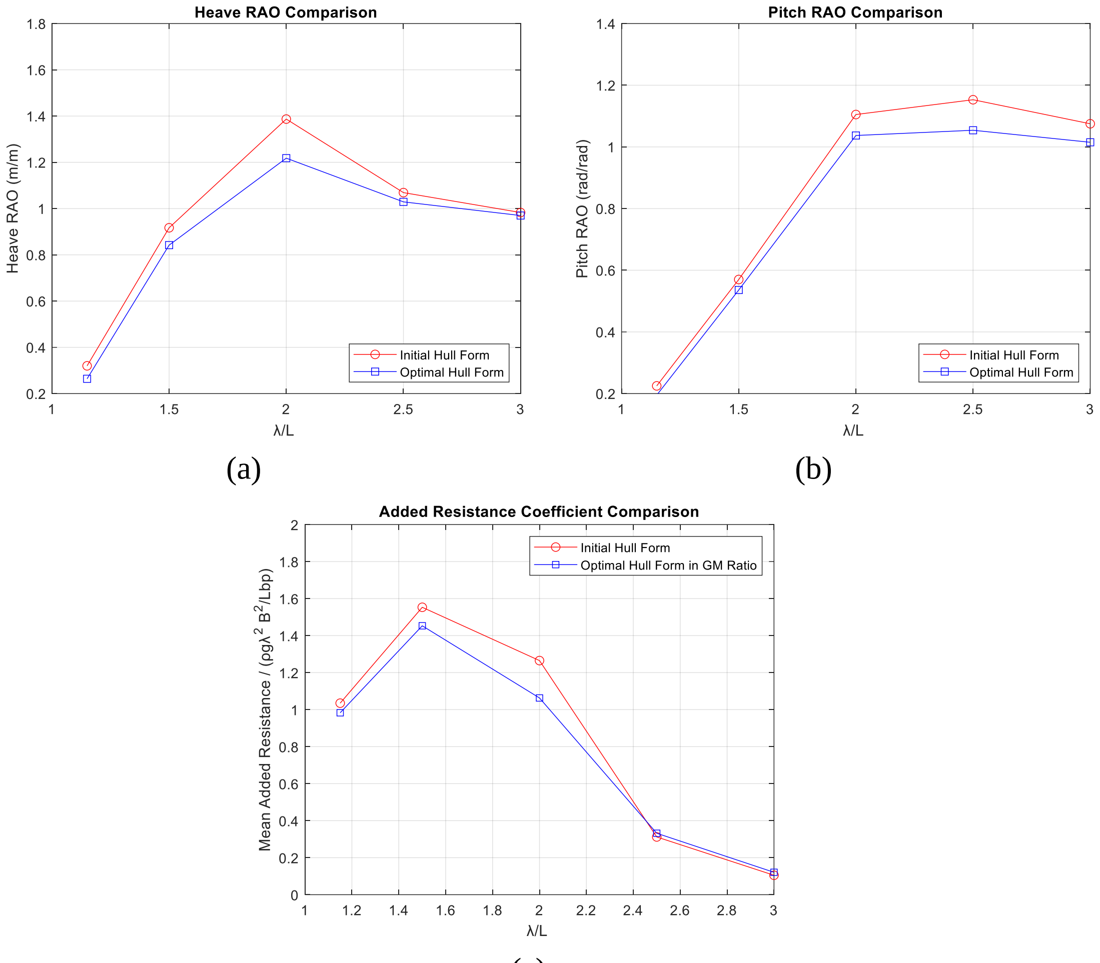

(a) (b)

(c)

Figure 8.14. Heave, pitch RAO and added resistance coefficient comparison

The optimal hull form in Huang et al. (2015), which used more complex hull form deformation by combining the global and local hull deformations, offered four alternatives. All of these alternatives displayed contradictory peak RAOs between the heave and pitch. When the peak of the heave RAO curve was lower than the initial, the peak of the pitch RAO curve became higher. In contrast, the heave and pitch RAO curves of the best hull form in this chapter show a single solution, which is lower than the initial one. The optimal location of the *LCB* in this chapter also aligns with the optimal position identified by Sarıöz (2009), shifted towards the bow.

The optimisation method presented in this chapter improves seakeeping performance by reducing heave and pitch motions, as well as the added resistance coefficients, using a single objective function focused on minimising the *GM* ratio and R_y. This approach is simpler than existing methodologies because it addresses all seakeeping issues without directly calculating seakeeping performance in optimisation process. The combination of a straightforward optimisation method with a single objective function is a significant contribution of this study to fishing vessel designers and operators, enabling them to enhance seakeeping performance and improve safety.

8.3.5. Results of Seakeeping Performance in Irregular Waves

The calculation of seakeeping performance in irregular waves in this chapter uses the same procedure described in Chapter 4. The FAO-01 fishing boat is assumed to operate in the Java Sea, Indonesia, requiring a wave scatter diagram that accurately reflects this specific sea area. However, not all peak periods (*Tp*) and significant wave heights (*Hs*) are included in the analysis. This study focuses on investigating the effects of three of the most frequent combinations of *Tp* and *Hs* on the responses of the fishing boat. Table 8.7 presents a partial wave scatter diagram of the Java Sea, highlighting the prevailing conditions. These selected *Hs*-*Tp* combinations account for 89.2% of the recorded sea conditions in the Java Sea over a one-year period.

Table 8.7. The highest occurrence of *Tp* and *Hs* in Java Seas, Indonesia

***Hs* (m) \ *Tp* (s)**	**3 – 4**	**4 – 5**	**5 – 6**
0.0 – 0.5	23.99%	7.30%	0.49%
0.5 – 1.0	11.27%	27.17%	6.43%
1.0 – 1.5	0.00%	2.52%	10.03%

The wave scatter data is provided in actual data (full-scale). the RAOs of the fishing vessel in model scale were scaled up to full scale, from non-dimensional RAO curves, to be dimensional, as conducted in Chapter 7. The criterion used to evaluate vertical motion in the working area is the RMS acceleration ($\sqrt{m_4}$). Due to the small size of the fishing boat and the typical positioning of fishermen at the boat's centre, it is assumed that there is no longitudinal distance contributing to vertical motion from pitch. Therefore, vertical motion is assessed based solely on heave motion.

Table 8.8. The comparison of RMS vertical acceleration ($\sqrt{m_4}$) in g unit

	***Tp* (s)**								
	3.5	**4.5**	**5.5**	**3.5**	**4.5**	**5.5**	**3.5**	**4.5**	**5.5**
***Hs* (m)**	**Initial**			**Optimum**			**Difference**		
0.25	0.056	0.036	0.027	0.051	0.033	0.024	-9.37%	-8.92%	-8.89%
0.75	0.168	0.109	0.080	0.152	0.099	0.072	-9.37%	-8.92%	-8.89%
1.25	0.279	0.182	0.133	0.253	0.166	0.121	-9.37%	-8.92%	-8.89%
Average							**-9.06%**		

Table 8.8 displays the results of RMS vertical accelerations in units of g (9.81 m/s^2). The criterion for acceptable vertical acceleration is below 0.2 g. Among the considered peak periods (*Tp*), the lowest significant wave height (*Hs*) identified as optimal for heave acceleration is 0.25 m, because the criterion across all conditions is passed. The optimal hull form demonstrates a substantial average reduction in heave accelerations, achieving up to a 9.06% reduction.

The seakeeping criterion for pitch motions is defined by the RMS pitch motion ($\sqrt{m_0}$), which is set at 3 degrees. Table 8.9 displays the RMS pitch outcomes. Across all scenarios, the fishing boat operates safely below the RMS pitch criterion when *Hs* = 0.25 m. The table highlights that the optimal hull form achieves an average reduction in RMS pitch of 7.00%.

Table 8.9. The comparison of RMS pitch response ($\sqrt{m_0}$) in degree

	***Tp* (s)**								
	3.5	**4.5**	**5.5**	**3.5**	**4.5**	**5.5**	**3.5**	**4.5**	**5.5**
***Hs* (m)**	**Original**			**Optimum**			**Difference**		
0.25	1.013	0.665	0.490	0.942	0.618	0.456	-6.99%	-6.98%	-7.02%
0.75	3.038	1.994	1.471	2.826	1.855	1.368	-6.99%	-6.98%	-7.02%
1.25	5.063	3.323	2.452	4.710	3.091	2.280	-6.99%	-6.98%	-7.02%
Average							**-7.00%**		

The final assessment of seakeeping focuses on added resistance. Due to no specific criterion is set for added resistance, the optimal hull forms are evaluated solely based on their reduction compared to the initial form. The results of mean added resistance ($2m_0$) are presented in Table 8.10. The average reduction varies with different peak periods (*Tp*), while remaining consistent for the same *Tp* regardless of changes in significant wave height (*Hs*). On average, the optimal hull form achieves a reduction in mean added resistance of 8.01%.

Based on these results, the seakeeping performance can be quantified, allowing an assessment of how much the seakeeping performance is improved by the reduction in vessel responses. The optimal hull form can reduce the RMS of vertical acceleration of 9.06% on average. It can also reduce the RMS pitch and mean added resistance by up to 7.00% and 8.01% on average, respectively. The single objective function used in this study is proven to enhance seakeeping performance.

Table 8.10. The comparison of mean added resistance in kilo Newton.

	***Tp* (s)**								
	3.5	**4.5**	**5.5**	**3.5**	**4.5**	**5.5**	**3.5**	**4.5**	**5.5**
***Hs* (m)**	**Initial**			**Optimum**			**Difference**		
0.25	0.049	0.020	0.011	0.044	0.019	0.010	-8.86%	-7.58%	-7.58%
0.75	0.437	0.184	0.096	0.398	0.170	0.089	-8.86%	-7.58%	-7.58%
1.25	1.214	0.510	0.267	1.107	0.471	0.247	-8.86%	-7.58%	-7.58%
Average							**-8.01%**		

8.4. Summary

This study successfully demonstrates two single-objective functions in the optimisation of seakeeping for the FAO-01 fishing vessel. The first objective function focuses on minimising the *GM* ratio by adjusting the longitudinal centre of buoyancy and block coefficient, to develop the optimal hull form. The second objective function targets minimising the radius of gyration in the y-direction (R_y) by adjusting the *LCG* and *KG* to find the optimal *CoG* for the hull form.

The optimisation technique employed the Response Surface Method, with a Central Composite Design used for the design of experiments to construct mathematical models of the responses. Subsequently, CFD simulations were conducted to compare the seakeeping performance, focusing solely on validating the optimised designs rather than the optimisation process itself. This comparison covered parametric roll conditions and evaluated heave, pitch, and added resistance performance in both regular and irregular waves.

Under parametric roll conditions, the initial hull form was set to be susceptible to experience the parametric roll, whereas the optimised hull form demonstrated enhanced seakeeping performance by avoiding the dangerous phenomenon, capsizing, with the same condition as the initial. Analysis of regular waves showed that the RAOs for heave, pitch, and added resistance coefficients were lower than those of the initial design across all wavelengths, indicating improved seakeeping performance. However, the extent of improvement was fully quantified only after conducting irregular wave analysis.

To assess seakeeping performance in irregular waves, spectral (short-term) analysis was conducted using the JONSWAP spectrum with three distinct *Tp* and *Hs* values derived from the most frequent occurrences in the Java Sea, as indicated by the wave scatter diagram. On average, the optimal hull form reduced RMS vertical acceleration, RMS pitch, and mean added resistance by up to 9.06%, 7.00%, and 8.01%, respectively. These findings highlight the effectiveness of both single objective functions in enhancing seakeeping performance. The optimised conditions significantly improved upon the original performance. This approach simplifies the complexity of seakeeping optimisation processes.

Future work could explore minimising calm water resistance. Additionally, employing multi-objective optimisation could address situations where optimal conditions for resistance differ from those for seakeeping, as illustrated in this study.

9. Hull form Optimisation to Minimise the Total Resistance and Dynamic Responses of Fishing Vessel

9.1. Introduction

Enhancing seakeeping performance by minimising the radius of gyration in the y-axis (R_y) was successfully carried out in Chapter 7. From this finding, it can be concluded that the location of optimal LCG and KG to achieve minimum R_y is close to the location of optimal LCG and KG for the total resistance in calm water. In other words, dynamic responses can be minimised, and the total resistance remains largely unchanged.

Conversely, as discussed in Chapter 8, minimising the GM ratio along with R_y can significantly reduce the dynamic responses. However, this reduction in dynamic response comes at the cost of increased total resistance in calm water due to changes in hull form by varying LCB and CB. From this finding, it can be inferred that it is important to minimise total resistance in calm water. Once this resistance is minimised, the mean total resistance in waves can reach its minimum value because the added resistance can be reduced along with the dynamic responses of the vessel by conducting seakeeping optimisation.

Moreover, it is essential to minimise the mean total resistance in waves to support decarbonisation efforts as recommended by the IMO. The carbon intensity of international shipping is targeted to be reduced by at least 40% by 2030, compared to 2008 levels. Minimising total resistance not only reduces the carbon footprint of fishing vessels but also lowers fuel consumption. This reduction in fuel consumption can significantly lower operational costs for fishermen, ultimately benefiting them economically.

The present chapter aims to optimise the hull form by minimising the total resistance in calm water as the objective function and minimise the dynamic response by minimising the R_y. Adopted the same procedure in Chapter 8, the Lackenby (1950) method was used to deform the initial hull form by varying the LCB and CB as design variables. The central composite design was applied as the design of experiment to gather the data (total resistance in calm water) from nine combination variations, which is used to construct the mathematical model and determine the optimal solution.

The optimal hull form in terms of total resistance is then compared with the initial hull form, as well as the optimal hull form in R_y from Chapter 8, in terms of calm water resistance. Finally, the comparison between the optimal loading condition from Chapter 7, the optimal hull form in GM Ratio from Chapter 8, and the optimal hull form in calm water resistance from the present chapter are compared each difference with the initial condition. The full-scale total resistance in waves is also compared.

9.2. Methodology

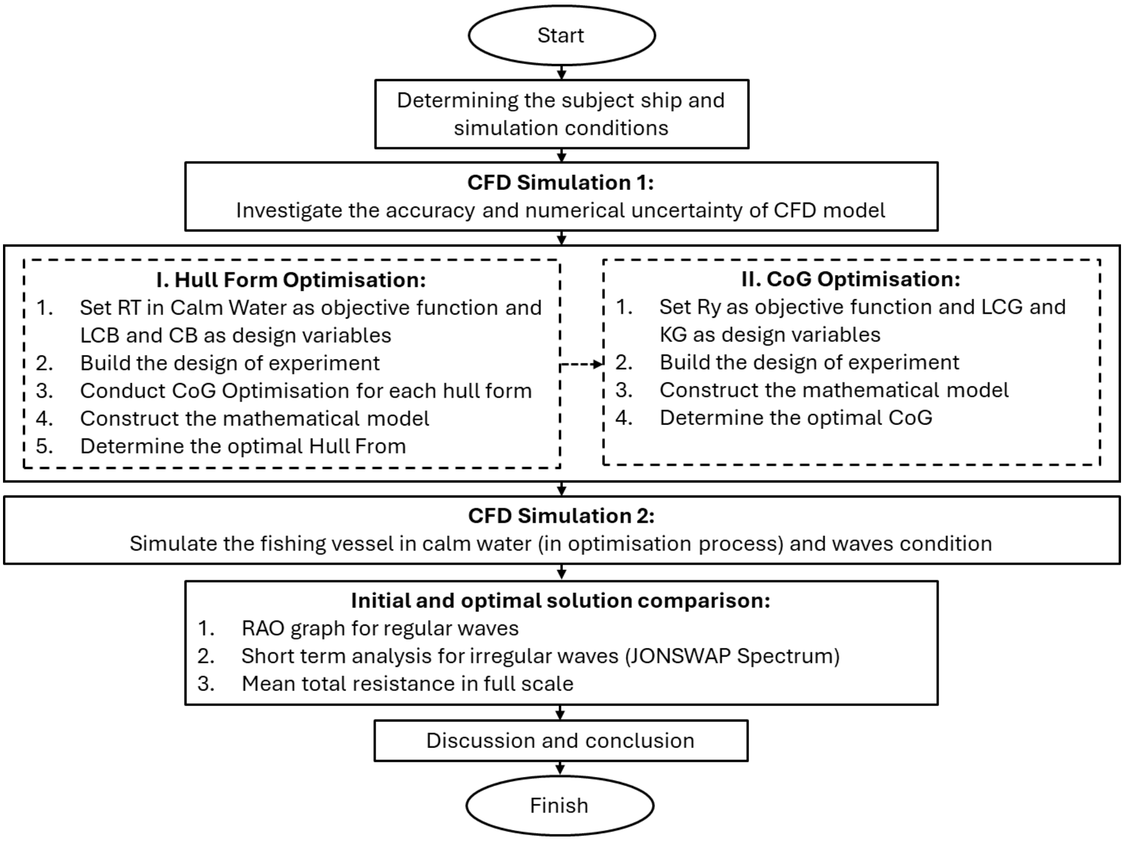

Figure 9.1. Research flowchart

The flowchart of this chapter is shown in Figure 9.1. After determining the subject ship and simulation conditions, the study proceeds with the study of the accuracy and numerical uncertainty of CFD model. This step was complete in Chapter 7. Following this, the two optimisations were carried out. The first optimisation involves deforming the hull form using the Lackenby (1950) method by varying the *LCB* and *CB*. Both combinations are determined by a design of experiments approach, Central Composite Design. Subsequently, the new hull form, based on the design experiment, is optimised for its centre of gravity by adjusting the *LCG* and *KG* to minimise the R_y. Then, the total resistance in calm water of each hull form variation is determined using CFD simulation to construct the mathematical model and finally the optimal hull form can be achieved.

Once the best hull form is obtained, further optimisation of the centre of gravity is conducted to define the optimal *LCG* and *KG* that minimise R_y. The solution will result in a hull form with minimal resistance and dynamic responses. The research continues with CFD simulations for both the initial and optimal hull forms in calm water and wave conditions, after ensuring the accuracy and numerical uncertainty. The final step of this study is to compare the seakeeping performance and mean total resistance at full scale between the initial and optimal hull forms. Discussion and conclusions are presented in sections 9.3 and 9.4.

9.2.1. Objective Function and Design Variables

Based on previous chapter, the added resistance ranges from 5% to 127% of the total resistance in calm water. Its value depends on the combination of significant wave height (*Hs*), wave peak period (*Tp*), and wave spectrum formula. Therefore, it is important to keep the total resistance in calm water as low as possible to reduce the mean total resistance in waves. By minimising the total resistance in calm water, the added resistance can be reduced, assuming its value is the same percentage of the calm water resistance. This is achieved by setting calm water resistance as an objective function to be minimised by altering the *LCB* and *CB* as design variables to deform the hull form. Table 9.1 presents the design variables and their corresponding codes for this scenario. The Longitudinal Centre of Buoyancy (*LCB*) is measured from the forward perpendicular (*FP*) as a percentage of the length between perpendiculars (L_{bp}).

Table 9.1. Design variable and code for transforming the hull form

Design Variables	**FAO-01**		
	-1	**0**	**1**
***LCB* (%), x_1**	51.196	53.890	56.585
***CB* (-), x_2**	0.254	0.267	0.280

However, the mean total resistance in waves consists of both the total resistance in calm water and the added resistance in waves. To ensure the added resistance is minimal, the vessel's dynamic response must be minimised due to the relationship between added resistance and seakeeping performance. This is done by setting R_y as an objective function to be minimised and using *LCG* and *KG* as design variables. The best hull form is then expected to have minimum total resistance in waves and dynamic responses, resulting in better seakeeping performance.

9.3. Results and Discussion

9.3.1. Hull Form Optimisation Results

Table 9.2 shows the results of nine combinations of *LCB* and *CB* to develop new hull form and the CFD results for total resistance in calm water. During the simulation, the position of *LCG* and *KG* for each hull form was obtained from *CoG* optimisation by minimising R_y with changes in *LCG* and *KG*. The mathematical model based on the Table 9.2 is shown in Eq. (9.1). The visualisation of the responses surface is shown in Figure 9.2-a and the plot of the actual RT based on CFD versus the predicted RT based on Eq. (9.1) are presented in Figure 9.2-b. The R^2 value of Eq. (9.1) is 0.9936, which is sufficiently high, explaining the relationship between *LCB* and *CB* to the total resistance in calm water. This is evidenced by the plot of actual versus predicted values, where both results align closely.

Table 9.2. Responses of RT for FAO-01 shifting load scenario

Hull Form	**X_1**	**X_2**	***LCB* (%)**	***CB* (-)**	**RT CFD (N)**
Initial	0	0	53.890	0.267	15.162
F-1	1	1	56.585	0.280	16.472
F-2	1	-1	56.585	0.254	14.871
F-3	-1	1	51.196	0.280	16.641
F-4	-1	-1	51.196	0.254	16.216
F-5	-1.414	0	50.079	0.267	16.817
F-6	1.414	0	57.701	0.267	16.041
F-7	0	-1.414	53.890	0.248	14.898
F-8	0	1.414	53.890	0.286	16.238

$$RT\ (N) = 15.162 - 0.326x_1 + 0.49x_2 + 0.647{x_1}^2 + 0.216{x_2}^2 + 0.294x_1x_2 \tag{9.1}$$

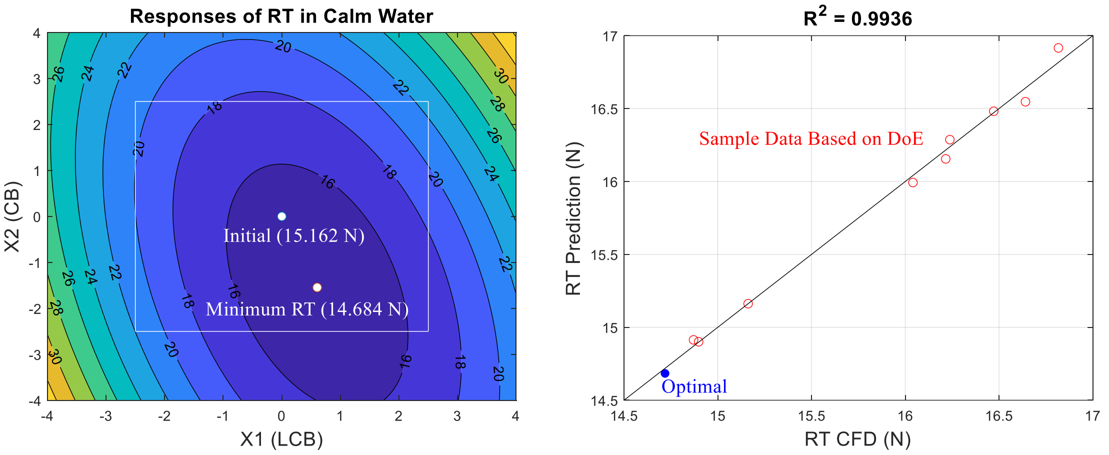

(a) (b)

Figure 9.2. The comparison of response surface result for RT influenced by LCB and CB with the constrains

Figure 9.3 presents a comparison of the lines plan between the initial and optimal hull forms in terms of calm water resistance (RT). The optimal hull form has an increased *LCB* percentage, measured from FP, resulting in the *LCB* shifting towards the stern. It should be noted that the total displacement is kept constant by maintaining the same length and draft. Consequently, the breadth of the fishing vessel has been adjusted, increasing from 0.678 m to 0.732 m.

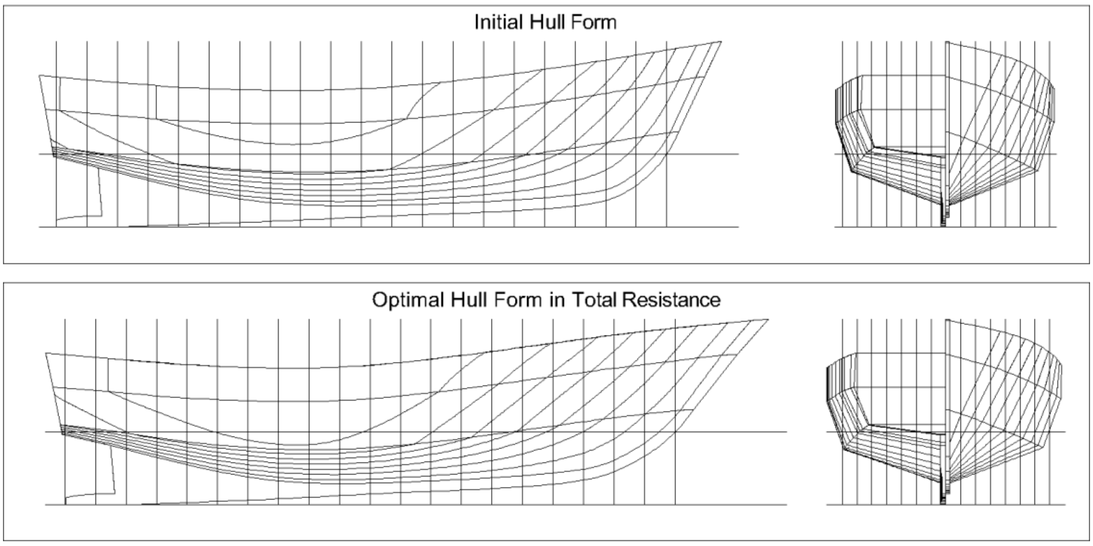

Figure 9.3. Hull form comparison between initial (a) and optimal (b) hull forms

9.3.2. Centre of Gravity Optimisation Results

As explained earlier in subchapter 9.3.1, after generating various hull forms during the design of experiments step, the location of the *LCG* and *KG* for each hull form was determined by *CoG* optimisation by minimising R_y. Then, the CFD simulation in calm water resistance could be carried out. The same procedure was repeated after identifying the hull form with the minimal resistance. Table 9.3 shows the comparison of the *LCG* and *KG* locations between the initial and optimal results. It should be noted that the initial *LCG* was determined based on the LCB location in the no-trim condition, while *KG* was determined as 75% of *KM*. Then, the optimal location can be achieved after the optimisation process.

Table 9.3. The comparison initial and optimal loading conditions for optimal hull form

Loading Condition	***LCG* (m)**	***KG* (m)**	**R_y**
Initial	0.908	0.415	0.5559
Optimal	0.929	0.363	0.5506
Difference (%)			**-0.95%**

9.3.3. Results of Seakeeping Performance in Regular Waves

Once the optimal hull form with the optimal loading condition has been determined, CFD simulations in both calm water and waves can be carried out. Table 9.4 shows the results of the total resistance in calm water for the optimal hull form in RT and compares them with the initial hull form. Based on Eq. (9.1), the optimal hull form can reduce the total resistance by up to 3.15%. However, the actual results from the CFD simulations show a reduction of 2.92%. The difference between the predicted and actual results is small, at -0.24%, which is below 0.5%. These optimisation results indicate that the optimal hull form in RT can reduce the total resistance with high accuracy.

Table 9.4. The comparison initial and optimal hull form in RT

Hull Form	x_1	x_2	***LCB* (%)**	***CB* (-)**	**RT CFD (N)**	**RT Eq. (9.1) (N)**	**Difference (%)**
Initial	0.00	0.00	53.820	0.267	15.162	15.162	0
Minimum RT	-2.50	0.342	47.093	0.272	14.719	14.684	-0.24
Difference (%)					**-2.92**	**-3.15**	

Unlike the optimal hull form in *GM* Ratio, the optimal hull form in RT shifted the *LCB* towards the stern. Then, the bow shape region become smaller (sharper), making the hull entrance angle lower. These conditions make the pressure force become lower than the initial hull form, as shown in Figure 9.4. The free surface elevation on the hull surface become lower as illustrated in Figure 9.5 and Figure 9.6.

Figure 9.7 presents a comparison of two different response surfaces: (a) response in R_y to minimise *GM* Ratio, and (b) responses in total resistance in calm water. Figure 9.7-a is taken from Chapter 8. It can be observed that according to the mathematical model in Eq. (9.1), the optimal hull form in R_y increases total resistance to 19.961 N, compared to the initial value of 15.162 N. Meanwhile, the optimum hull form in total resistance reduces the resistance to 14.684 N. Table 9.5 indicates that the total resistance from the CFD simulations is 19.632 N, which makes the result from mathematical model 1.67% higher than that obtained from CFD calculations.

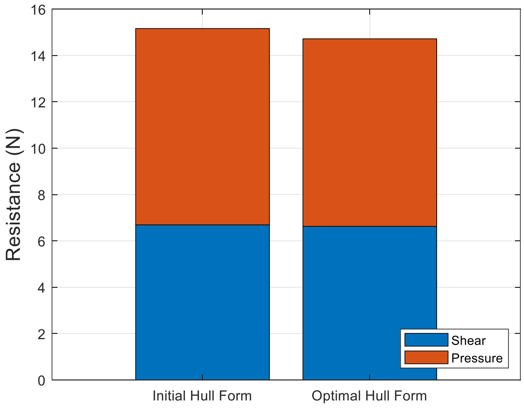

Figure 9.4. The comparison of total resistance decomposition between initial and optimal hull form

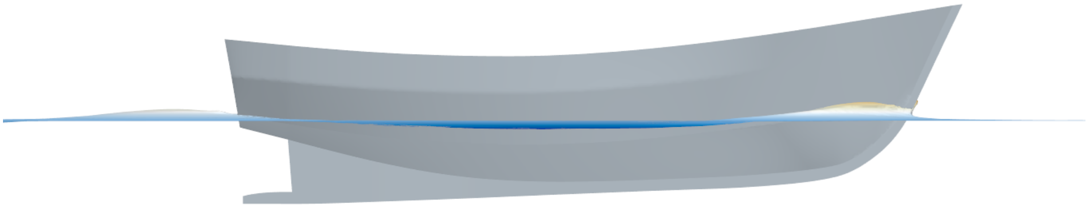

(Initial Hull Form – Resulted Trim = 0.27°)

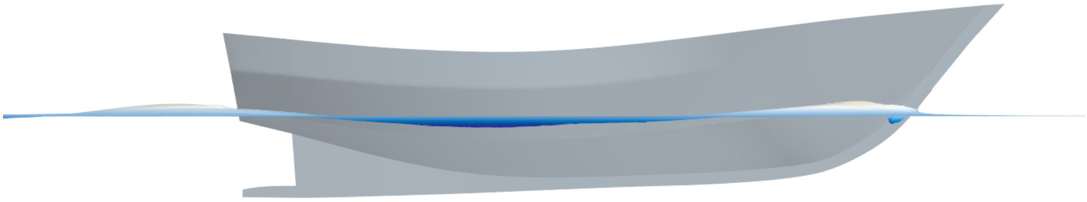

(Optimal Hull Form – Resulted Trim = 1.14°)

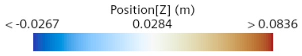

Figure 9.5. Result of CFD resistance simulation at $F_r = 0.33$

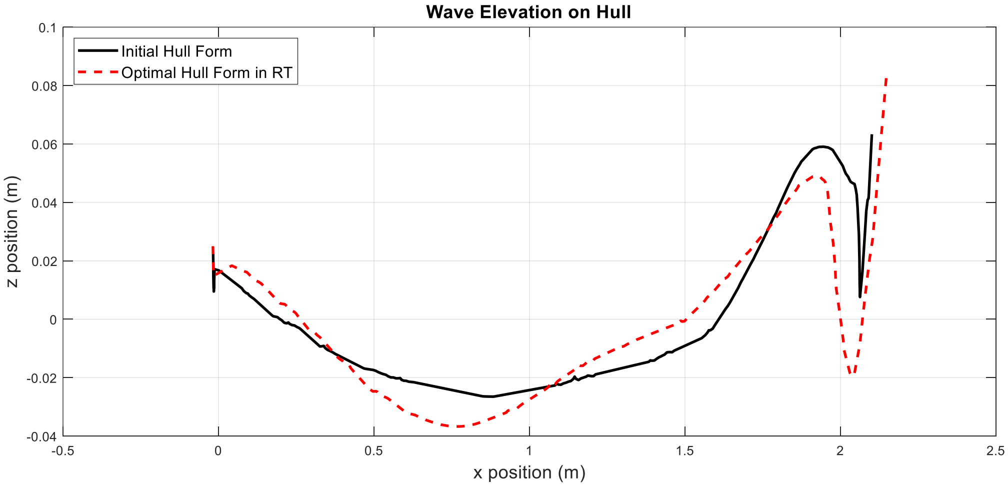

Figure 9.6. Comparison of free surface elevation on the hull between different Hull Form

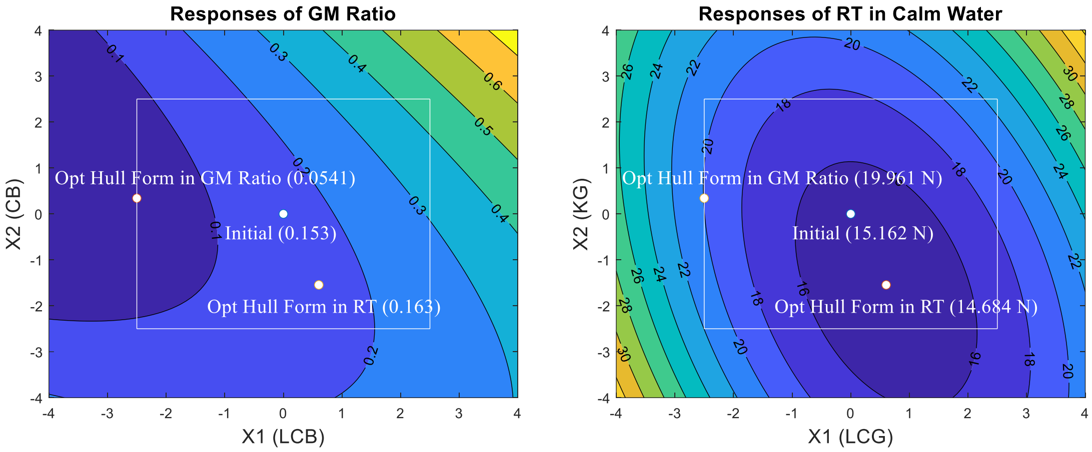

(a) (b)

Figure 9.7. The comparison of response surface result for *GM* ratio and rt influenced by lcb and cb with the constrains

Table 9.5. The comparison initial and two different optimal hull form

Hull Form	x_1	x_2	**LCB (%)**	**CB (-)**	**RT CFD (N)**	**RT Eq. (9.1) (N)**	**Difference (%)**
Initial	0.00	0.00	53.820	0.267	15.162	15.162	0
Minimum *GM* Ratio	-2.50	0.342	47.093	0.272	19.632	19.961	1.67%
Minimum RT	0.604	-1.545	55.517	0.246	14.719	14.684	-2.92

After predicting the total resistance in calm water, the CFD simulation in waves can be carried out. Figure 9.8 compares the mean total resistance in waves (RT) of the initial hull form and the optimal hull form, alongside other optimal solutions from Chapters 7 (minimal R_y) and 8 (minimal *GM* ratio). The figure also provides the calm water resistance result for each hull form. It can be observed that the optimal hull form in terms of *GM* ratio exhibits the highest RT at every wavelength ratio. However, the order of the mean RT in waves varies for the other hull forms. At low wavelength ratios, the optimal loading conditions and the optimal hull form in terms of RT show higher mean RT in waves compared to the initial hull form. However, when the wavelength ratio exceeds 1.5, both optimal solutions exhibit lower mean RT than the initial hull form.

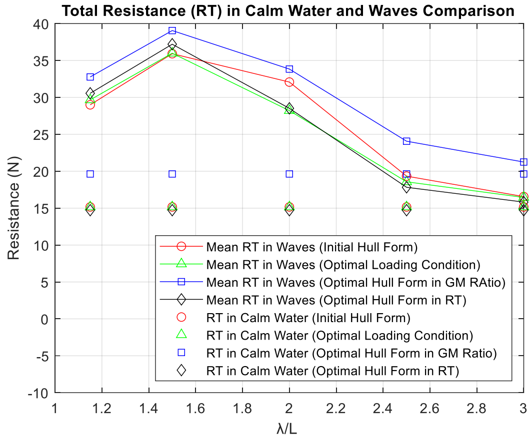

Figure 9.8. Total resistance in calm water and mean total resistance in waves

Table 9.6. Response amplitude operator comparison

λ/L	**Initial**			**Optimal Hull Form in RT**		
	Heave TF	**Pitch TF**	**C_{AW}**	**Heave TF**	**Pitch TF**	**C_{AW}**
1.15	0.320	0.225	1.035	0.351	0.253	1.185
1.5	0.917	0.570	1.553	0.956	0.617	1.682
2	1.387	1.105	1.265	1.299	1.101	1.032
2.5	1.069	1.153	0.312	1.034	1.073	0.232
3	0.983	1.075	0.105	0.959	1.016	0.082

Table 9.6 shows the Response Amplitude Operator (RAO) of heave and pitch motions and the added resistance between the initial hull form and the optimal one for total resistance in calm water (RT). Comparisons between other optimal solutions from Chapters 7 and 8 are presented in Figure 9.9. Based on the figure, it can be seen that the different hull forms, determined by their *GM* ratios, affect the RAO results. For example, the initial hull form (red line) with a *GM* ratio of 0.153 was optimised to minimise R_y (green line). Consequently, the RAO graph improves at wavelength ratios greater than two.

When the hull form was deformed to result in the lowest *GM* ratio (blue line), the RAO graph became the lowest at every wavelength, as the *GM* ratio value dropped to 0.0541. On the other hand, when the hull was deformed to minimise total resistance (black line), the *GM* ratio slightly increased to 0.163. Consequently, the RAO graph became higher at low wavelength ratios but lower at wavelength ratios greater than two, showing a similar trend but with higher values compared to the initial hull form with minimal R_y.

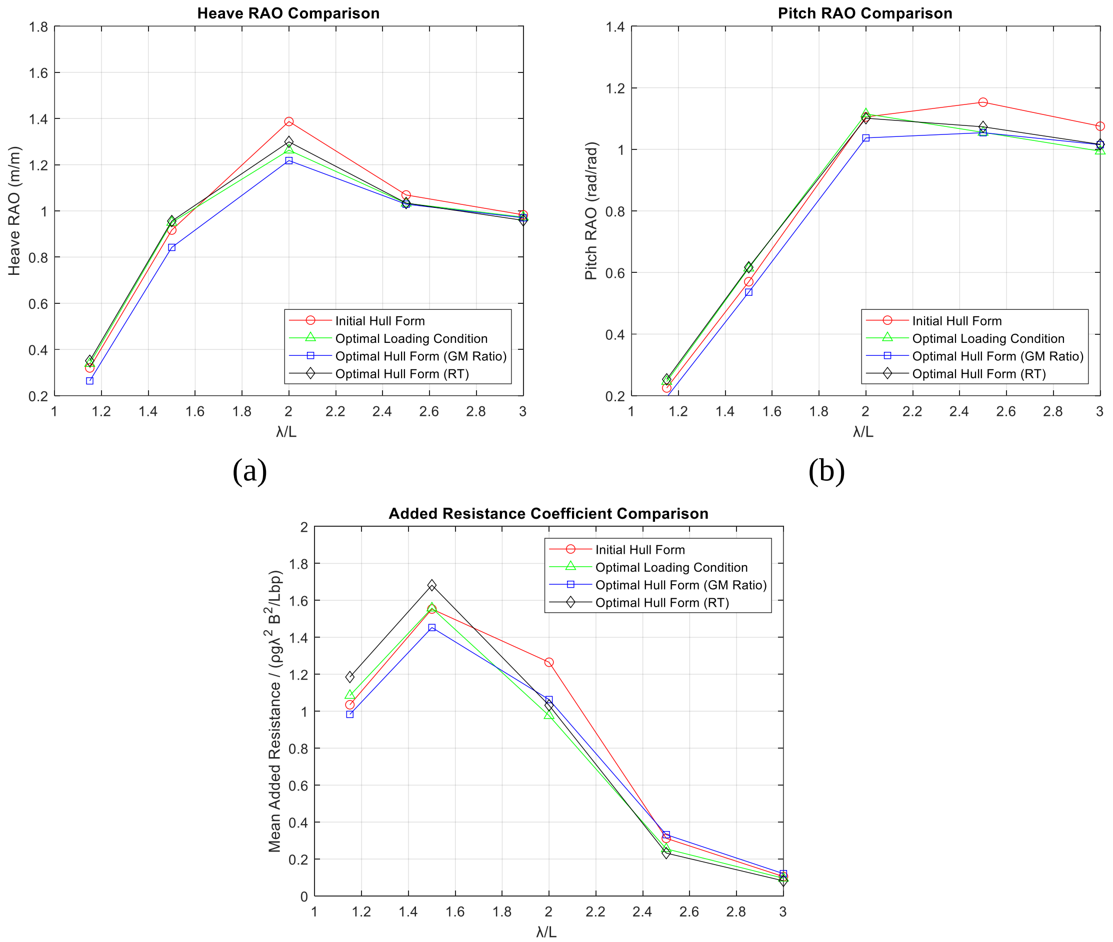

(a) (b)

(c)

Figure 9.9. Heave, pitch RAO and added resistance coefficient comparison

From this comparison, it is evident that the seakeeping performance of different hull forms can be quickly assessed based on their *GM* ratio, with a lower value indicating better performance. However, when evaluating the seakeeping performance of the same hull form, the R_y value provides a quick estimation, where again, a lower value signifies better performance. Both of these objective functions used in this thesis can predict seakeeping performance without the need for direct calculations, which is one of the novel contributions of this work.

9.3.4. Results of Seakeeping Performance in Irregular Waves

Same as the calculation in previous chapter, the FAO-01 fishing boat is assumed to operate in the Java Sea, Indonesia, necessitating a wave scatter diagram that accurately represents this specific region. However, the analysis does not encompass all peak periods (*Tp*) and significant wave heights (*Hs*). Instead, this study examines the effects of three of the most frequent *Tp* and *Hs* combinations on the boat's responses.

Table 9.7 presents a comparison of RMS vertical acceleration between the initial and optimal solutions. The data indicates that the difference is influenced by *Tp* rather than *Hs*. When *Tp* remains the same, the difference remains consistent despite varying *Hs*. The average reduction in RMS vertical acceleration across all *Tp* and *Hs* combinations is 1.79%.

Table 9.8 shows the comparison of RMS pitch response between the initial and optimal hull forms. Similar to the RMS vertical acceleration, the difference is significantly affected by *Tp*, while *Hs* does not impact the difference value. The optimal hull form achieves an average reduction in RMS pitch response of 1.51%.

The final evaluation of seakeeping performance in irregular waves, as shown in Table 9.9, involves mean added resistance. The influence of *Hs* and *Tp* on mean added resistance is consistent with the previous results. The optimal hull form yields an average reduction of 6.48%.

Table 9.7. The comparison of RMS vertical acceleration ($\sqrt{m_4}$) in g unit

	***Tp* (s)**								
	3.5	**4.5**	**5.5**	**3.5**	**4.5**	**5.5**	**3.5**	**4.5**	**5.5**
***Hs* (m)**	**Initial**			**Optimum in RT**			**Difference**		
0.25	0.056	0.036	0.027	0.055	0.036	0.026	-2.09%	-1.52%	-1.75%
0.75	0.168	0.109	0.080	0.164	0.108	0.078	-2.09%	-1.52%	-1.75%
1.25	0.279	0.182	0.133	0.273	0.179	0.130	-2.09%	-1.52%	-1.75%
Average							**-1.79%**		

Table 9.8. The comparison of RMS pitch response ($\sqrt{m_0}$) in degree

	***Tp* (s)**								
	3.5	**4.5**	**5.5**	**3.5**	**4.5**	**5.5**	**3.5**	**4.5**	**5.5**
***Hs* (m)**	**Original**			**Optimum in RT**			**Difference**		
0.25	1.013	0.665	0.490	0.999	0.655	0.482	-1.31%	-1.48%	-1.73%
0.75	3.038	1.994	1.471	2.998	1.964	1.446	-1.31%	-1.48%	-1.73%
1.25	5.063	3.323	2.452	4.997	3.274	2.410	-1.31%	-1.48%	-1.73%
Average							**-1.51%**		

Table 9.9. The comparison of mean added resistance in kilo Newton.

	***Tp* (s)**								
	3.5	**4.5**	**5.5**	**3.5**	**4.5**	**5.5**	**3.5**	**4.5**	**5.5**
***Hs* (m)**	**Initial**			**Optimum in RT**			**Difference**		
0.25	0.049	0.020	0.011	0.045	0.019	0.010	-7.35%	-5.61%	-6.47%
0.75	0.437	0.184	0.096	0.405	0.173	0.090	-7.35%	-5.61%	-6.47%
1.25	1.214	0.510	0.267	1.125	0.481	0.250	-7.35%	-5.61%	-6.47%
Average							**-6.48%**		

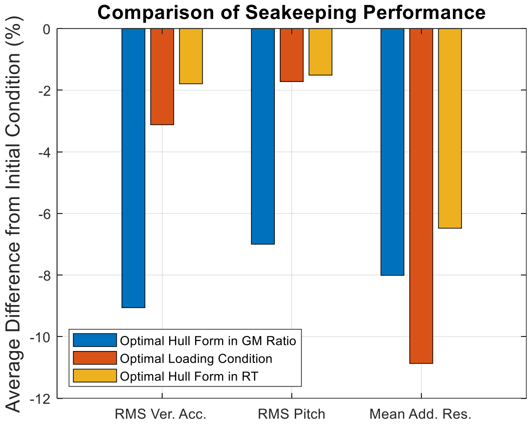

Figure 9.10. The comparison of seakeeping performance

With the three optimal solutions identified in Chapters 7, 8, and the current chapter, it is pertinent to summarise and compare their average differences from the initial conditions, as illustrated in Figure 9.10. The optimal solutions are arranged from the optimal hull form in *GM* Ratio from Chapter 8, Optimal *CoG* (loading condition) from Chapter 7, and optimal hull form in RT from this chapter. It is clear that the reduction in heave and pitch motions is influenced by the *GM* ratio value. Specifically, a hull form with lower *GM* ratio corresponds to reduced dynamic responses of the vessel, except for added resistance. Not only do the dynamic responses affect the added resistance, but the hull form's effect on total resistance in calm water also influences the added resistance. When assessing the seakeeping performance of the same hull form, the R_y value serves as a quick indicator, as detailed in Chapter 7. This metric provides a rapid prediction of seakeeping performance, allowing for efficient evaluations and comparisons.

9.3.5. The Comparison of Mean Total Resistance in Full Scale

Based on the finding in Chapter 7, the same hull form with optimal loading conditions does not significantly affect total resistance of the initial loading condition in calm water. However, added resistance in waves can lead to markedly different mean total resistance results. Thus, in addition to assessing seakeeping performance, it is essential to calculate the total resistance in waves after modifying the hull form for both seakeeping and resistance optimisations.

Total resistance in waves is decomposed into total resistance in calm water and mean added resistance in waves. The added resistance at full scale has already been calculated during the seakeeping assessment. Therefore, it is necessary to determine the total resistance in calm water for each hull form variation. In this study, the Froude method is employed to extrapolate the total resistance in calm water from the model scale results.

Table 9.10. The comparison of calm water total resistance in full scale (kN).

Hull Form	**Model**				**Full Scale**			
	RT (N)	**CT (*10^{3})**	**CF (*10^{3})**	**Cr (*10^{3})**	**CF (*10^{3})**	**CT (*10^{3})**	**RT (kN)**	**Power (kW)**
Initial	15.162	8.563	3.670	4.894	2.549	7.443	0.8434	2.603
Opt. LC	15.165	8.565	3.670	4.895	2.549	7.445	0.8436	2.603
Opt. HF in *GM* Ratio	19.632	1.055	3.670	6.881	2.549	9.430	1.1230	3.466
Opt. HF in RT	14.719	8.252	3.670	4.583	2.549	7.132	0.8141	2.512

Table 9.10 shows the results of calm water total resistance in full scale for different hull forms. The power of the initial hull form in full scale is then compared to the results from Pérez-Arribas et al. (2022) at a speed of 6 knots, as shown in Figure 9.11. It is shown that the power of the initial hull form lies between 2-4 kW (there is no specific value from the paper). The power of the initial hull form from the present study is 2.603 kW, as shown in Table 9.10, which is similar to Pérez-Arribas et al. (2022). The reduction for the optimal hull form in RT compared to the initial hull form is 3.47%. This achievement is lower than the additional dihedral bulbous bow, which can reduce resistance by up to 5%. However, the findings from this thesis show that the optimisation of the hull form in RT was successful, reducing the power close to the results achieved with the additional dihedral bulbous bow. Further investigation should be undertaken at higher speeds for a comprehensive comparison.

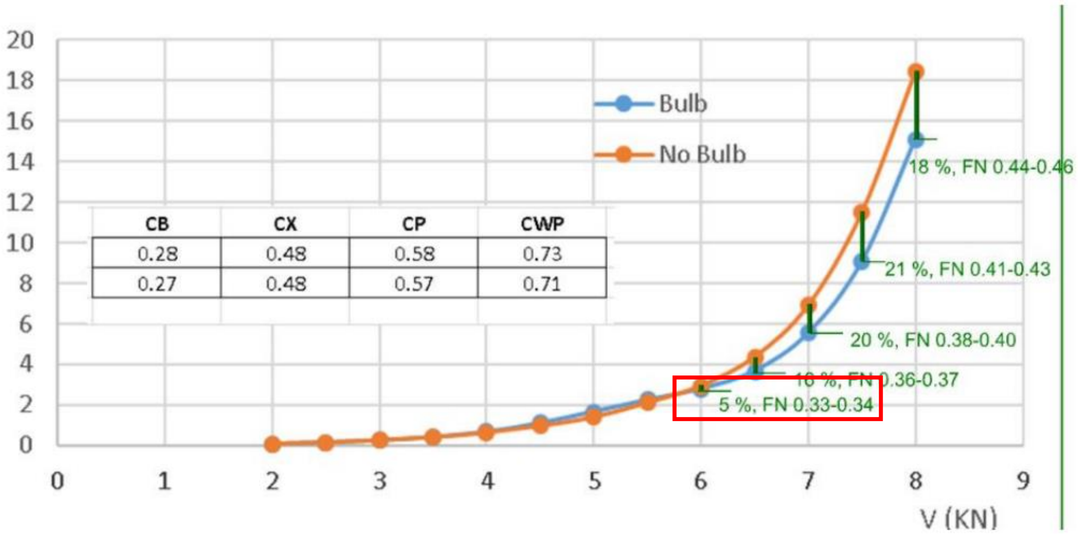

Figure 9.11. The total resistance of initial hull form and initial hull form with dihedral bow (Pérez-Arribas et al., 2022).

Table 9.11. The comparison of mean total resistance in waves in full scale (kN).

	***Tp* (s)**								
	3.5	**4.5**	**5.5**	**3.5**	**4.5**	**5.5**	**3.5**	**4.5**	**5.5**
***Hs* (m)**	**Initial**			**Opt. HF in *GM* Ratio**			**Difference**		
0.25	0.892	0.864	0.854	1.167	1.142	1.133	30.86%	32.19%	32.64%
0.75	1.281	1.027	0.940	1.521	1.293	1.212	18.81%	25.87%	28.98%
1.25	2.058	1.353	1.110	2.230	1.594	1.370	8.36%	17.80%	23.36%
						Average	**24.32%**		
***Hs* (m)**	**Initial**			**Optimum LC**			**Difference**		
0.25	0.892	0.864	0.854	0.886	0.862	0.853	-0.62%	-0.21%	-0.11%
0.75	1.281	1.027	0.940	1.229	1.009	0.929	-4.04%	-1.78%	-1.07%
1.25	2.058	1.353	1.110	1.914	1.302	1.082	-7.00%	-3.77%	-2.55%
						Average	**-2.35%**		
***Hs* (m)**	**Initial**			**Optimum HF in RT**			**Difference**		
0.25	0.892	0.864	0.854	0.859	0.833	0.824	-3.68%	-3.52%	-3.51%
0.75	1.281	1.027	0.940	1.219	0.987	0.904	-4.80%	-3.86%	-3.78%
1.25	2.058	1.353	1.110	1.939	1.296	1.064	-5.76%	-4.28%	-4.20%
						Average	**-4.15%**		

Table 9.11 presents the full scale of mean total resistance in regular waves for each optimal solution compared to the initial condition across different *Hs* and *Tp* combinations. It is shown that the optimal hull form with the optimal *GM* ratio increases total resistance in waves by up to 24.32% on average. Conversely, this hull form shows the highest improvement in seakeeping performance, as illustrated in Figure 9.10. The optimal hull form in this scenario shifted *LCB* position towards the bow from its initial position.

When compared to the optimal hull form in calm water total resistance, shifting the *LCB* to stern, results in an average reduction of 4.15% of mean total resistance. In contrast, the improvement of seakeeping performance of this hull form is the lowest compared to the other optimal solutions. It is shown that deforming hull form based on varying *LCB* and *CB* has an opposite effect both in seakeeping and resistance.

On the other hand, the initial hull form with optimal loading conditions (minimum R_y) also shows an average reduction in mean total resistance by 2.35%. Although this reduction is smaller than that achieved by the optimal hull form for calm water total resistance, the initial hull form with optimal loading condition performs better overall. Since the total resistance in calm water between the initial and optimal loading cases shows no significant difference, added resistance plays a crucial role in determining the total resistance in waves. The optimal loading condition can reduce added resistance, thereby lowering the total resistance in waves.

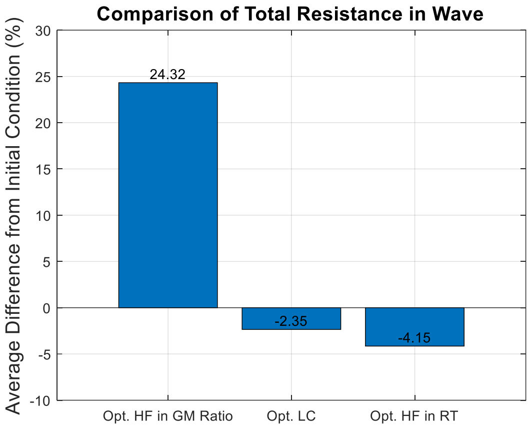

Figure 9.12. The comparison of mean total resistance in irregular waves

Figure 9.12 illustrates the comparison of the average differences between the three optimal solutions from the initial conditions. As in Figure 9.10, the data is arranged from the lowest to the highest *GM* ratio. The trend in Figure 9.12 presents opposite result to those in Figure 9.10. The hull form with the lowest *GM* ratio significantly enhances seakeeping performance but also increases the total resistance. The hull form with the highest *GM* ratio, which is optimised for minimal calm water total resistance, achieves the greatest reduction in mean total resistance in waves. However, it also shows the least improvement in seakeeping performance.

Interestingly, the initial hull form with minimal R_y, which lies between the two optimal hull forms for *GM* ratio and calm water total resistance, manages to improve seakeeping performance while also reducing mean total resistance. This balanced approach showcases the potential of optimising loading conditions to achieve both improved seakeeping and reduced resistance.

9.4. Summary

This chapter extends the optimisation of seakeeping performance to include calm water resistance. The total resistance in calm water was used as an objective function to be minimised, resulting in a reduction in total resistance in waves by using the same design variables as those used for minimising the *GM* ratio. Subsequently, the optimal loading condition of the optimal hull form was determined by minimising the radius of gyration in the y-axis (R_y).

A central composite design was employed to arrange the design of experiments for minimising both objective functions: calm water total resistance and R_y. Based on this design, a mathematical model was constructed to determine the optimal hull form with optimal loading conditions.

CFD simulations were used to compare the total resistance as well as the RAO for heave and pitch motion and the added resistance coefficient. Spectral analysis was conducted to quantify seakeeping performance in irregular waves, based on the wave scatter diagram representing the Java Sea, the operational area of the fishing vessel. The mean total resistance in irregular waves was determined from the added resistance and calm water resistance, both at full scale. The Froude method was used to extrapolate total resistance in calm water based on model scale data.

The findings show that this optimal hull form can reduce mean total resistance in waves by up to 4.11% and also improve seakeeping performance compared to the initial hull form. This study concludes that it is possible to simultaneously minimise mean total resistance in waves and improve seakeeping performance without involving complex multi-objective optimisation.

10. Conclusions, the Recommendations to the Stakeholder and Future Works

10.1. Introduction

In the present thesis, the dynamic performance of small fishing vessels in waves has been investigated under varied loading conditions. The research motivation, objectives, literature review, and focused investigations discussed in each chapter are presented in the previous chapters. This final chapter concludes by summarising the achieved main objectives outlined in the introduction. Additionally, future work and recommendations for stakeholders are presented.

10.2. Conclusions

The first objective listed in Chapter 1 was:

> *"To conduct a comprehensive literature review related to operability assessment, ship stability in waves, and strategies for enhancing seakeeping performance by identifying gaps that this research aims to fill as its novel contribution."*

This objective is achieved in Chapter 2, which presented the literature review related to the operability assessment, parametric roll (stability in waves), and the seakeeping optimisation. It was concluded that most operability assessments from the literature used a single loading condition and no operability assessment relate the stability curve in their calculations. As the loading condition varied, the single operability index is required to assess different vessel. The stability in waves, such as parametric roll, can be experienced by fishing vessel. In the literature, there is no parametric roll investigation that influence of loading condition, especially for fishing vessel. In the seakeeping optimisation, there is no existing literature which optimise the centre of gravity position and the hull form to improve seakeeping performance with a single objective function which indirectly calculate the seakeeping performance.

The second objective listed in Chapter 1 was:

> *"To assess the operability index of small fishing vessels and identify criteria that require improvement."*

This objective is achieved in Chapter 4. Based on the conventional operability index calculation the overall operability index for the small fishing boat is low, as there are some seakeeping criteria have low percentage. One of them is roll motion. The advance operability technique was used focusing on roll motion, namely operability robustness index. Three roll-related criteria were used to investigate the operability index for roll motion deeply: RMS of roll motion, angle of vanishing stability, and the down flooding angle. Each result showed a different trend due to different criteria value as a consequences of varied loading condition.

The third objective listed in Chapter 1 was:

> *"To investigate the best size for fishing vessels among various options using a single operability index."*

This objective is achieved in Chapter 5. Based on the finding in Chapter 4, a single fishing vessel which has multiple loading condition in their operation result in different operability index. When assessing the multiple vessels, it is non-trivial to determine which one exhibits the best performance. Developing a single operability assessment is therefore required. By utilising a single operability index which involve the multiple loading condition, this chapter revealed that fishing vessel with the same hull shape, position of centre of gravity relative to the vessel size, and Froude number showed a different index. The vessel with size of 20 m performed the highest operability index and suitable for operating in Java Sea. The vessel size which potentially has a 100% operability index is also revealed.

The fourth objective listed in Chapter 1 was:

> *"To examine how changes in payload and its position influence the occurrence of parametric roll."*

Chapter 6 addressed this objective. As the loading condition of fishing vessel is varied, the *GM* value, roll damping, the natural roll period/frequency are changed, which influenced the dynamic stability of the boats. From five loading condition scenarios, there are two conditions where the parametric roll is predicted to occur. The first one is the full load condition with high vertical centre of gravity (*KG*). In this case, the amplitude of parametric roll is relatively small. Another case is the lightship condition, where the fish tank is empty from the fish. Parametric roll occurred in this loading condition with large amplitude. The key parameter that influences parametric roll, the *GM* ratio, revealed that it affects the amplitude of heave and pitch motion with the same displacement.

The fifth objective listed in Chapter 1 was:

> *"To enhance the seakeeping performance by conducting optimisation for fish placement, represented by the Centre of Gravity (CoG), and hull form design to avoid parametric roll and potential capsizing, and to reduce the total resistance using novel single objective functions, the radius of gyration in the y-axis (R_y) and GM ratio, the ratio between GM in waves and calm water."*

This objective is addressed in detail in Chapter 7, Chapter 8, and Chapter 9. In Chapter 7, the optimisation for fish placement, represented by centre of gravity position was investigated. This chapter used y-axis radius gyration to be minimised to improve the seakeeping performance indirectly. The CFD simulation revealed that the best position of centre of gravity enhance the seakeeping performance. Moreover, the total resistance in calm water is not significantly changed from the initial case. The optimum centre of gravity location in R_y is also close to the optimum centre of gravity location in calm water resistance. This chapter revealed that the seakeeping can be improved without significantly changing the calm water resistance.

In Chapter 8, a second objective function was used, namely *GM* Ratio. The hull form was deformed by changing the longitudinal centre of buoyancy (*LCB*) and block coefficient to minimise the *GM* ratio and enhance the seakeeping performance indirectly. The best hull form, which has a minimum *GM* ratio, was achieved by shifting the LCB forward to the bow. Based on the CFD simulation, the seakeeping performance of the best hull form is enhanced. However, shifting the *LCB* forward to the bow is not beneficial for calm water resistance, which increased up to 30%.

In Chapter 9, the calm water resistance was used as an objective function to be minimised. With the same variable and hull form deformation as used in Chapter 8, the optimum hull form showed the opposite result from Chapter 8. The best *LCB* to minimise the calm water resistance shifted backward to the bow and showed the less improvement in seakeeping compared to the optimal hull form in Chapter 8. As the calm water resistance is minimal, the total resistance in wave become smaller compared to the initial and the best hull form in *GM* ratio, described in Chapter 8.

The sixth objective function listed in Chapter 1 was:

> *"To provide the recommendation to the stakeholders in the suitable fishing vessel size, fish placement, and the best hull form to be operated in Java Sea, including the optimisation method used in this thesis.*

This objective is addressed in the following subchapter.

10.3. Recommendations to the Stakeholder

Based on the results presented in this thesis, there are some recommendations to the stakeholders, theoretically and practically. The case study of fishing vessels in this thesis were examined in Java Sea, Indonesia. Therefore, the recommendations here are suitable used in Indonesia. However, the scientific methodology used in this thesis can be applied broadly to other fishing vessel operated in different area. The recommendations are described separately, according to stakeholders.

1. **Recommendations to Fishing Vessel Operators, Owners and Fishing Industry Associations:**

To enhance the safety of fishing vessels during operation by improving the seakeeping performance, it is recommended to use larger vessels to increase the operability index. A higher operability index allows the vessel to operate for longer durations. Conversely, a lower operability index restricts the vessel's operation, as certain sea conditions may prevent it from meeting seakeeping criteria. Then, during fishing, it is recommended to avoid having an empty fish tank while keeping the centre of gravity location low and close to the midship. The actual best position can be obtained by conducting the optimisation of the centre of gravity location by minimising the R_y value, which can be conducted by the ship builder or designer as demonstrated in this thesis.

2. **Recommendations to Fishing Vessel Designers and Ship Builder:**

The optimisation methodology to improve the seakeeping performance and reduce the total resistance, described in this thesis, can be applied by fishing vessel designers and ship builders to increase the efficiency in designing fishing vessels effectively. Therefore, they can provide the best hull form and provide the best position of centre gravity to the fishing vessel operator and owner in enhancing the fishing vessel safety and reducing the fuel consumption.

3. **Recommendations to Government Agencies and Insurance Companies:**

It is recommended to use the single operability index assessment, described in this thesis, by government agencies and insurance companies to assess the seaworthy of fishing vessel size before being built and be operated in Indonesia. The government agencies are recommended to make a policy in determining the fish placement by evaluating the R_y and GM ratio in every hull form design to enhance the safety.

4. **Recommendations to Academic and Research Institutions:**

The academic and research institution can expand the operability assessment and optimisation methodology in this thesis to be more comprehensive by developing the hull series that is suitable in a given operational area.

10.4. Future Work

The research in enhancing the safety of fishing through seakeeping performance presents many opportunities to be expanded. Even though the single operability assessment in this thesis covers multiple loading condition to be considered, the seakeeping criteria are key parameters in this assessment. Developing seakeeping criteria in Indonesian waters or other localised areas can be a piece of future work. The optimisation methodology in this thesis uses a single speed. The optimal result may be different when the speed changed. Therefore, the comprehensive optimisation can be carried out in the future by involving the speed changes.

The development of a sustainable fishing vessel hull series dedicated in some operational area is another future work. As different operational area has a different wave scatter diagram, the resulted hull form will be different too. The hull-propeller interaction in the resistance and powering simulation using computational fluid dynamics should be used to determine the efficient hull form in reducing fuel consumption. The influence of initial trim of fishing vessel hull form can be involved in design as it affects the manoeuvring performance.

References

Abdulkadir, I., Mohammed, B.S., Liew, M.S., Wahab, M.M.A., 2021. Modelling and multi-objective optimization of the fresh and mechanical properties of self-compacting high volume fly ash ECC (HVFA-ECC) using response surface methodology (RSM). Case Studies in Construction Materials 14, e00525.

American Bureau of Shipping (ABS), 2019. Guide For The Assessment Of Parametric Roll Resonance In The Design Of Container Carriers.

Bagheri, L., Ghassemi, H., Dehghanian, A., 2014. Optimizing the seakeeping performance of ship hull forms using genetic algorithm. TransNav: International Journal on Marine Navigation and Safety of Sea Transportation 8, 49–57.

Baitis, A.E., Holcombe, F., Conwell, S., Crossland, P., Colwell, J., Pattison, J., Strong, R., 1995. Motion Induced Interruption (MII) and Motion Induced Fatigue (MIF) Experiments at the Naval Biodynamics Laboratory.

Bales, N.K., 1980. Optimizing the seakeeping performance of destroyer type hulls, in: Published by: David W. Taylor Naval Ship Research \& Development Center, Ship Performance Department, Bethesda, Maryland, USA, Prepared for the 13th Symposium on Naval Hydrodynamics, ONR, Tokyo, Japan, 1980.

Bappenas, 2010. Presidential Regulation No. 5 of 2010 concerning the National Medium-Term Development Plan (in Indonesian).

Beck, R.F., Liapis, S., 1987. Transient motions of floating bodies at zero forward speed. Journal of ship research 31, 164–176.

Bezerra, M.A., Santelli, R.E., Oliveira, E.P., Villar, L.S., Escaleira, L.A., 2008. Response surface methodology (RSM) as a tool for optimization in analytical chemistry. Talanta 76, 965–977.

Bhattacharyya, R., 1978. Dynamics of Marine Vehicles. John Wiley & Sons Inc, New York.

Burmester, S., Vaz, G., el Moctar, O., 2020. Towards credible CFD simulations for floating offshore wind turbines. Ocean Engineering 209, 107237. https://doi.org/10.1016/j.oceaneng.2020.107237

Caamaño, L.S., Galeazzi, R., Nielsen, U.D., González, M.M., Casás, V.D., 2019. Real-time detection of transverse stability changes in fishing vessels. Ocean Engineering 189, 106369.

Caamaño, L.S., González, M.M., Casás, V.D., 2018. On the feasibility of a real time stability assessment for fishing vessels. Ocean Engineering 159, 76–87.

Celik, I.B., Ghia, U., Roache, J, P., Freitas, J, C., 2008. Procedure for Estimation and Reporting of Uncertainty Due to Discretization in CFD Applications. Journal of Fluids Engineering 130, 078001. https://doi.org/10.1115/1.2960953

Cho, J.-H., Lee, S.-H., Oh, D., Paik, K.-J., 2023. A numerical study on the added resistance and motion of a ship in bow quartering waves using a soft spring system. Ocean Engineering 280, 114620.

Datta, R., Rodrigues, J.M., Soares, C.G., 2011. Study of the motions of fishing vessels by a time domain panel method. Ocean Engineering 38, 782–792. https://doi.org/https://doi.org/10.1016/j.oceaneng.2011.02.002

Davis, B., Colbourne, B., Molyneux, D., 2019. Analysis of fishing vessel capsizing causes and links to operator stability training. Safety science 118, 355–363.

Deakin, B., 2006. Developing simple safety guidance for fishermen, in: 9th

International Conference on Stability of Ships and Ocean Vehicles, Rio de Janeiro, Brasil.

Deakin, B., 2005. An experimental evaluation of the stability criteria of the HSC Code, in: International Conference on Fast Sea Transportation, FAST.

Díaz-Ojeda, H.R., Pérez-Arribas, F., Turnock, S.R., 2023. The influence of dihedral bulbous bows on the resistance of small fishing vessels: A numerical study. Ocean Engineering 281, 114661.

Diez, M., Serani, A., Campana, E.F., Goren, O., Sarioz, K., Danisman, D.B., Grigoropoulos, G., Aloniati, E., Visonneau, M., Queutey, P., Stern, F., 2015. Multi-Objective Hydrodynamic Optimization of the DTMB 5415 for Resistance and Seakeeping, in: Day 2 Thu, September 03, 2015. SNAME, pp. 1–17. https://doi.org/10.5957/FAST-2015-034

Djatmiko, E.B., 2012. Behavior and Operability of Marine Buildings on Random Waves (in Indonesian). ITS-Press. Surabaya. Indonesia.

Domeh, V., Obeng, F., Khan, F., Bose, N., Sanli, E., 2021. Risk analysis of man overboard scenario in a small fishing vessel. Ocean Engineering 229, 108979.

Eriksen, J.H., Nona, R.A., Mas, C., 2000. Common procedures for seakeeping in the ship design process. STANAG 4154, 2000.

Faltinsen, O.M., 2005. Hydrodynamics of high-speed marine vehicles. Cambridge university press.

FAO, 2000. The State of World Fisheries and Aquaculture Part 2: Selected Issues Facing Fishers and Aquaculturists, the State of World Fisheries and Aquaculture. Food & Agriculture Org.

Fathi, D.E., 2018. ShipX Vessel Responses (VERES), User's Manual. SINTEF Ocean AS.

Fonseca, N., Soares, C.G., 2002. Sensitivity of the expected ships availability to different seakeeping criteria, in: International Conference on Offshore Mechanics and Arctic Engineering. pp. 595–603.

France, W.N., Levadou, M., Treakle, T.W., Paulling, J.R., Michel, R.K., Moore, C., 2003. An Investigation of Head-Sea Parametric Rolling and Its Influence on Container Lashing Systems. Marine Technology and SNAME News 40, 1–19. https://doi.org/10.5957/mt1.2003.40.1.1

Francescutto, A., 2001. An Experimental Investigation of Parametric Rolling in Head Waves. Journal of Offshore Mechanics and Arctic Engineering 123, 65–69. https://doi.org/10.1115/1.1355247

Galbraith, A., Boulougouris, E., 2015. Parametric rolling of the tumblehome hull using CFD, in: Proceedings of the 12th International Conference on the Stability of Ships and Ocean Vehicles. pp. 535–543.

Gammon, M.A., 2011. Optimization of fishing vessels using a Multi-Objective Genetic Algorithm. Ocean Engineering 38, 1054–1064. https://doi.org/10.1016/j.oceaneng.2011.03.001

Ghaemi, M.H., Olszewski, H., 2017. Total ship operability--review, concept and criteria. Polish maritime research 24, 74–81.

Ghamari, I., Faltinsen, O.M., Greco, M., Lugni, C., 2017. Parametric Resonance of a Fishing Vessel With and Without Anti-Roll Tank: An Experimental and Numerical Study, in: Volume 7A: Ocean Engineering. American Society of Mechanical Engineers, p. V07AT06A012. https://doi.org/10.1115/OMAE2017-62053

Ghamari, I., Greco, M., Faltinsen, O.M., Lugni, C., 2020. Numerical and experimental study on the parametric roll resonance for a fishing vessel with and without forward speed. Applied Ocean Research 101, 102272. https://doi.org/10.1016/j.apor.2020.102272

González, M.M., Sobrino, P.C., Álvarez, R.T., Casás, V.D., López, A.M., Peña, F.L., 2012. Fishing vessel stability assessment system. Ocean Engineering 41, 67–78.

Grigoropoulos, G.J., Loukakis, T.A., 1988. A new method for developing hull forms with superior seakeeping qualities. Proceedings of CADMO 88.

Guan, G., Wang, L., Geng, J., Zhuang, Z., Yang, Q., 2021. Parametric automatic optimal design of USV hull form with respect to wave resistance and seakeeping. Ocean Engineering 235, 109462. https://doi.org/10.1016/j.oceaneng.2021.109462

Guan, G., Zhuang, Z., Yang, Q., Wang, P., Jin, S., 2022. Hull form optimization design of SWATH with combination evaluations of resistance and seakeeping performance. Ocean Engineering 264, 112513. https://doi.org/10.1016/j.oceaneng.2022.112513

Gutsch, M., Sprenger, F., Steen, S., 2017. Design parameters for increased operability of offshore crane vessels, in: International Conference on Offshore Mechanics and Arctic Engineering. p. V009T12A029.

Gutsch, M., Steen, S., Sprenger, F., 2020. Operability robustness index as seakeeping performance criterion for offshore vessels. Ocean Engineering 217, 107931.

Hashimoto, H., Furusho, K., 2022. Influence of sea areas and season in navigation on the ship vulnerability to the parametric rolling failure mode. Ocean Engineering 266, 112714. https://doi.org/10.1016/j.oceaneng.2022.112714

Hasselmann, K.F., Barnett, T.P., Bouws, E., Carlson, H., Cartwright, D.E., Eake, K., Euring, J.A., Gicnapp, A., Hasselmann, D.E., Kruseman, P., others, 1973. Measurements of wind-wave growth and swell decay during the Joint North Sea Wave Project (JONSWAP). Ergaenzungsheft zur Deutschen Hydrographischen Zeitschrift, Reihe A.

He, G., Kashiwagi, M., 2014. A time-domain higher-order boundary element method for 3D forward-speed radiation and diffraction problems. Journal of Marine Science and Technology 19, 228–244.

Himeno, Y., 1981. Prediction of ship roll damping-state of the art. The University of Michigan, College of Engineering, Department of Naval Architecture and Marine Engineering, USA, Report No. 239.

Hirt, C.W., Nichols, B.D., 1981. Volume of fluid (VOF) method for the dynamics of free boundaries. Journal of computational physics 39, 201–225.

Hooft, J.P., 1987. Mathematical description of the manoeuvrability of high-speed surface ships.

Hooke, R., Jeeves, T.A., 1961. ``Direct Search''Solution of Numerical and Statistical Problems. Journal of the ACM (JACM) 8, 212–229.

Hosseini, S.H.S., 2009. CFD prediction of ship capsize: parametric rolling, broaching, surf-riding, and periodic motions. The University of Iowa.

Huang, F., Wang, L., Yang, C., 2015. Hull form optimization for reduced drag and improved seakeeping using a surrogate-based method, in: ISOPE International Ocean and Polar Engineering Conference. p. ISOPE--I.

Hüffmeier, J., Lundman, J., Elern, F., 2020. Trim and ballast optimization for a tnaker based on machine learning. Ecoprodigi, Intereg Baltic Sea region.

Ikeda, Y., 1979. On roll damping force of ship-effect of hull surface pressure created by bilge keels. University of Osaka Prefacture, Department of Naval Architecture, Japan, Report No. 00402, Published in: Journal of Society of Naval Architects of Japan, No. 165, 1979.

Ikeda, Y., Himeno, Y., Tanaka, N., 1977. On eddy making component of roll damping force on naked hull. Journal of the society of Naval Architects of Japan 1977, 54–64.

IMO, 2020. SDC 7/WP. 6 Finalization of Second Generation Intact Stability Criteria—Report of the Drafting Group on Intact Stability. IMO: London, UK.

IMO, 2008a. International Code of Intact Stability. London, UK.

IMO, 2008b. International Code on Intact Stability (IS Code).

Iqbal, M., Hadi, E.S., Pranamya, G., 2019. Geometry Optimization Of Centre Bulb To Reduce Wave Resistance On Catamaran Ship, in: International Conference on Ship and Offshore Technology (ICSOT) Indonesia. Semarang.

Iqbal, M., Terziev, M., Tezdogan, T., Incecik, A., 2024. Unsteady RANS CFD Simulation on the Parametric Roll of Small Fishing Boat under Different Loading Conditions. Journal of Marine Science and Application. https://doi.org/https://doi.org/10.1007/s11804-024-00427-0

Iqbal, M., Terziev, M., Tezdogan, T., Incecik, A., 2023. Operability analysis of traditional small fishing boats in Indonesia with different loading conditions. Ships and Offshore Structures 18, 1060–1079. https://doi.org/10.1080/17445302.2022.2107300

ISSC, 1964. Proceedings of the 2nd International Ship Structures Congress. Delft, The Netherlands.

ITTC, 2014. Practical Guidelines for Ship Resistance CFD, ITTC – Recommended Procedures and Guidelines 27th.

ITTC, 2002. Final report and recommendations to the 23rd ITTC. Proceeding of 23rd ITTC: The Specialist Committee on Waves.

ITTC, I., 2011. Practical guidelines for ship CFD applications. Recommended Procedures and Guidelines 18.

Jin, D., Thunberg, E., 2005. An analysis of fishing vessel accidents in fishing areas off the northeastern United States. Safety Science 43, 523–540.

Kato, H., 1957. On the frictional resistance to the rolling of ships. Journal of Zosen Kiokai 1957, 115–122.

Khosravi Babadi, M., Ghassemi, H., 2024. Optimization of ship hull forms by changing CM and CB coefficients to obtain optimal seakeeping performance. Plos one 19, e0302054.

Kim, H., Yang, C., 2010. A new surface modification approach for CFD-based hull form optimization. Journal of Hydrodynamics 22, 503–508.

Lackenby, H., 1950. On the systematic geometrical variation of ship forms. Transactions of the TINA 92, 289–316.

Liapis, S.J., Beck, R., 1985. Seekeeping computations using time-domain analysis, in: Proceeding of the Fourth International Symposium on Numerical Hydrodynamics. pp. 34–54.

Lin, W.-M., Salvesen, N., 1997. Nine Years of Progress with LAMP-The Large Amplitude Motion Program. Science Applications International Corp Report SAIC-97/1079.

Liu, L., Chen, M., Wang, X., Zhang, Z., Yu, J., Feng, D., 2021. CFD prediction of full-scale ship parametric roll in head wave. Ocean Engineering 233, 109180. https://doi.org/10.1016/j.oceaneng.2021.109180

Liu, L., Feng, D., Wang, X., Zhang, Z., Yu, J., Chen, M., 2022. Numerical study on the effect of sloshing on ship parametric roll. Ocean Engineering 247, 110612. https://doi.org/10.1016/j.oceaneng.2022.110612

Liu, P.C., 1971. Normalized and equilibrium spectra of wind waves in Lake Michigan. Journal of physical oceanography 1, 249–257.

Liu, W., Demirel, Y.K., Djatmiko, E.B., Nugroho, S., Tezdogan, T., Kurt, R.E., Supomo, H., Baihaqi, I., Yuan, Z., Incecik, A., 2019. Bilge keel design for the traditional fishing boats of Indonesia's East Java. International Journal of Naval Architecture and Ocean Engineering 11, 380–395. https://doi.org/10.1016/j.ijnaoe.2018.07.004

Liu, Y., Liu, L., Maki, A., Bu, S., Dostal, L., 2023. Research on second level of vulnerability criteria of parametric rolling with stochastic stability theory. Ocean Engineering 284, 115043. https://doi.org/10.1016/j.oceaneng.2023.115043

Lu, J., Gu, M., Umeda, N., 2016. A study on the effect of parametric roll on added resistance in regular head seas. Ocean Engineering 122, 288–292. https://doi.org/10.1016/j.oceaneng.2016.06.016

Ma, S., Ge, W., Ertekin, R.C., He, Q., Duan, W., 2018. Experimental and Numerical Investigations of Ship Parametric Rolling in Regular Head Waves. China Ocean Engineering 32, 431–442. https://doi.org/10.1007/s13344-018-0045-6

Mantari, J.L., e Silva, S.R., Soares, C.G., 2011. Intact stability of fishing vessels under combined action of fishing gear, beam waves and wind. Ocean engineering 38, 1989–1999.

Marín López, J.R., Villamarín, E.G., Mendoza, J.I., Paredes, R.J., Datla, R., 2021. Conceptual design recommendations to improve seakeeping of small high-speed craft providing interisland transportation in Galápagos, in: SNAME International Conference on Fast Sea Transportation. p. D021S003R004.

Marlantes, K.E., Kim, S. (Peter), Hurt, L.A., 2021. Implementation of the IMO Second Generation Intact Stability Guidelines. Journal of Marine Science and Engineering 10, 41. https://doi.org/10.3390/jmse10010041

Maruo, H., 1963. Resistance in waves, research on seakeeping qualities of ships in Japan. The Society of Naval Architects of Japan 8, 67–102.

Maruyama, Y., Maki, A., Dostal, L., Umeda, N., 2023. Estimation of acceleration probability density function for parametric rolling using PLIM. Ocean Engineering 280, 114561. https://doi.org/10.1016/j.oceaneng.2023.114561

Mata-Álvarez-Santullano, F., Souto-Iglesias, A., 2014. Stability, safety and operability of small fishing vessels. Ocean Engineering 79, 81–91. https://doi.org/10.1016/j.oceaneng.2014.01.011

Mathews, S.T., 1972. A critical review of the 12th ITTC Wave Spectrum Recommendations, Report of Seakeeping Committee, Appendix 9. Proceedings of 13th I TTC, Berlin 973–986.

Menter, F.R., 1994. Two-equation eddy-viscosity turbulence models for engineering applications. AIAA Journal 32, 1598–1605. https://doi.org/10.2514/3.12149

Miao, A., Chen, T., Qi, X., Wan, D., 2018. Multi-objective optimization design of KCS based on seakeeping performance, in: ISOPE International Ocean and Polar Engineering Conference. p. ISOPE--I.

Miller, E.R., 1974. Roll Damping. Technical Report 6136-74-280, 1974, NAVSPEC.

Muawanah, U., Yusuf, G., Adrianto, L., Kalther, J., Pomeroy, R., Abdullah, H., Ruchimat, T., 2018. Review of national laws and regulation in Indonesia in relation to an ecosystem approach to fisheries management. Marine Policy 91, 150–160.

Muzaferija, S., 1998. Computation of free surface flows using interface-tracking and interface-capturing methods. Nonlinear water-wave interaction. Computational Mechanics, Southampton.

Myrhaug, D., Dahle, E.A., 1994. Chapter 2: Ship capsize in breaking waves, in: Chakrabarti, S.K. (Ed.), Fluid Structure InteracƟon in Offshore Engineering.

Nakos, D., Sclavounos, P., 1991. Ship motions by a three-dimensional Rankine panel method.

Neves, M.A.S., 2002. Experimental Analysis on Parametric Resosnance for Two Fishing Vessels in Head Seas, in: Proceedings of the 6th International Ship Stability Workshop, Webb Institute, Proceedings. Paper: P2002-1.

Neves, M.A.S., Pérez, N.A., Lorca, O.M., Rodr\'\iguez, C.A., 2011. An Investigation on Head-Sea Parametric Rolling for Two Fishing Vessels, in: Contemporary Ideas on Ship Stability and Capsizing in Waves. Springer, pp. 231–252.

Neves, M.A.S., Pérez, N.A., Valerio, L., 1999. Stability of small fishing vessels in longitudinal waves. Ocean Engineering 26, 1389–1419. https://doi.org/10.1016/S0029-8018(98)00023-7

Neves, M.A.S., Rodríguez, C.A., 2006. On unstable ship motions resulting from strong non-linear coupling. Ocean Engineering 33, 1853–1883. https://doi.org/10.1016/j.oceaneng.2005.11.009

Nielsen, I.R., 1987. Assessment of ship performance in a seaway. Publisher: NORDFORSK, Sortedam Dossering 19, DK-200 Copenhage, Denmark, ISBN: 87-982637-1-4.

Niklas, K., Pruszko, H., 2019. Full scale CFD seakeeping simulations for case study ship redesigned from V-shaped bulbous bow to X-bow hull form. Applied Ocean Research 89, 188–201.

O'Hanlon, J.F., McCauley, M.E., 1973. Motion sickness incidence as a function of the frequency and acceleration of vertical sinusoidal motion.

Obeng, F., Domeh, V., Khan, F., Bose, N., Sanli, E., 2022a. Capsizing accident scenario model for small fishing trawler. Safety science 145, 105500.

Obeng, F., Domeh, V., Khan, F., Bose, N., Sanli, E., 2022b. Analyzing operational risk for small fishing vessels considering crew effectiveness. Ocean Engineering 249, 110512.

Ochi, M.K., 1964. Prediction of occurrence and severity of ship slamming at sea, in: David Taylor Model Basin, Naval Ship Research and Development Center, Washington DC, USA, Proceedings of the 5th Symposium on Naval Hydrodynamics, ONR, Bergen, Norway, Pp. 545-596, Paper: P1964-2 Proceedings.

Ochi, M.K., Hubble, E.N., 1976. Six-parameter wave spectra, in: Proceedings of the 15th Coastal Engineering Conference. Honolulu, USA, pp. 301–328.

Ozmen, G., 1995. Hull Form Optimisation of Fishing Vessels With Respect to Seakeeping. Phd Thesis. University of Glasgow.

Ozturk, D., Delen, C., Mancini, S., Serifoglu, M.O., Hizarci, T., 2021. Full-Scale CFD Analysis of Double-M Craft Seakeeping Performance in Regular Head Waves. Journal of Marine Science and Engineering 9, 504.

https://doi.org/10.3390/jmse9050504

Park, D.-M., Kim, Y., Song, K.-H., 2013. Sensitivity in numerical analysis of parametric roll. Ocean Engineering 67, 1–12. https://doi.org/10.1016/j.oceaneng.2013.04.008

Paulling, J.R., Rosenberg, R.M., 1959. On Unstable Ship Motions Resulting From Nonlinear Coupling. Journal of Ship Research 3, 36–46. https://doi.org/10.5957/jsr.1959.3.2.36

Pérez-Arribas, F., Silva-Campillo, A., D\'\iaz-Ojeda, H.R., 2022. Design of Dihedral Bows: A New Type of Developable Added Bulbous Bows—Experimental Results. Journal of Marine Science and Engineering 10, 1691.

Perez, T., 2015. Ship seakeeping operability, motion control, and Autonomy-A Bayesian Perspective. IFAC-PapersOnLine 48, 217–222.

Pierson Jr, W.J., Moskowitz, L., 1964. A proposed spectral form for fully developed wind seas based on the similarity theory of SA Kitaigorodskii. Journal of geophysical research 69, 5181–5190.

Ravenna, R., Song, S., Shi, W., Sant, T., De Marco Muscat-Fenech, C., Tezdogan, T., Demirel, Y.K., 2022. CFD analysis of the effect of heterogeneous hull roughness on ship resistance. Ocean Engineering 258, 111733. https://doi.org/10.1016/j.oceaneng.2022.111733

Reichel, M., Minchev, A., Larsen, N.L., 2014. Trim optimisation-theory and practice. TransNav: International Journal on Marine Navigation and Safety of Sea Transportation 8.

Riberio e Silva, S., Turk, A., Guedes Soares, C., PRPIĆ-ORŠIĆ, J., 2010. On the parametric rolling of container vessels. Brodogradnja: Teorija i praksa brodogradnje i pomorske tehnike 61, 347–358.

Richardson, L.F., 1911. IX. The approximate arithmetical solution by finite differences of physical problems involving differential equations, with an application to the stresses in a masonry dam. Philosophical Transactions of the Royal Society of London. Series A, Containing Papers of a Mathematical or Physical Character 210, 307–357. https://doi.org/10.1098/rsta.1911.0009

Roache, P.J., 1998. Verification and validation in computational science and engineering. Hermosa Albuquerque, NM.

Rodríguez, C.A., Ramos, I.S., Esperança, P.T.T., Oliveira, M.C., 2020. Realistic estimation of roll damping coefficients in waves based on model tests and numerical simulations. Ocean Engineering 213, 107664. https://doi.org/10.1016/j.oceaneng.2020.107664

Romanowski, A., Tezdogan, T., Turan, O., 2019. Development of a CFD methodology for the numerical simulation of irregular sea-states. Ocean Engineering 192, 106530.

Romero-Tello, P., Gutierrez-Romero, J.E., Serván-Camas, B., 2022. Seakeeping optimization of cruise ship based on artificial neural networks. Trends in Maritime Technology and Engineering 435–441.

Rotteveel, E., Hekkenberg, R., van der Ploeg, A., 2017. Inland ship stern optimization in shallow water. Ocean Engineering 141, 555–569.

Roy, R., Hinduja, S., Teti, R., 2008. Recent advances in engineering design optimisation: Challenges and future trends. CIRP annals 57, 697–715.

Sadat-Hosseini, H., Stern, F., Olivieri, A., Campana, E.F., Hashimoto, H., Umeda, N., Bulian, G., Francescutto, A., 2010. Head-wave parametric rolling of a surface combatant. Ocean Engineering 37, 859–878. https://doi.org/10.1016/j.oceaneng.2010.02.010

Salvesen, N., Tuck, E.O., Faltinsen, O., 1970. Ship Motions and Sea Loads. Transactions of the Society of Naval Architects and Marine Engineers 78, 250–287.

Sandvik, E., Gutsch, M., Asbjørnslett, B.E., 2018. A simulation-based ship design methodology for evaluating susceptibility to weather-induced delays during marine operations. Ship Technology Research 65, 137–152.

Sariöz, K., Sariöz, E., 2006. Practical seakeeping performance measures for high speed displacement vessels. Naval engineers journal 118, 23–36.

Sarıöz, E., 2009. Inverse design of ship hull forms for seakeeping. Ocean Engineering 36, 1386–1395. https://doi.org/10.1016/j.oceaneng.2009.08.011

Sayli, A., Alkan, A.D., Nabergoj, R., Uysal, A.O., 2007. Seakeeping assessment of fishing vessels in conceptual design stage. Ocean Engineering 34, 724–738.

Schumacher, A., Ribeiro e Silva, S., Guedes Soares, C., 2016. Experimental and numerical study of a containership under parametric rolling conditions in waves. Ocean Engineering 124, 385–403. https://doi.org/10.1016/j.oceaneng.2016.07.034

Scott, J.R., 1965. A sea spectrum for model tests and long-term ship prediction. Journal of ship research 9, 145–152.

Serani, A., Ficini, S., Grigoropoulos, G., Bakirtzogou, C., Broglia, R., Diez, M., Papadakis, G., Goren, O., Danisman, D.B., Scholcz, T., others, 2022. Resistance and seakeeping optimization of a naval destroyer by multi-fidelity methods. VCG 1000, 0–56.

Shivachev, E., Khorasanchi, M., Day, S., Turan, O., 2020. Impact of trim on added resistance of KRISO container ship (KCS) in head waves: An experimental and numerical study. Ocean Engineering 211, 107594.

Siemens, 2022. Star-CCM+ User Guide version 17.02.

Simonsen, C.D., Otzen, J.F., Joncquez, S., Stern, F., 2013. EFD and CFD for KCS heaving and pitching in regular head waves. Journal of Marine Science and Technology 18, 435–459.

Spanos, D., Papanikolaou, A., 2007. Numerical simulation of parametric roll in head seas. International Shipbuilding Progress 54, 249–267.

Spanos, D., Papanikolaou, A., 2006. Numerical simulation of a fishing vessel in parametric roll in head seas. Marine Systems & Ocean Technology 2, 39–44. https://doi.org/10.1007/BF03449182

St Denis, M., Pierson, W.J., 1953. On the motions of ships in confused seas. Trans. Soc. Naval Architects and Marine Engineers 61, 280–357.

Statistics Indonesia, 2019. Number of Boats/Ships by Province and Type of Boats/Ships for Marine Fisheries, 2000-2016 (In Indonesian).

Stern, F., Wilson, R. V, Coleman, H.W., Paterson, E.G., 2001. Comprehensive Approach to Verification and Validation of CFD Simulations—Part 1: Methodology and Procedures. Journal of Fluids Engineering 123, 793–802. https://doi.org/10.1115/1.1412235

Tello, M., Ribeiro E Silva, S., Guedes Soares, C., 2011. Seakeeping performance of fishing vessels in irregular waves. Ocean Engineering 38, 763–773. https://doi.org/10.1016/j.oceaneng.2010.12.020

Tello, M., Ribeiro E Silva, S., Guedes Soares, C., 2009. Fishing Vessels Responses in

Waves under Operational Conditions, in: Proceedings of the XXI Naval Architecture Pan-American Conference (COPINAVAL'09). pp. 18–22.

Terziev, M., Tezdogan, T., Incecik, A., 2022. Scale effects and full-scale ship hydrodynamics: A review. Ocean Engineering 245, 110496. https://doi.org/10.1016/j.oceaneng.2021.110496

Tezdogan, T., Demirel, Y.K., Kellett, P., Khorasanchi, M., Incecik, A., Turan, O., 2015. Full-scale unsteady RANS CFD simulations of ship behaviour and performance in head seas due to slow steaming. Ocean Engineering 97, 186–206. https://doi.org/10.1016/j.oceaneng.2015.01.011

Tezdogan, T., Incecik, A., Turan, O., 2016. Full-scale unsteady RANS simulations of vertical ship motions in shallow water. Ocean Engineering 123, 131–145. https://doi.org/10.1016/j.oceaneng.2016.06.047

Tezdogan, T., Incecik, A., Turan, O., 2014. Operability assessment of high speed passenger ships based on human comfort criteria. Ocean Engineering 89, 32–52.

Tezdogan, T., Shenglong, Z., Demirel, Y.K., Liu, W., Leping, X., Yuyang, L., Kurt, R.E., Djatmiko, E.B., Incecik, A., 2018. An investigation into fishing boat optimisation using a hybrid algorithm. Ocean Engineering 167, 204–220. https://doi.org/10.1016/j.oceaneng.2018.08.059

Tran, T.G., Nguyen, H.V., Huynh, Q. Van, 2023. A method for optimizing the hull form of fishing vessels. Journal of Ship Research 67, 72–91.

Ugurlu, F., Yildiz, S., Boran, M., Ugurlu, Ö., Wang, J., 2020. Analysis of fishing vessel accidents with Bayesian network and Chi-square methods. Ocean Engineering 198, 106956.

Utomo, B., Iqbal, M., 2020. Vertical Motion Optimization of Series 60 Hull Forms Using Response Surface Methods. Kapal: Jurnal Ilmu Pengetahuan dan Teknologi Kelautan 17, 130–137.

Vernengo, G., Brizzolara, S., Bruzzone, D., 2015. Resistance and seakeeping optimization of a fast multihull passenger ferry. International Journal of Offshore and Polar Engineering 25, 26–34.

Wackers, J., Koren, B., Raven, H.C., van der Ploeg, A., Starke, A.R., Deng, G.B., Queutey, P., Visonneau, M., Hino, T., Ohashi, K., 2011. Free-Surface Viscous Flow Solution Methods for Ship Hydrodynamics. Archives of Computational Methods in Engineering 18, 1–41. https://doi.org/10.1007/s11831-011-9059-4

Wang, J., Pillay, A., Kwon, Y.S., Wall, A.D., Loughran, C.G., 2005. An analysis of fishing vessel accidents. Accident Analysis & Prevention 37, 1019–1024.

Wang, S.M., Ma, S., Duan, W.Y., 2018. Seakeeping optimization of trimaran outrigger layout based on NSGA-II. Applied Ocean Research 78, 110–122. https://doi.org/10.1016/j.apor.2018.06.010

Wen, P., Fadillah, A., 2022. The Effect of Trim on Stability and Seakeeping of Tanker, Container, and Bulk Carrier, in: IOP Conference Series: Earth and Environmental Science. p. 12037.

Wulandari, A.I., Utama, I., Rofidayanti, A., Hudson, D., 2024. Numerical analysis of ship motion of crew boat with variations of wave period on ship operational speed. CFD Letters 16.

Xiaobo, Z., 2017. Comparison of response surface method and Kriging method for approximation modeling, in: 2017 2nd International Conference on Power and Renewable Energy (ICPRE). pp. 66–70.

Xing, T., Stern, F., 2010. Factors of safety for Richardson extrapolation.

Yu, L., Ma, N., Wang, S., 2019. Parametric roll prediction of the KCS containership in head waves with emphasis on the roll damping and nonlinear restoring moment. Ocean Engineering 188, 106298. https://doi.org/10.1016/j.oceaneng.2019.106298

Yu, L., Taguchi, K., Kenta, A., Ma, N., Hirakawa, Y., 2018. Model experiments on the early detection and rudder stabilization of KCS parametric roll in head waves. Journal of Marine Science and Technology 23, 141–163. https://doi.org/10.1007/s00773-017-0463-9

Yulianti, S., Samuel, S., Nainggolan, T.S., Iqbal, M., 2022. Meshing generation strategy for prediction of ship resistance using CFD approach. IOP Conference Series: Earth and Environmental Science 1081, 012027. https://doi.org/10.1088/1755-1315/1081/1/012027

Zhang, L., Zhang, J., Shang, Y., 2021. A practical direct URANS CFD approach for the speed loss and propulsion performance evaluation in short-crested irregular head waves. Ocean Engineering 219, 108287.

Zhang, S., Tezdogan, T., Zhang, B., Xu, L., Lai, Y., 2018. Hull form optimisation in waves based on CFD technique. Ships and Offshore Structures 13, 149–164. https://doi.org/10.1080/17445302.2017.1347231

Zhao, C., Wang, W., Jia, P., Xie, Y., 2021. Optimisation of hull form of ocean-going trawler. Brodogradnja: An International Journal of Naval Architecture and Ocean Engineering for Research and Development 72, 33–46.

Zhou, Y., 2019. Further validation study of hybrid prediction method of parametric roll. Ocean Engineering 186, 106103. https://doi.org/10.1016/j.oceaneng.2019.06.008

Zhou, Y., Ma, N., Lu, J., Gu, M., 2016. A study of hybrid prediction method for ship parametric rolling. Journal of Hydrodynamics 28, 617–628. https://doi.org/10.1016/S1001-6058(16)60666-2

Zhou, Y., Sun, Q., Shi, X., 2022. Experimental and numerical study on the parametric roll of an offshore research vessel with extended low weather deck. Ocean Engineering 262, 111914. https://doi.org/10.1016/j.oceaneng.2022.111914

Abdulkadir, I., Mohammed, B.S., Liew, M.S., Wahab, M.M.A., 2021. Modelling and multi-objective optimization of the fresh and mechanical properties of self-compacting high volume fly ash ECC (HVFA-ECC) using response surface methodology (RSM). Case Studies in Construction Materials 14, e00525.

American Bureau of Shipping (ABS), 2019. Guide For The Assessment Of Parametric Roll Resonance In The Design Of Container Carriers.

Bagheri, L., Ghassemi, H., Dehghanian, A., 2014. Optimizing the seakeeping performance of ship hull forms using genetic algorithm. TransNav: International Journal on Marine Navigation and Safety of Sea Transportation 8, 49–57.

Baitis, A.E., Holcombe, F., Conwell, S., Crossland, P., Colwell, J., Pattison, J., Strong, R., 1995. Motion Induced Interruption (MII) and Motion Induced Fatigue (MIF) Experiments at the Naval Biodynamics Laboratory.

Bales, N.K., 1980. Optimizing the seakeeping performance of destroyer type hulls, in: Published by: David W. Taylor Naval Ship Research \& Development Center, Ship Performance Department, Bethesda, Maryland, USA, Prepared for the 13th Symposium on Naval Hydrodynamics, ONR, Tokyo, Japan, 1980.

Bappenas, 2010. Presidential Regulation No. 5 of 2010 concerning the National Medium-Term Development Plan (in Indonesian).

Beck, R.F., Liapis, S., 1987. Transient motions of floating bodies at zero forward speed. Journal of ship research 31, 164–176.

Bezerra, M.A., Santelli, R.E., Oliveira, E.P., Villar, L.S., Escaleira, L.A., 2008. Response surface methodology (RSM) as a tool for optimization in analytical chemistry. Talanta 76, 965–977.

Bhattacharyya, R., 1978. Dynamics of Marine Vehicles. John Wiley & Sons Inc, New York.

Burmester, S., Vaz, G., el Moctar, O., 2020. Towards credible CFD simulations for floating offshore wind turbines. Ocean Engineering 209, 107237. https://doi.org/10.1016/j.oceaneng.2020.107237

Caamaño, L.S., Galeazzi, R., Nielsen, U.D., González, M.M., Casás, V.D., 2019. Real-time detection of transverse stability changes in fishing vessels. Ocean Engineering 189, 106369.

Caamaño, L.S., González, M.M., Casás, V.D., 2018. On the feasibility of a real time stability assessment for fishing vessels. Ocean Engineering 159, 76–87.

Celik, I.B., Ghia, U., Roache, J, P., Freitas, J, C., 2008. Procedure for Estimation and Reporting of Uncertainty Due to Discretization in CFD Applications. Journal of Fluids Engineering 130, 078001. https://doi.org/10.1115/1.2960953

Cho, J.-H., Lee, S.-H., Oh, D., Paik, K.-J., 2023. A numerical study on the added resistance and motion of a ship in bow quartering waves using a soft spring system. Ocean Engineering 280, 114620.

Datta, R., Rodrigues, J.M., Soares, C.G., 2011. Study of the motions of fishing vessels by a time domain panel method. Ocean Engineering 38, 782–792. https://doi.org/https://doi.org/10.1016/j.oceaneng.2011.02.002

Davis, B., Colbourne, B., Molyneux, D., 2019. Analysis of fishing vessel capsizing causes and links to operator stability training. Safety science 118, 355–363.

Deakin, B., 2006. Developing simple safety guidance for fishermen, in: 9th International Conference on Stability of Ships and Ocean Vehicles, Rio de Janeiro, Brasil.

Deakin, B., 2005. An experimental evaluation of the stability criteria of the HSC Code, in: International Conference on Fast Sea Transportation, FAST.

Díaz-Ojeda, H.R., Pérez-Arribas, F., Turnock, S.R., 2023. The influence of dihedral bulbous bows on the resistance of small fishing vessels: A numerical study. Ocean Engineering 281, 114661.

Diez, M., Serani, A., Campana, E.F., Goren, O., Sarioz, K., Danisman, D.B., Grigoropoulos, G., Aloniati, E., Visonneau, M., Queutey, P., Stern, F., 2015. Multi-Objective Hydrodynamic Optimization of the DTMB 5415 for Resistance and Seakeeping, in: Day 2 Thu, September 03, 2015. SNAME, pp. 1–17. https://doi.org/10.5957/FAST-2015-034

Djatmiko, E.B., 2012. Behavior and Operability of Marine Buildings on Random Waves (in Indonesian). ITS-Press. Surabaya. Indonesia.

Domeh, V., Obeng, F., Khan, F., Bose, N., Sanli, E., 2021. Risk analysis of man overboard scenario in a small fishing vessel. Ocean Engineering 229, 108979.

Eriksen, J.H., Nona, R.A., Mas, C., 2000. Common procedures for seakeeping in the ship design process. STANAG 4154, 2000.

Faltinsen, O.M., 2005. Hydrodynamics of high-speed marine vehicles. Cambridge university press.

FAO, 2000. The State of World Fisheries and Aquaculture Part 2: Selected Issues

Facing Fishers and Aquaculturists, the State of World Fisheries and Aquaculture. Food & Agriculture Org.

Fathi, D.E., 2018. ShipX Vessel Responses (VERES), User's Manual. SINTEF Ocean AS.

Fonseca, N., Soares, C.G., 2002. Sensitivity of the expected ships availability to different seakeeping criteria, in: International Conference on Offshore Mechanics and Arctic Engineering. pp. 595–603.

France, W.N., Levadou, M., Treakle, T.W., Paulling, J.R., Michel, R.K., Moore, C., 2003. An Investigation of Head-Sea Parametric Rolling and Its Influence on Container Lashing Systems. Marine Technology and SNAME News 40, 1–19. https://doi.org/10.5957/mt1.2003.40.1.1

Francescutto, A., 2001. An Experimental Investigation of Parametric Rolling in Head Waves. Journal of Offshore Mechanics and Arctic Engineering 123, 65–69. https://doi.org/10.1115/1.1355247

Galbraith, A., Boulougouris, E., 2015. Parametric rolling of the tumblehome hull using CFD, in: Proceedings of the 12th International Conference on the Stability of Ships and Ocean Vehicles. pp. 535–543.

Gammon, M.A., 2011. Optimization of fishing vessels using a Multi-Objective Genetic Algorithm. Ocean Engineering 38, 1054–1064. https://doi.org/10.1016/j.oceaneng.2011.03.001

Ghaemi, M.H., Olszewski, H., 2017. Total ship operability--review, concept and criteria. Polish maritime research 24, 74–81.

Ghamari, I., Faltinsen, O.M., Greco, M., Lugni, C., 2017. Parametric Resonance of a Fishing Vessel With and Without Anti-Roll Tank: An Experimental and Numerical Study, in: Volume 7A: Ocean Engineering. American Society of Mechanical Engineers, p. V07AT06A012. https://doi.org/10.1115/OMAE2017-62053

Ghamari, I., Greco, M., Faltinsen, O.M., Lugni, C., 2020. Numerical and experimental study on the parametric roll resonance for a fishing vessel with and without forward speed. Applied Ocean Research 101, 102272. https://doi.org/10.1016/j.apor.2020.102272

González, M.M., Sobrino, P.C., Álvarez, R.T., Casás, V.D., López, A.M., Peña, F.L., 2012. Fishing vessel stability assessment system. Ocean Engineering 41, 67–78.

Grigoropoulos, G.J., Loukakis, T.A., 1988. A new method for developing hull forms with superior seakeeping qualities. Proceedings of CADMO 88.

Guan, G., Wang, L., Geng, J., Zhuang, Z., Yang, Q., 2021. Parametric automatic optimal design of USV hull form with respect to wave resistance and seakeeping. Ocean Engineering 235, 109462. https://doi.org/10.1016/j.oceaneng.2021.109462

Guan, G., Zhuang, Z., Yang, Q., Wang, P., Jin, S., 2022. Hull form optimization design of SWATH with combination evaluations of resistance and seakeeping performance. Ocean Engineering 264, 112513. https://doi.org/10.1016/j.oceaneng.2022.112513

Gutsch, M., Sprenger, F., Steen, S., 2017. Design parameters for increased operability of offshore crane vessels, in: International Conference on Offshore Mechanics and Arctic Engineering. p. V009T12A029.

Gutsch, M., Steen, S., Sprenger, F., 2020. Operability robustness index as seakeeping performance criterion for offshore vessels. Ocean Engineering 217, 107931.

Hashimoto, H., Furusho, K., 2022. Influence of sea areas and season in navigation on the ship vulnerability to the parametric rolling failure mode. Ocean Engineering 266, 112714. https://doi.org/10.1016/j.oceaneng.2022.112714

Hasselmann, K.F., Barnett, T.P., Bouws, E., Carlson, H., Cartwright, D.E., Eake, K., Euring, J.A., Gicnapp, A., Hasselmann, D.E., Kruseman, P., others, 1973. Measurements of wind-wave growth and swell decay during the Joint North Sea Wave Project (JONSWAP). Ergaenzungsheft zur Deutschen Hydrographischen Zeitschrift, Reihe A.

He, G., Kashiwagi, M., 2014. A time-domain higher-order boundary element method for 3D forward-speed radiation and diffraction problems. Journal of Marine Science and Technology 19, 228–244.

Himeno, Y., 1981. Prediction of ship roll damping-state of the art. The University of Michigan, College of Engineering, Department of Naval Architecture and Marine Engineering, USA, Report No. 239.

Hirt, C.W., Nichols, B.D., 1981. Volume of fluid (VOF) method for the dynamics of free boundaries. Journal of computational physics 39, 201–225.

Hooft, J.P., 1987. Mathematical description of the manoeuvrability of high-speed surface ships.

Hooke, R., Jeeves, T.A., 1961. ``Direct Search''Solution of Numerical and Statistical Problems. Journal of the ACM (JACM) 8, 212–229.

Hosseini, S.H.S., 2009. CFD prediction of ship capsize: parametric rolling, broaching, surf-riding, and periodic motions. The University of Iowa.

Huang, F., Wang, L., Yang, C., 2015. Hull form optimization for reduced drag and improved seakeeping using a surrogate-based method, in: ISOPE International Ocean and Polar Engineering Conference. p. ISOPE--I.

Hüffmeier, J., Lundman, J., Elern, F., 2020. Trim and ballast optimization for a tnaker based on machine learning. Ecoprodigi, Intereg Baltic Sea region.

Ikeda, Y., 1979. On roll damping force of ship-effect of hull surface pressure created by bilge keels. University of Osaka Prefacture, Department of Naval Architecture, Japan, Report No. 00402, Published in: Journal of Society of Naval Architects of Japan, No. 165, 1979.

Ikeda, Y., Himeno, Y., Tanaka, N., 1977. On eddy making component of roll damping force on naked hull. Journal of the society of Naval Architects of Japan 1977, 54–64.

IMO, 2020. SDC 7/WP. 6 Finalization of Second Generation Intact Stability Criteria—Report of the Drafting Group on Intact Stability. IMO: London, UK.

IMO, 2008a. International Code of Intact Stability. London, UK.

IMO, 2008b. International Code on Intact Stability (IS Code).

Iqbal, M., Hadi, E.S., Pranamya, G., 2019. Geometry Optimization Of Centre Bulb To Reduce Wave Resistance On Catamaran Ship, in: International Conference on Ship and Offshore Technology (ICSOT) Indonesia. Semarang.

Iqbal, M., Terziev, M., Tezdogan, T., Incecik, A., 2024. Unsteady RANS CFD Simulation on the Parametric Roll of Small Fishing Boat under Different Loading Conditions. Journal of Marine Science and Application. https://doi.org/https://doi.org/10.1007/s11804-024-00427-0

Iqbal, M., Terziev, M., Tezdogan, T., Incecik, A., 2023. Operability analysis of traditional small fishing boats in Indonesia with different loading conditions. Ships and Offshore Structures 18, 1060–1079.

https://doi.org/10.1080/17445302.2022.2107300

ISSC, 1964. Proceedings of the 2nd International Ship Structures Congress. Delft, The Netherlands.

ITTC, 2014. Practical Guidelines for Ship Resistance CFD, ITTC – Recommended Procedures and Guidelines 27th.

ITTC, 2002. Final report and recommendations to the 23rd ITTC. Proceeding of 23rd ITTC: The Specialist Committee on Waves.

ITTC, I., 2011. Practical guidelines for ship CFD applications. Recommended Procedures and Guidelines 18.

Jin, D., Thunberg, E., 2005. An analysis of fishing vessel accidents in fishing areas off the northeastern United States. Safety Science 43, 523–540.

Kato, H., 1957. On the frictional resistance to the rolling of ships. Journal of Zosen Kiokai 1957, 115–122.

Khosravi Babadi, M., Ghassemi, H., 2024. Optimization of ship hull forms by changing CM and CB coefficients to obtain optimal seakeeping performance. Plos one 19, e0302054.

Kim, H., Yang, C., 2010. A new surface modification approach for CFD-based hull form optimization. Journal of Hydrodynamics 22, 503–508.

Lackenby, H., 1950. On the systematic geometrical variation of ship forms. Transactions of the TINA 92, 289–316.

Liapis, S.J., Beck, R., 1985. Seekeeping computations using time-domain analysis, in: Proceeding of the Fourth International Symposium on Numerical Hydrodynamics. pp. 34–54.

Lin, W.-M., Salvesen, N., 1997. Nine Years of Progress with LAMP-The Large Amplitude Motion Program. Science Applications International Corp Report SAIC-97/1079.

Liu, L., Chen, M., Wang, X., Zhang, Z., Yu, J., Feng, D., 2021. CFD prediction of full-scale ship parametric roll in head wave. Ocean Engineering 233, 109180. https://doi.org/10.1016/j.oceaneng.2021.109180

Liu, L., Feng, D., Wang, X., Zhang, Z., Yu, J., Chen, M., 2022. Numerical study on the effect of sloshing on ship parametric roll. Ocean Engineering 247, 110612. https://doi.org/10.1016/j.oceaneng.2022.110612

Liu, P.C., 1971. Normalized and equilibrium spectra of wind waves in Lake Michigan. Journal of physical oceanography 1, 249–257.

Liu, W., Demirel, Y.K., Djatmiko, E.B., Nugroho, S., Tezdogan, T., Kurt, R.E., Supomo, H., Baihaqi, I., Yuan, Z., Incecik, A., 2019. Bilge keel design for the traditional fishing boats of Indonesia's East Java. International Journal of Naval Architecture and Ocean Engineering 11, 380–395. https://doi.org/10.1016/j.ijnaoe.2018.07.004

Liu, Y., Liu, L., Maki, A., Bu, S., Dostal, L., 2023. Research on second level of vulnerability criteria of parametric rolling with stochastic stability theory. Ocean Engineering 284, 115043. https://doi.org/10.1016/j.oceaneng.2023.115043

Lu, J., Gu, M., Umeda, N., 2016. A study on the effect of parametric roll on added resistance in regular head seas. Ocean Engineering 122, 288–292. https://doi.org/10.1016/j.oceaneng.2016.06.016

Ma, S., Ge, W., Ertekin, R.C., He, Q., Duan, W., 2018. Experimental and Numerical Investigations of Ship Parametric Rolling in Regular Head Waves. China Ocean Engineering 32, 431–442. https://doi.org/10.1007/s13344-018-0045-6

Mantari, J.L., e Silva, S.R., Soares, C.G., 2011. Intact stability of fishing vessels under combined action of fishing gear, beam waves and wind. Ocean engineering 38, 1989–1999.

Marín López, J.R., Villamarín, E.G., Mendoza, J.I., Paredes, R.J., Datla, R., 2021. Conceptual design recommendations to improve seakeeping of small high-speed craft providing interisland transportation in Galápagos, in: SNAME International Conference on Fast Sea Transportation. p. D021S003R004.

Marlantes, K.E., Kim, S. (Peter), Hurt, L.A., 2021. Implementation of the IMO Second Generation Intact Stability Guidelines. Journal of Marine Science and Engineering 10, 41. https://doi.org/10.3390/jmse10010041

Maruo, H., 1963. Resistance in waves, research on seakeeping qualities of ships in Japan. The Society of Naval Architects of Japan 8, 67–102.

Maruyama, Y., Maki, A., Dostal, L., Umeda, N., 2023. Estimation of acceleration probability density function for parametric rolling using PLIM. Ocean Engineering 280, 114561. https://doi.org/10.1016/j.oceaneng.2023.114561

Mata-Álvarez-Santullano, F., Souto-Iglesias, A., 2014. Stability, safety and operability of small fishing vessels. Ocean Engineering 79, 81–91. https://doi.org/10.1016/j.oceaneng.2014.01.011

Mathews, S.T., 1972. A critical review of the 12th ITTC Wave Spectrum Recommendations, Report of Seakeeping Committee, Appendix 9. Proceedings of 13th I TTC, Berlin 973–986.

Menter, F.R., 1994. Two-equation eddy-viscosity turbulence models for engineering applications. AIAA Journal 32, 1598–1605. https://doi.org/10.2514/3.12149

Miao, A., Chen, T., Qi, X., Wan, D., 2018. Multi-objective optimization design of KCS based on seakeeping performance, in: ISOPE International Ocean and Polar Engineering Conference. p. ISOPE--I.

Miller, E.R., 1974. Roll Damping. Technical Report 6136-74-280, 1974, NAVSPEC.

Muawanah, U., Yusuf, G., Adrianto, L., Kalther, J., Pomeroy, R., Abdullah, H., Ruchimat, T., 2018. Review of national laws and regulation in Indonesia in relation to an ecosystem approach to fisheries management. Marine Policy 91, 150–160.

Muzaferija, S., 1998. Computation of free surface flows using interface-tracking and interface-capturing methods. Nonlinear water-wave interaction. Computational Mechanics, Southampton.

Myrhaug, D., Dahle, E.A., 1994. Chapter 2: Ship capsize in breaking waves, in: Chakrabarti, S.K. (Ed.), Fluid Structure InteracΘon in Offshore Engineering.

Nakos, D., Sclavounos, P., 1991. Ship motions by a three-dimensional Rankine panel method.

Neves, M.A.S., 2002. Experimental Analysis on Parametric Resosnance for Two Fishing Vessels in Head Seas, in: Proceedings of the 6th International Ship Stability Workshop, Webb Institute, Proceedings. Paper: P2002-1.

Neves, M.A.S., Pérez, N.A., Lorca, O.M., Rodr\'\iguez, C.A., 2011. An Investigation on Head-Sea Parametric Rolling for Two Fishing Vessels, in: Contemporary Ideas on Ship Stability and Capsizing in Waves. Springer, pp. 231–252.

Neves, M.A.S., Pérez, N.A., Valerio, L., 1999. Stability of small fishing vessels in longitudinal waves. Ocean Engineering 26, 1389–1419. https://doi.org/10.1016/S0029-8018(98)00023-7

Neves, M.A.S., Rodríguez, C.A., 2006. On unstable ship motions resulting from strong non-linear coupling. Ocean Engineering 33, 1853–1883. https://doi.org/10.1016/j.oceaneng.2005.11.009

Nielsen, I.R., 1987. Assessment of ship performance in a seaway. Publisher: NORDFORSK, Sortedam Dossering 19, DK-200 Copenhage, Denmark, ISBN: 87-982637-1-4.

Niklas, K., Pruszko, H., 2019. Full scale CFD seakeeping simulations for case study ship redesigned from V-shaped bulbous bow to X-bow hull form. Applied Ocean Research 89, 188–201.

O'Hanlon, J.F., McCauley, M.E., 1973. Motion sickness incidence as a function of the frequency and acceleration of vertical sinusoidal motion.

Obeng, F., Domeh, V., Khan, F., Bose, N., Sanli, E., 2022a. Capsizing accident scenario model for small fishing trawler. Safety science 145, 105500.

Obeng, F., Domeh, V., Khan, F., Bose, N., Sanli, E., 2022b. Analyzing operational risk for small fishing vessels considering crew effectiveness. Ocean Engineering 249, 110512.

Ochi, M.K., 1964. Prediction of occurrence and severity of ship slamming at sea, in: David Taylor Model Basin, Naval Ship Research and Development Center, Washington DC, USA, Proceedings of the 5th Symposium on Naval Hydrodynamics, ONR, Bergen, Norway, Pp. 545-596, Paper: P1964-2 Proceedings.

Ochi, M.K., Hubble, E.N., 1976. Six-parameter wave spectra, in: Proceedings of the 15th Coastal Engineering Conference. Honolulu, USA, pp. 301–328.

Ozmen, G., 1995. Hull Form Optimisation of Fishing Vessels With Respect to Seakeeping. Phd Thesis. University of Glasgow.

Ozturk, D., Delen, C., Mancini, S., Serifoglu, M.O., Hizarci, T., 2021. Full-Scale CFD Analysis of Double-M Craft Seakeeping Performance in Regular Head Waves. Journal of Marine Science and Engineering 9, 504. https://doi.org/10.3390/jmse9050504

Park, D.-M., Kim, Y., Song, K.-H., 2013. Sensitivity in numerical analysis of parametric roll. Ocean Engineering 67, 1–12. https://doi.org/10.1016/j.oceaneng.2013.04.008

Paulling, J.R., Rosenberg, R.M., 1959. On Unstable Ship Motions Resulting From Nonlinear Coupling. Journal of Ship Research 3, 36–46. https://doi.org/10.5957/jsr.1959.3.2.36

Pérez-Arribas, F., Silva-Campillo, A., D\'\iaz-Ojeda, H.R., 2022. Design of Dihedral Bows: A New Type of Developable Added Bulbous Bows—Experimental Results. Journal of Marine Science and Engineering 10, 1691.

Perez, T., 2015. Ship seakeeping operability, motion control, and Autonomy-A Bayesian Perspective. IFAC-PapersOnLine 48, 217–222.

Pierson Jr, W.J., Moskowitz, L., 1964. A proposed spectral form for fully developed wind seas based on the similarity theory of SA Kitaigorodskii. Journal of geophysical research 69, 5181–5190.

Ravenna, R., Song, S., Shi, W., Sant, T., De Marco Muscat-Fenech, C., Tezdogan, T., Demirel, Y.K., 2022. CFD analysis of the effect of heterogeneous hull roughness on ship resistance. Ocean Engineering 258, 111733. https://doi.org/10.1016/j.oceaneng.2022.111733

Reichel, M., Minchev, A., Larsen, N.L., 2014. Trim optimisation-theory and practice. TransNav: International Journal on Marine Navigation and Safety of Sea

Transportation 8.

Riberio e Silva, S., Turk, A., Guedes Soares, C., PRPIĆ-ORŠIĆ, J., 2010. On the parametric rolling of container vessels. Brodogradnja: Teorija i praksa brodogradnje i pomorske tehnike 61, 347–358.

Richardson, L.F., 1911. IX. The approximate arithmetical solution by finite differences of physical problems involving differential equations, with an application to the stresses in a masonry dam. Philosophical Transactions of the Royal Society of London. Series A, Containing Papers of a Mathematical or Physical Character 210, 307–357. https://doi.org/10.1098/rsta.1911.0009

Roache, P.J., 1998. Verification and validation in computational science and engineering. Hermosa Albuquerque, NM.

Rodríguez, C.A., Ramos, I.S., Esperança, P.T.T., Oliveira, M.C., 2020. Realistic estimation of roll damping coefficients in waves based on model tests and numerical simulations. Ocean Engineering 213, 107664. https://doi.org/10.1016/j.oceaneng.2020.107664

Romanowski, A., Tezdogan, T., Turan, O., 2019. Development of a CFD methodology for the numerical simulation of irregular sea-states. Ocean Engineering 192, 106530.

Romero-Tello, P., Gutierrez-Romero, J.E., Serván-Camas, B., 2022. Seakeeping optimization of cruise ship based on artificial neural networks. Trends in Maritime Technology and Engineering 435–441.

Rotteveel, E., Hekkenberg, R., van der Ploeg, A., 2017. Inland ship stern optimization in shallow water. Ocean Engineering 141, 555–569.

Roy, R., Hinduja, S., Teti, R., 2008. Recent advances in engineering design optimisation: Challenges and future trends. CIRP annals 57, 697–715.

Sadat-Hosseini, H., Stern, F., Olivieri, A., Campana, E.F., Hashimoto, H., Umeda, N., Bulian, G., Francescutto, A., 2010. Head-wave parametric rolling of a surface combatant. Ocean Engineering 37, 859–878. https://doi.org/10.1016/j.oceaneng.2010.02.010

Salvesen, N., Tuck, E.O., Faltinsen, O., 1970. Ship Motions and Sea Loads. Transactions of the Society of Naval Architects and Marine Engineers 78, 250–287.

Sandvik, E., Gutsch, M., Asbjørnslett, B.E., 2018. A simulation-based ship design methodology for evaluating susceptibility to weather-induced delays during marine operations. Ship Technology Research 65, 137–152.

Sariöz, K., Sariöz, E., 2006. Practical seakeeping performance measures for high speed displacement vessels. Naval engineers journal 118, 23–36.

Sarıöz, E., 2009. Inverse design of ship hull forms for seakeeping. Ocean Engineering 36, 1386–1395. https://doi.org/10.1016/j.oceaneng.2009.08.011

Sayli, A., Alkan, A.D., Nabergoj, R., Uysal, A.O., 2007. Seakeeping assessment of fishing vessels in conceptual design stage. Ocean Engineering 34, 724–738.

Schumacher, A., Ribeiro e Silva, S., Guedes Soares, C., 2016. Experimental and numerical study of a containership under parametric rolling conditions in waves. Ocean Engineering 124, 385–403. https://doi.org/10.1016/j.oceaneng.2016.07.034

Scott, J.R., 1965. A sea spectrum for model tests and long-term ship prediction. Journal of ship research 9, 145–152.

Serani, A., Ficini, S., Grigoropoulos, G., Bakirtzogou, C., Broglia, R., Diez, M., Papadakis, G., Goren, O., Danisman, D.B., Scholcz, T., others, 2022. Resistance and seakeeping optimization of a naval destroyer by multi-fidelity methods. VCG 1000, 0–56.

Shivachev, E., Khorasanchi, M., Day, S., Turan, O., 2020. Impact of trim on added resistance of KRISO container ship (KCS) in head waves: An experimental and numerical study. Ocean Engineering 211, 107594.

Siemens, 2022. Star-CCM+ User Guide version 17.02.

Simonsen, C.D., Otzen, J.F., Joncquez, S., Stern, F., 2013. EFD and CFD for KCS heaving and pitching in regular head waves. Journal of Marine Science and Technology 18, 435–459.

Spanos, D., Papanikolaou, A., 2007. Numerical simulation of parametric roll in head seas. International Shipbuilding Progress 54, 249–267.

Spanos, D., Papanikolaou, A., 2006. Numerical simulation of a fishing vessel in parametric roll in head seas. Marine Systems & Ocean Technology 2, 39–44. https://doi.org/10.1007/BF03449182

St Denis, M., Pierson, W.J., 1953. On the motions of ships in confused seas. Trans. Soc. Naval Architects and Marine Engineers 61, 280–357.

Statistics Indonesia, 2019. Number of Boats/Ships by Province and Type of Boats/Ships for Marine Fisheries, 2000-2016 (In Indonesian).

Stern, F., Wilson, R. V, Coleman, H.W., Paterson, E.G., 2001. Comprehensive Approach to Verification and Validation of CFD Simulations—Part 1: Methodology and Procedures. Journal of Fluids Engineering 123, 793–802. https://doi.org/10.1115/1.1412235

Tello, M., Ribeiro E Silva, S., Guedes Soares, C., 2011. Seakeeping performance of fishing vessels in irregular waves. Ocean Engineering 38, 763–773. https://doi.org/10.1016/j.oceaneng.2010.12.020

Tello, M., Ribeiro E Silva, S., Guedes Soares, C., 2009. Fishing Vessels Responses in Waves under Operational Conditions, in: Proceedings of the XXI Naval Architecture Pan-American Conference (COPINAVAL'09). pp. 18–22.

Terziev, M., Tezdogan, T., Incecik, A., 2022. Scale effects and full-scale ship hydrodynamics: A review. Ocean Engineering 245, 110496. https://doi.org/10.1016/j.oceaneng.2021.110496

Tezdogan, T., Demirel, Y.K., Kellett, P., Khorasanchi, M., Incecik, A., Turan, O., 2015. Full-scale unsteady RANS CFD simulations of ship behaviour and performance in head seas due to slow steaming. Ocean Engineering 97, 186–206. https://doi.org/10.1016/j.oceaneng.2015.01.011

Tezdogan, T., Incecik, A., Turan, O., 2016. Full-scale unsteady RANS simulations of vertical ship motions in shallow water. Ocean Engineering 123, 131–145. https://doi.org/10.1016/j.oceaneng.2016.06.047

Tezdogan, T., Incecik, A., Turan, O., 2014. Operability assessment of high speed passenger ships based on human comfort criteria. Ocean Engineering 89, 32–52.

Tezdogan, T., Shenglong, Z., Demirel, Y.K., Liu, W., Leping, X., Yuyang, L., Kurt, R.E., Djatmiko, E.B., Incecik, A., 2018. An investigation into fishing boat optimisation using a hybrid algorithm. Ocean Engineering 167, 204–220. https://doi.org/10.1016/j.oceaneng.2018.08.059

Tran, T.G., Nguyen, H.V., Huynh, Q. Van, 2023. A method for optimizing the hull form of fishing vessels. Journal of Ship Research 67, 72–91.

Ugurlu, F., Yildiz, S., Boran, M., Ugurlu, Ö., Wang, J., 2020. Analysis of fishing vessel accidents with Bayesian network and Chi-square methods. Ocean Engineering 198, 106956.

Utomo, B., Iqbal, M., 2020. Vertical Motion Optimization of Series 60 Hull Forms Using Response Surface Methods. Kapal: Jurnal Ilmu Pengetahuan dan Teknologi Kelautan 17, 130–137.

Vernengo, G., Brizzolara, S., Bruzzone, D., 2015. Resistance and seakeeping optimization of a fast multihull passenger ferry. International Journal of Offshore and Polar Engineering 25, 26–34.

Wackers, J., Koren, B., Raven, H.C., van der Ploeg, A., Starke, A.R., Deng, G.B., Queutey, P., Visonneau, M., Hino, T., Ohashi, K., 2011. Free-Surface Viscous Flow Solution Methods for Ship Hydrodynamics. Archives of Computational Methods in Engineering 18, 1–41. https://doi.org/10.1007/s11831-011-9059-4

Wang, J., Pillay, A., Kwon, Y.S., Wall, A.D., Loughran, C.G., 2005. An analysis of fishing vessel accidents. Accident Analysis & Prevention 37, 1019–1024.

Wang, S.M., Ma, S., Duan, W.Y., 2018. Seakeeping optimization of trimaran outrigger layout based on NSGA-II. Applied Ocean Research 78, 110–122. https://doi.org/10.1016/j.apor.2018.06.010

Wen, P., Fadillah, A., 2022. The Effect of Trim on Stability and Seakeeping of Tanker, Container, and Bulk Carrier, in: IOP Conference Series: Earth and Environmental Science. p. 12037.

Wulandari, A.I., Utama, I., Rofidayanti, A., Hudson, D., 2024. Numerical analysis of ship motion of crew boat with variations of wave period on ship operational speed. CFD Letters 16.

Xiaobo, Z., 2017. Comparison of response surface method and Kriging method for approximation modeling, in: 2017 2nd International Conference on Power and Renewable Energy (ICPRE). pp. 66–70.

Xing, T., Stern, F., 2010. Factors of safety for Richardson extrapolation.

Yu, L., Ma, N., Wang, S., 2019. Parametric roll prediction of the KCS containership in head waves with emphasis on the roll damping and nonlinear restoring moment. Ocean Engineering 188, 106298. https://doi.org/10.1016/j.oceaneng.2019.106298

Yu, L., Taguchi, K., Kenta, A., Ma, N., Hirakawa, Y., 2018. Model experiments on the early detection and rudder stabilization of KCS parametric roll in head waves. Journal of Marine Science and Technology 23, 141–163. https://doi.org/10.1007/s00773-017-0463-9

Yulianti, S., Samuel, S., Nainggolan, T.S., Iqbal, M., 2022. Meshing generation strategy for prediction of ship resistance using CFD approach. IOP Conference Series: Earth and Environmental Science 1081, 012027. https://doi.org/10.1088/1755-1315/1081/1/012027

Zhang, L., Zhang, J., Shang, Y., 2021. A practical direct URANS CFD approach for the speed loss and propulsion performance evaluation in short-crested irregular head waves. Ocean Engineering 219, 108287.

Zhang, S., Tezdogan, T., Zhang, B., Xu, L., Lai, Y., 2018. Hull form optimisation in waves based on CFD technique. Ships and Offshore Structures 13, 149–164. https://doi.org/10.1080/17445302.2017.1347231

Zhao, C., Wang, W., Jia, P., Xie, Y., 2021. Optimisation of hull form of ocean-going trawler. Brodogradnja: An International Journal of Naval Architecture and Ocean Engineering for Research and Development 72, 33–46.

Zhou, Y., 2019. Further validation study of hybrid prediction method of parametric roll. Ocean Engineering 186, 106103. https://doi.org/10.1016/j.oceaneng.2019.06.008

Zhou, Y., Ma, N., Lu, J., Gu, M., 2016. A study of hybrid prediction method for ship parametric rolling. Journal of Hydrodynamics 28, 617–628. https://doi.org/10.1016/S1001-6058(16)60666-2

Zhou, Y., Sun, Q., Shi, X., 2022. Experimental and numerical study on the parametric roll of an offshore research vessel with extended low weather deck. Ocean Engineering 262, 111914. https://doi.org/10.1016/j.oceaneng.2022.111914

Publications

The following publications have been published or submitted to publication as research output from this Ph.D thesis.

Journal Articles:

1. Iqbal, M., Terziev, M., Tezdogan, T., Incecik, A., 2023. Operability analysis of traditional small fishing boats in Indonesia with different loading conditions. Ships and Offshore Structures 18, 1060–1079. https://doi.org/10.1080/17445302.2022.2107300

2. Iqbal, M., Terziev, M., Tezdogan, T., Incecik, A., 2024. Unsteady RANS CFD Simulation on the Parametric Roll of Small Fishing Boat under Different Loading Conditions. Journal of Marine Science and Application. https://doi.org/https://doi.org/10.1007/s11804-024-00427-0

3. Iqbal, M., Terziev, M., Tezdogan, T., Incecik, A., 2024. Minimising Radius of Gyration to Enhance Seakeeping Performance of Small Fishing Vessels. (Submitted to Journal of Marine Science and Tecnology, Japan).

4. Iqbal, M., Terziev, M., Tezdogan, T., Incecik, A., 2024. Minimising GM Ratio to Enhanced Seakeeping Performance of Small Fishing Vessels. (Submitted to Ship Technology Research).

5. Iqbal, M., Terziev, M., Tezdogan, T., Incecik, A., 2024. Hull form Optimisation to Minimise the Total Resistance and Dynamic Responses of Small Fishing Vessels. (Submitted to Ocean Engineering).

Conference Papers:

1. Iqbal, M. 2023. Assessing fishing vessel operability under changing loads: a case study in the Java Sea. In International Conference on Postgraduate Research in Maritime Technology 2023.
2. Iqbal, M., Terziev, M., Tezdogan, T., & Incecik, A. 2024. Improving seakeeping performance of fishing boats by minimising radius of gyration. in Global Maritime Congress, Istanbul, Turkiye.

Conference Posters:

1. Iqbal, M. 2024. Fish Placement Strategy for Fisherman Safety. STEM for Britain Competition (as a finalist), London, United Kingdom.

2. Iqbal, M., Terziev, M., Tezdogan, T., & Incecik, A. 2024. Fisherman Safety from Onboard Fish Deployment Perspective. in UK Marine Technology Postgraduate Conference (MTPC), Southampton, United Kingdom.

e-Book:

1. Iqbal, M. 2024. Introduction to the Bacis CFD (in Indonesian). Andi Publihser: Yogyakarta, Indonesia. Available at: https://play.google.com/store/books/details/Muhammad_Iqbal_Pengantar_Dinamika_Fluida_Komputasi?id=5ab8EAAAQBAJ